IN-27
311337

AN INVESTIGATION OF RELIABILITY MODELS FOR CERAMIC MATRIX COMPOSITES AND THEIR IMPLEMENTATION INTO FINITE ELEMENT CODES

Final Report

Principal Investigator:
Professor Stephen F. Duffy PhD, PE

Reporting Period:
June 9, 1993 - June 30, 1998

Cleveland State University
1983 East 24th Street
Cleveland, Ohio 44115

Grant Number:
NASA Cooperative Agreement NCC 3-305

NASA GRANTEE
NEW TECHNOLOGY REPORT

NASA requires each research grantee, research contractor, and research subcontractor to report new technology to the NASA Technology Utilization Office. The required reports and corresponding schedules are as follows:

Title of Report	Form Number	Timetable
Individual Disclosure	NASA 666A	The grantee discloses each discovery of new technology individually, at the time of its discovery.
Interim Report	NASA C-3043	For multi-year grants, the grantee summarizes the previous year's disclosures on an annual basis. The first Interim New Technology (NT) Report is due exactly 12 months from the effective date of the grant.
Final Report	NASA C-3043	The grantee submits a cumulative summary of all disclosed discoveries. This Final NT Report is submitted immediately following the grant's technical period of performance.

Grantee Name and Address:
Stephen F. Duffy, Ph.D., P.E.
Department of Civil & Environmental Engineering
Cleveland State University
Cleveland, Ohio 44115

Report Submitted by: Stephen F. Duffy, Ph.D., P.E.

Telephone Number: (216) 687-3874

NASA Grant Title: "An Investigation of Reliability Models for Ceramic Matrix Composites and Their Implementation Into Finite Element Codes"

NASA Grant Number: NCC 3- 305

NASA Project Manager: Noel M. Nemeth

Grant Completion Date: 06/ 30/ 98

Today's Date: 09/ 25/ 98

New technology may be either reportable items or subject inventions.

A **reportable item** is any invention or discovery, whether or not patentable, that was conceived or first actually reduced to practice during the performance of the grant, contract or subcontract. Large business contractors and subcontractors must disclose reportable items as they are discovered and submit a noncumulative list of these new technology items on an annual basis [ref: Interim NT Report] and a cumulative list at the completion of the grant, contract (or subcontract) period [ref: Final NT Report].

A **subject invention** is any invention or discovery, which is or may be patentable, that was conceived or first actually reduced to practice during the performance of the contract or subcontract. Grantees, small business contractors and subcontractors must, at a minimum, disclose subject inventions as they are discovered and submit a cumulative list of these new technology items on an annual basis [ref: Interim NT Report] and at the completion of the grant, contract (or subcontract) period [ref: Final NT Report].

Grantees, small business contractors and small business subcontractors are only required to disclose and report patentable items (subject inventions). However, we encourage that grantees, small business contractors and small business subcontractors disclose both patentable and nonpatentable (reportable) items, both of which are automatically evaluated for publication as NASA tech briefs and considered for NASA *Tech Brief* awards.

PLEASE COMPLETE THE REVERSE SIDE OF THIS FORM AND MAIL TO THE FOLLOWING ADDRESS:

NASA Lewis Research Center
Attn: Kathy Kerrigan
Technology Utilization Office; Mail Stop 7-3
Cleveland, Ohio 44135

CLEVELAND STATE UNIVERSITY
GRANT EQUIPMENT INVENTORY

UPDATE: ☐ **INTERIM:** ☐ **FINAL:** ☒

GRANT NO.: NCC-3-305 **SUPPL.NO. (If Applicable)** ______ **ORS No:** DFY-R-6

GRANT BEGINNING DATE: June 9, 1993 **GRANT EXPIRES ON:** June 30, 1998

PRINCIPAL INVESTIGATOR: Stephen F. Duffy, Ph.D., P.E. (SIGNATURE) 9/25/98 (DATE)

GRANT TITLE: "An Investigation of Reliability Models for Ceramic Matrix Composites and Their Implementation Into Finite Element Codes"

GRANTEE-ACQUIRED EQUIPMENT: EQUIPMENT WHOSE ACQUISITION COST IS $1,000 OR GREATER THAT WAS PURCHASED OR FABRICATED WITH GRANT FUNDS BY A GRANTEE.

Description	Model#	CSU REQ. NO.	ACQ. DATE	Equip Cost	*Cond. Code	TAG NO.	Location
NONE							

THE PRINCIPAL INVESTIGATOR WISHES TO RETAIN POSSESSION OF THIS EQUIPMENT UPON EXPIRATION OF THE GRANT: **YES** ☐ **NO** ☐

*Equipment Condition Codes:

4= Good
5 = Fair

7=Repairs Req'd (<15% of Acq Cost)
8=Reparis Req'd (16-40% of Acq Cost)
9=Repairs Req'd (41-65% of Acq Cost)

X=Salvage (>65% of Acq Cost)
S=Scrap(Value is material Content only

GOVERNMENT-FURNISHED EQUIPMENT INVENTORY

Grant No.: NCC-3-305

ORS No: DFY-R-6

Principal Investigator: Stephen F. Duffy, Ph.D., P.E.

Grant Expiration: June 30, 1998

Status: Final

DISPOSITION INSTRUCTIONS

☐ RETURN

☐ TRANSFER TO ANOTHER GRANT

☐ RETAIN

Description	Model#	Furnished Date	Equip Cost	*Cond. Code	Location
NONE					

September 25, 1998
(Date)

(I, the principal investigator, certify that the above information is correct)

*Equipment Condition Codes:

4= Good
5 = Fair
6=Poor

7=Repairs Req'd (<15% of Acq Cost)
8=Reparis Req'd (16-40% of Acq Cost)
9=Repairs Req'd (41-65% of Acq Cost)

X=Salvage (>65% of Acq Cost)
S=Scrap(Value is material Content only)

Introduction

The development of modeling approaches for the failure analysis of ceramic-based material systems used in high temperature environments was the primary objective of this research effort. These materials have the potential to support many key engineering technologies related to the design of aeropropulsion systems. Monolithic ceramics exhibit a number of useful properties such as retention of strength at high temperatures, chemical inertness, and low density. However, the use of monolithic ceramics has been limited by their inherent brittleness and a large variation in strength. This behavior has motivated material scientists to reinforce the monolithic material with a ceramic fiber. The addition of a second ceramic phase with an optimized interface increases toughness and marginally increases strength. The primary purpose of the fiber is to arrest crack growth, not to increase strength. The material systems of interest in this research effort were laminated ceramic matrix composites, as well as two- and three-dimensional fabric reinforced ceramic composites. These emerging composite systems can compete with metals in many demanding applications. However, the ongoing metamorphosis of ceramic composite material systems, and the lack of standardized design data has in the past tended to minimize research efforts related to structural analysis. Many structural components fabricated from ceramic matrix composites (CMC) have been designed by "trial and error." The justification for this approach lies in the fact that during the initial developmental phases for a material system fabrication issues are paramount. Emphasis is placed on demonstrating feasibility rather than fully understanding the processes controlling mechanical behavior. This is understandable during periods of rapid improvements in material properties for any composite system. But to avoid the ad hoc approach, the analytical methods developed under this effort can be used to develop rational structural design protocols.

In regards to predicting composite failure behavior, there is a philosophical division that separates analytical schools of thought into microstructural methods (usually based on principles of fracture mechanics), and phenomenological methods. Analysts from the first school would design the material in the sense that the constituents are distinct structural components, and the composite ply (or lamina) is considered a structure in its own right. Rigorous fracture mechanics criteria have been proposed that adopt the microstructural viewpoint, but all are deterministic criteria. Mature reliability based design methods using fracture mechanics concepts will not surface until a coherent mixed mode fracture criterion has been proposed and verified experimentally.

Analysts from the latter school of thought would design with the material (i.e., analyze structural components fabricated from the material). Here the ply (or lamina) is represented as a homogenized material with strength properties that are determined from a number of well planned phenomenological experiments. This philosophy was embraced in this research effort. There are practical reasons for adopting this viewpoint. It is recognized that the failure characteristics of laminated ceramic composites are controlled by a number of local phenomena including matrix cracking, debonding and slipping between matrix and fibers, and fiber breakage, all of which strongly interact. Understanding the analytical concepts associated with the microstructural viewpoint provides insight and intuition prior to constructing multiaxial failure theories that reflect certain aspects of local behavior. It is noted that future work could extend reliability methods to the constituent level in a rational and practical manner. However, a top-down approach, that is proposing failure criteria at the ply level (the approach adopted in this research effort), established a viable and working design protocols. Adopting the bottom-up approach allowed the possibility of becoming mired in detail (experimental and analytical) when multiaxial reliability analyses were required.

There is a great deal of intrinsic variability in the strength of each brittle constituent of a ceramic matrix composite, but depending on the composite system, the transverse matrix cracking strength may either be deterministic or probabilistic. Experimental evidence has appeared in the open literature that strongly indicates a large variation in the stress at which transverse matrix cracking occurs in CMC material systems of interest in aerospace applications. Statistical models are a necessity for those composite systems which exhibit scatter in strength. For this research effort strength is treated in a probabilistic fashion, requiring that a deterministic value for strength be a limiting case that is readily obtained from the proposed reliability model. A number of macroscopic reliability theories existed at the start of this research effort that treat unidirectional composites as homogenized, anisotropic materials. These methods use phenomenological strength data directly without hypothesizing specific crack shapes or distributions. Theories of this genre are generally termed noninteractive if individual stress components are compared to their strengths separately. This modeling approach results in component reliability computations that are quite tractable. Work by Duffy and Arnold (1990), Duffy and Manderscheid (1990), and Duffy et al. (1990) are representative of multiaxial noninteractive reliability models for anisotropic materials. Alternatively, one can assume that for multiaxial states of stress, failure depends on specific stochastic combinations of material strengths (i.e., the random strength variables interact). An interactive failure criterion was developed by the principal investigator and his colleagues (see Palko, 1992, for a complete overview). This model was formulated for isotropic whisker-toughened ceramic composites, where the probability of failure for a given stress state is computed using Monte Carlo methods. It was demonstrated that models of this type can readily be extended to other composite architectures in a manner outlined by and Duffy and Palko, 1992.

In the following sections a more detailed report of the work and accomplishments associated with this research effort is presented in a chronological fashion.

C/CARES Algorithm (1993-1994)

As in other types of structural analysis of components (e.g., deformation analysis, stability analysis, etc.), the stress field must be characterized in order to perform reliability computations. Several commercial finite element programs (e.g., MSC/NASTRAN, MARC, ABAQUS, and ANSYS) have laminate analysis capabilities that allow the design engineer to determine the structural response of components subjected to thermo-mechanical loads. Coupling these finite element programs to an integrated probabilistic composite design program that evaluates component reliability is an attractive analytical tool. The test-bed computer program C/CARES (Composite Ceramics Analysis and Reliability Evaluation of Structures preliminary details are outlined in Duffy and Gyekenyesi, 1990; Duffy et. al., 1991; and Starlinger et. al., 1992) is representative of this type of integrated design program. The primary function of the C/CARES program is the computation of quasi-static reliability of laminated structural components subjected to multiaxial load conditions. Through the use of this computer algorithm, design engineers can maximize component reliability by optimizing ply lay-ups, component geometry, and applied loads. A preliminary version of the algorithm has been completed and released to several American companies.

A preliminary version of the C/CARES program was completed and several improvements were implemented under this research effort. Specifically, an interface for the ANSYS finite element program was added to the algorithm. This program is operational with

ANSYS version 5.0. This interface supports the use of the subelement technique outlined in Starlinger et. al., 1992. Several suggestions from users were also implemented in the code.

An article about the algorithm was written by the research associate and submitted to the 1993 International Gas Turbine Institute Technology Report. This article was included in the report thus providing C/CARES with international exposure. This technology report targets a key design community which is interested in the advancement of CMC material systems. Other similar articles highlighting the algorithm have appeared in reports such as the 1993 NASA Research and Technology Report, and branch brochures.

User support was provided for the code. This includes the presentation of the algorithm in a workshop at NASA Lewis Research Center which showcased several codes developed under the HITEMP program. A number of American industrial clients were invited to partake in the interactive workshop. The workshop included a presentation highlighting the technical details of the C/CARES algorithm, as well as a hands on example session where the participants interactively used the algorithm in a simulated design analysis. As a result of this workshop and continual effort on the part of the research associate sponsored by this grant, the C/CARES users base grew moderately. A continuous and stable support system has also been established where the research associate provides hot-line support for the user community.

The C/CARES code has also been presented to participants in the DOE sponsored Continuous Fiber Ceramic Composite program. Meetings were held at NASA LeRC which were attended by participants in this program. The details of C/CARES and example problems were presented to the participants to make them aware of its capabilities. The intent was to include C/CARES in the CFCC program as a design option for ceramic composite components. Along these lines, the C/CARES algorithm was used in the design of a laminated CMC heat exchanger for industrial furnace applications. The results of this design analysis were presented at the 6th Annual HITEMP Review (see Palko and Duffy, 1993). This is another example of technology transfer and support provided to American industry under the auspices of this grant.

Interactive Reliability Models (1993-1994)

An interactive reliability criteria for laminated composite materials was developed during this time period. To increase efficiency of the programs, steps have been taken to implement fast probability integration in place of Monte Carlo simulation when implementing these interactive routines. Along these lines a research associate supported by this grant attended "A Short Course of Modern Reliability Methods" at NASA Marshall Space Flight Center in Huntsville, Alabama. This class covered methods that were needed to implement the alternative integration schemes for interactive failure models.

Alternative Fiber Architecture (1993-1994)

Fabricating structural components from laminated ceramic composite materials represents a progressive step forward in the utilization of advanced materials. However, in some design applications this material is not suitable due to the lack of through thickness reinforcing or poor transverse properties. For this reason, alternative fiber architectures were explored which include two- and three- dimensional weaves. Several models have been developed to predict the behavior of composites fabricated with these types of architectures (see Chou, 1992). These models are based on a unit-cell approach, where certain mechanical properties such as stiffness are evaluated for a single unit cell, and are then used to predict the structural response of a component. These models were studied during this time period for potential use in the C/CARES algorithm.

Publication (1993-1994)

✓ 1. "Parameter Estimation Based on Optimizing Goodness-of-Fit Statistics for Structural Reliability," A. Starlinger, S.F. Duffy, and J.L. Palko, Presented at the 10th Biennial ASME Conference on Stress Analysis, Reliability, and Failure Prevention, Sept. 19-22, 1993, Albuquerque, NM.

✓ 2. "Design of a Laminated CMC Heat Exchanger Using the C/CARES Algorithm," J.L. Palko and S.F. Duffy, Presented at the 6th Annual HITEMP Review, October 26-27, 1993, Westlake, OH.

/ 3. "Interactive Reliability Model for Whisker-Toughened Ceramics," J.L. Palko, NASA CR 191948, 1993.

✓ 4. "Structural Reliability Analysis of Laminated CMC Components," S.F. Duffy, J.L. Palko, and J.P. Gyekenyesi, *Transactions of the ASME - Journal of Engineering for Gas Turbines and Power*, Vol. 115, No. 1, pp. 103-108, January, 1993 (also published as NASA TM-103685).

/ 5. "Reliability Analysis of Structural Components Fabricated from Ceramic Materials Using a Three-Parameter Weibull Distribution," S.F. Duffy, L.M. Powers, and A. Starlinger, *Transactions of the ASME - Journal of Engineering for Gas Turbines and Power*, Vol. 115, No. 1, pp. 109-116, January, 1993 (also published as NASA TM-105370).

C/CARES Algorithm (1994-1995)

As in other types of structural analysis of components (e.g., deformation analysis, stability analysis, etc.), the stress field must be characterized in order to perform reliability computations. Several commercial finite element programs (e.g., MSC/NASTRAN, MARC, ABAQUS, ANSYS and COSMOS/M) have laminate analysis capabilities that allow the design engineer to determine the stress field of components subjected to thermo-mechanical loads. Coupling these finite element programs to an integrated probabilistic composite design program that evaluates component reliability is an attractive analytical tool. The test-bed computer program C/CARES (Composite Ceramics Analysis and Reliability Evaluation of Structures preliminary details are outlined in Duffy and Gyekenyesi, 1990; Duffy et. al., 1991; and Starlinger et. al., 1992) is representative of this type of integrated design program.

The primary function of the C/CARES program is the computation of quasi-static reliability of laminated structural components subjected to multiaxial load conditions. Through the use of this computer algorithm, design engineers can maximize component reliability by optimizing ply lay-ups, component geometry, and applied loads. A preliminary version of the algorithm has been completed and released to several American companies for beta testing. Thus during the past year efforts by grant personnel include distribution of the algorithm to American Industry, maintenance of the algorithm, and providing a users hot-line support. In addition, an interface for the COSMOS/M (version 1.70) finite element program was added to the algorithm in response to a request from the Department of Energy (DoE) Oak Ridge National Laboratory (ORNL). This interface utilizes the sub-element technique implemented with other C/CARES interfaces. This analytical technique is outlined in Starlinger et. al. (1992).

Several workshops on the use and implementation of the C/CARES program were conducted. This included a workshop held in conjunction with the 6th Annual NASA HITEMP Conference. Another workshop was held that preceded a biannual meeting reviewing the progress of the DoE Continuous Fiber Ceramic Composite (CFCC) program. These workshops provide American industries the basic reliability concepts and focus attention on the stochastic tools available in the C/CARES algorithm.

Interactive Reliability Model (1994-1995)

Details concerning the implementation of the Tsai-Hill interactive failure theory into a reliability model were investigated. Other interactive failure criteria came under consideration during this time period. These criteria focus on stochastic models for components fabricated from intermetallic material systems. These material systems exhibit brittle failure characteristics and a significant amount of scatter in failure strength. Additionally, the material strength varies depending on material direction. It was anticipated that these failure patterns could be captured through the use of models similar to that developed under this grant in previous years. A summary of this approach covering material characterization through component reliability analysis was presented at the 7th Annual HITEMP meeting (see Palko et. al., 1994).

Alternative Fiber Architectures (1994-1995)

A literature review was conducted that focused on design strategies for these material with alternative fiber architectures, which included two- and three- dimensional weaves. The information from the review proved essential as grant personnel become involved in a CMC nozzle project being coordinated by the NASA Marshal Space Flight Center.

Publications (1994-1995)

✓ 1. "Reliability Analysis of Single Crystal NiAl Turbine Blades," J.L. Palko, S.F. Duffy, J.A. Salem, R.D. Noebe, D.R. Wheeler, and F. Holland, Presented at the 7th Annual HITEMP Review, October 24-26, 1994, Westlake, OH.

✓ 2. "Reporting Strength Data and Estimating Weibull Distribution Parameters for Advanced Ceramics," S.F. Duffy, G.D. Quinn and C.A. Johnson, ASTM Standard Practice C 1239 - 94.

✓ 3. "Composites Research at NASA Lewis Research Center," S.R. Levine, S.F. Duffy, A. Vary, M.V. Nathal, R.V. Miner, S.M. Arnold, M.G. Castelli, D.A. Hopkins, and M.A. Meador, *Composites Engineering*, Vol. 4, No. 8, pp. 787-810.

✓ 4. "An Overview of Engineering Concepts and Current Design Algorithms for Probabilistic Structural Analysis," S.F. Duffy, J. Hu, and D.A. Hopkins, in Proceedings of the 1995 Design Engineering Technical Conferences - Volume 2, DE-Vol. 83, Boston, Massachusetts, pp. 3-16, September, 1995.

Time Dependent Reliability Analyses (1995-1998)

Expanding use of ceramic based material systems in high temperature applications has increased the need for robust analytical tools that particularly focus on life. As processing technologies advance, design methodologies must keep pace to provide the ceramics community with the appropriate set of analytical tools. Historically, two government agencies, the Department of Energy (DOE) and NASA, have sponsored research and development efforts in this area. Several design tools have been made available to the engineering design community that aid the design engineer in the analysis of components fabricated from ceramic material systems. One of the more popular algorithms is the NASA CARES (Ceramic Analysis and Reliability Evaluation of Structures) program which enables the prediction of component reliability for complex multiaxial stress states. This algorithm has been released to over 100 industrial institutions world-wide. In addition, a derivative of the CARES program (referred to earlier in this report as the C/CARES algorithm) has been developed for ceramic matrix composites. These integrated design programs are of great use to the companies involved in the fabrication of ceramic components or sub-systems such as segments of the automotive, aerospace, biomedical and electronics industries. Given the fact that the composites segment of the market is not a commercial success yet and the technologies needed to design components are relatively new, these industries have relied heavily on the government for analytical support when designing with these material systems. Specifically, several generations of the CARES program and other derivatives of this algorithm have been widely accepted by the design community. The original version of CARES addressed fast fracture of ceramic material systems. Later versions have included parameter estimation capabilities, and one current derivative concentrates on time dependent as well as cyclic loading issues (CARES/Life). During this time period efforts focused on providing support to make this software user friendly and computationally efficient. Specifically, work focused on error checking the CARES/Creep algorithm which is in the beta release phase. Likewise, work began on developing a time dependent version of the C/CARES algorithm. The CCARES/Life program is evolving, and assistance in developing this algorithm continued to the end of this research effort.

One shortcoming of the subcritical crack growth and creep damage theories is the fact that when implemented in a design analysis elastic stress fields are utilized. In addition, the assumption that the material behaves the same in tension and compression presents another possible area of improvement. A number of constitutive theories for materials that exhibit sensitivity to the hydrostatic component of stress have been proposed that characterize deformation using time-independent classical plasticity as a foundation. One such criterion for concrete, proposed by Willam and Warnke (1975) admits a dependence on the hydrostatic component of stress and explicitly allows different material responses in tension and compression. Several formulations of their model exist, i.e., a three-parameter formulation and a five-parameter formulation. For simplicity the work presented here builds on the three-parameter formulation. The aforementioned theories are somewhat lacking in that they are unable to capture creep, relaxation and rate-sensitive phenomena exhibited by ceramic materials at high temperature. When subjected to elevated service temperatures, ceramic materials exhibit complex thermo-mechanical behavior that is inherently time dependent, and hereditary in the sense that current behavior depends not only on current conditions, but also on thermo-mechanical history. This work presents the formulation of a macroscopic continuum theory that captures these time dependent phenomena. Specifically, the overview contained in this paper focuses on the complete multiaxial derivation of the constitutive model, and examines the attending geometrical implications when the Willam-Warnke yield function is utilized as a scalar threshold function. In response to this, efforts funded under this grant have focused on the development of a multiaxial constitutive theory for deformation that addresses these critical issues and can be applied to ceramic materials. This work has been published in a paper by Janosik and Duffy (1998).

Publications (1995-1998)

1. "Comparison of Tension and Flexure to Determine Fatigue Life Prediction Parameters at Elevated Temperatures," S.R. Choi, J.A. Salem, and J.L. Palko, in Life Prediction Methodologies and Data for Ceramic Materials, ASTM STP 1201, C.R. Brinkman and S.F. Duffy, Eds., American Society for Testing and Materials, 1994, pp. 98-111.
2. "A Viscoplastic Constitutive Theory for Monolithic Ceramics - I," L.A. Janosik and S.F. Duffy, *Transactions of the ASME - Journal of Engineering for Gas Turbines and Power*, Vol. 120, No. 1, pp. 155-161, January, 1998
3. "Design with Brittle Materials," S.F. Duffy and L.A. Janosik, in Engineered Materials Handbook: Volume 20 Material Selection and Design, G. Dieter, volume chair, ASM International, pp. 622-638, 1997.

The American Society of
Mechanical Engineers

Reprinted From
**DE-Vol. 55, Reliability, Stress
Analysis, and Failure Prevention
Editor: Richard J. Schaller
Book No. G00816 - 1993**

PARAMETER ESTIMATION TECHNIQUES BASED ON OPTIMIZING GOODNESS-OF-FIT STATISTICS FOR STRUCTURAL RELIABILITY

Alois Starlinger[1]
Structural Integrity Br.
NASA Lewis Research Center
Cleveland, Ohio

Stephen F. Duffy and Joseph L. Palko
Dept. of Civil Engineering
Cleveland State University
Cleveland, Ohio

ABSTRACT

New methods are presented that utilize the optimization of goodness-of-fit statistics in order to estimate Weibull parameters from failure data. It is assumed that the underlying population is characterized by a three-parameter Weibull distribution. Goodness-of-fit tests are based on the empirical distribution function (EDF). The EDF is a step function, calculated using failure data, and represents an approximation of the cumulative distribution function for the underlying population. Statistics (such as the Kolmogorov-Smirnov statistic and the Anderson-Darling statistic) measure the discrepancy between the EDF and the cumulative distribution function (CDF). These statistics are minimized with respect to the three Weibull parameters. Due to nonlinearities encountered in the minimization process, Powell's numerical optimization procedure is applied to obtain the optimum value of the EDF. Numerical examples show the applicability of these new estimation methods. The results are compared to the estimates obtained with Cooper's nonlinear regression algorithm.

INTRODUCTION

Typically, structural analysis techniques used to estimate the reliability of components fabricated from ceramic material systems (see Thomas and Wetherhold, 1991, and Palko et al., 1993) assume that the random strength parameters are characterized by a Weibull probability density function (PDF). This broad assumption, i.e., the use of a Weibull distribution as opposed to the use of other distributions such as a log-normal probability distribution necessitates some reflection. A wealth of experience indicates the Weibull distribution works well for monolithic ceramics. In fact, as Tracy et al. (1982) point out, if a structural component can be adequately modeled as a weakest link (or series) system, then the PDF of choice is the Weibull distribution. Alternatively, for parallel systems the log-normal distribution is appropriate. The structural analysis community has for the most part adopted the viewpoint (based on supporting experimental evidence) that monolithic ceramics behave in a weakest link fashion. However, very little failure data exists for laminated ceramic matrix composite (CMC) material systems, and definitely not enough to justify the use of a specific probability density function.

Accepting the use of a Weibull distribution for monolithic ceramics, the authors point out that several researchers (Margetson and Cooper, 1984 Duffy et al., 1993 and Foley et al., 1993) have presented data indicating certain monolithic ceramics exhibit threshold behavior. In addition, a threshold in the fiber direction of ceramic composites is intuitively plausible. The existence of a threshold for any type of ceramic material system should be approached with an open mind until a sufficient data base is assembled for a specific material system. If a material clearly exhibits zero-threshold behavior, and the underlying population can be characterized by the Weibull distribution, the very robust two parameter maximum

---

[1] National Research Council; Currently with Airex Composite Engineering

likelihood estimation algorithm is recommended (see ASTM Standard Practice C-1239). Alternatively, if the failure data suggests a threshold, then the estimation techniques presented here may apply.

In general, the objective of parameter estimation is to derive functions (or estimators) that yield, in some sense, optimized values of the underlying population parameters. Here the functional value of an estimator is a point estimate (in contrast to an interval estimate) of the true population parameter. The estimated values must be dependent on failure data. The values of point estimates computed from a number of samples obtained from a single population will vary from sample to sample. Thus the estimates can also be considered statistics. A sample is a collection (i.e., more than one) of observations taken from a well defined population, where a population represents the totality of observations about which statistical inferences are made. Here, the observations are the failure strengths of test specimens fabricated from ceramic material systems (where the system may be monolithic or composite).

As Stephens (1986) points out, the empirical distribution function (EDF) was originally developed as an aid in measuring the performance of a given parameter estimation technique. Statistics directly related to the EDF are appropriately referred to as goodness-of-fit statistics. In this article, goodness-of-fit statistics are utilized in directly computing parameter estimates, instead of the more traditional role of quantifying the performance of an estimator. Methods are proposed where parameter estimates are obtained by optimizing EDF statistics. Specifically, the first parameter estimation method minimizes the Kolmogorov-Smirnov goodness -of-fit statistic (D). A second estimation method that minimizes the Anderson-Darling goodness-of-fit statistic estimator (A^2) is also presented. The effectiveness of these estimation methods are studied by comparing results with the least-squares method originally developed by Cooper (1988), and later modified by Duffy et al. (1993).

GOODNESS-OF-FIT STATISTICS

The EDF is a step function, denoted here as $F_N(x)$, that is dependent on the number and individual values of failure observations within a sample. The function serves as an approximation of the cumulative distribution function for the underlying population. Statistics associated with the EDF, such as the Kolmogorov-Smirnov statistic and the Anderson-Darling statistic are measures of the discrepancy between the EDF and the cumulative distribution function (CDF), which is identified as $F(x)$. Thus a decision regarding the type of CDF (or PDF) must be made a priori in order to calculate either EDF statistic. Traditionally, the EDF statistics have been employed to assess the relative merits in choosing a particular CDF. Focusing attention on the Weibull PDF, the three parameter function has the form

$$f(x) = \frac{\alpha}{\beta}\left(\frac{x-\gamma}{\beta}\right)^{(\alpha-1)} exp\left\{-\left(\frac{x-\gamma}{\beta}\right)^{\alpha}\right\} \tag{1}$$

for a continuous random variable x, when $0 \le \gamma \le x$, and

$$f(x) = 0 \tag{2}$$

for $x \le \gamma$. The Weibull CDF is given by the expression

$$F(x) = 1 - exp\left\{-\left(\frac{x-\gamma}{\beta}\right)^{\alpha}\right\} \tag{3}$$

for $x > \gamma$, and

$$F(x) = 0 \tag{4}$$

for $x \le \gamma$. Here α is the Weibull modulus or shape parameter, β is the material scale parameter, and γ is the threshold parameter. β can be described as the Weibull characteristic strength of a specimen with unit volume loaded in uniform uniaxial tension. The parameter β has units of stress $*$ $(\text{volume})^{(1/\alpha)}$, α is dimensionless, and γ has the units of stress. The estimates for α and β are restricted to non-negative values, and estimates of γ are restricted to non-negative values.

The first goodness-of-fit statistic discussed is the Kolmogorov-Smirnov (KS) statistic. This goodness-of-fit statistic (denoted as D) belongs to the supremum class of EDF statistics, and is defined as

$$\begin{aligned} D &= sup \ |F_N(x) - F(x)| \\ &= max\ (D^+, D^-) \end{aligned} \tag{5}$$

where

$$D^+ = sup\ \{F_N(x) - F(x)\} \tag{6}$$

$$D^- = sup\ \{F(x) - F_N(x)\} \tag{7}$$

Here D is a measure of the largest difference (i.e., the supremum) in functional value between the EDF and the

CDF. To facilitate computations, notation adopted by Stephens is followed where

$$Z_i = F(x_i) \tag{8}$$

is used to denote the value of the CDF for an individual failure datum, x_i. By arranging the Z_i values in ascending order such that

$$Z_1 < Z_2 < \cdots < Z_N \tag{9}$$

where N is the number of specimens in a sample, suitable formulas for the KS statistic D^+ and D^- can be derived using Z_i, i.e.,

$$D^+ = \max_i \left\{ \frac{i}{N - Z_i} \right\} \quad for\ 1 \le i \le N \tag{10}$$

$$D^- = \max_i \left\{ Z_i - \frac{i-1}{N} \right\} \quad for\ 1 \le i \le N \tag{11}$$

When applying the concepts above to strength data of ceramic materials, insertion of Eq. 3 into Eq. 8 yields

$$Z_i = 1 - exp\left[-\left(\frac{\sigma_i - \gamma}{\beta} \right)^{\alpha} \right] \tag{12}$$

Here σ_i (which replaces x_i in Eq. 3) is the maximum stress at failure for each test specimen. If estimated values of α, β, and γ were available, the KS statistic would be obtained from Eqs. 10 and 11. Typically, maximum likelihood techniques and linear regression methods have been employed to determine estimated values of α, β, and γ. Alternatively, the authors propose to directly minimize the KS statistic with respect to the parameters α, β, and γ. Powell's optimization method (discussed in the next section) is applied to obtain the minimum value of this statistic. The results, which correspond to the minimum value of D, are estimates of the three Weibull parameters (i.e. $\tilde{\alpha}$, $\tilde{\beta}$, and $\tilde{\gamma}$). Utilizing Eqs. 3 and 8 assumes that the test specimen geometry is a unit volume and the specimen is subjected to a uniaxial tensile stress. To circumvent this restriction, the expression

$$Z_i = 1 - exp\left(- \left[V_T \left(\frac{\sigma_i - \tilde{\gamma}}{\tilde{\beta}} \right) \right]^{\tilde{\alpha}} \right) \tag{13}$$

is substituted for tensile specimens where all failures occur within the volume (V_T) of the gage section. Here $\tilde{\alpha}$, $\tilde{\beta}$, and $\tilde{\gamma}$ represent estimated values of the underlying population parameters.

Two basic failure populations were admitted in the formulations presented here, i.e., failures attributed to surface flaws and those due to volume flaws. This traditional approach of grouping failure origins into volume and surface flaws is an artifact from parameter estimation techniques developed for monolithic ceramics. Due to the lack of experimental data, this division (which must be based on fractographic analysis) may, or may not be appropriate for ceramic composites. At the present time, maintaining uniform densities throughout the bulk of a ceramic composite material is a major impediment that restricts the widespread commercialization of ceramic composites. Therefore, it is anticipated that the majority of failures will initiate within the volume of a ceramic composite. However, this may change as processing techniques are improved. If failures occur along the surface of the tensile specimen, the expression

$$Z_i = 1 - exp\left(- \left[A_T \left(\frac{\sigma_i - \tilde{\gamma}}{\tilde{\beta}} \right) \right]^{\tilde{\alpha}} \right) \tag{14}$$

is used where A_T is the surface area of the gage section for the tensile specimen.

Since the individual failure data (σ_i) represent the failure strength of a given ceramic test specimen, the estimators presented here were formulated for two widely used test configurations: the four-point bend test and the uniaxial tensile test (which was discussed above). Currently, the four-point bend-bar is the more popular test geometry used in strength tests of ceramic materials. When failures occur within the volume of a bend-bar specimen, the expression for Z_i takes the form

$$Z_i = 1 - exp\left\{ - \frac{V_B}{2(\tilde{\alpha} + 1)} \left(\frac{\sigma_i - \tilde{\gamma}}{\sigma_i} \right) \left(\frac{\sigma_i - \tilde{\gamma}}{\tilde{\beta}} \right)^{\tilde{\alpha}} \right\} \tag{15}$$

This expression corresponds to pure bending. This is an acceptable assumption when failure of all test specimens within a sample occurs between the inner loads depicted in Figure 1. Ignoring observations that fail outside the gage section will effectively censor the sample, and the methods presented here will not be valid. In Eq. 15, V_B represents the volume of the bend-bar specimen within the inner load span. Using this expression for Z_i, the KS statistic D is once again minimized with respect to the three Weibull parameters. Using Powell's optimization method, the results are the three Weibull parameters that minimize the statistic D for a given sample (i.e. $\tilde{\alpha}$, $\tilde{\beta}$, and $\tilde{\gamma}$).

If failure of the bend specimens is due to surface flaws, Z_i takes the form

$$Z_i = 1 - exp\left[- \frac{1}{2(h+b)} \left(\frac{\sigma_i - \tilde{\gamma}}{\tilde{\beta}}\right)^{\tilde{\alpha}} \left[\frac{h}{\tilde{\alpha}+1} \left(\frac{\sigma_i - \tilde{\gamma}}{\sigma_i}\right) + b \right] \right] \tag{16}$$

The dimensions h and b are the height and thickness of the bar, as identified in Figure 1. Once again failure observations must occur between the inner load span (i.e., the region of pure bending) for reasons mentioned above.

The Anderson-Darling (AD) statistic (A^2) is the second goodness-of-fit statistic considered. This statistic belongs to the Cramer-von Mises class of quadratic statistics and is defined by the expression

$$A^2 = N \int_{-\infty}^{\infty} \{F_N(x) - f(x)\}^2 \, [F(x)\,(1 - F(x))]^{-1} \, dF(x) \tag{17}$$

where the terms $f(x)$, $F_N(x)$, $F(x)$, and N have been previously defined. Using the notation developed for the KS statistic, the AD statistic can be expressed as

$$A^2 = -N - (1/N) \sum_{i=1}^{N} \{(2i-1)\,[\ln Z_i + \ln(1 - Z_{N+1-i})]\} \tag{18}$$

As before the sum of Z_i depends on the test configuration and the failure mode (assuming that the Weibull distribution characterizes the underlying failure population). For the case where the uniaxial tensile test is used, and failure is the result of volume flaws, Z_i takes the form given in Eq. 13. When failures of a uniaxial tensile specimen are due to surface flaws, Z_i takes the form given in Eq. 14. For the case where a four point bend configuration is used, and the failures are the result of volume flaws, the Z_i function is given by Eq. 15. When failures of four point bend tests are the result of surface flaws, the form for Z_i is given by Eq. 16.

POWELL'S OPTIMIZATION METHOD

As noted previously, Powell's optimization method (see Press et al., 1986) minimizes the EDF statistics for each specimen configuration presented above. This optimization method is an iterative scheme, where the search for a minimum functional value is conducted along a specified set of direction vectors. The number of direction vectors corresponds to the number of parameters(constrained or unconstrained) associated with the function. The EDF statistics (i.e., the function being optimized) will depend on specimen geometry, individual failure observations, and the estimated parameters $\tilde{\alpha}$, $\tilde{\beta}$, and $\tilde{\gamma}$. However, the specimen geometry will not change for a given sample, thus the EDF statistics are optimized with respect to the parameters α, β, and γ. In essence this method locates, in succession, an optimum point along each direction vector. An arbitrary set of direction vectors can be utilized to optimize a given function; however, Powell's method employs noninterfering (or conjugate) directions in order to speed convergence. This alleviates difficulties which arise when optimization along one direction vector is disturbed by a subsequent search along a new direction vector. The method formulates and updates n mutually conjugate directions, where n (for this case equals three i.e., α, β, and γ) defines the size of the parameter space. The set of direction vectors is updated by discarding the direction vector that produced the maximum change during an iteration. The average direction defined by the initial and final point of an iteration is substituted, and becomes the initial direction vector for the next iteration. Note that this method does not produce quadratic convergence, but nevertheless is very robust.

As indicated above, the optimized parameter space is defined by the estimates of the Weibull parameters α, β, and γ. Since a good choice of starting values ($\tilde{\alpha}_0$, $\tilde{\beta}_0$, and $\tilde{\gamma}_0$) is essential in quickly locating the optimum point, the results of Cooper's modified least-squares estimation method are used as the initial vector for Powell's method. Further restrictions are imposed on the optimization process. Negative values for the estimated Weibull parameters, and estimated threshold parameters ($\tilde{\gamma}$) larger than the smallest failure stress in a given sample, are not physically meaningful. Thus directions that produce these parameter values are discarded in the update of the direction vectors, and parameter values are reset to the minimum allowable values.

Example

Since failure data for CMC material systems are sparse, only failure data for a monolithic sintered silicon nitride (grade SNW-1000, GTE Wesco Division) are used to illustrate the relative merits of the proposed estimation techniques. This data was published by Chao and Shetty (1991) and is reprinted in Table 1. These values represent the maximum stress at failure for 27 four-point bend specimens. The outer support span for the test fixture was 40.4 mm, and the inner load span was 19.6 mm. The cross sections of the test specimens were 4.0 mm wide, and 3.1 mm in height. All failures occurred within the 19.6 mm inner load span, thus it was assumed that each specimen was subjected to pure bending.

Chao and Shetty performed a fractographic analysis of each specimen using optical and scanning electron microscopy. These studies indicated that all failures were initiated at subsurface pores (i.e., volume defects). Hence, equations for bending associated with volume defects are used for parameter estimation. Five methods were used to estimate the Weibull parameters from this set of failure data. These were Cooper's three parameter least squares method, the three parameter modified least squares method outlined by Duffy et al. (1993), minimizing the KS statistic, minimizing the AD statistic, and a two parameter estimation using the maximum likelihood estimation technique outlined in the ASTM Standard Practice C-1239. The Kolmogorov-Smirnov statistic (D) and Anderson-Darling statistic (A^2) were computed for each set of parameter estimates. The values of these EDF statistics, and the estimated parameters for each method are listed in Table 2.

A comparison of estimates obtained by both least-squares methods shows small differences in the estimated Weibull threshold parameter $\tilde{\gamma}$. Larger differences are present between the two methods in the estimates of the other parameters. Specifically, the modified least squares method provided a higher estimate for $\tilde{\alpha}$ than did Cooper's method, and a lower estimate for $\tilde{\beta}$ Furthermore, both goodness-of-fit statistics (D and A^2) are smaller for Cooper's method than for the modified least- squares method. Duffy et al. (1993) demonstrated that the modified least squares method is theoretically more rigorous than Cooper's original work since the modified method attempts to minimize a true residual. However, it is apparent from this example that Cooper's original approach yields better goodness-of-fit statistics. This discrepancy in part motivated the development of estimators based on minimizing goodness- of-fit statistics.

Estimates of the Weibull parameters obtained by minimizing the KS statistic result in the smallest value of D, which is not surprising. Similarly, estimates of the parameters obtained by minimizing the AD statistic result in the smallest value of A^2 in comparison to the other estimation methods. However, the Weibull parameters obtained by optimizing the goodness-of-fit statistics differ considerably from the estimates obtained using the least-squares techniques. Specifically, the value of $\tilde{\beta}$ from minimizing the goodness-of-fit statistics is nearly twice the value obtained with the least-squares techniques. As an additional comparison, parameter estimates from using a maximum likelihood estimator assuming a two-parameter Weibull distribution are included in Table 2. These estimates produce the highest values for both goodness-of-fit statistics.

Finally, cumulative distribution functions for all of the parameter estimates are plotted on a single Weibull diagram (see Figure 2). All of the failure data fall relatively close to all four of the three-parameter curves. This type of visual assessment (along with its highly subjective interpretation) should provide the motivation for the use of quantitative measures in determining the goodness-of-fit.

CONCLUSION

New methods of parameter estimation are proposed that are based on the minimization of goodness-of-fit statistics. These methods are used to estimate Weibull parameters from failure data whose population is assumed to be characterized by a three-parameter Weibull distribution. As an example, the proposed methods were compared with other parameter estimation methods, using failure data from a monolithic ceramic material. The proposed methods provided a better fit to the failure data in terms of the EDF statistics. However, to completely test the proposed methods, performance criteria like bias and invariance have to be evaluated through the use of Monte Carlo simulations.

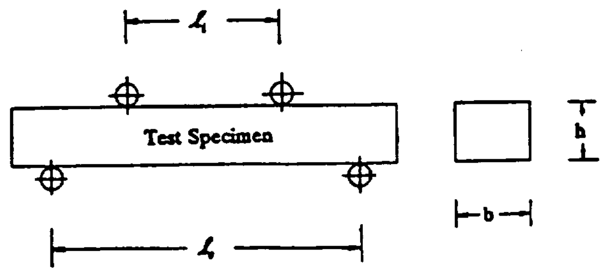

FIGURE 1 GEOMETRY AND NOTATION FOR A FOUR-POINT BEND TEST SPECIMEN.

TABLE 1 FOUR-POINT BEND FAILURE DATA FOR SILICON NITRIDE.

Specimen No.	Strength (MPa)
1	613.9
2	623.4
3	639.3
4	642.1
5	653.8
6	662.4
7	669.5
8	672.8
9	681.3
10	682.0
11	699.0
12	714.5
13	717.4
14	725.5
15	741.6
16	744.9
17	751.0
18	761.7
19	763.9
20	774.2
21	791.6
22	795.2
23	829.8
24	838.4
25	856.4
26	868.3
27	882.9

TABLE 2 PARAMETER ESTIMATES OBTAINED FROM FOUR-POINT BEND FAILURE DATA

Estimation Method	$\tilde{\alpha}$	$\tilde{\beta}$ ($MPa \cdot mm^{(3/\tilde{\alpha})}$)	$\tilde{\gamma}$ (MPa)	D ($\times 10^{-2}$)	A^2 ($\times 10^{-1}$)
Cooper's Least Squares	1.625	892.37	560.84	9.404	1.749
Modified Least Squares	1.677	861.93	558.08	9.538	1.798
KS Estimator	1.375	1298.44	558.08	6.080	1.963
AD Estimator	1.168	1537.03	581.09	7.676	1.406
Two-Parameter MLE	10.119	974.09	0.00	11.20	5.394

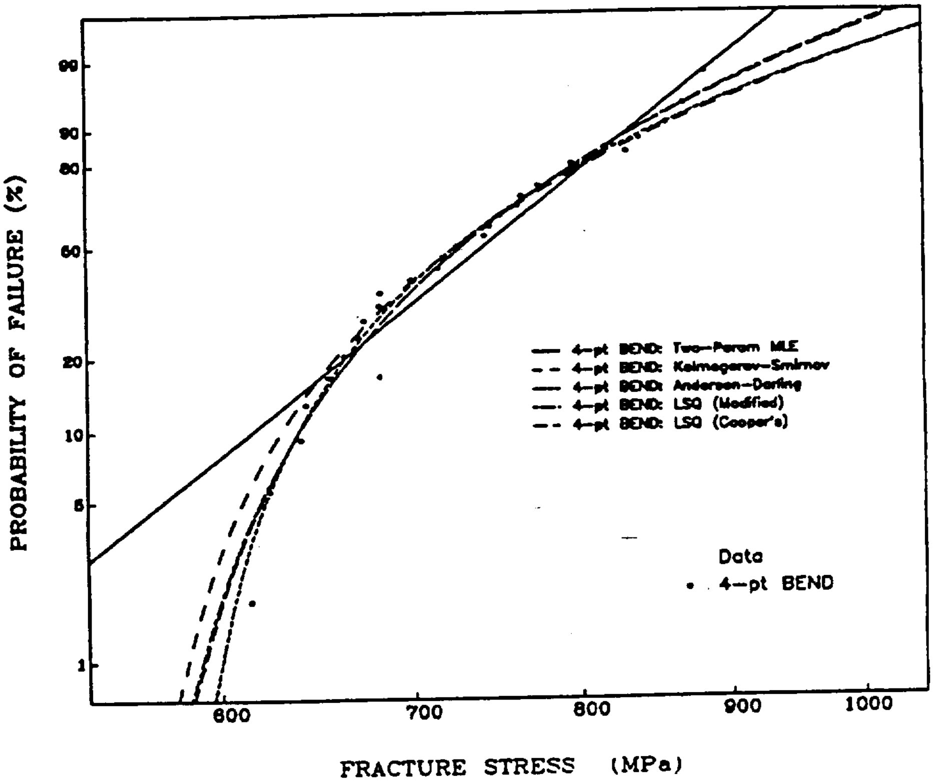

FIGURE 2 WEIBULL DIAGRAM FOR FIVE PARAMETER ESTIMATES

REFERENCES

Antle, C.E., and Klimko L.A., 1973, "Choice of Model for Reliability Analysis and Related Topics, II," ARL 73-73-0121, Aerospace Research Laboratories, Wright-Patterson AFB, Ohio, AD-772775.

Chao, L.-Y., and Shetty, D.K., 1991, "Reliability Analysis of Structural Ceramics Subjected to Biaxial Flexure," *Journal of the American Ceramic Society*, Vol.74, pp. 333-344.

Cooper, N.R., 1988, "Probabilistic Failure Prediction of Rocket Motor Components," PhD Thesis, Royal Military College of Science, Shrivenham, Swindon, Wilts.

Duffy S.F., Powers, L.M., and Starlinger A., 1993, "Reliability Analysis Using Three Parameter Weibull Distribution," *Transactions of the ASME, Journal of Engineering for Gas Turbines and Power*, Vol. 115, pp.109-116.

Duffy, S.F., Quinn, G.D., and Johnson, C.A., 1992, "Reporting Uniaxial Strength Data and Estimating Weibull Distribution Parameters for Advanced Ceramics," ASTM Standard Practice C-1239, Subcommittee C28.02.

Foley, M.R., Pujari, V.K., Sales, L.C., and Tracey, D.M., 1993, "Silicon Nitride Tensile Strength Database from CTAHE Processing for Reliability Project," Life Prediction Methodologies and Data for Ceramic Materials, ASTM STP 1201, C.R. Brinkman and S.F. Duffy, Eds., American Society for Testing and Materials, Philadelphia, PA.

Margetson, J., and Cooper N.R., 1984, "Brittle Material Design Using Three Parameter Weibull Distributions," *Probabilistic Methods in the Mechanics of Solids and Structures, Symposium*, Stockholm, Sweden, (Eggwertz, S., and Lind, N.C., ed.), Springer-Verlag.

Palko, J.L., Starlinger A., Duffy S.F., and Thomas D.J., 1993, "Ceramic Composite Analysis and Reliability Evaluation of Structures (C/CARES) - User's and Programmer's Manual," NASA TP (in review).

Press, W.H., Flannery, B.P., Teukolsky, S.A., and Vetterling, W.T., 1986, Numerical Recipes - The Art of Scientific Computing, Cambridge University Press, New York.

Stephens, M.A., 1986, "Tests Based on EDF Statistics," Goodness-of-Fit Techniques, R.B. D'Agostino and M.A. Stephens, eds. Marcel Dekker, Inc., New York, pp. 97-194.

Thomas D.J., and Wetherhold, R.C., 1991, "Reliability Analysis of Continuous Fiber Composite Laminates", *Composite Structures*, Vol. 17, pp. 277-293.

Tracy P.G., Rich T.P., Bowser R., and Tramontozzi L.R., 1982, "On the Statistical Nature of Fracture," *International Journal of Fracture*, Vol. 18, pp. 253-277.

Weibull, W., 1939, "A Statistical Theory of the Strength of Materials," *Ingeniors Vetenskap Akadiem Handlingar*, No. 151, pp. 5-45.

Weibull, W., 1951, "A Statistical Distribution Function of Wide Applicability," *Journal of Applied Mechanics*, Vol. 73, pp. 293-297.

NASA Conference Publication 19117

HITEMP Review 1993

Advanced High Temperature Engine Materials Technology Program

Volume III: Turbine Materials—CMC's Fibers

NOTICE

This report contains information which falls under the purview of the U.S. Munitions List, as defined in the International Traffic in Arms Regulations. It shall not be transferred to foreign nationals in the U.S., or abroad, without specific approval. Penalty for violations is described in ITAR, Section 127.

Proceedings of the 6th Annual HITEMP Review
held at the Westlake Holiday Inn
sponsored by NASA Lewis Research Center
Cleveland, Ohio
October 25–27, 1993

DESIGN OF A LAMINATED CMC HEAT EXCHANGER USING THE C/CARES ALGORITHM

JOSEPH L. PALKO and Stephen F. Duffy
Department of Civil Engineering
Cleveland State University
Cleveland, Ohio 44115

INTRODUCTION

Ceramic matrix composites (CMC) are under consideration in a number of commercial applications where components are exposed to severe service environments. However, before design engineers are willing to utilize a component fabricated from a ceramic composite they must have confidence in their ability to predict the response of the component prior to placing it in service. This need to predict component behavior initially arises from a desire to achieve a certain level of product function, and continues through the product life cycle with design upgrades. Thus commercialization of ceramic matrix composites (which has been an objective of a number of federally funded research programs including HITEMP) requires sound predictive capabilities predicated on coherent design methodologies. The C/CARES (Composite Ceramics Analysis and Reliability Evaluation of Structures) algorithm was specifically developed to contribute towards achieving this objective.

The ongoing metamorphosis of CMC systems and the lack of standardized design data has in the past tended to minimize the emphasis on modeling a component based on sound engineering principles. Prototypes were fabricated and designed by trial and error, since demonstrating feasibility took precedent over characterizing component behavior. This is understandable during periods of rapid improvements in material properties. The research effort that spawned the C/CARES algorithm required the development and implementation of a rational structural design protocol. In order to ascertain the utility of the C/CARES algorithm, a joint feasibility study of an advanced heat exchanger (AHX) was undertaken. The heat exchanger is a prototype being developed by Babcock & Wilcox under a project funded by the Department of Energy. The AHX is a critical component of a waste heat recovery system placed in the exhaust path of an industrial furnace (ref. 1) that produces highly corrosive flue gases. Due to this corrosive environment a ceramic composite was selected for the AHX.

Research engineers at Babcock & Wilcox have generally recognized that the scatter in strength associated with ceramic material systems poses a unique design constraint. They have also recognized the need to utilize current technology available in all sectors of the ceramic community. The C/CARES algorithm (developed under the auspices of the NASA HITEMP program) represents unique design technology that is able to account for variability in material strength by utilizing a stochastic failure criterion which also reflects the anisotropic nature of ceramic composites. The authors (who are resident research associates at NASA Lewis Research Center) were invited to join the design project team in an advisory capacity. This type of partnership allows for an immediate transfer of state-of-the-art technology from government to industry. It also permits federally sponsored researchers to gain valuable insight into key issues that drive commercial application of research concepts. American industries benefit from this technology transfer since they obtain a high level of technical insight from individual researchers who have spent years studying certain aspects of a research concept. In turn the government receives valuable input regarding applications that either validate or redirect research efforts. Also under certain limited conditions, performance data (some of which is proprietary) is made available to federal researchers who participate in the design project. This type of open interaction (where industry is protected by proprietary and/or space act agreements) is essential in making the partnership a success and has a tendency to shorten the research innovation cycle.

THE C/CARES ALGORITHM

C/CARES is a computer algorithm based on probabilistic design philosophies (ref. 2 and 3), and was developed specifically for laminated composites. A macroscopic approach is taken where a material is treated as an homogenized continuum; hence, the individual properties of the constituents are not accounted for explicitly. A weakest link formulation is used at the ply level. The failure function currently used in C/CARES accounts for five failure modes in each ply. These include failure in the fiber direction due to tension and compression, failure due to tension and compression in the direction transverse to the fiber, and an in-plane shear failure. Each failure mode is characterized by a three-parameter Weibull distribution.

The recently completed ABAQUS interface is used to import information pertaining to the stress analysis and component geometry generated by ABAQUS to the C/CARES algorithm. This interface supports the subelement technique described in ref. 3. The stresses are provided at the integration points of each finite element; thus reliability is evaluated within a subelement that is defined by an integration point. The use of the subelement technique refines a reliability prediction for a component since the stress field is more accurately characterized. The reliability of each ply is computed using the following expression

$$R_i = \exp\left(-\int_{V_i} \psi_i \, dV\right) \tag{1}$$

where ψ_i is the failure function per unit volume given by the expression

$$\begin{aligned} \psi_i = {} & \left(\frac{\langle\langle \sigma_F - \gamma_1 \rangle\rangle}{\beta_1}\right)^{\alpha_1} + \left(\frac{\langle\langle \sigma_T - \gamma_2 \rangle\rangle}{\beta_2}\right)^{\alpha_2} + \left(\frac{\langle\langle |\tau| - \gamma_3 \rangle\rangle}{\beta_3}\right)^{\alpha_3} \\ & + \left(\frac{\langle\langle (-1)(\sigma_F - \gamma_4) \rangle\rangle}{\beta_4}\right)^{\alpha_4} + \left(\frac{\langle\langle (-1)(\sigma_T - \gamma_5) \rangle\rangle}{\beta_5}\right)^{\alpha_5} \end{aligned} \tag{2}$$

where

$$\langle x \rangle = \begin{cases} 0 & x \leq 0 \\ x & x > 0 \end{cases} \tag{3}$$

and V_i is the volume of the ply. The term σ_F is the stress in the fiber direction, σ_T is the stress in the direction transverse to the fiber, and τ is the in-plane shear stress. The α's, β's and γ's are the Weibull parameters for the individual failure modes. The component reliability (R_{comp}) is the product of the individual ply reliabilities, i.e.,

$$R_{comp} = \prod_{i=1}^{n} R_i \tag{4}$$

where n is the number of plies in the finite element model. A flow chart of the C/CARES algorithm is shown in Figure 2.

DESIGN APPLICATION

The AHX is a key component of an innovative waste heat recovery system that will be placed in an industrial furnace downstream of the flue exhaust. A schematic of the system and the CMC tube are shown in Figure 3. The proposed waste heat system is an array of nine bayonet-type heat exchangers, where each bayonet consists of two concentric tubes. The outer tube is fabricated from a ceramic composite that consists of a zirconia matrix and an alumina-zirconia fiber. Ceramic insulation surrounds the top of the outer tube and serves as an expansion joint between the tube and the plenum. The inner tube, which is not exposed to process flue gases, is fabricated from kanthal. The stainless steel tube connects to an upper plenum, which serves as the inlet for clean supply air which is recirculated. The clean supply air enters the upper plenum, proceeds down the inner tube, exits the base of the inner tube, reverses direction and moves up between the stainless steel and ceramic composite tubes. As the clean air travels up the bayonet, it is heated from the flue gas passing along the outside of the ceramic composite tube. The heated air collects in the lower plenum located at the top of the ceramic section of the bayonet. At this point, the preheated air begins the return path back to the combustion section of the process. Discussions here regarding the design application will focus on the CMC portion of the AHX.

During the feasibility study a stress analysis for the AHX was conducted using the ABAQUS finite element program. PATRAN was used for the pre- and post- processing of the finite element model. The C/CARES algorithm maintains interfaces for both of these commercially available codes (as well as others, see ref. 2). A schematic of the finite element mesh is depicted in Figure 4. A total of 1656 elements was used to model the outer CMC tube and the surrounding insulation. Of these 1656 elements 1296 *QUAD/8* elements were used to model the laminated CMC tube, and 360 *HEX/20* elements were used to model the insulation surrounding the tube, and the built-up flange of the tube (which is hidden in this particular view). The built-up flange was fabricated from several unidirectional plies where the fibers in each ply were wound in the hoop direction (0°). It was determined during preliminary design analyses that the flange section of the bayonet and the insulation were not critical subcomponents. The insulation, which is relatively more compliant, was modeled as an isotropic material.

The temperature distribution depicted in Figure 5 was applied along the length of the tube. This temperature distribution was obtained from a thermal analysis which was conducted as part of the feasibility study. The resulting thermal stresses were three orders of magnitude larger than any stresses resulting from internal pressure or dead load (19 psi (0.13 MPa) and 42 psi (0.29 MPa), respectively). Hence mechanical loads were neglected during preliminary analyses. An initial design guideline suggested that allowable stresses in the fiber direction would be maintained at or below 12,000 psi (82.73 MPa). For the thermal distribution presented here, this particular design condition was met. Figure 6 depicts the hoop stress distribution (σ_r ; i.e., stress in the fiber direction) in the inner layer resulting from the applied temperature distribution shown in Figure 5. Note that a maximum tensile stress of 11,927 psi (82.18 MPa) is present in the inner layer, and a maximum compressive stress of -12,432 psi (-85.66 MPa) is present in the outer layer of the tube (both of which occur in the fiber direction).

The reliability analysis of the four-ply laminate outer tube begins with the specification of the Weibull parameters. The parameters used in the analysis of the AHX are listed in Table 1. These parameters were chosen arbitrarily since failure data was not available at the time of this analysis. A data base for each failure mode must be assembled in order to uniquely characterize the material. Note that a conservative assumption was made by taking the threshold parameter equal to zero for each failure mode. This implies that a finite probability of failure exists for each failure mode at all stress levels. The overall component reliability of the AHX was 99.97%. The least reliable ply was the inner ply with a reliability of 99.97%. The other plies had a reliability of 100%.

During the course of the design analysis, it was determined that the critical design parameter from a reliability standpoint is the shape parameter for the tensile strength in the direction transverse to the fiber (α_2). In the initial reliability analysis, a value of 15 was used for this parameter. Table 2 shows the effect that variations of this parameter have on the reliability analysis while all other Weibull parameters remain the same. Note that for values of α_2 below 7, reliability drops off significantly. This indicates that the shape parameter for this failure mode must be at this level or higher for this component to maintain a reliability of 90% for this given load.

REFERENCES

1. DeBellis, C.L.; and Kniedel, K.E.: Thermal and Fluid Design of a High-Temperature Ceramic Fiber Composite Heat Exchanger. Presented at the AIChE Sessions of the 24th National Heat Transfer Conference, Pittsburgh, PA, Aug. 9-12, 1987.

2. Palko, J.L.; Duffy, S.F.; Starlinger, A.; and Thomas, D.J.: *Composite Ceramics Analysis and Reliability Evaluation of Structures (C/CARES), User's and Programmer's Manual.* NASA-TM, In Review, 1993.

3. Starlinger, A.; Duffy, S.F.; and Gyekenyesi, J.P.: Reliability Analysis of Laminated CMC Components Through Shell Subelement Techniques. NASA TM 105413, 1992.

TABLE 1: Weibull Parameters

	α	β $(psi \cdot V^{1/\alpha})$	γ (psi)
Fiber - Tensile	25.0	17,500	0.0
Transverse - Tensile	15.0	12,500	0.0
In-Plane Shear	22.0	7,500	0.0
Fiber - Compressive	30.0	50,000	0.0
Transverse - Compressive	30.0	40,000	0.0

TABLE 2: Reliability as a Function of the Transverse Tensile Shape Parameter

α_2	Reliability , %
15.0	99.97
12.5	99.83
10.0	99.00
7.5	94.19
7.0	91.78
6.5	88.42
6.0	83.80
5.5	77.56
5.0	69.36

OBJECTIVE

Incorporate a reliability analysis into the design of a laminated ceramic composite heat exchanger

APPROACH

Utilize the C/CARES algorithm and the recently completed ABAQUS interface to conduct the reliability analysis

Fig. 1

CD-93-66360

C/CARES PROCEDURAL DIAGRAM

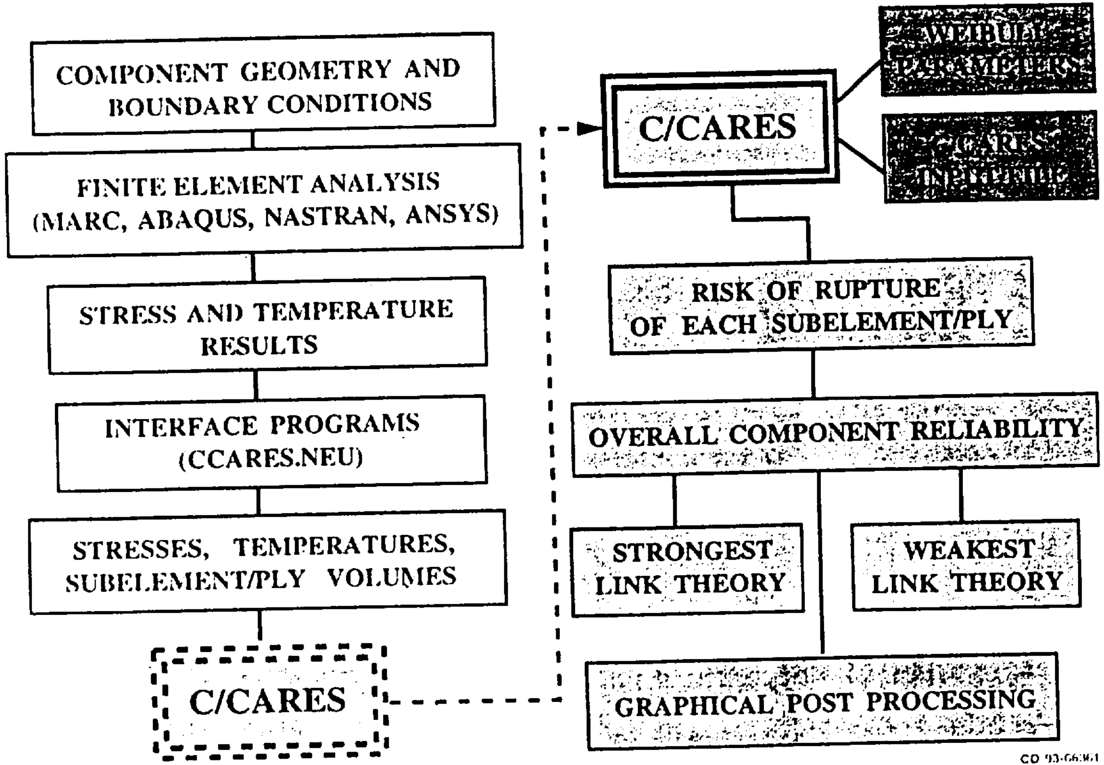

COMPONENT GEOMETRY AND BOUNDARY CONDITIONS

FINITE ELEMENT ANALYSIS (MARC, ABAQUS, NASTRAN, ANSYS)

STRESS AND TEMPERATURE RESULTS

INTERFACE PROGRAMS (CCARES.NEU)

STRESSES, TEMPERATURES, SUBELEMENT/PLY VOLUMES

C/CARES

C/CARES

WEIBULL PARAMETERS

C/CARES INPUT FILE

RISK OF RUPTURE OF EACH SUBELEMENT/PLY

OVERALL COMPONENT RELIABILITY

STRONGEST LINK THEORY

WEAKEST LINK THEORY

GRAPHICAL POST PROCESSING

Fig. 2

CD 93-66361

Advanced Heat Exchanger

Full Assembly

CMC Tube

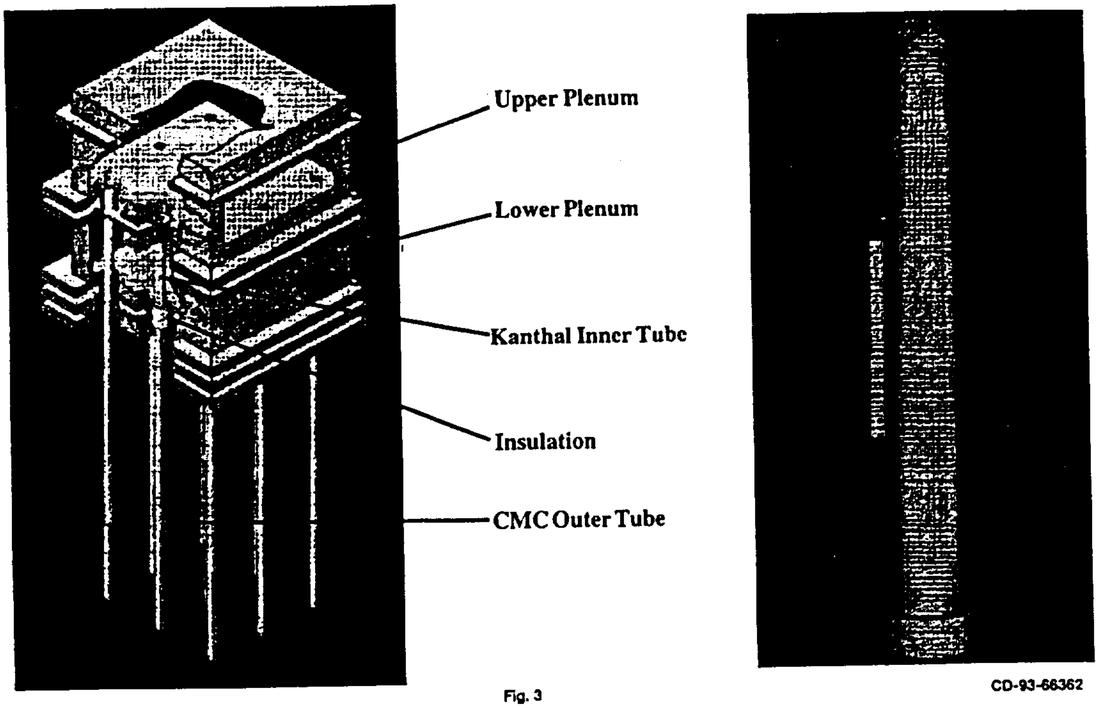

Fig. 3

CD-93-66362

Finite Element Mesh of the AHX Tube and Insulation

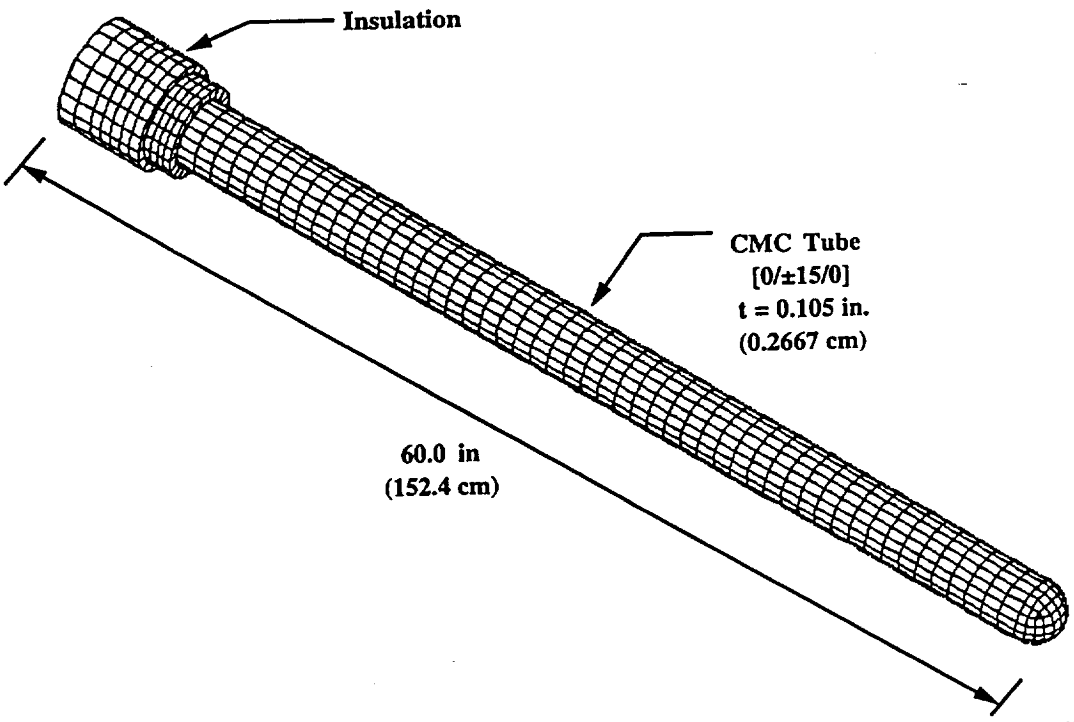

Fig. 4

CD-93-66363

AHX Zirconia Tube

Temperature vs Axial Position

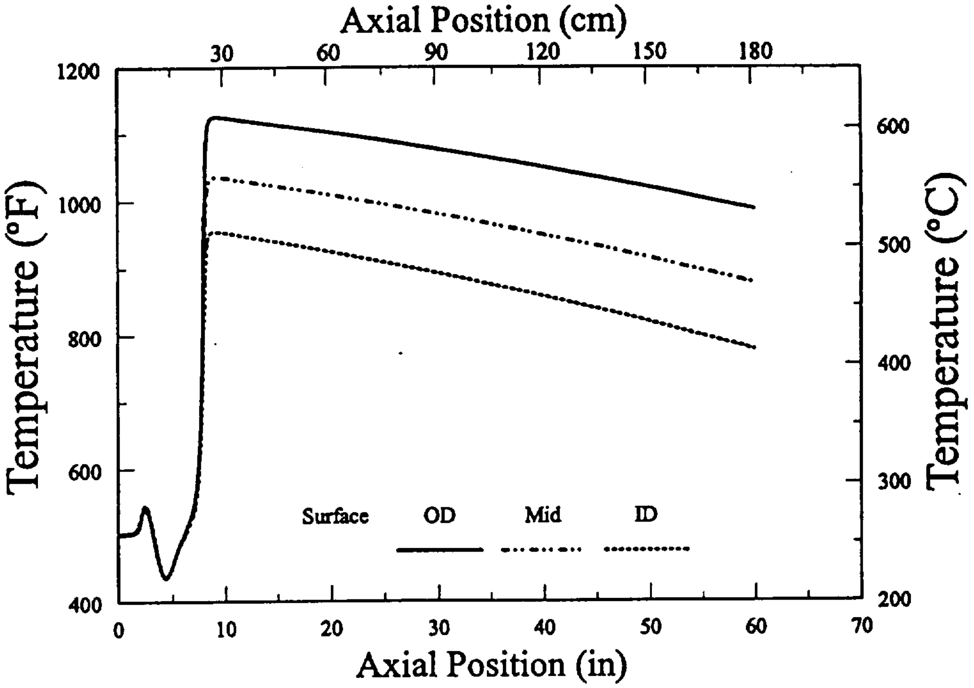

Fig. 5

CD-93-66364

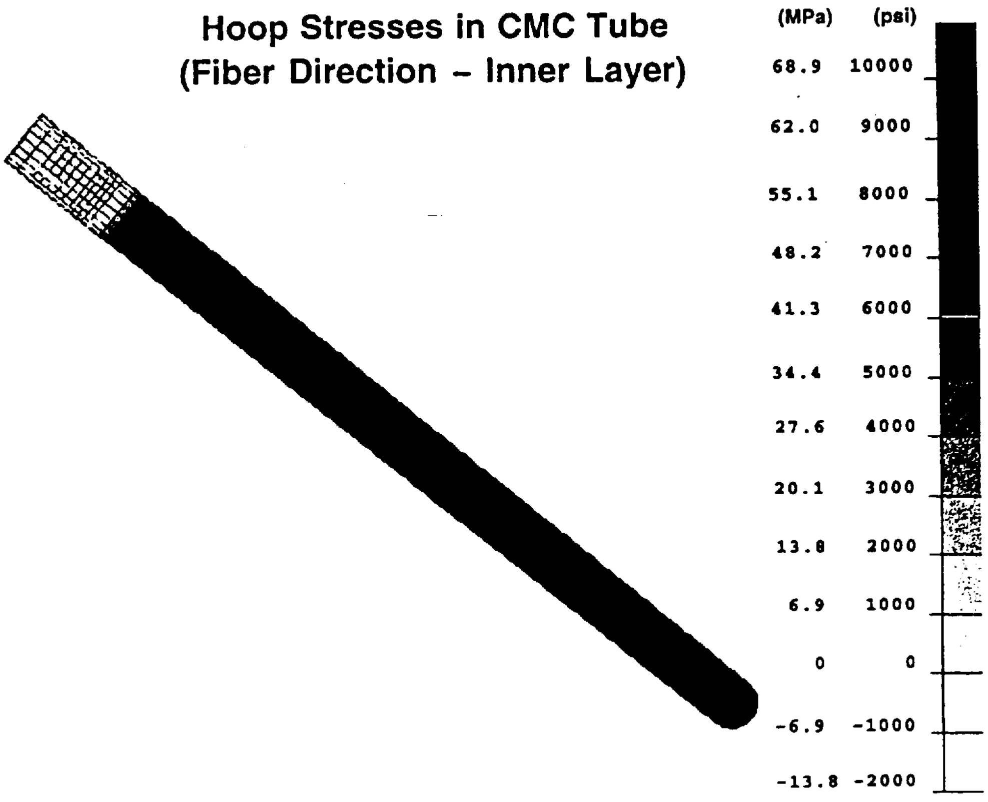

Fig. 6

CD-93-66365

SUMMARY

- Reliability study of the AHX was conducted
- Preliminary reliability analysis focused on a single critical parameter
- All parties involved benefit from Government/Industry interaction

Fig. 7

CD-93-66366

FUTURE DIRECTION

- Parameter estimates for each failure mode must be obtained from experimental data base
- Time dependent failure behavior must be addressed

Fig. 8

CD-93-66367

NASA Contractor Report 191048

Interactive Reliability Model for Whisker-Toughened Ceramics

Joseph L. Palko
Cleveland State University
Cleveland, Ohio

April 1993

Prepared for
Lewis Research Center
Under Grant NCC3–81

National Aeronautics and
Space Administration

INTERACTIVE RELIABILITY MODEL FOR WHISKER-TOUGHENED CERAMICS

Joseph L. Palko
Cleveland State University
Cleveland, Ohio

ABSTRACT

Wider use of ceramic matrix composites (CMC) will require the development of advanced structural analysis technologies. This report focuses on the use of an interactive model to predict the time-independent reliability of a component subjected to multiaxial loads. The deterministic, three-parameter Willam-Warnke failure criterion serves as the theoretical basis for the reliability model. The strength parameters defining the model are assumed to be random variables, thereby transforming the deterministic failure criterion into a probabilistic criterion. The ability of the model to account for multiaxial stress states with the same unified theory is an improvement over existing models. The new model has been coupled with a public-domain finite element program through an integrated design program. This allows a design engineer to predict the probability of failure of a component. A simple structural problem is analyzed using the new model, and the results are compared to existing models.

CHAPTER I

INTRODUCTION

The ability of structural components, fabricated from both monolithic and composite ceramic material systems, to maintain their structural integrity while subjected to thermomechanical loads is beginning to capture the attention of many design engineers. Attractive properties such as low density, high strength, high stiffness, creep resistance, and corrosion resistance are allowing ceramic materials to supplant metal alloys in numerous applications. Current applications include heat exchangers, cutting tools, and wear parts. Larsen and Vyas (1988), Buljan, Pasto, and Kim (1989), and Clarke (1990) present commercial data regarding the expanding use of ceramic components for these rigorous applications. Unlike some metal alloys used in demanding service conditions (notably the superalloys), ceramic components are fabricated from nonstrategic materials. This has helped spur research efforts in both processing technology and structural analysis. This report focuses on issues related to the field of structural analysis, where design protocols are replacing the ad hoc trial-and-error method of developing and testing structural prototypes.

In the field of material science, efforts to improve the structural performance of ceramic materials include adding a second ceramic phase to the matrix. This second phase can take the form of whiskers, short (usually chopped) fibers, continuous fiber reinforcement, and woven fabrics. This report will focus on ceramic composites that incorporate whisker reinforcement (and under certain conditions, particulate reinforcement). The addition of whiskers improves the failure behavior of the material system by arresting crack growth in the matrix by pinning, bridging, and deflecting cracks. The improvement of fracture toughness, usually in certain material directions, is dependent on processing. As a result, this material can exhibit anisotropic behavior. However, if the whiskers are homogeneously distributed and randomly oriented, the isotropic nature of the matrix material is preserved. The work presented here will deal exclusively with the isotropic whisker-toughened material system. Analytical efforts that allow for material anisotropy are mentioned in chapter V.

Even though the second phase enhances the failure behavior of the material, whisker-toughened ceramics still fail in a brittle fashion. In addition, there is a great deal of intrinsic variability in the strength of this material. Failure of structural components fabricated from whisker-toughened ceramics is governed by random flaw populations inherent to the material's microstructure. Usually these material imperfections are generated during processing. It is assumed that the location and orientation of the flaws are randomly distributed throughout a component. The resulting scatter in failure strength of these materials requires a departure from traditional design philosophies. The random nature of the microstructural flaws forces the design engineer to rethink the design philosophy that treats material strength as a single-valued design parameter. For monolithic ceramics, the factor of safety approach (a deterministic design procedure commonly used for metal alloys) has been abandoned in favor of a reliability-based approach. Work by Gyekenyesi (1986), Cooper, Margetson, and Humble (1986), and Lamon (1990) are representative of the reliability design philosophy used in analyzing structural components fabricated from monolithic ceramics.

Adopting a similar probabilistic philosophy for the structural analysis of a component fabricated from whisker-toughened material allows the design engineer to account for brittle behavior, variability in strength, and decreasing bulk strength with increasing component volume (the so-called size effect). Using probabilistic methods, the component is discretized using finite element techniques, and each discrete element is treated as a link in a chain. Philosophically, this means that when one element fails, the component fails. Thus the component is only as strong as the weakest link in the chain. From the standpoint of reliability theory, the component is treated as a series system, where failure of the system occurs when one of the subsystems fails. Alternatively, in a parallel system, failure of a single subsystem does not cause the system to fail since the remaining elements of the system may sustain load through redistribution. Models that use the analogy of a parallel system lead to what has been referred to in the literature as bundle theories. The basic principles underlying bundle theories were originally discussed by Daniels (1945) and Coleman (1958). Bundle theories have been applied exclusively to long-fiber ceramic composites. Thus, further discussion of these theories will not be pursued here. See the work of Harlow and Phoenix (1981), and Phoenix (1974, 1979) for an in-depth treatment of the bundle theory.

In general, two categories of weakest link theories have emerged. One group is based on the principles of fracture mechanics. The other group adopts a phenomenological viewpoint. The fracture mechanics approach assumes that the stress state in the near vicinity of the critical crack and the orientation of the crack are the controlling design variables. Material strength and crack orientation are treated as random variables. All other design variables (e.g., load, geometry, stiffness, etc.) are treated in a deterministic fashion. In contrast, phenomenological reliability models take a more global approach. Only material strength is treated as a random variable since attention is not focused on a critical flaw. Phenomenological models can be either interactive or noninteractive. Interactive models allow functional forms that include terms that are products of different material strengths. Noninteractive theories allow material strength parameters to appear only as separate and distinct terms. Throughout this report, the fracture mechanics and the phenomenological criterion will be discussed for the purpose of comparison, but the attention will be focused mainly on interactive models. In chapter II, a literature survey is presented that outlines different methods of modeling reliability.

With the exception of the work by Adams and Sines (1978), Alpa (1984), and Powers (1989), reliability theories for ceramic components have neglected compressive stress states and the effect of hydrostatic stress in particular. Models such as the principle of independent action (PIA), which was originally proposed by Barnett et al. (1967) and Freudenthal (1968), and the familiar Batdorf theory (Batdorf and Crose, 1974) do not allow compressive states of stress to influence component reliability. Since the compressive strength of ceramic materials is often an order of magnitude larger than the tensile strength, compressive stress states were assumed not to contribute to failure, or treated in an ad hoc fashion in a manner similar to Gyekenyesi (1986). Although data in the open literature are limited, experimental evidence by Adams (1975), Ikeda and Igaki (1984) and Ikeda, Igaki, and Kuroda (1986) clearly indicates that compressive stress states have a decided effect on ceramic materials. The phenomenological criterion that is discussed later allows for multiaxial states of stress, and specifically treats compressive stress in a rational manner as outlined in chapter IV. The criterion (and the reliability model that is derived from this criterion) is unified in the sense that ad hoc rules are not used to model different regions in the stress state. The analytical details of the parent deterministic failure model are given in chapter III. Failure surfaces projected into various stress spaces are presented to illustrate different mechanistic aspects of the theory. Finally, the tests necessary to determine the parameters are outlined.

Casting the deterministic failure theory into a reliability model using Monte Carlo methods is presented in chapter IV. Numerical aspects of the Monte Carlo simulation are discussed. Features of the interactive reliability model are compared with existing models. The reliability model is incorporated into a test-bed software program given the acronym TCARES (Toughened Ceramics Analysis and Reliability Evaluation of Structures), which was originally discussed by Duffy et al. (1989). Coupling the reliability algorithm with a general-purpose finite element program (i.e., MSC/NASTRAN) enables one to predict the time-independent reliability of a structural component. A structural component is analyzed that illustrates the interactive model highlighted in this report. These results are compared with an analysis made using previous models that did not allow compressive stress states to affect component reliability. It is shown that these previous models yield unconservative results in certain situations.

Chapter V summarizes this effort and indicates future research. Future direction includes improving numerical efficiency through the use of fast probability integration techniques proposed by Wu (1984). Applying this type of analysis to anisotropic whisker-toughened ceramics is outlined.

CHAPTER II

SURVEY OF RELIABILITY THEORIES

Traditional failure analyses of structural components have used deterministic approaches where failure is assumed to occur when some allowable stress level, or equivalent quantity, is exceeded. This assumes that deformation is not controlling component design. Since structural ceramics maintain high stiffness, even at elevated temperatures, deformation has not played a significant role in component design. Certain design methods have attempted to incorporate the relevant physics of failure using fracture mechanics. Here the critical design parameter is the stress intensity factor, which takes into account load and component geometry. In this approach the stress intensity factor is compared to a fracture toughness value that is a characteristic property of the material. However, for most structural ceramics the combination of ultimate strength and fracture toughness (quantified by K_{1C}) yields flaw sizes so small that current nondestructive evaluation (NDE) methods are unable to detect the critical defect. On the other hand, phenomenological failure theories make use of macroscopic strength parameters that do not focus on a critical microstructural defect. Multiaxial failure theories can be systematically formulated using this approach if the material is homogeneous, with strength properties that can be deduced from well chosen phenomenological experiments. Failure theories such as the maximum normal stress, the maximum normal strain, the maximum shear stress, and the maximum distortional energy criteria are examples of phenomenological models that are successful in predicting the onset of brittle failure or yielding. However, for reasons mentioned in the introduction, these deterministic techniques are not relevant when analyzing structural components fabricated from ceramic-based material systems.

Weibull (1939, 1951) proposed the first probabilistic model that accounted for scatter in failure strength and the size effect encountered in brittle materials. His approach is based on the weakest link theory (WLT) attributed to Midgley and Pierce (1926). This earlier research (sponsored by the textile industry) focused on modeling yarn strength. Unlike Midgley and Pierce, who assumed a Gaussian distribution for yarn strength, Weibull proposed a unique probability density function for failure strength that now bears his name. Weibull's two-parameter probability density function has the following form:

$$f(x) = \left[\frac{\alpha}{\beta}\right]\left[\frac{x}{\beta}\right]^{(\alpha-1)} \exp\left[-\left[\frac{x}{\beta}\right]^{\alpha}\right] \tag{2.1}$$

for a continuous random variable x, when $x > 0$, and

$$f(x) = 0 \tag{2.2}$$

for $x \leq 0$. The cumulative distribution function is given by the expression

$$F(x) = 1 - \exp\left[-\left[\frac{x}{\beta}\right]^{\alpha}\right] \tag{2.3}$$

for $x > 0$, and

$$F(x) = 0 \tag{2.4}$$

for $x \leq 0$. Here α (> 0) is the Weibull modulus (or the shape parameter), and β (> 0) is the scale parameter. Reliability theories with theoretical frameworks based on Weibull's original concepts are presented in this chapter. Theories based on phenomenological principles and fracture mechanics theories are discussed. Initially, Weibull's (1939) normal stress averaging technique is presented. This is followed by a discussion of the PIA model, and recent extensions of the PIA model to composite materials. Next, a reliability model developed by Batdorf and Crose (1974), founded on principles of fracture mechanics, is presented. Finally, a model that accounts for compressive states of stress (Powers, 1989) is discussed.

Weibull's Normal Stress Averaging Method

Weibull adopted the weakest link theory where a brittle material is considered a chain with links connected in series. The overall strength of a brittle component is then governed by the strength of its weakest link. Focusing on a single link, the failure probability of an individual link can be expressed as

$$p_f = \psi \Delta V \tag{2.5}$$

where ΔV is the volume of the link, and ψ is a failure function per unit volume of material. By defining r as the reliability of a single link, then

$$r = 1 - \psi \Delta V \tag{2.6}$$

The failure of an individual link is assumed to be an independent statistical event, implying that the events leading to failure of an individual link are not influenced by other links in the chain. As a result, the reliability of the component, denoted as R, becomes

$$R = \lim_{N \to \infty} \left[\prod_{\lambda=1}^{N} r_\lambda \right] = \lim_{N \to \infty} \left[\prod_{\lambda=1}^{N} \left[1 - \psi\left(\sigma_{ij}, x_i\right) \Delta V \right]_\lambda \right] \tag{2.7}$$

where N is the number of links in the component, $\psi(\sigma_{ij}, x_i)$ is the failure function per unit volume at position x_i within the component, and σ_{ij} is the Cauchy stress tensor at x_i. Unless noted otherwise, lowercase Roman letter subscripts in italics denote tensor indices with an implied range from 1 to 3, and Greek letter subscripts are associated with products or summations with ranges that are explicit in each expression. By adopting the argument originally proposed by Weibull, the reliability of the component takes the integral form

$$R = \exp\left[- \int_V \psi\left(\sigma_{ij}, x_i\right) dV \right] \tag{2.8}$$

where V is the volume of the component. Similarly, the probability of failure for the component takes the form

$$P_f = 1 - R = 1 - \exp\left[- \int_V \psi\left(\sigma_{ij}, x_i\right) dV \right] \tag{2.9}$$

The state of stress in every link of the chain must be characterized to conduct a reliability analysis using equation (2.8). This approach lends itself to analytical techniques that use finite element methods. If a component is modeled as a chain with individual links connected in series, then each link would correspond to an element within a mesh. The reliability models that are discussed in this section, and in later sections, adopt this theoretical framework (eqs. (2.5) to (2.9)) in computing component reliability, and all are amenable to finite element methods. The differences between various reliability models occur in the formulation of the failure function ψ.

Weibull assumed that the failure strength of a specimen subjected to a uniaxial state of stress is a random variable. Application of equation (2.9) for a uniaxial tensile stress field in a homogeneous isotropic material yields

$$P_f = 1 - \exp\left[-\left(\frac{\sigma}{\beta}\right)^{\alpha} V\right] \tag{2.10}$$

where σ is the applied tensile stress, and V is the volume of the specimen. For this case Weibull took the failure function (ψ) as

$$\psi = \left(\frac{\sigma}{\beta}\right)^{\alpha} = k\sigma^{\alpha} \tag{2.11}$$

Here k is referred to in the literature as Weibull's coefficient for a uniaxial state of stress. Weibull extended this uniaxial model to multiaxial states of stress by defining an average tensile stress. He defined this average tensile stress by considering the stress traction on an arbitrary plane (see fig. 2.1). Specifically the shear component of the stress traction $\tilde{\tau}$ is ignored, and it is assumed that only the normal component $\tilde{\sigma}$ causes failure. To gain a clear understanding of this method, consider a sphere centered at the origin of the coordinate axis (x_1, x_2, x_3) associated with the principal directions σ_1, σ_2, and σ_3. The normal component of stress traction acting on an arbitrary plane is given by the expression

$$\tilde{\sigma} = \sin^2\phi\left(\sigma_1\cos^2\theta + \sigma_2\sin^2\theta\right) + \sigma_3\cos^2\phi \tag{2.12}$$

Here ϕ and θ are the polar and azimuthal angles of the unit vector normal to the arbitrary plane in stress space. These angles and their relationship to the coordinate axes (x_1, x_2, x_3) are shown in figure 2.2. Since the normal stress component varies with each planar orientation defined by ϕ and θ, Weibull defined the following weighted average

$$(\bar{\sigma})^{\alpha} = \frac{8\int_0^{\pi/2}\int_0^{+\theta}\tilde{\sigma}^{\alpha}\sin\phi\, d\theta\, d\phi}{\int_A dA} \tag{2.13}$$

Here A is the area of the unit sphere, and the limits of θ coincide with those orientations where $\tilde{\sigma}$ changes from a tensile stress to a compressive stress. For the limiting case where $\tilde{\sigma}$ is tensile over the entire sphere, θ takes the value of $\pi/2$. Both limits are zero if $\tilde{\sigma}$ is compressive over the entire unit sphere, and this results in $(\bar{\sigma})^{\alpha} = 0$. The general convention analyzes this integral over one octant of the unit sphere, which accounts for the limits of integration for ϕ (i.e., 0 and $\pi/2$), and the factor 8 in the numerator.

The quantity $(\bar{\sigma})^{\alpha}$ given by equation (2.13) is equated to σ^{α} in equation (2.11) such that

$$\psi = k(\bar{\sigma})^{\alpha} \tag{2.14}$$

where k is Weibull's coefficient for a multiaxial stress state. This coefficient is the multiaxial extension of the parameter k defined in equation (2.11), and must be defined in a consistent fashion such that equation (2.14) yields equation (2.11) for a uniaxial state of stress. Equating Weibull's multiaxial formulation of ψ defined in equation (2.14) to the uniaxial case defined in equation (2.11) results in the following relationship (see Gyekenyesi (1986) for details):

$$k = \mathrm{k}(2\alpha + 1) = \frac{(2\alpha + 1)}{\beta^{\alpha}} \tag{2.15}$$

Thus for the multiaxial state of stress,

$$P_f = 1 - \exp\left[-\int_V k(\bar{\sigma})^{\alpha}\, dV\right] \tag{2.16}$$

from which the uniaxial form expressed in equation (2.10) can be obtained. Although the extension to multiaxial states of stress described here is intuitively plausible, it is somewhat arbitrary because it disregards the shear component of the stress traction. In addition, since the method lacks a closed-form solution, use of this model requires computationally intensive numerical methods.

Principle of Independent Action Method

Barnett et al. (1967) and Freudenthal (1968) proposed an alternative to Weibull's normal stress averaging approach for multiaxial states of stress. Here only principal stresses are considered, and the basic assumption is that each acts independently in reducing the survival probability of an element (hence the name principal of independent action). The failure function for this theory takes the form

$$\psi = \left[\frac{\sigma_1}{\beta}\right]^{\alpha} + \left[\frac{\sigma_2}{\beta}\right]^{\alpha} + \left[\frac{\sigma_3}{\beta}\right]^{\alpha} \tag{2.17}$$

where $\sigma_1 \geq \sigma_2 \geq \sigma_3 \geq 0$. Since the principal stresses appear in separate terms (i.e., they do not interact) in the formulation of ψ, this model is classified as a noninteractive reliability model. Qualitatively, the PIA theory is equivalent in a probabilistic sense to the maximum stress failure theory.

Extensions of the PIA Method

Duffy and Arnold (1990) formulated an extension of the PIA model for transversely isotropic materials. A unit vector was used to identify the local material orientation, and, subsequently, to define stress invariants. The unit vector d_i was introduced to define the direction normal to the plane of isotropy. Here the failure function ψ depends on the stress state and local material orientation such that

$$\psi = \psi\left(\sigma_{ij}, d_i\right) \tag{2.18}$$

Since ψ is a scalar valued function, it must remain form invariant. To ensure this, an integrity basis was developed for ψ that contained certain combinations of invariants of the Cauchy stress tensor and an orientation tensor defined as $d_i d_j$. The invariants formed an integrity basis and were used to construct other invariants that correspond to specific components of the state of stress in an element. This approach yields the following functional dependence

$$\psi = \psi\left(\hat{I}_1, \hat{I}_2, \hat{I}_3, \hat{I}_4\right) \tag{2.19}$$

Here $\hat{I}_1$ corresponds to the magnitude of the stress vector $\sigma_{ij} d_j$ projected onto the material orientation vector d_i. The invariant $\hat{I}_2$ represents the magnitude of the shear component of the stress traction. The invariants $\hat{I}_3$ and $\hat{I}_4$ represent the magnitudes of the maximum and minimum principal stresses in the plane of isotropy. Thus each invariant corresponds to a strength in a well-defined material direction, and because of this the invariants can be treated as random variables with underlying Weibull distributions. Analogous to the principle of independent action, it is assumed that the different invariants are statistically independent such that the failure function takes the form

$$\psi = \left[\frac{\langle \hat{I}_1 \rangle}{\beta_1}\right]^{\alpha_1} + \left[\frac{|\hat{I}_2|}{\beta_2}\right]^{\alpha_2} + \left[\frac{\langle \hat{I}_3 \rangle}{\beta_3}\right]^{\alpha_3} + \left[\frac{\langle \hat{I}_4 \rangle}{\beta_3}\right]^{\alpha_3} \tag{2.20}$$

where the individual α's and β's are the Weibull parameters associated with a strength variable in a particular material direction. It should be noted that compressive stresses associated with $\langle \hat{I}_1 \rangle$, $\langle \hat{I}_3 \rangle$, and $\langle \hat{I}_4 \rangle$ are assumed not to contribute to a reduction in reliability such that

$$\langle \hat{I}_1 \rangle = \begin{cases} \hat{I}_1 & \hat{I}_1 > 0 \\ 0 & \hat{I}_1 \leq 0 \end{cases} \tag{2.21}$$

$$\langle \hat{I}_3 \rangle = \begin{cases} \hat{I}_3 & \hat{I}_3 > 0 \\ 0 & \hat{I}_3 \leq 0 \end{cases} \tag{2.22}$$

and

$$\langle \hat{I}_4 \rangle = \begin{cases} \hat{I}_4 & \hat{I}_4 > 0 \\ 0 & \hat{I}_4 \leq 0 \end{cases} \tag{2.23}$$

Duffy and Manderscheid (1990) formulated an extension of the PIA model for orthotropic materials. Here two mutually orthogonal unit vectors (a_i and b_i) were used to define local material directions. An integrity basis was developed from the functional dependence

$$\psi = \psi\left(\sigma_{ij}, a_i\, b_j\right) \tag{2.24}$$

where $a_i b_j$ serves as a direction tensor. Like the transversely isotropic case, the failure function depends on certain invariants that correspond to components of the local stress tensor; that is,

$$\psi = \psi\left(\tilde{I}_1, \tilde{I}_2, \tilde{I}_3, \tilde{I}_4, \tilde{I}_5\right) \tag{2.25}$$

Here the invariants $\tilde{I}_1$ and $\tilde{I}_3$ represent the magnitude of the normal stress components in the directions of a_i and b_i, respectively. The invariants $\tilde{I}_2$ and $\tilde{I}_4$ represent the shear stresses across the directions a_i and b_i respectively. The invariant $\tilde{I}_5$ represents the normal stress in the direction defined by the cross product of the vectors a_i and b_i. Once again, it is assumed that the invariants are statistically independent such that

$$\psi = \left[\frac{\langle\tilde{I}_1\rangle}{\beta_1}\right]^{\alpha_1} + \left[\frac{|\tilde{I}_2|}{\beta_2}\right]^{\alpha_2} + \left[\frac{\langle\tilde{I}_3\rangle}{\beta_3}\right]^{\alpha_3} + \left[\frac{|\tilde{I}_4|}{\beta_4}\right]^{\alpha_4} + \left[\frac{\langle\tilde{I}_5\rangle}{\beta_5}\right]^{\alpha_5} \tag{2.26}$$

where the individual α's and β's are again associated with strength variables in particular material directions. The invariants $\tilde{I}_1$, $\tilde{I}_3$, and $\tilde{I}_5$ are normal stresses, and do not contribute to a reduction in reliability if they are compressive; that is,

$$\langle\tilde{I}_1\rangle = \begin{cases} \tilde{I}_1 & \tilde{I}_1 > 0 \\ 0 & \tilde{I}_1 \leq 0 \end{cases} \tag{2.27}$$

$$\langle\tilde{I}_3\rangle = \begin{cases} \tilde{I}_3 & \tilde{I}_3 > 0 \\ 0 & \tilde{I}_3 \leq 0 \end{cases} \tag{2.28}$$

and

$$\langle\tilde{I}_5\rangle = \begin{cases} \tilde{I}_5 & \tilde{I}_5 > 0 \\ 0 & \tilde{I}_5 \leq 0 \end{cases} \tag{2.29}$$

The reliability models for both the transversely isotropic and orthotropic materials allow the material orientation to vary along a family of curves within the component. Thus the material is locally anisotropic. The models were constructed using invariant formulations which indicate the maximum number and forms of the stress invariants necessary to define the failure function ψ. In both cases, a subset of the integrity basis for ψ

was constructed, resulting in reliability models that are similar in nature to the PIA reliability model for monolithic ceramics.

Batdorf's Theory–Surface Flaw Analysis

Reliability theories based on fracture mechanics assume that failure of a component emanates from a single flaw with a critical size and orientation. This flaw belongs to a population that in general contains surface flaws and volume flaws. Either type of flaw is assumed to be uniformly distributed and randomly oriented. Surface flaws are imperfections that are the result of machining, grinding, or other surface finishing operations. Volume flaws are the direct result of processing. Both types of flaw populations exhibit different failure behavior characterized by distinct strength distribution parameters. For surface flaws, the presence of a traction-free surface reduces a three-dimensional state of stress to a state of plane stress. Because of this simplifying condition, the details of a surface flaw analysis are presented. In general, the surface flaw analysis can be viewed as a special case of volume flaw analysis.

Batdorf and Heinisch (1978) proposed a surface flaw model which is an extension of an earlier volume flaw analysis proposed by Batdorf and Crose (1974). This two-dimensional theory is based on weakest link principles, and accommodates mode I, mode II, or mixed mode fracture criteria. For the following discussion, the coplanar strain energy release rate, a mixed mode criterion, is used. This criterion allows for mode I and mode II behavior, and takes the form

$$\left[\frac{K_I}{K_{IC}}\right]^2 + \left[\frac{K_{II}}{K_{IC}}\right]^2 = 1 \tag{2.30}$$

where K_I and K_{II} are the mode I and mode II stress intensity factors, respectively. These stress intensity factors are functions of the applied far-field stress state and the crack geometry. For a Griffith crack (a sharp through-crack of length 2a), the stress intensity factors for a two-dimensional infinite plate are

$$K_I = \sigma\sqrt{\pi a} \tag{2.31}$$

and

$$K_{II} = \tau\sqrt{\pi a} \tag{2.32}$$

Here σ is the far-field normal stress, and τ is the far-field shear stress. Substituting equations (2.31) and (2.32) into equation (2.30) yields the following expression:

$$\left[\frac{K_{IC}^2}{\pi a}\right]^{1/2} = \sqrt{\sigma^2 + \tau^2} \tag{2.33}$$

At this point, index notation is briefly suspended in order to use notation that has been widely accepted in discussing Batdorf's theory. By defining

$$\sigma_{cr} = \left[\frac{K_{1C}^{2}}{\pi a}\right]^{1/2} \tag{2.34}$$

as a critical stress, then equation (2.33) (together with eq. (2.34)) defines a failure envelope which is dependent on the material's fracture toughness and crack size. This failure envelope is shown in figure 2.3. Since the size (denoted as "a" in the denominator of eq. (2.34)) and orientation of the critical crack will vary, σ_{cr} represents a random variable. Thus there is a family of failure envelopes corresponding to each value of the random variable σ_{cr}. Batdorf used this concept to transform a deterministic fracture criterion into a reliability model.

The Batdorf theory stipulates that the probability of failure of a single link is the product of two probabilities; that is,

$$p_f = p_1 p_2 \tag{2.35}$$

Here p_1 is the probability that a crack exists such that the applied stress is in the range of σ_{cr} to $(\sigma_{cr} + d\sigma_{cr})$. This probability is defined by the expression

$$p_1 = \Delta A \left[\frac{dN\left(\sigma_{cr}\right)}{d\sigma_{cr}}\right] d\sigma_{cr} \tag{2.36}$$

where ΔA is the differential area of the link, and $N(\sigma_{cr})$ is a crack density function (i.e., N has units of cracks per unit area). The crack density function is defined as

$$N\left(\sigma_{cr}\right) = k_B \sigma_{cr}^{\alpha} \tag{2.37}$$

and quantifies the number of cracks per unit area with an applied far-field stress that is greater than or equal to σ_{cr}. Here k_B is the Batdorf constant (which is functionally dependent on the Weibull scale parameter) and α is the Weibull modulus of the material. Both parameters can be determined experimentally by using the parameter estimation techniques outlined in Pai and Gyekenyesi (1988).

The quantity p_2 is the probability that a crack is oriented such that the critical stress is exceeded by an applied far-field stress. To illustrate this point, consider a state of plane stress using Mohr's circle where $0 < \sigma_2 < \sigma_1$ (see fig. 2.3). Define the angle ω as the initial orientation of the crack where the critical stress is exceeded. Note that the crack orientation varies between 0 and 2π radians, and there may be more than one orientation where the critical stress is exceeded. Next, overlay the fracture envelope expressed in equation (2.33) on the same set of axes. The angle between the σ axis and the line OA defines 2ω. Here point O is the center of Mohr's circle defined by the in-plane principal stresses σ_1 and σ_2. Point A is the intersection of the failure envelope given by equation (2.33) and Mohr's circle and defines the initial orientation of a crack where the critical stress is exceeded. Any point on Mohr's circle outside the failure envelope represents a possible failure stress state. Thus the probability that a crack is oriented such that the critical stress is exceeded by the applied far-field stress is

$$p_2 = \frac{\omega}{\pi/2} \tag{2.38}$$

where $0 \leq p_2 \leq 1$.

The geometry in figure 2.3 is used to established the form of equation (2.38). The applied far-field stress is equal to σ_{cr} at point A; thus

$$\omega = \cos^{-1}\left[\frac{\sigma_{cr}^2 - \sigma_2^2}{\sigma_1^2 - \sigma_2^2}\right]^{1/2} \tag{2.39}$$

Hence,

$$p_2 = \frac{2}{\pi}\cos^{-1}\left[\frac{\sigma_{cr}^2 - \sigma_2^2}{\sigma_1^2 - \sigma_2^2}\right]^{1/2} \tag{2.40}$$

when $\sigma_2 \leq \sigma_{cr} \leq \sigma_1$, and

$$p_2 = 1 \tag{2.41}$$

when $\sigma_{cr} \leq \sigma_2$. For the case where $\sigma_2 < \sigma_1 < \sigma_{cr}$,

$$p_2 = 0 \tag{2.42}$$

Following the argument outlined in equations (2.5) to (2.7), with the results of equations (2.36) and (2.40), then the reliability of a component is given as

$$R = \exp\left[-\int_A \int_0^{\sigma_1}\left[\frac{dN(\sigma_{cr})}{d\sigma_{cr}}\right]\frac{2\omega}{\pi}\, d\sigma_{cr} dA\right] \tag{2.43}$$

Similarly, the probability of failure of a component becomes

$$P_f = 1 - \exp\left[-\int_A \int_0^{\sigma_1}\left[\frac{dN(\sigma_{cr})}{d\sigma_{cr}}\right]\frac{2\omega}{\pi}\, d\sigma_{cr} dA\right] \tag{2.44}$$

Note that the limit of integration defined by A is the area of the component, and the limits of integration for σ_{cr} assume that σ_1 is the largest principal stress. In the context of the preceding discussion concerning reliability models, the failure function for Batdorf's model is defined by the integral

$$\psi = \int_0^{\sigma_1} \left[\frac{dN(\sigma_{cr})}{d\sigma_{cr}} \right] \frac{2\omega}{\pi} d\sigma_{cr} \tag{2.45}$$

The above analysis assumes that compressive stresses do not contribute to failure. For discussion on Batdorf's model for a volume analysis, see Batdorf and Crose (1974).

Power's Extension of Batdorf's Theory

The Powers model (Powers, 1989) represents a hybrid approach to reliability analysis in the sense that Batdorf's approach is adopted to predict reliability of a single link when both of its principal stresses are tensile, and the Mohr-Coulomb failure theory is used when both are compressive. When one principal stress is tensile and the other is compressive, a transition from the phenomenological criterion to the fracture criterion is necessary. The details concerning the transition are rather complex and will not be reviewed here. Thus the remainder of this section outlines the details of how Powers uses Mohr-Coulomb theory to predict reliability of monolithic ceramic components. Mohr-Coulomb theory defines failure when the shear stress on an unspecified failure plane reaches a critical value. Thus the shear stress at failure is a function of the coefficient of internal friction (μ), a compressive stress acting normal to the failure plane, and σ_{cr} (which was defined previously). The failure criterion takes the form

$$|\tau| + \mu\sigma = \sigma_{cr} \tag{2.46}$$

Powers assumes that the envelope for the Mohr-Coulomb failure criterion coincides with the envelope from Batdorf's fracture criterion at $\sigma = 0$, which results in $\tau = \sigma_{cr}$ at this point. This represents a major drawback and is discussed later. When viewed in Mohr's stress space, the Mohr-Coulomb failure envelope is linear; hence a slope and a point completely define the envelope. In her analysis, Powers specifies the slope as the material parameter μ. This quantity is defined as a single valued deterministic parameter. The associated point is the quantity σ_{cr} from Batdorf's analysis. This quantity is the only random variable in the analysis.

Powers defines an additional quantity σ_{max} in her analysis. When viewing a state of stress in Mohr's stress space, this represents the point where the failure envelope becomes tangent to Mohr's circle. In terms of the principal stresses and the parameter μ, σ_{max} takes the form

$$\sigma_{max} = \sqrt{1 + \mu^2}\ \frac{\sigma_1 - \sigma_2}{2} + \mu\ \frac{\sigma_1 + \sigma_2}{2} \tag{2.47}$$

Again, index notation is briefly suspended in order to use the notation as it appears in Powers' original work. This quantity is referred to as a "maximum" because it defines the limit of relevance from a reliability standpoint; that is, no reduction in reliability occurs if the failure envelope lies above this point.

The significance of σ_{max} is easily seen when deriving the failure function. Since plane stress conditions simplify the analysis, again only the details of a surface flaw analysis are presented. In a manner similar to Batdorf's approach, a critical stress and orientation of a failure plane must be defined in order to formulate the failure function. However, it must be emphasized that the Mohr-Coulomb theory makes no allowance for information concerning the physics of a crack (i.e., it is not a fracture criterion). Powers expresses the failure function as

$$\psi = \alpha k_B \sigma_{max}^{\alpha} \int_0^1 \bar{\omega} S_{cr}^{\alpha-1} dS_{cr} \tag{2.48}$$

where S_{cr} is a ratio of the critical stress (σ_{cr}) to the maximum stress (σ_{max}) for a given state of stress; i.e.,

$$S_{cr} = \frac{\sigma_{cr}}{\sigma_{max}} \tag{2.49}$$

The ratio S_{cr} facilitates the numerical integration of equation (2.48). By varying this ratio from 0 to 1, σ_{cr} is varied from 0 to σ_{max}. This guarantees that all relevant stress states are considered in the reliability prediction. Also note that $\bar{\omega}$ is similar in nature to the angle ω defined in equation (2.39) (the details will be discussed shortly), and the other terms in equation (2.48) have been defined in previous sections.

Several combinations of the failure envelope and Mohr's circle must be studied. Figure 2.4 shows that the failure envelope may not intersect Mohr's circle, the envelope may be tangent to the circle, or the envelope may intersect the circle at no more than two points. To determine the location of the intersection points and the portion of the circumference of Mohr's circle intersected, Powers formulates equation (2.46) in terms of the principal stresses, the ratio S_{cr}, and $\cos^2 \phi$. Here ϕ locates the intersection points on the circle. The equation now becomes quadratic in terms of $\cos^2 \phi$, and thus ϕ has two values, ϕ_1 and ϕ_2. The quantity $\bar{\omega}$, which appears in equation (2.48), is functionally dependent on the two angles ϕ_1 and ϕ_2 in the following manner:

$$\bar{\omega} = \frac{2(\phi_1 - \phi_2)}{\pi} \tag{2.50}$$

The angles ϕ_1 and ϕ_2 vary depending on the stress state. When there is no contact between the failure envelope and Mohr's circle (see fig. 2.4(a)), $\phi_1 = \phi_2 = 0$, and $\bar{\omega} = 0$. When the failure envelope and Mohr's circle are tangent at a point (fig. 2.4(b)), $\phi_1 = \phi_2 \neq 0$, and once again $\bar{\omega} = 0$. When the failure envelope intercepts Mohr's circle twice (fig. 2.4(c)), $\bar{\omega}$ represents the portion of Mohr's circle that lies outside of the failure envelope. With this interpretation of $\bar{\omega}$, and the definition of ψ given by equation (2.48), Powers' model yields the following expression

$$R = \exp\left[-\int_A \alpha k^B \sigma_{max}^{\alpha} \int_0^1 \bar{\omega} S_{cr}^{\alpha-1} dS_{cr} dA\right] \tag{2.51}$$

for component reliability when both principal stresses are negative.

The Mohr-Coulomb theory is a two-parameter failure theory that represents a straight line in the Mohr circle stress space. The slope and a point of intersection on the τ axis are used to define the linear envelope. Broad assumptions are made that μ is deterministic and σ_{cr} is a random variable. The effects of these assumptions are evident when comparing compression reliability predictions to tensile reliability predictions. Since μ is not treated as a random variable, the predicted scatter in strength (quantified by the Weibull modulus) is the same for simple compression and tensile tests using Powers' model. This result has never been supported by experimental data for a given material. In fact, intuition says that the scatter should be greatly reduced in compression. Thus the Weibull modulus for compression data should be substantially higher than the

Weibull modulus for tensile data. Accommodating this type of behavior is not a problem with the reliability model presented in chapter IV.

The following chapter presents the details of a three-parameter phenomenological failure model (the Mohr-Coulomb failure model is a two-parameter model). The method of transforming this deterministic phenomenological failure criterion into a reliability model is discussed in chapter IV. Basically, each of the three model parameters are treated as random variables with separate Weibull distributions. This leads to much greater flexibility in modeling reliability for multiaxial states of stress.

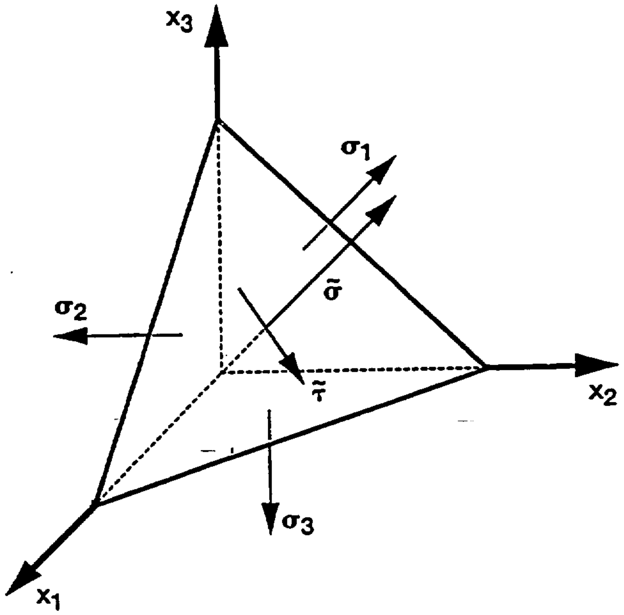

Figure 2.1.—Stress traction on an arbitrary plane.

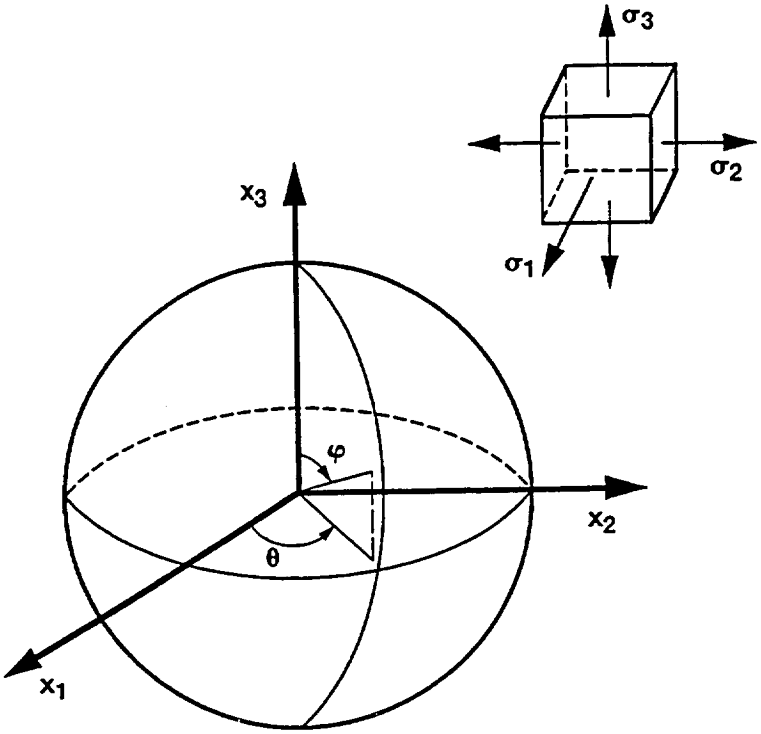

Figure 2.2.—Unit sphere in three-dimensional space.

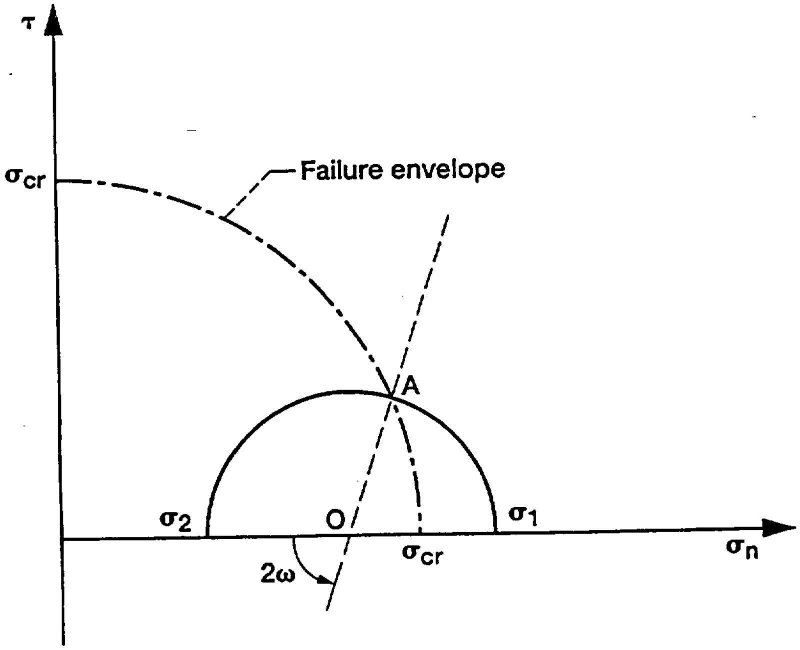

Figure 2.3.—Intersection of Mohr's circle and Batdorf's failure envelope.

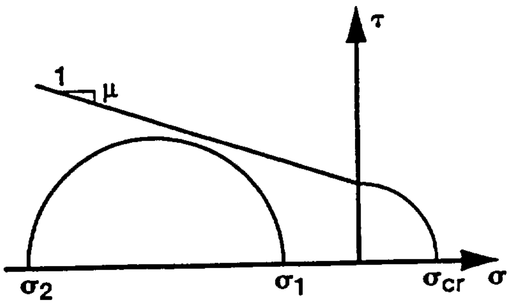

(a) No intersection between failure envelope and Mohr's circle.

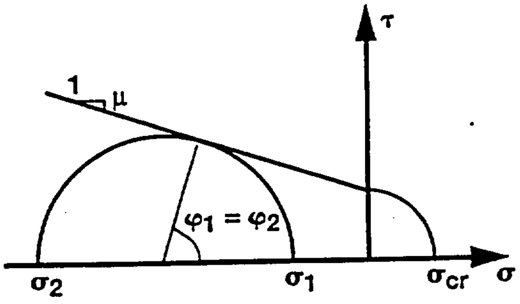

(b) Envelope tangent to circle at a point.

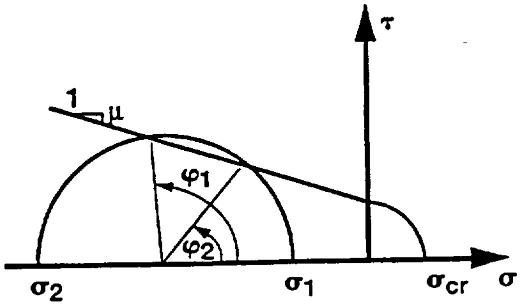

(c) Failure envelope cuts through Mohr's circle.

Figure 2.4.—Power's failure envelope and Mohr's circle.

CHAPTER III

WILLAM-WARNKE FAILURE CRITERION

A failure criterion defines a limit state. Within this limit state, a structural component will perform its design application in some acceptable fashion. A primary function of the design engineer is to define what is acceptable performance. Performance standards depend on the design variables used to define the limit state. Design variables, which may include strength parameters, cyclic load limits, and allowable deformation, can be assembled in an n-dimensional vector

$$\mathcal{Y}_\alpha = \left(Y_1, Y_2, \ldots, Y_n\right) \tag{3.1}$$

and the limit state function, which stipulates how the design variables interact, is expressed in general as

$$g\left(\mathcal{Y}_\alpha\right) = 0 \tag{3.2}$$

This function defines a surface in the n-dimensional design variable state. If a design point (i.e., an operational state where each design variable has a specified value) lies within the surface, then the design point represents a successful operational state. If the design point falls on the surface, the component fails. For deterministic analyses, points outside of the failure surface are inaccessible, since failure results once the surface is reached.

In this report, the design variable space, defined by the vector $\mathcal{Y}_\alpha$, is limited to strength parameters for ceramic material systems. Since strength parameters are associated with components of the Cauchy stress tensor, the general functional dependence of a limit state function is expressed as

$$g = g\left(\mathcal{Y}_\alpha, \sigma_{ij}\right) \tag{3.3}$$

where σ_{ij} represents the Cauchy stress tensor. A three-parameter strength criterion developed by Willam and Warnke (1975) will serve as the limit state function of primary interest here. The Willam-Warnke failure criterion (developed for isotropic materials) is a unified failure criterion in the sense that one limit state function defines failure for all regions of the stress space. As a comparison, Powers' model adopted Batdorf's theory for tensile regions of the stress space and Mohr-Coulomb theory for compressive regions of the stress space. The Willam-Warnke criterion uses stress invariants to define the functional dependence on the Cauchy stress σ_{ij}, specifically

$$g\left(\mathcal{Y}_\alpha, I_1, J_2, J_3\right) = 0 \tag{3.4}$$

This guarantees that the function is form invariant under all proper orthogonal transformations. Here I_1 is the first invariant of the Cauchy stress σ_{ij}, J_2 is the second invariant of the deviatoric stress S_{ij}, and J_3 is the third invariant of the deviatoric stress. These quantities are defined as

$$S_{ij} = \sigma_{ij} - \frac{1}{3}\delta_{ij}\sigma_{kk} \tag{3.5}$$

$$I_1 = \sigma_{kk} \tag{3.6}$$

$$J_2 = \frac{1}{2} S_{ij} S_{ji} \tag{3.7}$$

$$J_3 = \frac{1}{3} S_{ij} S_{jk} S_{ki} \tag{3.8}$$

where σ_{ij} is the identity tensor. Admitting I_1 to the function allows for a dependence on hydrostatic stress. The invariant J_3 allows different behavior in tension and compression since this invariant changes sign when the direction of a stress component is reversed.

Willam and Warnke defined the limit state function with the following expression

$$g\left(\mathscr{Y}_\alpha, I_1, J_2, J_3\right) = \lambda\left[\frac{\sqrt{J_2}}{Y_c}\right] + B\left[\frac{I_1}{Y_c}\right] - 1 \tag{3.9}$$

where

$$B = B\left(\mathscr{Y}_\alpha\right) \tag{3.10}$$

and

$$\lambda = \lambda\left(\mathscr{Y}_\alpha, J_3\right) \tag{3.11}$$

The functions B and λ will be defined momentarily. The strength parameters that comprise the design vector $\mathscr{Y}_\alpha$ include the uniaxial tensile strength of the material Y_t the equal biaxial compressive strength Y_{bc}, and the uniaxial compressive strength Y_c. This model is referred to as a three-parameter model, since three strength parameters, $\mathscr{Y}_\alpha = (Y_t, Y_c, Y_{bc})$, are used to define the limit state function. Failure occurs when $g = 0$ and the multiaxial criterion is completely defined in all regions of the six-dimensional stress space.

Since the limit state function is dependent on the six components of the Cauchy stress tensor, a design point and its relative position to the failure surface can be depicted in various stress spaces. Graphical representations can take place in a two- or three-dimensional stress space, using the components of the Cauchy stress tensor as coordinate axes. However, the function and the physical implications associated with the function can be viewed completely in the three-dimensional stress space where the principal stresses serve as orthogonal coordinate axes (see fig. 3.1(a)). This space is known as the Haigh-Westergard stress space. In this coordinate system, a given stress state, that is, a design point $P(\sigma_1, \sigma_2, \sigma_3)$, can be readily decomposed into hydrostatic and deviatoric components. This decomposition is shown in figure 3.1(b). Line d in figure 3.1(b) represents the hydrostatic axis where $\sigma_1 = \sigma_2 = \sigma_3$. Point P in this stress space represents an arbitrary state of stress. The vector NP represents the deviatoric component of the arbitrary stress state, and the vector ON represents the hydrostatic component.

The plane passing through the origin normal to the hydrostatic line is called the π-plane. For an isotropic material, a failure surface projected onto the π-plane must exhibit a sixfold symmetry. In the most general case where the isotropic material possesses equal strengths in tension and compression, the failure surface in the π-plane can be represented by two limiting cases (see fig. 3.2). The first case is represented by a circular failure surface, and the second is represented by a polygon inscribed within the circular failure surface. Any failure surface that does not fall within these two surfaces permits nonconvex regions to exist along the failure surface. However, proof of convexity also implies that level surfaces of a function are closed surfaces. An open region of the failure surface allows the existence of a load path along which failure will never occur. Thus for a convex surface, load paths cannot be traversed towards open regions of the failure surface, since open regions will not exist.

A failure surface projected onto the π-plane can be described conveniently with polar coordinates (r, θ). Here θ is defined as an angle measured clockwise from the σ_1-axis, and $r(\theta)$ is the distance from the hydrostatic axis to the failure surface (see fig. 3.2). Note that $r(\theta)$ is a function of θ for the inscribed polygon, and a constant for the circular failure surface. Physically, $r(\theta)$ represents the deviatoric component of a stress state, since this vector lies in the π-plane. In figure 3.2, the distance from the hydrostatic axis to the failure surface along a compressive principal axis r_c is equal to the distance along a tensile principal axis r_t for both limiting cases. However, ceramic material systems exhibit very different strengths in tension and compression. Failure models must account for this behavior, and this can be done simply by constructing the function $r(\theta)$ such that the intercepts along the tensile and compressive principal axes are different. The Willam-Warnke criterion accounts for this type of behavior by taking $r_c > r_t$ (see fig. 3.3).

As mentioned previously, isotropic materials must exhibit a sixfold symmetry in the π-plane. Willam and Warnke postulated that a single sector $(0 \leq \theta \leq \pi/3)$ of the failure surface in the π-plane could be represented as a segment of an ellipse. The major and minor axes of the ellipse were formulated as functions of the intercepts r_c and r_t (see fig. 3.4). Note that the minor axis of the ellipse is assumed to coincide with a tensile axis. However, the center of the ellipse does not necessarily coincide with the hydrostatic axis. The intercepts r_t and r_c depend on the strength parameters Y_t, Y_c, and Y_{bc}. Equations are given later that detail the interrelationships. In general the distance $r(\theta)$ is defined as

$$r(\theta) = \frac{2r_c\left(r_c^2 - r_t^2\right)\cos\theta + r_c\left(2r_t - r_c\right)\left[4\left(r_c^2 - r_t^2\right)\cos^2\theta + 5_t^2 - 4r_t r_c\right]^{1/2}}{4\left(r_c^2 - r_t^2\right)\cos^2\theta + \left(r_c - 2r_t\right)^2} \tag{3.12}$$

where $0 \leq \theta \leq \pi/3$. A detailed derivation of this expression can be found in Chen (1982). Note that equation (3.12) yields $r(\theta) = r_t$ for the special case of $\theta = 0$. Similarly $r(\theta) = r_c$ for $\theta = \pi/3$.

With the definition of $r(\theta)$ given in equation (3.12), λ from equation (3.9) can be expressed as

$$\lambda = (2/5)^{1/2}\left[1/r(\theta)\right] \tag{3.13}$$

Here λ is implicitly dependent on J_3 through the angle θ. The dependence of θ on J_3 results from the similarities between the trigonometric identity

$$\cos^3\theta - \frac{3}{4}\cos\theta - \frac{1}{4}\cos(3\theta) = 0 \tag{3.14}$$

and the cubic equation used to find the deviatoric invariants

$$S^3 - J_2 S - J_3 = 0 \tag{3.15}$$

where the roots (S_1, S_2, S_3) are the eigenvalues of the deviatoric stress matrix. Substituting $S = \gamma\cos\theta$ into equation (3.15) yields

$$\cos^3\theta - \frac{J_2\cos\theta}{\gamma^2} - \frac{J_3}{\gamma^3} = 0 \tag{3.16}$$

By comparing this expression with equation (3.14), it becomes apparent that

$$\gamma = \frac{2\sqrt{J_2}}{\sqrt{3}} \tag{3.17}$$

and

$$\cos(3\theta) = \frac{3\sqrt{3}\,J_3}{2\sqrt{(J_2)^3}} \tag{3.18}$$

The angle θ was first defined by Lode (1926), and the relationship between this angle and the deviatoric invariants was given by Nayak and Zienkiewicz (1972).

Details of the derivation for the Willam-Warnke criterion have been discussed in the context of the π-plane. Since the criterion is represented by a conic surface in the three-dimensional Haigh-Westergard stress space, and the function is sensitive to the hydrostatic component of the stress state, details obtained from the two-dimensional π-plane are not sufficient to completely describe the criterion. To gain a complete view of the criterion, a cutting plane is passed through the conic surface such that the entire length of the hydrostatic axis is contained in the cutting plane. This plane will intersect the surface along two lines. By definition, these lines are termed meridians.

Meridians define the profile of the conic failure surface in the Haigh-Westergard stress space. The relative position of each meridian is defined by the angle θ. For the tensile meridian $\theta = 0$, and for the compressive meridian $\theta = \pi/3$. In the π-plane, a compressive meridian is represented by point Q in figure 3.3, and a tensile meridian is represented by point T. For the Willam-Warnke criterion the meridians are linear, which is evident from the $I_1 - \sqrt{J_2}$ stress space in figure 3.5 and equation (3.9). Since the meridians are linear, two points on a meridian will define its position. For the tensile meridian the two points used to determine its position are defined by a uniaxial tensile load path, an equal biaxial compressive load path, and their intersection with the meridian. For both load paths equation (3.18) yields a value of $\theta = 0$. Considering a uniaxial tensile load case, failure results when σ_1 ($\sigma_1 = \sigma$) reaches Y_t (with $\sigma_2 = \sigma_3 = 0$). The load path for this case is defined by the ratio

$$\frac{I_1}{\sqrt{J_2}} = 1.73 \tag{3.19}$$

The value of I_1 ($= \sigma$) and $\sqrt{J_2}$ ($= \sigma/\sqrt{3}$) at failure will fix the position of one point on the meridian. In a similar fashion, the ratio

$$\frac{I_1}{\sqrt{J_2}} = 3.46 \tag{3.20}$$

defines the load path for equal biaxial compression where $\sigma_1 = \sigma_2$ ($= \sigma$) and $\sigma_3 = 0$. This load path fixes the position of a second point on the meridian. Here $I_1 = 2\sigma$ and $\sqrt{J_2} = \sigma\sqrt{(2/3)}$. Failure results when $\sigma_1 = \sigma_2 = Y_{bc}$. Both load paths are shown in figure 3.5. To clearly illustrate the load paths, the figure is not drawn to scale. The meridian is then defined by the line connecting these two points on the failure surface.

Similarly two points are used to determine the position of the compressive meridian. The points are defined by a uniaxial compressive load path and the intersection of the tensile meridian with the I_1-axis. The load path for the uniaxial compressive case is defined by the ratio

$$\frac{I_1}{\sqrt{J_2}} = 1.73 \tag{3.21}$$

where $I_1 = \sigma$ and $\sqrt{J_2} = (1/\sqrt{3})\,\sigma$. This path is shown in figure 3.5, and equation (3.18) yields a value of $\theta = \pi/3$. Failure results when $\sigma_1 = Y_c$ with $\sigma_2 = \sigma_3 = 0$. The second point on the compression meridian is the tip of the failure cone. Since the tensile meridian is completely defined by the parameters Y_t and Y_{bc}, the intersection of this line with the I_1 axis provides a second point for the location of the compressive meridian. This point is shown in figure 3.5 as point V. The distance ρ from point V to the origin represents the hydrostatic tensile stress at failure. Physically, this stress state is not easily produced in an experiment. However, this parameter is used to define B in equation (3.9). The parameter B is related to ρ by the simple expression

$$B = \frac{1}{3}\rho \tag{3.22}$$

As noted previously, the Willam-Warnke criterion is a three-parameter model. The parameters ρ, r_c, and r_t may be used to define the criterion in lieu of the strength parameters Y_c, Y_{bc}, and Y_t. The relationships are

$$\rho = \frac{y_{bc}\, y_t}{y_{bc} - y_t} \tag{3.23}$$

$$r_t = \left(\frac{6}{5}\right)^{1/2}\left[\frac{y_{bc}\, y_t}{2y_{bc} - y_t}\right] \tag{3.24}$$

and

$$r_c = \left(\frac{6}{5}\right)^{1/2}\left[\frac{y_{bc}\, y_t}{3y_{bc}y_t + y_{bc} - y_t}\right] \tag{3.25}$$

Here the expressions

$$y_{bc} = \frac{Y_{bc}}{Y_c} \tag{3.26}$$

and

$$y_t = \frac{Y_t}{Y_c} \tag{3.27}$$

are used to simplify equations (3.23) to (3.25). Once again, the derivations of these expressions were given by Chen (1982).

To gain further insight regarding physical implications of the criterion, consider the failure envelope projected onto the $\sigma_1 - \sigma_2$ stress plane, which is depicted in figure 3.6. Again this is a cutting plane that passes through the conic surface in the Haigh-Westergard stress space. Note that, in this figure, the function defines a smooth failure surface for any combination of the principal stresses. Also, the differences between the tensile strength and compressive strength of a material are readily apparent. The ratio of the intercepts along the tensile and the compressive axes is equal to the ratio of Y_t to Y_c. This stress space is encountered again in the next chapter, where reliability concepts are described.

Finally, the Willam-Warnke failure criterion degenerates to simpler models under special conditions. For the case of $r_c = r_t = r_o$, where r_o is the same for any angle θ, the surface degenerates to a circle in the π-plane and to a cone in the three-dimensional Haigh-Westergard stress space. This is the Drucker-Prager failure criterion, which is a two-parameter formulation. For the special case where $r_c = r_t = r_o$ and $\rho = \infty$, the model reduces to the single-parameter Von Mises criterion. For this case, the failure surface again becomes a circle in the π-plane, but a right circular cylinder in the three-dimensional Haigh-Westergard stress space. Since this criterion exhibits no dependence on hydrostatic stress, its meridians never intersect the I_1-axis in the $I_1 - \sqrt{J_2}$ stress space.

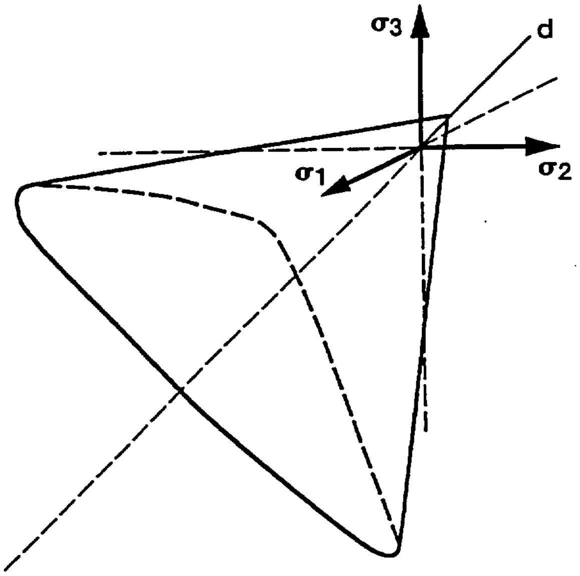

(a) Generalized failure surface in principal stress space.

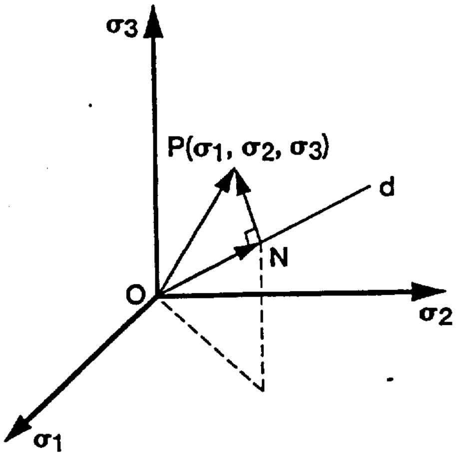

(b) Stress at a point in principal stress space.

Figure 3.1.—Principal stress space.

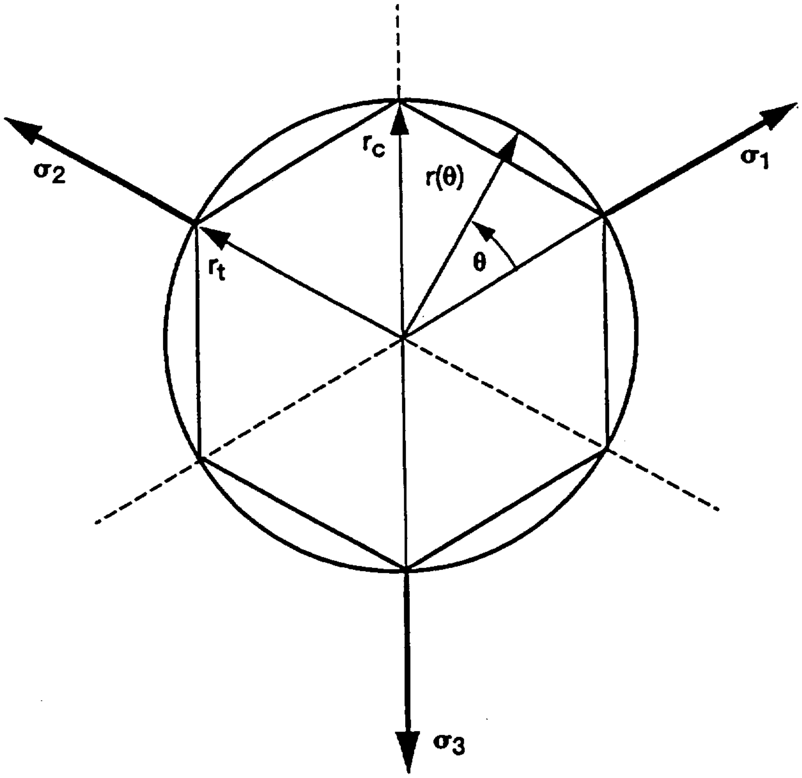

Figure 3.2.—Failure surface depleted in π-plane for a material with equal tensile and compressive strengths.

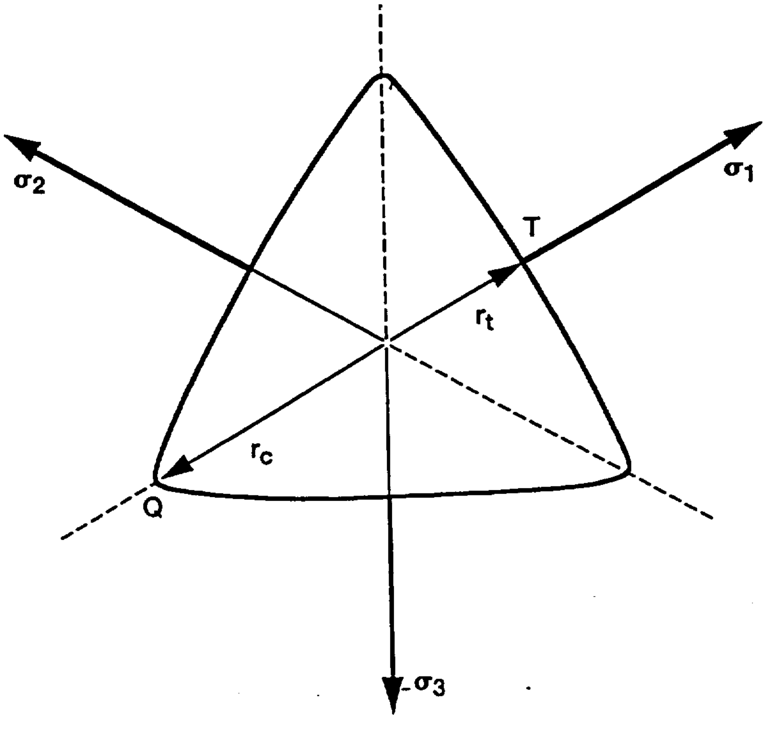

Figure 3.3.—Willam-Warnke failure surface depicted in π-plane.

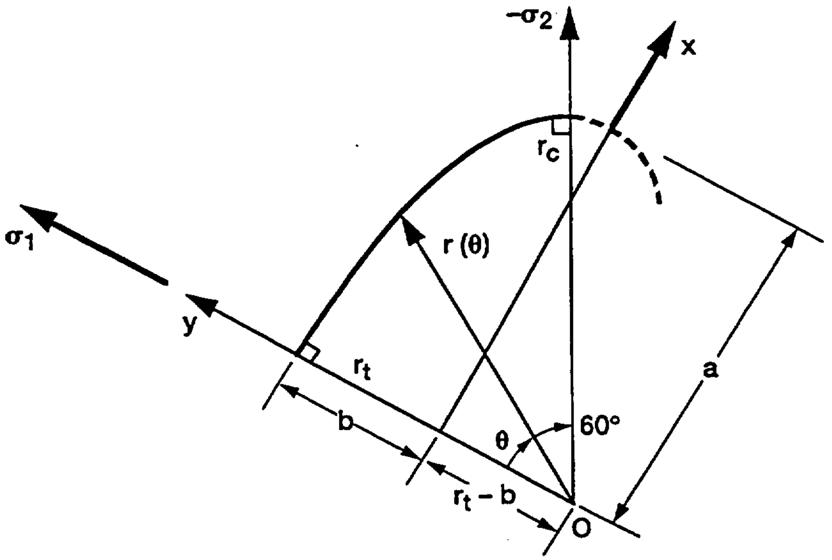

Figure 3.4.—A 60° sector of Willam-Warnke failure surface depicted in π-plane.

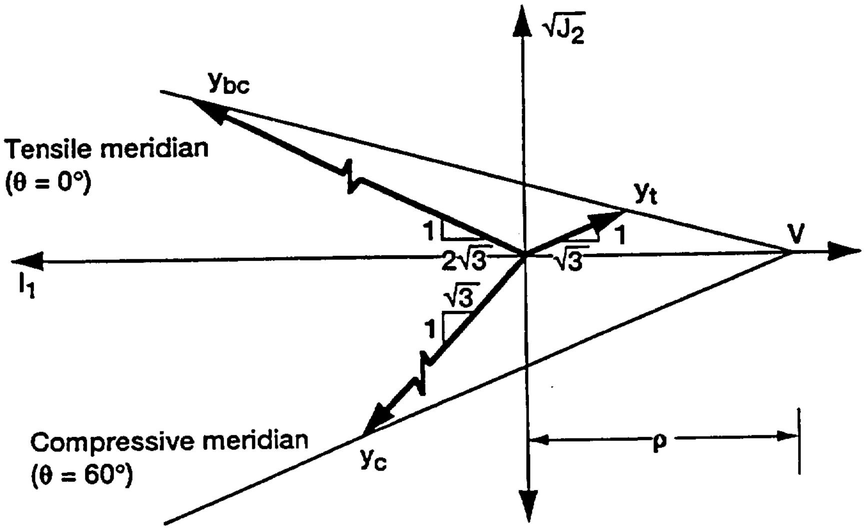

Figure 3.5.—Tensile and compressive meridians viewed in I_1-$\sqrt{J_2}$ stress space.

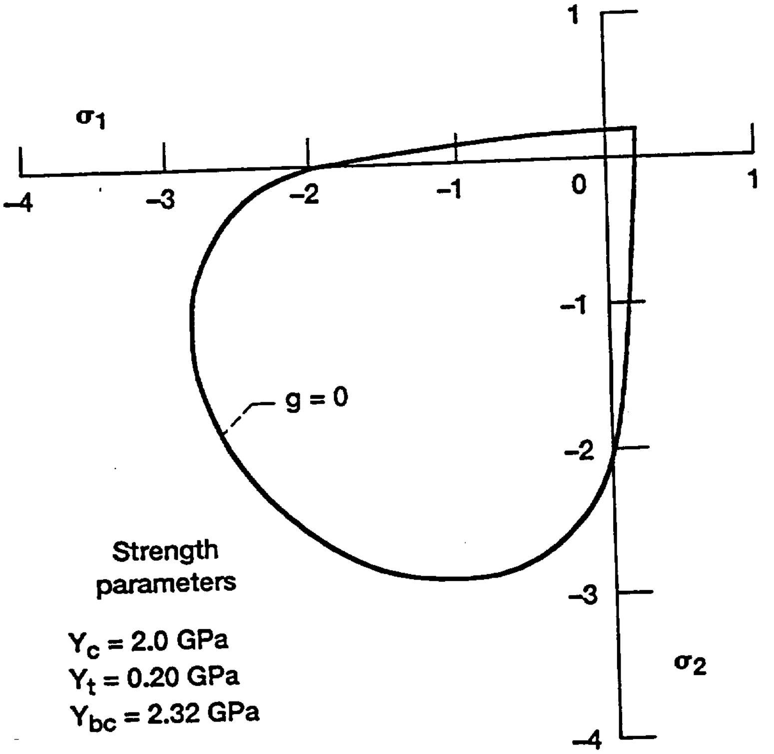

Figure 3.6.—Willam-Warnke failure surface depicted in σ_1–σ_2 stress space.

CHAPTER IV

INTERACTIVE RELIABILITY MODEL

In this chapter the details of transforming the Willam-Warnke failure function into an interactive probabilistic model are presented. Rather than predicting a fail/no fail design condition, this stochastic approach predicts the probability of failure of a component. The design issues discussed here are similar to those outlined in chapter II. The interactive reliability model accounts for a reduction in reliability due to compressive stresses, and also accounts for decreased scatter in failure for compressive stress states in comparison to tensile stress states. Note that the strength parameters used in the Willam-Warnke failure criterion are treated as random variables. Other quantities such as stiffness and loads can be treated in a probabilistic fashion (see Cruse et al., 1988), but since the strength of ceramic-based material systems commonly varies by 100 percent or more, only the strength parameters are treated as random variables.

Reliability is calculated under the assumption that the three strength parameters (Y_c, Y_t, and Y_{bc}) are independent random variables. It is assumed that each parameter is characterized by a two-parameter Weibull distribution (eqs. (2.1) to (2.4)); however, other distributions can be used with this approach. Using separate probability density functions for each random variable is versatile since other statistical distributions such as a three-parameter Weibull distribution or a log-normal distribution can be used to characterize the random variables. The selection of the distribution is always dictated by the failure data. However, for the purpose of simplicity and illustration, only the two-parameter Weibull distribution is considered here. To define the probability density distributions for each strength parameter, a Weibull modulus α and a scale parameter β must be determined experimentally. In general, a significant number of failure tests (a quantity which is dependent on the precision required for the parameter estimates of α and β) are necessary to characterize the probability density function for each random variable. See Pai and Gyekenyesi (1988) for methods of parameter estimation.

Here the functional dependence of the failure function $g(\mathscr{Y}_\alpha, \sigma_{ij})$ is given by equation (3.9). In general the reliability of a unit volume is computed from the expression

$$\mathscr{R} = \text{Probability}\Big[g\big(\mathscr{Y}_\alpha, \sigma_{ij}\big) < 0\Big] \tag{4.1}$$

where $\mathscr{R}$ represents the reliability. It is assumed that the element is homogeneous in stress; that is, no stress gradients exist throughout the element. Initially, the reliability calculations are based on unit volumes. Later, adjustments that account for arbitrary volumes are introduced. To calculate the reliability for an element of unit volume, the joint density must be integrated over the design space defined by the failure function. This integration takes the form

$$\mathscr{R} = \int\int_{\partial_s}\int \Omega\big(y_c, y_t, y_{bc}\big) dy_c \, dy_t \, dy_{bc} \tag{4.2}$$

where $\Omega\,(y_c, y_t, y_{bc})$ is the joint density function of the random variables that correspond to the material strength parameters, and ∂_s is the design space. By definition, the design space is that portion of the stress space bounded by the failure surface. Under the assumption that the random variables appearing in equation (4.2) are statistically independent, the reliability expression takes the form

$$\mathcal{R} = \int\int_{\partial_s}\int p_1(y_c)p_2(y_t)p_3(y_{bc})dy_c\, dy_t\, dy_{bc} \tag{4.3}$$

where $p_1(y_c)$, $p_2(y_t)$, and $p_3(y_{bc})$ are the marginal probability density functions. These density functions are characterized by the two-parameter Weibull distribution.

The integration defined by equation (4.3) yields the reliability of a unit volume. This type of integration, and the technique for defining the limits of integration were outlined in Sun and Yamada (1978), and Wetherhold (1983). To illustrate the approach, one of the simpler models presented in these references (i.e., the Tsai-Wu criterion) is used as an example since a closed-form solution can be obtained. Application of this type of criterion has been proposed for the analysis of laminate composites, since each ply is analyzed by assuming that the ply is an orthotropic plate subject to plane stress conditions. Here the failure function takes the form

$$\left[\frac{\sigma_1}{Y_1}\right]^2 - \left[\frac{\sigma_1\sigma_2}{Y_1^2}\right] + \left[\frac{\sigma_2}{Y_2}\right]^2 + \left[\frac{\sigma_6}{Y_6}\right]^2 - 1 = 0 \tag{4.4}$$

where σ_1 and σ_2 are in the in-plane normal stresses, and σ_6 is the in-plane shear stress. The strengths Y_1, Y_2, and Y_6 are the random variables associated with the strength in the primary material direction (Y_1), transverse to the primary material direction (Y_2), and an in-plane shear strength (Y_6). The reliability calculation follows the format outlined in equations (4.1) to (4.3), specifically,

$$R = \int_0^w \int_0^{v(Y_6)} \int_0^{u(Y_6,Y_2)} p(y_1)\, p(y_2)\, p(y_6)\, dy_1\, dy_2\, dy_6 \tag{4.5}$$

Here $p(y_1)$, $p(y_2)$, and $p(y_6)$ are the marginal probability density functions for the respective strength variables, and the limits of integration are defined by systematically solving equation (4.4) for each random variable, and then suppressing the random variable. Thus the first limit of integration is defined by the expression

$$u\left(Y_2, Y_6\right) = \left[\frac{\sigma_1^2 - \sigma_1\sigma_2}{1^2 - \left(\sigma_2/Y_2\right)^2 - \left(\sigma_6/Y_6\right)^2}\right]^{1/2} \tag{4.6}$$

Next, terms containing the random variable Y_1 are suppressed in equation (4.4), and the remainder of the equation is solved for Y_2 resulting in

$$v\left(Y_6\right) = \left[\frac{\sigma_2^2}{1^2 - \left(\sigma_6/Y_6\right)^2}\right]^{1/2} \tag{4.7}$$

To solve for the limits of y_6, terms containing both Y_1 and Y_2 are suppressed in equation (4.4), hence

$$w = \sigma_6 \tag{4.8}$$

Note that each term in this particular failure function (eq. 4.4) contains one strength variable. However, for the Willam-Warnke model each term in the interactive formulation contains all three strength parameters. Deriving the limits would require substitution of equations (3.12), (3.23), (3.24), and (3.25) into equation (3.9), and solving for each of the strength parameters explicitly to obtain expressions similar to equations (4.6) to (4.8). Developing closed-form expressions is intractable because of the definition of $r(\theta)$. For this reason, the triple integral was evaluated using Monte Carlo methods.

The Monte Carlo technique involves generating a uniform random sample of size K for each random variable. A value is selected for each strength parameter via a random number generator. This random number is used with the assumed marginal probability density function (i.e., two-parameter Weibull, three-parameter Weibull, log normal, etc.) to obtain values for the random strength variables. Details of this computational procedure are outlined in Wetherhold (1983). For a given stress state, the failure function is evaluated for each sample of random variables. Initially an element of unit volume subject to a homogeneous stress state is considered. If $g(\mathscr{Y}_\alpha, \sigma_{ij}) < 0$ for a given trial, then that trial is recorded as a success. By repeating this process a suitable number of times for a given state of stress, the reliability (or cumulative distribution) of the element is generated. In essence, the Monte Carlo method provides a means of simulating failure experiments on a computer. This assumes that the marginal probability density functions have been suitably characterized; that is, the values of the α's and the β's are known a priori. For a sufficiently large simulation sample size, reliability is computed by the simple expression

$$\mathscr{R} = \frac{n}{K} \tag{4.9}$$

where n is the number of successful trials (i.e., the number of trials where $g(\mathscr{Y}_\alpha, \sigma_{ij}) < 0$).

Figure 4.1 shows a comparison of the Monte Carlo calculations with the underlying Weibull distribution assumed for the tensile strength random variable. This is a plot of probability of failure versus failure strength. For this case, the reliability of an element of unit volume is given by

$$\mathscr{R} = \exp\left[-\left(\frac{\sigma}{\beta}\right)^{\alpha}\right] \tag{4.10}$$

where σ is the applied tensile stress. For graphical purposes the natural logarithm of both sides of the expression is taken twice. By introducing a constant C defined as

$$C = \left(\frac{1}{\beta}\right)^{\alpha} \tag{4.11}$$

then the form of equation (4.10) is

$$\ln\left[\ln\left(\frac{1}{\mathscr{R}}\right)\right] = \ln C + \alpha \ln \sigma \tag{4.12}$$

Here the Weibull shape parameter for tensile strength defines the slope of the line depicted in figure 4.1. For this illustration $\alpha = 5$ and $\beta = 0.2$. The three points represent estimates using the Monte Carlo method for the uniaxial failure strength where the specified reliabilities are 5, 50, and 95 percent. A computer algorithm which numerically evaluates equation (4.5) using the Monte Carlo technique was used. For this example the desired reliability, the Weibull parameters defining the marginal probability density functions for the strength parameters, and the desired number of Monte Carlo simulations are specified. The simulated tensile load path is described in chapter III. The stress state is increased incrementally along the specified load path until the desired reliability is found to within some predetermined error bound. The data points in figure 4.1 were generated using 100 Monte Carlo trials. As a comparison, figures 4.2 to 4.4 show Monte Carlo estimates for different sample sizes. Figure 4.2 depicts predictions for 500 Monte Carlo trials; figure 4.3, 1000 trials; and figure 4.4, 10 000 trials. Note that as the number of trials increases, the points converge to the line representing the underlying Weibull distribution for the parameter Y_t. This indicates that the numerical approach for evaluating equation (4.5) asymptotically converges to the underlying distribution as the sample size K increases.

To illustrate behavior along other load paths, simulations were conducted for the strength parameters Y_c and Y_{bc}. Figure 4.5 shows the relations for the strength parameter Y_c, and figure 4.6 shows the relations for the parameter Y_{bc}. The Weibull parameters were arbitrarily stipulated. For the uniaxial compressive case, $\alpha = 35$ and $\beta = 2.0$, and for the biaxial compressive case, $\alpha = 35$ and $\beta = 2.32$. Note that the α's were assigned higher values for the compressive strength variables than for the tensile strength variable. Although strength data for isotropic whisker-toughened ceramics are not available, there are sufficient experimental data for monolithic ceramics to indicate that compressive failure modes generally do not exhibit as much scatter as tensile failure modes. It is believed that similar behavior will be exhibited by isotropic whisker-toughened materials. As in the uniaxial tensile case, estimates of reliability for 5, 50, and 95 percent were compared to the linear form of the Weibull equation associated with each load path. Again, all points converged with the line for 10 000 trials.

This technique was also used in calculating the reliability contours shown in figure 4.7. This figure represents the σ_1–σ_2 stress space. The reliability contours represent a homogeneously stressed material element of unit volume. Here the Weibull parameters associated with the tensile strength random variable are arbitrarily chosen to coincide with the example cited in the preceding paragraph, specifically $\alpha_t = 5$ and $\beta_t = 0.2$. Similarly, the Weibull parameters associated with the compressive strength random variable are arbitrarily specified, with $\alpha_c = 35$ and $\beta_c = 2$. Finally the Weibull parameters associated with the equal biaxial compressive strength random variable are $\alpha_{bc} = 35$ and $\beta_{bc} = 2.32$. The three surfaces depicted in figure 4.7 correspond to $\mathscr{R} = 5$, 50, and 95 percent. Note that the reliability contours retain the general behavior of the deterministic failure surface. In general, as the α's increase, the spacing between contours diminishes. Eventually with increasing α the contours would not be distinct and they would effectively map out a deterministic failure surface. An increase in the β's shifts the relative position of the contours in an outward direction indicating an increase in strength. Also note that the α's for the tensile and compressive load paths are different and can be specified independently of each other. This is a distinct advantage relative to the Powers model discussed in chapter II. Since only a tensile Weibull modulus is specified in the Powers model, the same scatter would occur for both tensile and compressive load paths.

The details for computing the reliability of a single element have been presented assuming a homogeneous state of stress and a unit volume. To design a structural component with a varying stress field, the component is discretized and the stress field is characterized using finite element methods. Since component failure may initiate in any of the discrete elements (which typically do not have unit volumes or areas), it is useful to consider a component from a systems viewpoint. A discretized component is a series system if it fails when one of the discrete elements fails. This approach gives rise to weakest-link reliability theories. In a parallel system, failure of a single element does not necessarily cause the component to fail, since the remaining elements may sustain the load through redistribution. Parallel systems lead to what have been referred to in the literature as bundle theories. Since it is assumed that qualitatively the failure behavior of whisker-toughened ceramics mimics monolithic ceramics, a weakest-link reliability theory is adopted for designing structural components.

If the failure of an individual element is considered a statistical event, and these events are assumed to be independent, then the probability of failure of a discretized component is given as

$$P_f = 1 - \prod_{i=1}^{N} R_i \tag{4.13}$$

where N is the number of discrete finite elements for a given component, and R_i is the reliability of the i^{th} discrete element. This reliability is computed in the following manner. Recall that $\mathcal{R}$ (the reliability based on a unit volume) is defined by equations (4.1) to (4.3), but calculated using the Monte Carlo techniques described previously. These same techniques can be used to compute R_i if the Weibull scale parameters are adjusted to reflect the size of the element. In general each scale parameter (β_t, β_c, and β_{bc}) is adjusted by using the following transformation

$$\beta^* = \beta\left[\frac{1}{V_i}\right]^{1/\alpha} \tag{4.14}$$

Here V_i is the volume of the i^{th} element and β^* is the adjusted scale parameter. No adjustment is necessary for the Weibull moduli. The preceding discussion on the reliability model implied that failure of whisker-toughened CMC originates from volume flaws. It is quite possible that component failure is caused by surface and/or volume flaws; that is, competing failure modes may exist. These competing failure modes usually have distinctly different Weibull parameters that characterize the marginal probability density functions. Accordingly, equation (4.14) can be used for surface flaw analyses if V_i is replaced by the area of the i^{th} element, A_i. However, for brevity, only volume flaw analysis is considered here.

This numerical procedure has been incorporated in a public domain test bed computer algorithm given the acronym TCARES (Toughened Ceramics Analysis and Reliability Evaluation of Structures). Currently this algorithm is coupled to the MSC/NASTRAN finite element code. For a complete description of the TCARES algorithm, see Duffy, Manderscheid, and Palko (1989). Before using TCARES, the proposed interactive reliability model that has been implemented into TCARES must be characterized using an extensive data base that includes multiaxial experiments. It is not sufficient to simply characterize the Weibull parameters for each random strength variable. Multiaxial experiments should be conducted to assess the accuracy of the interactive modeling approach. However, once the Weibull parameters have been characterized for each random strength variable, the algorithm allows a design engineer to predict the reliability of a structural component subject to quasi-static multiaxial loads. Isothermal conditions are considered for the application that follows. However, the algorithm is capable of nonisothermal analyses if the Weibull parameters are specified at a sufficient and appropriate number of temperature values. To illustrate certain aspects of the interactive model and the TCARES algorithm, a reliability analysis is performed on a test specimen which is known as the Brazilian disk.

The Brazilian disk is used to circumvent the alignment difficulties encountered in tensile testing brittle materials. In addition the Brazilian disk has been used to determine tensile strengths of brittle materials that exhibit reduced tensile strengths relative to the compressive strength (e.g., concrete and rock). The analytical details concerning the stress field of the Brazilian disk have been discussed by a number of authors including Hondros (1959), Vardar and Finnie (1975), Chong, Smith, and Borgman (1982), and Fessler and Fricker (1984). Most researchers assume that tensile failure usually occurs along the diameter directly beneath the applied load (see fig. 4.8), splitting the disk. However, the region of the disk directly beneath the load experiences very large compressive stress states that dissipate slowly. The interactive model presented here allows for a reduction in reliability when compressive stress states are present. Thus the Brazilian disk can be used to compare the interactive model with other widely used reliability models that do not account for compressive stress states. For simplicity, the interactive model is compared with the Principle of Independent Action (PIA) reliability model.

It is assumed that the disk is fabricated from an isotropic whisker-toughened CMC material with a Young's modulus of 300 GPa and a Poisson ratio of 0.2. A compressive pressure load of 1000 MPa was applied to the disk, and the subtended angle η for this example is 0.039 rad. The Weibull parameters associated with each random strength variable were arbitrarily chosen. Specifically the Weibull parameters associated with the tensile strength random variable are $\alpha_t = 15$ and $\beta_t = 250$. The Weibull parameters associated with the compressive strength random variable are $\alpha_c = 35$ and $\beta_c = 2500$. Similarly the Weibull parameters associated with the equal biaxial strength random variable are $\alpha_{bc} = 35$ and $\beta_{bc} = 2900$. Note that the β parameters have units of MPa$\cdot$(mm)$^{3/\alpha}$. The disk has a radius of 50 cm and a thickness of 5.0 cm, and was modeled using 1/8 symmetry with 1044 finite elements (see fig. 4.9). The elements used in the structural analysis were 8-node brick elements (MSC/NASTRAN HEX/8). The tensile stress in the x-direction near the center of the disk was 24.8 MPa. This stress remains fairly constant along the vertical diameter, except in the near vicinity of the load, where this stress component changes sign and becomes compressive (see fig. 4.10). The elements near the loads experience large compressive stresses (~997 MPa) in the y-direction that dissipate slowly down the diameter (see fig. 4.11). The stresses in this direction are compressive throughout the disk.

When this particular discretized component was analyzed using the PIA model (with $\alpha = 15$ and $\beta = 250$) the component reliability was 99.9 percent. Note that compressive stress states (specifically compressive principal stresses) do not affect component reliability when using the PIA model. This assumption is similarly adopted for other reliability theories such as Batdorf's reliability model. This lack of accounting for compressive stress states may be a nonconservative assumption depending on the values of the Weibull parameter that characterize the compressive strength random variables. Analyzing the disk using the interactive reliability model presented here resulted in a component reliability of 77.7 percent. Again the Weibull parameters for the compressive strength random variables were arbitrarily specified. However, α values of 35 begin to approach values for metals which have deterministic strength parameters, and an increase in the β values of over an order of magnitude relative to β_t represent conservative estimates of these Weibull parameters. Thus in comparing the component reliability from the PIA model and the interactive reliability model, it is evident that accounting for compressive stress states may play an important role in the analysis of structural components.

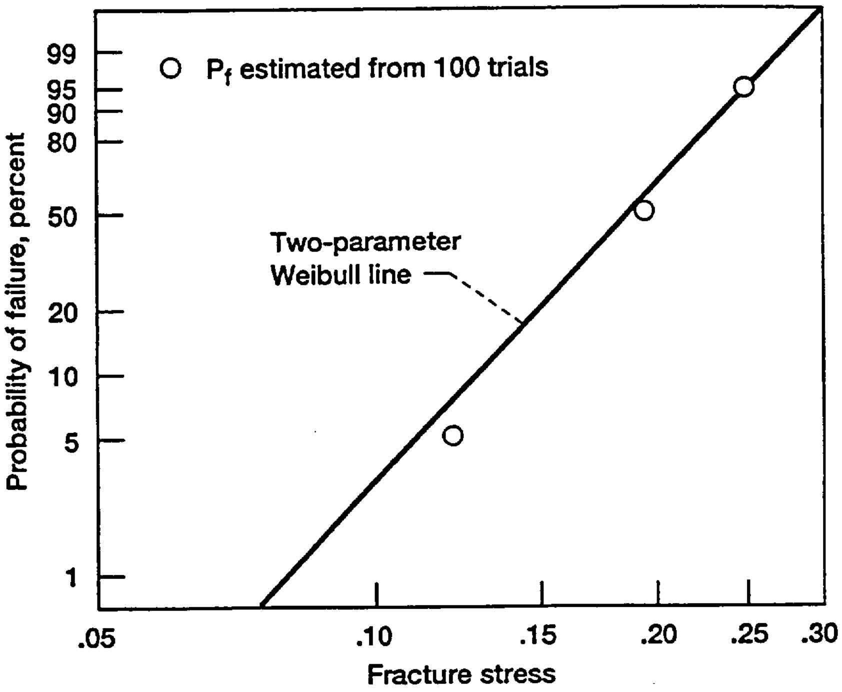

Figure 4.1.—Reliability estimates of uniaxial tensile strengths using 100 Monte Carlo simulations.

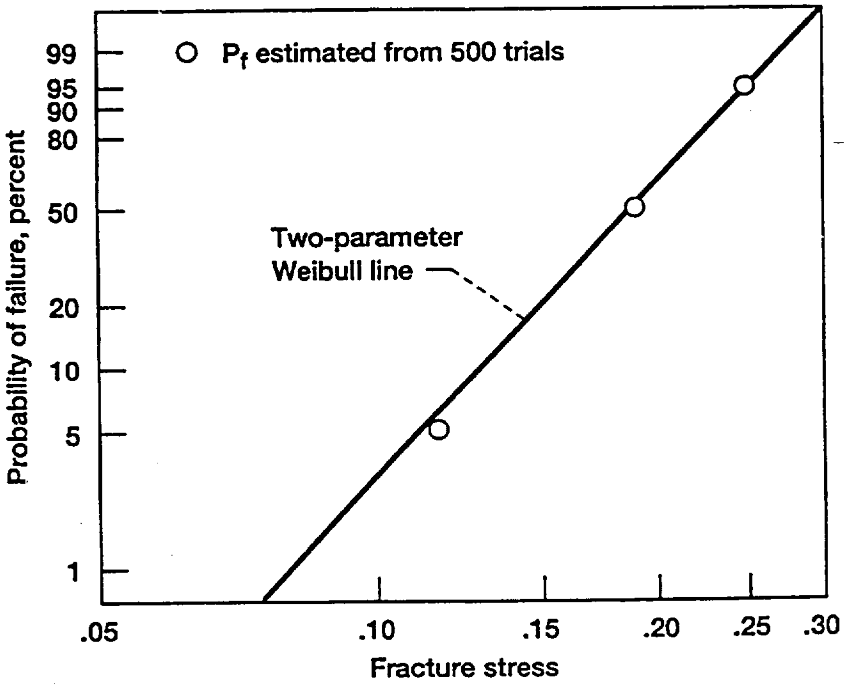

Figure 4.2.—Reliability estimates of uniaxial tensile strengths using 500 Monte Carlo simulations.

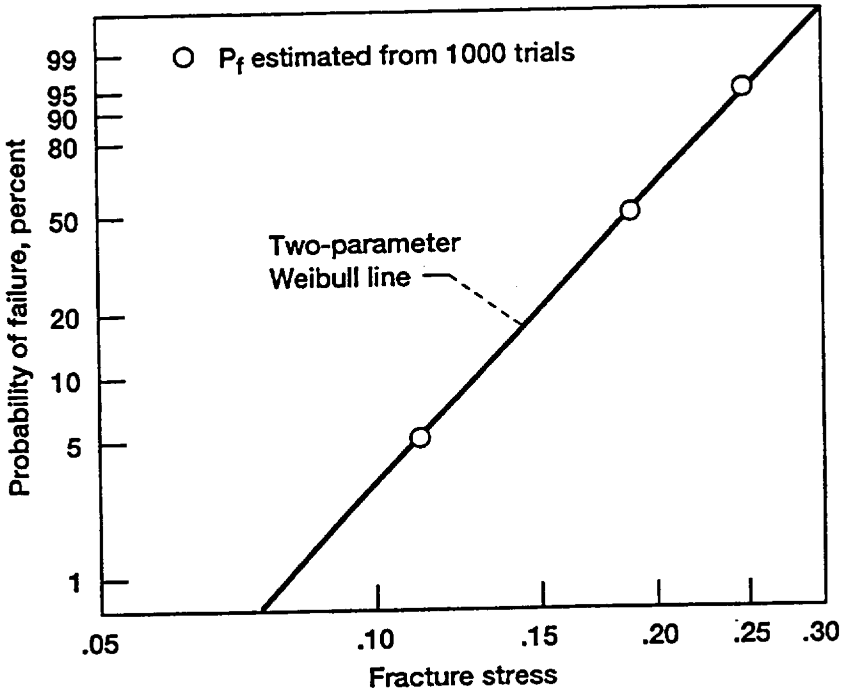

Figure 4.3.—Reliability estimates of uniaxial tensile strengths using 1000 Monte Carlo simulations.

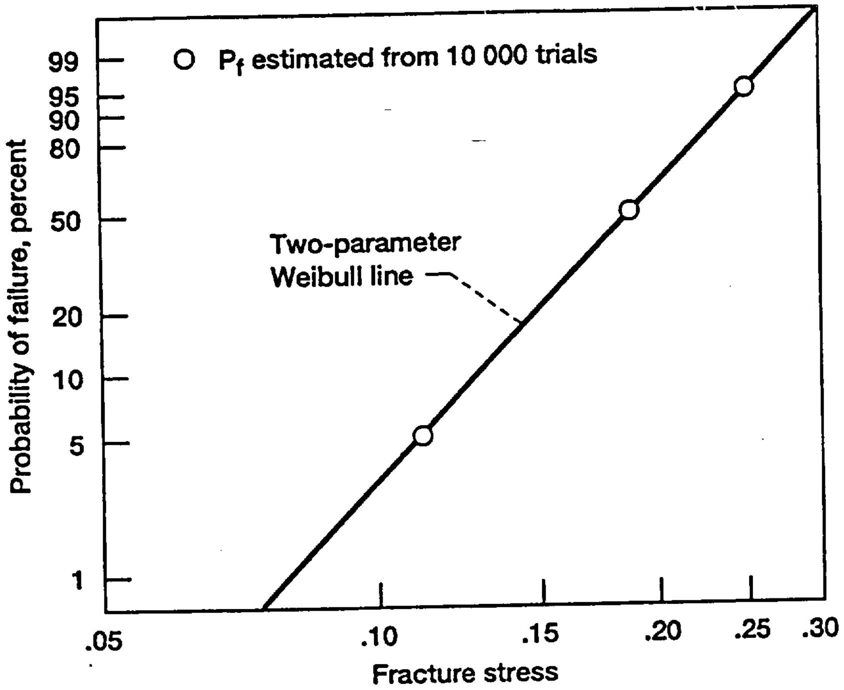

Figure 4.4.—Reliability estimates of uniaxial tensile strengths using 10 000 Monte Carlo simulations.

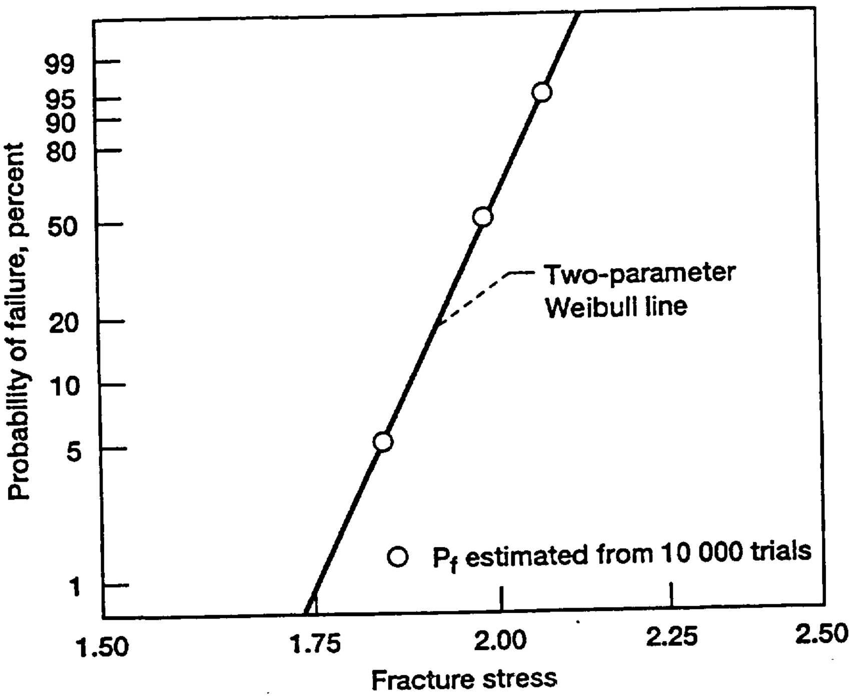

Figure 4.5.—Reliability estimates of uniaxial compressive strengths using 10 000 Monte Carlo simulations.

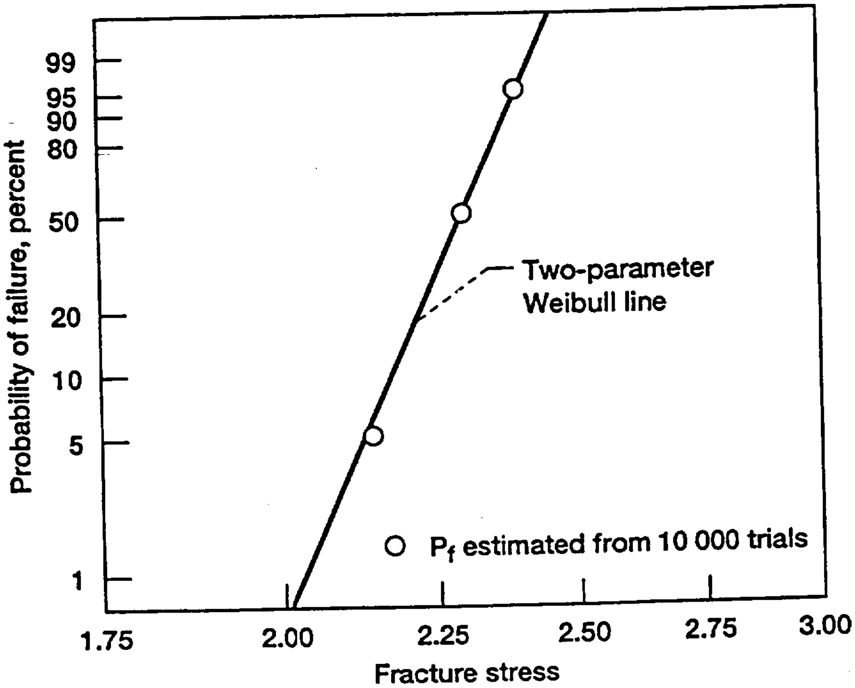

Figure 4.6.—Reliability estimates of biaxial compressive strengths using 10 000 Monte Carlo simulations.

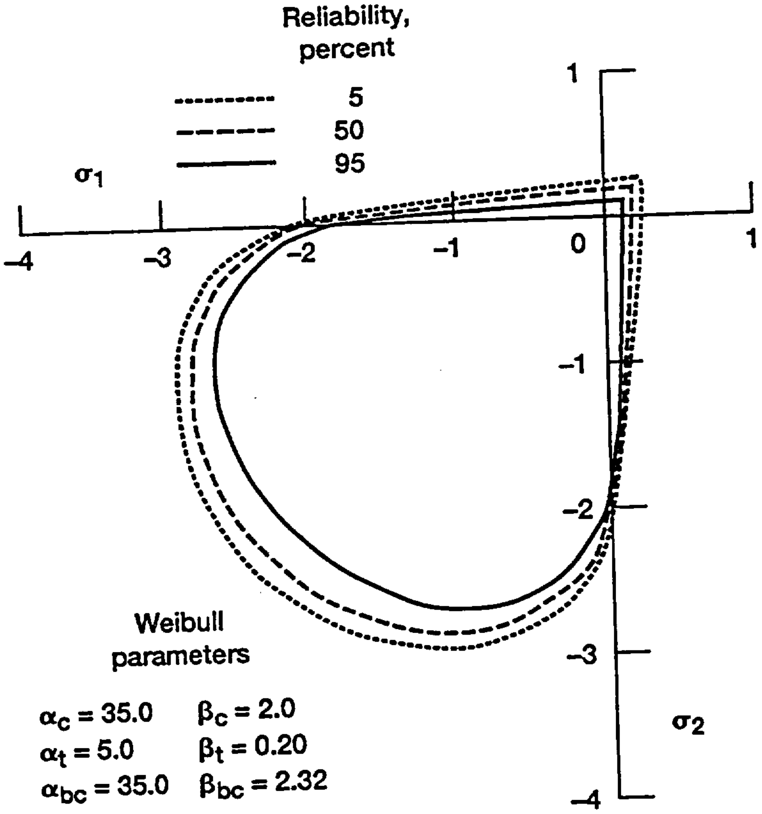

Figure 4.7.—Reliability contours using the reliability model projected onto σ_1–σ_2 stress space.

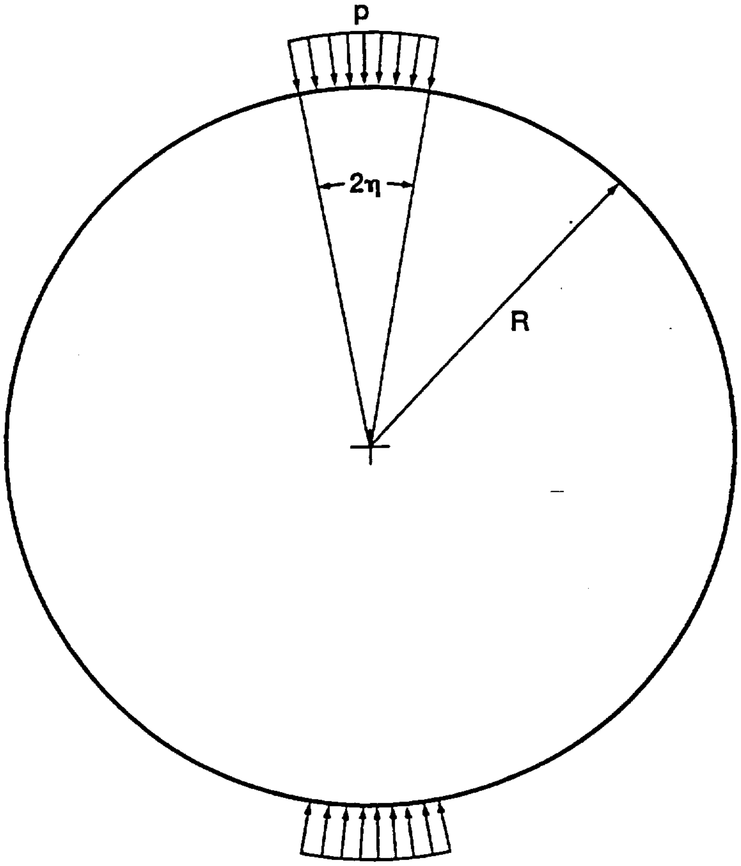

Figure 4.8.—Geometry and pressure load for Brazilian disk test specimen.

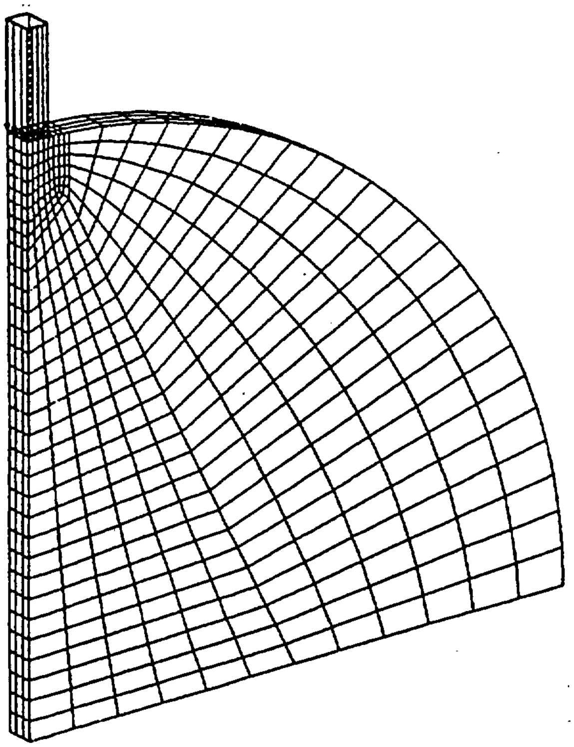

Figure 4.9.—Finite element model for Brazilian disk test specimen.

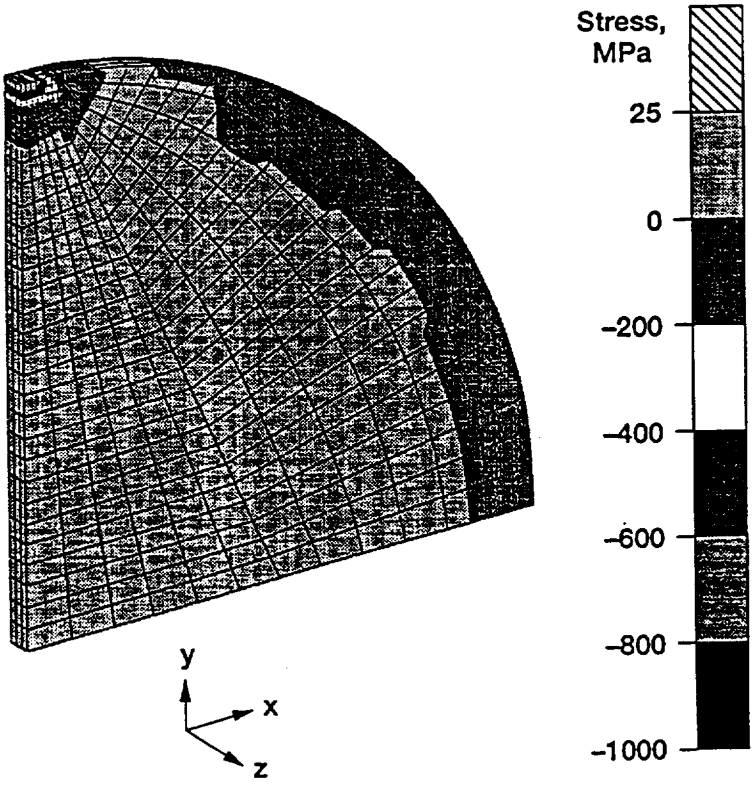

Figure 4.10.—Stresses acting on disk in normal x-direction.

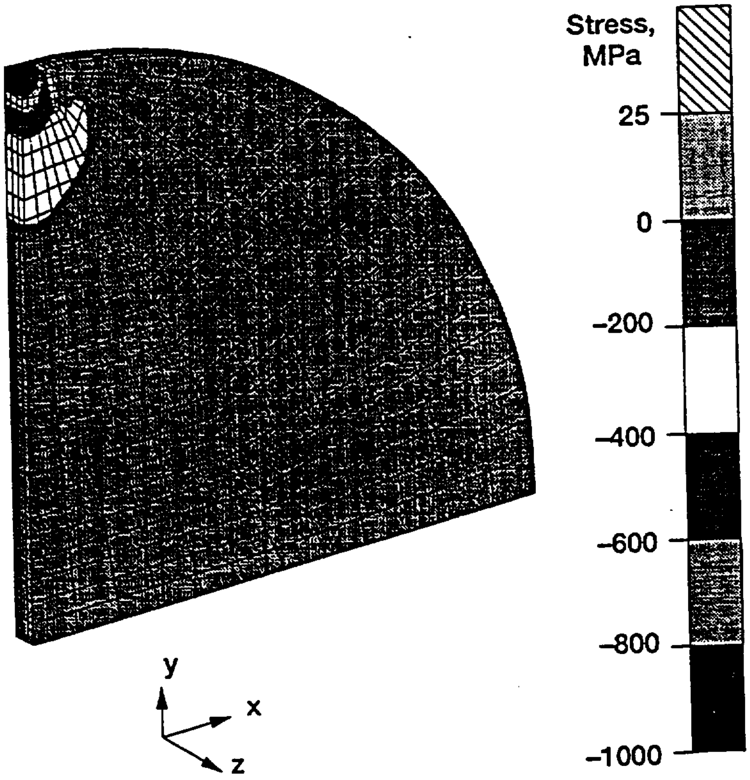

Figure 4.11.—Stresses acting on disk in normal y-direction.

CHAPTER V

CONCLUDING REMARKS AND FUTURE DIRECTION

The basic features of conducting a reliability analysis by deriving an interactive reliability model have been illustrated. The deterministic Willam-Warnke failure criterion serves as the theoretical foundation on which the reliability model was constructed. Fundamental to the work presented here is the assumption that the strength parameters associated with a deterministic failure criterion can be treated as random variables. As a result, the proposed reliability model retains the phenomenological behavior that was present in the deterministic failure criterion, such as sensitivity to hydrostatic stress and reduced tensile strength. The predictive capabilities of the interactive model were examined assuming that the two-parameter Weibull distributions characterized the marginal probability density functions for each random strength variable. This included both uniaxial and multiaxial load paths. The interactive reliability model was implemented into TCARES, a test-bed software program. Since this algorithm has been coupled with a general-purpose finite element program, design engineers are now able to use the code as a postprocessor in order to predict the reliability of a structural component subject to quasi-static multiaxial load conditions. A simple structural problem was presented to illustrate the reliability model and the computer algorithm.

In addition, this type of reliability model can be extended to account for material anisotropy. Using orthotropic materials as an example, the parent deterministic failure function must reflect the stress state (as was done in this report) and the appropriate material symmetry. For orthotropy this requires that

$$g = g\left(\tilde{Y},\ \sigma_{ij},\ a_i,\ b_i\right) \tag{5.1}$$

where a_i and b_i are orthogonal unit vectors that represent the local orthotropic material directions. Because g is a scalar function, it must remain form invariant under arbitrary proper orthogonal transformations. Work by Reiner (1945), Rivlin and Smith (1969), Spencer (1971) and others demonstrated that by applying the Cayley-Hamilton theorem and the elementary properties of tensors, a finite set of invariants (known as an integrity basis) can be derived for scalar functions that are dependent on first- and second-order tensor quantities. See Duffy (1987) for the details regarding the application of the Cayley-Hamilton theorem for this purpose. Form invariance of the scalar functions is ensured if the functions depend on invariants that constitute either the integrity basis, or any subset thereof. A number of authors (Lance and Robinson (1971), Boehler and Sawczuk (1977), Arnold (1989), and Robinson and Duffy (1990)) have used this methodology to develop scalar valued functions that are dependent on stress (a second-order tensor) and material directions (usually characterized by first-order tensors as in eq. (5.1)). Clearly, the future direction alluded to here (i.e., incorporating material symmetry using direction tensors) is not without precedent. However, for anisotropic whisker-toughened ceramic composites the failure function must not only reflect the material anisotropy, but also account for reduced tensile strength, and a dependence on the hydrostatic component of stress, if this behavior is exhibited experimentally.

Recall that the proposed model calculates reliability using the Monte Carlo method. For each stress state 10 000 trials are used to compute reliability. Since this approach is used in conjunction with finite element methods, it could easily challenge the computational capacity of even a supercomputer as the number of discrete finite elements increases. In order to optimize computational efficiency, future work will also concentrate on using numerical schemes referred to as Fast Probability Integration (FPI) techniques. Wu (1984) outlined several fast probability integrators, including the methods of Rackwitz and Fiessler (1978) and Chen and Lind (1982). These are first-order methods since it is assumed that the limit state is linear at the design point. Quadratic methods have been proposed, but the added complexity is not justified by dramatic increases in accuracy. In his work, Wu proposed an improvement to the Rackwitz-Fiessler method. This method uses a least squares technique to fit an approximated cumulative distribution function for each random variable to the true cumulative distribution. This approach increases accuracy with a minimal increase in computational efforts.

REFERENCES

1. Adams, M.A.: The Strength of Brittle Ceramics in Compressive Stress States. Ph.D. Thesis, University of California, Los Angeles, CA, 1975.

2. Adams, M.; and Sines, G.: A Statistical, Micromechanical Theory of the Compressive Strength of Brittle Materials. J. Am. Ceram. Soc., vol. 61, no. 3-4, 1978, pp. 126-131.

3. Alpa, G.: On a Statistical Approach to Brittle Rupture for Multiaxial States of Stress. Eng. Fract. Mech., vol. 19, no. 5, 1984, pp. 881-901.

4. Arnold, S.M.: A Transversely Isotropic Thermoelastic Theory. NASA TM-101302, 1988.

5. Barnett, R.L., et al.: Fracture of Brittle Materials Under Transient Mechanical and Thermal Loading. Report AFFDL-TR-66-220. IIT Research Institute, Chicago, IL, 1967.

6. Batdorf, S.B.; and Crose, J.G.: A Statistical Theory for the Fracture of Brittle Structures Subjected to Nonuniform States of Stress. J. Appl. Mech., vol. 41, no. 2, 1974, pp. 459-464.

7. Batdorf, S.B.; and Heinisch, H.L., Jr.: Fracture Statistics of Brittle Materials with Surface Cracks. Eng. Fract. Mech., vol. 10, no. 4, 1978, pp. 831-841.

8. Boehler, J.P.; and Sawczuk, A.: On Yielding of Oriented Solids. Acta Mech., vol. 27, no. 1-4, 1977, pp. 185-204.

9. Buljan, S.; Pasto, A.E.; and Kim, H.J.: Ceramic Whisker- and Particulate-Composites: Properties, Reliability, and Applications. Am. Ceram. Bull. vol. 68, no. 2, 1989, pp. 387-394.

10. Chen, W.F.: Plasticity in Reinforced Concrete. McGraw-Hill, New York, 1982.

11. Chen, X.; and Lind, N.C.: A New Method of Fast Probability Integration. Solid Mechanics Division, University of Waterloo, Canada, June 1982.

12. Chong, K.P.; Smith, J.W.; and Borgman, E.S.: Tensile Strengths of Colorado and Utah Oil Shales. J. Energy, vol. 6, no. 2, Mar.-Apr. 1982, pp. 81-85.

13. Clarke, D.: Industrial Applications and Markets for Ceramic Matrix Composites. Rolls-Royce Report No. PNR90753, 1990.

14. Coleman, B.D.: On the Strength of Classical Fibers and Fiber Bundles. J. Mech. Phy. Solids, vol. 7, no. 1, 1958, pp. 60-70.

15. Cooper, N.R.; Margetson, J.; and Humble, S.: Probability of Failure Calculations and Confidence Band Estimates for an Annular Brittle Disc Fractured Under Centrifugal Loading. J. Strain Anal., vol. 21, no. 3, 1986, pp. 121-126.

16. Cruse, T.A., et al.: Probabilistic Structural Analysis Methods For Select Space Propulsion System Structural Components (PSAM). Comput. Struct., vol. 29, no. 5, 1988, pp. 891-901.

17. Daniels, H.E.: The Statistical Theory of the Strength of Bundles of Threads. I. Proc. R. Soc. London A, vol. 183, 1945, pp. 405-435.

18. Duffy, S.F.: A Viscoplastic Constitutive Theory for Transversely Isotropic Metal Alloys. Ph.D. Thesis, University of Akron, Akron, OH, 1987.

19. Duffy, S.F.; and Arnold, S.M.: Noninteractive Macroscopic Reliability Model for Whisker-Reinforced Ceramic Composites. J. Compos. Mater., vol. 24, Mar., 1990, pp. 293-308.

20. Duffy, S.F.; and Manderscheid, J.M.: Noninteractive Macroscopic Reliability Model for Ceramic Matrix Composites with Orthotropic Material Symmetry. J. Eng. Gas Turbines Power, vol. 112, Oct. 1990, pp. 507-511.

21. Duffy, S.F.; Manderscheid, J.M.; and Palko, J.L.: Analysis of Whisker-Toughened Ceramic Components - A design Engineer's Viewpoint. Am. Ceram. Bull., vol. 68, no. 12, 1989, pp. 2078-2083.

22. Fessler, H.; and Fricker, D.C.: Multiaxial Strength Tests for Brittle Materials. J. Strain Anal. Eng. Des., vol. 19, no. 3, 1984, pp. 197-208.

23. Freudenthal, A.M.: Statistical Approach to Brittle Fracture. Fracture, An Advanced Treatise, Vol. 2: Mathematical Fundamentals, H. Liebowitz, ed., Academic Press, New York, 1968, pp. 591-619.

24. Gyekenyesi, J.P.: SCARE - A Post-Processor Program to MSC/NASTRAN for the Reliability Analysis of Ceramic Components. J. Eng. Gas Turbines Power, vol. 108, no. 3, July 1986, pp. 540-546.

25. Harlow, D.G.; and Phoenix, S.L.: Probability Distributions for the Strength of Composite Materials I : Two-Level Bounds. Int. J. Fract., vol. 17, no. 4, 1981, pp. 347-372.

26. Hondros, G.: The Evaluation of Poisson's Ratio and the Modulus of Materials of a Low Tensile Resistance by the Brazilian Test. Aust. J. App. Sci., vol. 10, no. 3, 1959, pp. 243-268.

27. Ikeda, K.; and Igaki, H.: Fracture Criterion for Alumina Ceramics Subjected to Triaxial Stresses. J. Amer. Ceram. Soc., vol. 67, no. 8., 1984, pp. 538-544.

28. Ikeda, K.; Igaki, H.; and Kuroda, T.: Fracture Strength of Alumina Ceramics Under Uniaxial and Triaxial Stress States. Am. Ceram. Bull. vol. 65, no. 4, 1986, pp. 683-688.

29. Lamon, J.: Reliability Analysis of Ceramics Using the CERAM Computer Program. ASME Paper No. 90-GT-98, 1990.

30. Lance, R.H.; and Robinson, D.N.: A Maximum Shear Stress Theory of Plastic Failure of Fiber-Reinforced Materials. J. Mech. Phys. Solids, vol. 19, no. 2, 1971, pp. 49-60.

31. Larsen, R.P.; and Vyas, A.D.: The Outlook for Ceramics in Heat Engines, 1990-2010: Results of a Worldwide Delphi Survey. Report CONF-88-0279-1, Angonne National Lab., II, 1988.

32. Lode, W.: Versuche ueber den Einfuss der mitt leren Hauptspannung auf das Fliessen der Metalle Eisen Kupfer und Nickel. Z. Phys., vol. 36, 1926, pp. 913-939.

33. Midgley, E.; and Pierce, F.T.: Tensile Tests for Cotton Yarns, V. The "Weakest Link" Theorems on the Strength of Long and of Composite Specimens. J. Text. Inst., vol. 17, no. 7, 1926, pp. T335 - T368.

34. Nayak, G.C.; and Zienkiewicz, F.: Convenient Forms of Stress Invariants for Plasticity. J. Struct. Div., vol. 98, no. ST4, Apr. 1972, pp. 949-954.

35. Pai, S.; and Gyekenyesi, J.P.: Calculation of Weibull Strength Parameters and Batdorf Flaw Density Constants for Volume- and Surface-Flaw-Induced Fracture in Ceramics. NASA TM-100890, 1988.

36. Phoenix, S.L.: Probabilistic Concepts in Modeling the Tensile Strength Behavior of Fiber Bundles and Unidirectional Fiber/Matrix Composites. Composite Materials: Testing and Design, Proceedings of the Third Conference, ASTM STP-546, American Society for Testing Materials, Philadelphia, PA, 1974, pp. 130-151.

37. Phoenix, S.L.: Statistical Aspects of Failure of Fibrous Materials. Composite Materials: Testing and *Design*, Proceedings of the Fifth Conference, ASTM STP-674, S.W. Tsai, ed., American Society for Testing Materials, Philadelphia, PA, 1979, pp. 455-483.

38. Powers, L.M.: Reliability-Based Failure Analysis of Brittle Materials. Master's Thesis, Cleveland State University, Cleveland, OH, 1989.

39. Rackwitz, R.; and Fiessler, B.: Structural Reliability Under Combined Random Load Sequences. J. Compos. Struct., vol. 9, 1978, pp. 489-494.

40. Reiner, M.: A Mathematical Theory of Dilatancy. Am. J. Math., vol. 67, 1945, pp. 350-362.

41. Rivlin, R.S.; and Smith, G.F.: Orthogonal Integrity Basis for N Symmetric Matrices. Contributions to Mechanics, D. Abir, ed., Pergamon Press, Oxford, NY, 1969, pp. 121-141.

42. Robinson, D.N.; and Duffy, S.D.: Continuum Deformation Theory for High-Temperature Metallic Composites. J. Eng. Mech., vol. 116, no. 4, 1990, pp. 832-844.

43. Spencer, A.J.M.: Theory of Invariants. Continuum Physics, Vol. I: Mathematics, A. C. Eringen, ed., Academic Press, New York, 1971, pp. 239-255.

44. Sun, C.T.; and Yamada, S.E.: Strength Distribution of a Unidirectional Fiber Composite. J. Compos. Mater., vol. 12, Apr., 1978, pp. 169-176.

45. Vardar, O.; and Finnie, I.: An Analysis of the Brazilian Disk Fracture Test Using the Weibull Probabilistic Treatment of Brittle Strength. Int. J. Fract., vol. 11, no. 3, 1975, pp. 495-508.

46. Weibull, W.: A Statistical Theory of the Strength of Materials. Ing. Vetensk. Akad. Handl., vol. 151, 1939, pp. 5-45.

47. Weibull, W.: A Statistical Distribution Function of Wide Applicability. J. Appl. Mech., vol. 73, no. 3, 1951, pp. 293-297.

48. Wetherhold, R.C.: Statistics of Fracture of Composite Materials Under Multiaxial Loading. Ph.D. Thesis, University of Delaware, Newark, DE, 1983.

49. Willam, K.J.; and Warnke, E.P.: Constitutive Models for the Triaxial Behavior of Concrete. Int. Assoc. Bridge Struct. Eng. Proc., vol. 19, 1975, pp. 1-30.

50. Wu, Y.T.: Efficient Methods for Mechanical and Structural Reliability Analysis and Design. Ph.D. Thesis, The University of Arizona, Tuson, AZ, 1984.

REPORT DOCUMENTATION PAGE

Form Approved
OMB No. 0704-0188

1. AGENCY USE ONLY (*Leave blank*)	**2. REPORT DATE** April 1993	**3. REPORT TYPE AND DATES COVERED** Final Contractor Report

4. TITLE AND SUBTITLE Interactive Reliability Model for Whisker-Toughened Ceramics	**5. FUNDING NUMBERS** WU-778-32-11 NCC3-81
6. AUTHOR(S) Joseph L. Palko	
7. PERFORMING ORGANIZATION NAME(S) AND ADDRESS(ES)	**8. PERFORMING ORGANIZATION REPORT NUMBER** E-7513
9. SPONSORING/MONITORING AGENCY NAMES(S) AND ADDRESS(ES) National Aeronautics and Space Administration Lewis Research Center Cleveland, Ohio 44135-3191	**10. SPONSORING/MONITORING AGENCY REPORT NUMBER** NASA CR-191048

11. SUPPLEMENTARY NOTES
Project Manager, John P. Gyekenyesi, Structures Division, NASA Lewis Research Center, (216) 433-5587. A similar version of this report was submitted by Joseph L. Palko as a thesis in partial fulfillment of the requirements for the degree Master's of Science in Engineering Mechanics to Cleveland State University, Cleveland, Ohio.

12a. DISTRIBUTION/AVAILABILITY STATEMENT Unclassified - Unlimited Subject Category 27	**12b. DISTRIBUTION CODE**

13. ABSTRACT ***(Maximum 200 words)***

Wider use of ceramic matrix composites (CMC) will require the development of advanced structural analysis technologies. This report focuses on the use of an interactive model to predict the time-independent reliability of a component subjected to multiaxial loads. The deterministic, three-parameter Willam-Warnke failure criterion serves as the theoretical basis for the reliability model. The strength parameters defining the model are assumed to be random variables, thereby transforming the deterministic failure criterion into a probabilistic criterion. The ability of the model to account for multiaxial stress states with the same unified theory is an improvement over existing models. The new model has been coupled with a public-domain finite element program through an integrated design program. This allows a design engineer to predict the probability of failure of a component. A simple structural problem is analyzed using the new model, and the results are compared to existing models.

14. SUBJECT TERMS Whiskers; Ceramics; Composites; Weibull distribution; Interactive; Reliability; Brazilian disk; Finite element analysis	**15. NUMBER OF PAGES** 48 **16. PRICE CODE** A03

17. SECURITY CLASSIFICATION OF REPORT Unclassified	**18. SECURITY CLASSIFICATION OF THIS PAGE** Unclassified	**19. SECURITY CLASSIFICATION OF ABSTRACT** Unclassified	**20. LIMITATION OF ABSTRACT**

S. F. Duffy[1]

J. L. Palko[1]

Cleveland State University,
Department of Civil Engineering,
Cleveland, OH 44115

J. P. Gyekenyesi

NASA Lewis Research Center,
Structural Integrity Branch,
Cleveland, OH 44135

Structural Reliability Analysis of Laminated CMC Components

For laminated ceramic matrix composite (CMC) materials to realize their full potential in aerospace applications design, methods and protocols are a necessity. This paper focuses on the time-independent failure response of these materials and presents a reliability analysis associated with the initiation of matrix cracking. It highlights a public domain computer algorithm that has been coupled with the laminate analysis of a finite element code and which serves as a design aid to analyze structural components made from laminated CMC materials. Issues relevant to the effect of the size of the component are discussed, and a parameter estimation procedure is presented. The estimation procedure allows three parameters to be calculated from a failure population that has an underlying Weibull distribution.

Introduction

Structural components produced from laminated ceramic matrix composite (CMC) materials are being considered for a broad range of aerospace applications that include propulsion subsystems in the national aerospace plane, the space shuttle main engine, and advanced gas turbine engines. Specifically, composite ceramics may be used as segmented engine liners, small missile engine turbine rotors, and exhaust nozzles. These materials will improve fuel efficiency by increasing engine temperatures and pressures, which will, in turn, generate more power and thrust. Furthermore, these materials have significant potential for raising the thrust-to-weight ratio of gas turbine engines by tailoring directions of high specific reliability. The emerging composite systems, particularly those with a silicon nitride or silicon carbide matrix, can compete with metals in many demanding applications. The capabilities of laminated CMC prototypes have already been demonstrated at temperatures approaching 1400°C, well beyond the operational limits of most metallic materials.

Adding a second ceramic phase with an optimized interface to a brittle matrix improves fracture toughness, decreases the sensitivity of the brittle ceramic matrix to microscopic flaws, and could also improve strength. The presence of fibers in the vicinity of the crack tip modifies fracture behavior by increasing the required crack driving force by several mechanisms. These mechanisms include crack pinning, fiber bridging, fiber debonding, and fiber pull-out. This increase in fracture toughness allows for "graceful" rather than catastrophic failure. A unidirectional ply loaded in the fiber direction retains substantial strength capacity beyond the initiation of matrix cracking despite the fact that neither of the constituents would exhibit such behavior if tested alone. First matrix cracking consistently occurs at strains greater than in the monolithic matrix material. As additional load is applied, the matrix tends to break in a series of cracks bridged by the ceramic fibers, until the ultimate strength of the composite is reached. The region of a typical stress-strain curve between the first matrix cracking and the ultimate tensile strength illustrates an intrinsic damage tolerance not present in monolithic ceramics.

Laminated CMC material systems have several mechanical characteristics that must be considered in the design of structural components. In regard to an individual ply, the most deleterious of these characteristics are low strain tolerance, low fracture toughness, and a large variation in failure strength in the material orientation transverse to the fiber direction. Thus analyses of components fabricated from ceramic materials require a departure from the usual deterministic philosophy of designing metallic structural components (i.e., the factor-of-safety approach). Although the so-called size effect has been reported to be non-existent in the fiber direction (see DiCarlo, 1989), the bulk strength of unidirectional-reinforced ply will decrease transverse to the fiber direction as the component volume increases. Since failure in the transverse direction will be dominated by the scatter in strength, statistical design approaches must be employed. These approaches must, on the one hand, allow for elevated strength, reduced variability in strength, and a diminished effect of bulk specimen size in the fiber direction, and, on the other hand, increased scatter in strength and effects of bulk size in the transverse direction. Simply stated, a reliability analysis must rationally account for material symmetry imposed by the reinforcement. Computational structural mechanics philosophies must emerge that address the issues of scatter in strength, size effect, and material anisotropy. There is a need for test-bed software programs that incorporate stochastic design protocols, that are user friendly, that are computationally efficient, and that have flexible architectures that can readily incorporate changes in design philosophy. The C/CARES (Composite Ceramics Analysis and Reliability Evaluation of Structures) program, which will be highlighted in this article, was developed to fulfill this need. C/CARES is a public domain computer algorithm, coupled to a general purpose finite element program, which predicts the fast fracture reliability of a laminated structural component under multiaxial loading conditions.

---

[1] NASA Resident Research Associate at Lewis Research Center.

Contributed by the International Gas Turbine Institute and presented at the 36th International Gas Turbine and Aeroengine Congress and Exposition, Orlando, Florida, June 3-6, 1991. Manuscript received at ASME Headquarters March 4, 1991. Paper No. 91-GT-210. Associate Technical Editor: L. A. Riekert.

Stochastic Design Issues

For a number of composite material systems, several authors (see for example Batdorf and Ghaffarian, 1984; Wu, 1989) have reported a diminished size effect in the fiber direction; and DiCarlo (1989) has reported this effect for ceramic composites, in particular. This phenomenon is an important feature that must be addressed by any reliability model. How it is addressed depends on whether the material is modeled as a series system, a parallel system, or a combination. Current analytical practice uses finite element methods to determine the state of stress throughout the component. It is assumed that failure depends on the stress state in a component, such that deformations are not controlling design. Since failure may initiate in any of the discrete volumes (elements), it is useful to consider a component from a systems viewpoint. A component comprised of discrete volumes is a series system if it fails when one of the discrete volumes fail. This approach gives rise to weakest-link theories. In a parallel system, failure of a single element does not necessarily cause the component to fail, since the remaining elements may be able to sustain the load through redistribution. The parallel system approach leads to what has been referred to in the literature as "bundle" theories.

The basic principles underlying these bundle theories were originally discussed by Daniels (1945) and Coleman (1958). Their work was extended to polymer matrix composites by Rosen (1964) and Zweben (1968). Here, a relatively soft matrix serves to transfer stress between fibers and contributes little to the composite tensile strength. Hence, when a fiber breaks, the load is transferred only to neighboring fibers. Their analysis is rather complex and limited to establishing bounds on the stress at which the first fiber breaks and the stress at which all the fibers are broken. Harlow and Phoenix (1978) proposed a rather abstract approach that established a closed-form solution for all the intermediate stress levels in a two-dimensional problem, and Batdorf (1982) used an approximate solution to establish the solutions for the three-dimensional problem. Batdorf's model includes the two-dimensional model as a special case. In both of the latter two models, the authors proposed that the effective Weibull modulus increases with increasing component volume. This implies a diminished size effect. However, these current bundle theories are predicated on the fact that fibers are inherently much stronger and stiffer than the matrix. In laminated CMC materials this is not always the case. The strength and stiffness of both the fiber and matrix are usually closer in magnitude. For this reason bundle theories will not be considered in this paper.

We advocate the use of a weakest-link reliability theory for designing components manufactured from laminated CMC materials that do not exhibit strong size effects in specific directions. Assuming that a laminated structure behaves in a weakest-link manner allows a conservative estimate of structural reliability to be calculated. Thomas and Wetherhold (1990) point out that this assumption is equivalent to predicting the probability of the first matrix crack occurring in an individual ply. For most applications the design failure stress for a laminated material is assumed to coincide with this first ply matrix cracking because matrix cracking usually allows the fibers to oxidize at high temperatures, embrittling the composite.

Next, we address the righteousness of applying weakest-link theory to a material that in some sense does not exhibit size effects. In general, the mean strength of a sample population representing uniaxial tension test specimens can be obtained by integrating the probability of survival P_s with respect to the applied tensile stress; that is,

$$\bar{\sigma} = \int_0^\infty P_s d\sigma \tag{1}$$

Here $\bar{\sigma}$ is the mean tensile strength, σ is the applied tensile stress, and P_s is the probability of survival. The form of P_s depends on the probability density function that best represents the failure data, which in turn depends on whether the structural component acts as a parallel or series system. Adopting a three-parameter Weibull cumulative distribution function, and assuming a weakest-link system (a conservative assumption) gives the following form to Eq. (1):

$$\bar{\sigma} = \int_\gamma^\infty \exp\left[-\left(\frac{\sigma-\gamma}{\beta}\right)^\alpha V\right] d\sigma \tag{2}$$

Here V is the volume of the tensile test specimen, β is the scale parameter, α is the Weibull shape parameter, and γ is the threshold stress. This integral has the following closed-form solution (see DeSalvo, 1970):

$$\bar{\sigma} = \gamma + \left[\frac{\beta}{(V)^{1/\alpha}}\right]\Gamma\left(1+\frac{1}{\alpha}\right) \tag{3}$$

which depends on volume, the Weibull parameters, and the gamma function Γ. When an argument originally outlined by Jayatilaka (1979) is followed, two uniaxial tensile specimen populations with distinctly different specimen volumes will yield different mean strengths. Associating $\bar{\sigma}_1$ with V_1 gives

$$\bar{\sigma}_1 = \gamma + \left[\frac{\beta}{(V_1)^{1/\alpha}}\right]\Gamma\left(1+\frac{1}{\alpha}\right) \tag{4}$$

Similarly associating $\bar{\sigma}_2$ with V_2 gives

$$\bar{\sigma}_2 = \gamma + \left[\frac{\beta}{(V_2)^{1/\alpha}}\right]\Gamma\left(1+\frac{1}{\alpha}\right) \tag{5}$$

If the effective mean is defined as

$$(\bar{\sigma})_{\text{eff}} = \bar{\sigma} - \gamma \tag{6}$$

then the ratio of the effective mean strengths depends only on the specimen volume and the Weibull modulus; that is,

$$\frac{(\bar{\sigma}_1)_{\text{eff}}}{(\bar{\sigma}_2)_{\text{eff}}} = \frac{\bar{\sigma}_1 - \gamma}{\bar{\sigma}_2 - \gamma} = \left(\frac{V_2}{V_1}\right)^{1/\alpha} \tag{7}$$

As the Weibull modulus of a particular material increases, the ratio of the effective mean strengths approaches unity. In this situation the material exhibits no size effect (even though the distribution of failure strength may be represented by a Weibull probability density function). From a practical standpoint, doubling the specimen size of a material whose Weibull modulus is ≈ 15 would yield less than a 5 percent difference in the effective mean failure strengths of the two populations. We expect an elevated Weibull modulus to be associated with the strength of CMC materials in the fiber direction. Reports of an apparent lack of size effect associated with the strength in the fiber direction (see DiCarlo, 1989) could easily be an artifact of an increasing shape parameter (or small sample size). However, at this time there is an insufficient quantity of CMC failure data from which to estimate the Weibull parameters. In general, the weakest-link theory allows for diminishing size effects as the Weibull modulus increases.

Reliability Model

The ongoing metamorphosis of ceramic material systems and the lack of standardized design data have in the past tended to minimize the emphasis on modeling. Many structural components fabricated from ceramic materials were designed by "trial and error," since emphasis was placed on demonstrating feasibility rather than on fully understanding the processes controlling behavior. (This is understandable during periods of rapid improvements in material properties for any system.) In predicting failure behavior, there is a philosophical division that separates analytical schools of thought into microstructural methods (usually based on principles of fracture mechanics) and phenomenological methods. Blass and Ruggles

(1990) point out that analysts from the first school would design the material assuming that the constituents are distinct structural components and would consider the composite ply (or lamina) a structure in its own right. Analysts from the latter school of thought would design with the material (i.e., they would analyze structural components fabricated from the material). Rigorous fracture mechanics criteria have been proposed (e.g., Budiansky et al., 1986; Marshall et al., 1985) that adopt the microstructural viewpoint, but since they are all deterministic criteria, they will not be considered here. Fracture mechanics has been combined with a probabilistic Weibull analysis of failure location to determine the stress-strain behavior and subsequent work of fracture for unidirectional composites (e.g., Thouless and Evans, 1988; Sutcu, 1989). However, the focus here is first matrix cracking, and we note that mature reliability-based design methods using fracture mechanics concepts will not surface until a coherent mixed-mode fracture criterion has been proposed.

The aforementioned second school of thought represents the ply (or lamina) as a homogenized material with strength properties that are determined from a number of well-planned phenomenological experiments. The authors currently embrace this philosophy, and there are practical reasons for initially adopting this viewpoint. We fully recognize that the failure characteristics of these composites are controlled by a number of local phenomena, including matrix cracking, debonding and slipping between matrix and fibers, and fiber breakage, all of which interact strongly. Understanding the underlying analytical concepts associated with the microstructural viewpoint allows one to gain insight and intuition prior to constructing multiaxial failure theories that in some respect reflect the local behavior. Tensile failure in the fiber direction is dependent on these local mechanisms, and the future intent is to extend reliability methods to the constituent level in a rational and practical manner. However, a top-down approach, that is first proposing design models at the ply level, will establish viable and working design protocols. Initially adopting the bottom-up approach allows for the possibility of becoming mired in detail (experimental and analytical) when multiaxial reliability analyses are conducted at the constituent level.

There is a great deal of intrinsic variability in the strength of each brittle constituent of a ceramic matrix composite, but depending on the composite system, the transverse matrix cracking strength may either be deterministic or probabilistic. Statistical models are a necessity for those composite systems that exhibit any scatter in the initiation of first matrix cracking. We treat it in a probabilistic fashion, requiring that deterministic strength be a limiting case that is readily obtainable from the proposed reliability model. Predicting the reduction in reliability due to loads in the fiber direction addresses an upper bound for ply reliability in a structural design problem. Conversely, a tensile load applied transverse to the fiber direction results in failure behavior similar to a monolithic ceramic, which corresponds to the lower bound of ply reliability. Thus multiaxial design methods must be capable of predicting these two bounds as well as account for the reduction in reliability due to an in-plane shear stress, and compressive stresses in the fiber direction and transverse to the fiber direction.

A number of macroscopic theories exist that treat unidirectional composites as homogenized, anisotropic materials. These methods use phenomenological strength data directly without hypothesizing specific crack shapes or distributions. Theories of this genre generally are termed noninteractive if individual stress components are compared to their strengths separately. In essence, failure mechanisms are assumed not to interact, and this results in component reliability computations that are quite tractable. Work by Thomas and Wetherhold (1990), Duffy and Arnold (1990), Duffy and Manderscheid (1990), and Duffy et al. (1990) is representative of multiaxial noninteractive reliability models for anisotropic materials. In addition Wu (1989), and Hu and Goetschel (1989) have proposed simpler unidirectional reliability models for laminated composites that can be classified as noninteractive. Alternatively, one can assume that for multiaxial states of stress, failure mechanisms interact and depend on specific stochastic combinations of material strengths. Usually a failure criterion is adapted from existing polymer matrix design technologies. The probability that the criterion has been violated for a given stress state is computed using Monte Carlo methods (de Roo and Paluch, 1985) or first-order-second-moment (FOSM) methods (Yang, 1989; Miki et al., 1989). The interactive approach often results in computationally intensive reliability predictions.

In this paper a noninteractive phenomenological approach has been chosen such that a unidirectional ply is considered a two-dimensional structure, assumed to have five basic strengths (or failure modes). They include a tensile and compressive strength in the fiber direction, a tensile and compressive strength in the direction transverse to the fiber direction, and an in-plane shear strength. In addition each ply is discretized into individual sub-ply volumes. For reasons discussed in the previous section we assume that failure of a ply is governed by its weakest link (or sub-ply volume). Under this assumption, events leading to failure of a given link do not affect other links (see, for example, Batdorf and Heinisch, 1978; Wetherhold, 1983; Cassenti, 1984); thus the reliability of the ith ply is given by the following expression:

$$R_i = \exp\left(- \int_V \psi_i dV \right) \tag{8}$$

where V is the component volume. Here, $\psi_i(x_j)$ is the failure function per unit volume at position x_j within the ply, given by

$$\psi_i = \left[\frac{\langle \sigma_1 - \gamma_1 \rangle}{\beta_1} \right]^{\alpha_1} + \left[\frac{|\tau_{12} - \gamma_2|}{\beta_2} \right]^{\alpha_2} + \left[\frac{\langle \sigma_2 - \gamma_3 \rangle}{\beta_3} \right]^{\alpha_3} + \left[\frac{\langle (-1)(\sigma_1 + \gamma_4) \rangle}{\beta_4} \right]^{\alpha_4} + \left[\frac{\langle (-1)(\sigma_2 + \gamma_5) \rangle}{\beta_5} \right]^{\alpha_5} \tag{9}$$

The α's associated with each term in Eq. (9) correspond to the Weibull shape parameters, the β's correspond to Weibull scale parameters, and the γ's correspond to the Weibull threshold stresses. In addition, σ_1 and σ_2 represent the in-plane normal stresses that are aligned with and transverse to the fiber direction, respectively. Also, τ_{12} is the in-plane shear stress. The normal stresses appear twice, and this allows for different failure modes to emerge in tension and compression. Note that the brackets indicate a unit step function; i.e.,

$$\langle x \rangle = x \cdot u[x] = \begin{cases} x & x > 0 \\ 0 & x \leq 0 \end{cases} \tag{10}$$

Inserting Eq. (9) into the volume integration given by Eq. (8) yields the reliability of the ith ply, and the probability of first ply failure for the laminate is given by the expression

$$P_{fpf} = 1 - \prod_{i=1}^{n} R_i \tag{11}$$

where n is the number of plies.

This reliability model can be readily integrated with laminate analysis options available in several commercial finite element codes. A preliminary version of a public domain computer algorithm (C/CARES) that is coupled with MSC/NASTRAN has been developed at NASA Lewis Research Center to perform this analysis. A simple benchmark application illustrates the approach. A thin-wall tube is subjected to an internal pressure and an axial compressive load. The component is fabricated from a three-ply laminate, with a 90°/θ/90° layup. Here angle θ is measured relative to the longitudinal axis of

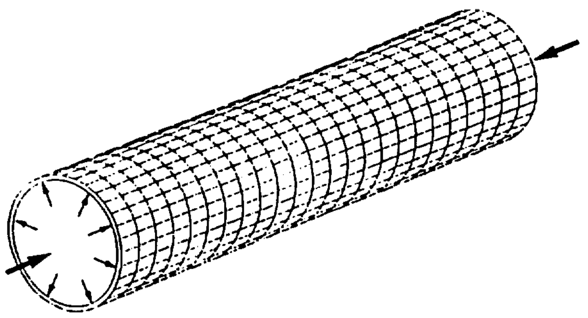

Fig. 1 Finite element mesh of thin-wall tube with three-ply (90°/θ/90°) layup; internal pressure, 4.25 MPa; axial compressive stress, 87.5 MPa

Table 1 Composite Weibull parameters for thin-wall tube [Weibull threshold stress, $\gamma_i = 0$]

Index[a]	Type and direction of stress	Weibull parameters	
		Shape, α_i	Scale, β_i
1	Normal tensile stress in fiber direction	25	450
2	In-plane shear stress	22	420
3	Normal tensile stress transverse to fiber direction	10	350
4	Normal compressive stress in fiber direction	35	4500
5	Normal compressive stress transverse to fiber direction	30	3500

[a] Indices correspond to subscripts in Eq. (9).

the tube (see Fig. 1). An arbitrary internal pressure of 4.25 MPa and an axial compressive stress of 87.5 MPa were applied to the tube. The Weibull parameters were also arbitrarily chosen (see Table 1). Note that the threshold stresses are taken as zero for simplicity. In design, setting the threshold stresses equal to zero would represent a conservative assumption. The overall component reliability is depicted as a function of the midply orientation angle (θ) in Fig. 2. The ply orientation has a decided effect on component reliability, as expected. Similar studies could demonstrate the effects of component geometry, ply thickness, load, and/or Weibull parameters on component reliability. Hence, the C/CARES code allows the design engineer a wide latitude to optimize a component relative to a number of design parameters.

Parameter Estimation

We anticipate that laminated CMC materials will exhibit threshold behavior, at least in the fiber direction. Hence, a three-parameter Weibull distribution is used in the stochastic failure analysis of the components. The threshold stress parameter is included to allow for zero probability of failure when the load is below a predetermined level. The three-parameter distribution has been somewhat ignored due to difficulties encountered in extracting the parameters from experimental data. Several authors (including Weibull, 1939; Weil and Daniel, 1964; Schneider and Palazotto, 1979) have proposed estimation methods for the three-parameter distribution. For various reasons, these techniques have not been widely accepted. However, Cooper (1988) recently proposed a nonlinear regression method to estimate parameters. Regression analysis postulates a relationship between two variables. In an experiment, typically one variable can be controlled (the independent variable) while the response variable (or dependent variable) is uncontrolled. In simple failure experiments the material dictates the strength at failure, indicating that the failure stress is the response variable. The ranked probability of failure $\mathcal{P}_i$ can be controlled by the experimentalist since it is functionally dependent on the sample size N. If the observed failure stresses ($\sigma_1, \sigma_2, \sigma_3, \ldots, \sigma_N$) are placed in ascending order, then

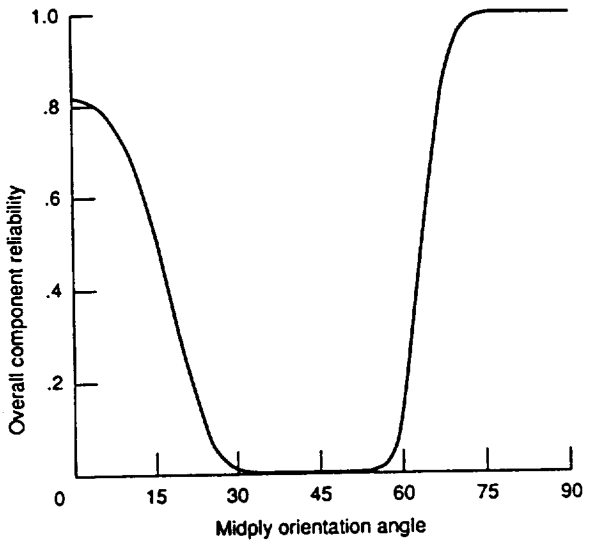

Fig. 2 Component reliability versus midply orientation angle for thin wall tube

$$\mathcal{P}_i(\sigma_i) = \frac{i-0.3}{N+0.4} \tag{12}$$

Clearly one can influence the ranked probability for a given stress level by increasing or decreasing the sample size. Cooper's procedure adopts this philosophy, and the specimen failure stress is treated as the dependent variable. The associated ranked probability of failure then becomes the independent variable. The basic three-parameter Weibull expression for probability of failure can be expressed as

$$\tilde{\sigma}_i = \tilde{\gamma} + \tilde{\beta}\left[\ln\left(\frac{1}{1-\mathcal{P}_i}\right)\right]^{1/\tilde{\alpha}} \tag{13}$$

where $\tilde{\sigma}_i$ is an estimate of the dependent variable, and $\tilde{\gamma}$, $\tilde{\beta}$, and $\tilde{\alpha}$ are estimates of the threshold parameter, the characteristic strength, and the shape parameter, respectively. Defining

$$\delta_i = \tilde{\sigma}_i - \sigma_i \tag{14}$$

as the ith residual, where as before σ_i is the ith failure stress, then

$$\sum_{i=1}^{N} (\delta_i)^2 = \sum_{i=1}^{N} (\tilde{\gamma} + \tilde{\beta} W_i^{1/\tilde{\alpha}} - \sigma_i)^2 \tag{15}$$

where we adopt Cooper's notation and take

$$W_i = \ln\left(\frac{1}{1-\mathcal{P}_i}\right) \tag{16}$$

Setting the partial derivatives of the sum of the squares of the residuals with respect to $\tilde{\gamma}$, $\tilde{\beta}$, and $\tilde{\alpha}$ equal to zero yields the following three expressions:

$$\tilde{\beta} = \frac{N\left[\sum_{i=1}^{N} \sigma_i (W_i)^{1/\tilde{\alpha}}\right] - \left[\sum_{i=1}^{N} \sigma_i\right]\left[\sum_{i=1}^{N} (W_i)^{1/\tilde{\alpha}}\right]}{N\sum_{i=1}^{N} (W_i)^{2/\tilde{\alpha}} - \left[\sum_{i=1}^{N} (W_i)^{1/\tilde{\alpha}}\right]\left[\sum_{i=1}^{N} (W_i)^{1/\tilde{\alpha}}\right]} \tag{17}$$

$$\tilde{\gamma} = \frac{\left[\sum_{i=1}^{N} (W_i)^{2/\tilde{\alpha}}\right]\left[\sum_{i=1}^{N} \sigma_i\right] - \left[\sum_{i=1}^{N} \sigma_i (W_i)^{1/\tilde{\alpha}}\right]\left[\sum_{i=1}^{N} (W_i)^{1/\tilde{\alpha}}\right]}{N\sum_{i=1}^{N} (W_i)^{2/\tilde{\alpha}} - \left[\sum_{i=1}^{N} (W_i)^{1/\tilde{\alpha}}\right]\left[\sum_{i=1}^{N} (W_i)^{1/\tilde{\alpha}}\right]} \tag{18}$$

Table 2 Monolithic alumina failure data[a]

Speci-men number	Stress, MPa	Speci-men number	Stress, MPa	Speci-men number	Stress, MPa	Speci-men number	Stress, MPa
1	307	10	337	19	357	28	385
2	308	11	343	20	364	29	388
3	322	12	345	21	371	30	395
4	328	13	347	22	373	31	402
5	328	14	350	23	374	32	411
6	329	15	352	24	375	33	413
7	331	16	353	25	376	34	415
8	332	17	355	26	376	35	456
9	335	18	356	27	381		

[a] For specimen shown in Fig. 3.

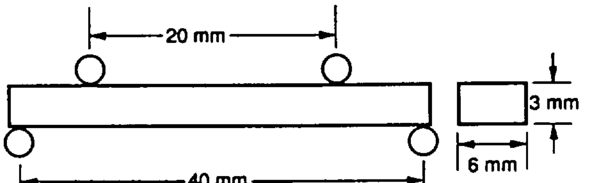

Fig. 3 Monolithic alumina specimen geometry

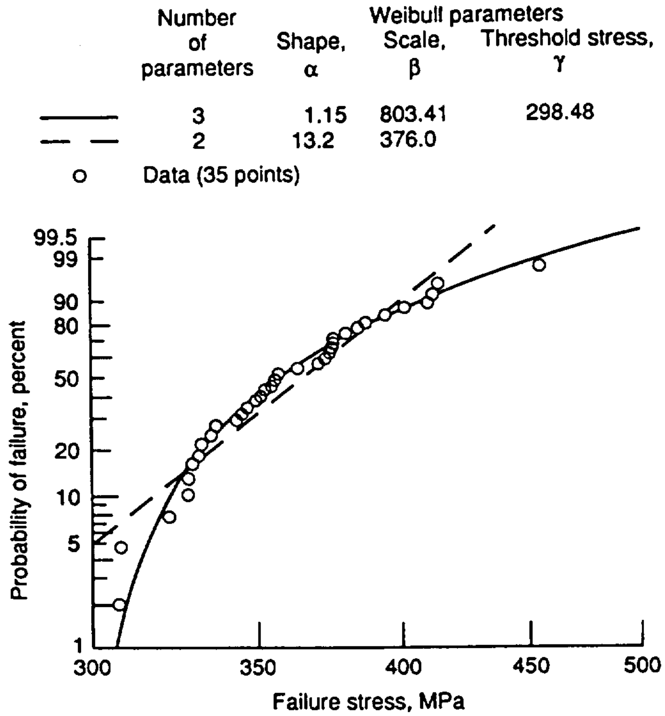

Fig. 4 Two-parameter and three-parameter distributions determined from the alumina failure

and

$$\sum_{i=1}^{N} \sigma_i (W_i)^{1/\tilde{\alpha}} \ln(W_i) = \tilde{\gamma} \sum_{i=1}^{N} (W_i)^{1/\tilde{\alpha}} \ln(W_i) + \tilde{\beta} \sum_{i=1}^{N} (W_i)^{2/\tilde{\alpha}} \ln(W_i) \qquad (19)$$

in terms of the parameter estimates. The solution of this system of equations is iterative. One assumes an initial value for $\tilde{\alpha}$ (a small value, usually equal to 1), computes $\tilde{\beta}$ from Eq. (17) and $\tilde{\gamma}$ from Eq. (18). These values of the parameter estimates are then inserted into Eq. (19), and this expression is checked to see if it satisfies some predetermined tolerance. If Eq. (19) is not satisfied, $\tilde{\alpha}$ is increased and a new iteration is conducted. This procedure continues until a set of parameter estimates are determined that satisfy Eqs. (17)–(19).

Currently we do not have enough CMC failure data to estimate Weibull parameters for a given material orientation. So to illustrate the technique, parameter estimates were determined for two-parameter and three-parameter distributions from a failure population representing a monolithic ceramic (alumina) reported by Quinn (1989). The failure data and specimen geometry are shown in Table 2 and Fig. 3. Figure 4 is a plot of probability of failure versus failure stress for the data. The straight line represents the two-parameter fit to the data, using Quinn's (1989) values for the shape and scale parameters. The nonlinear curve represents the three-parameter fit to the data. Note that the three-parameter distribution is more efficient in predicting the failure data in the high reliability region.

Summary and Future Directions

In this paper we discuss stochastic issues related to size effects in the fiber direction of a unidirectional CMC material. In addition, we present a reliability model along with a simple application that highlighted the C/CARES computer algorithm. (This public domain algorithm is capable of predicting component reliability from the state of stress and temperature distribution within the component.) The authors anticipate that CMC materials will exhibit threshold behavior; hence a nonlinear regression analysis was outlined to determine three parameters for a Weibull distribution from failure data.

Ceramic material systems will play a significant role in future elevated-temperature applications. To this end, there are a number of issues that must be addressed by the structural mechanics research community. We begin by pointing out that total failure of an individual ply effectively reduces the overall laminate stiffness. This causes local redistribution of the load to adjacent layers. In addition, delamination between plies relaxes the constraining effects among layers, allowing in-plane strains to vary in a stepwise fashion within a laminate. These effects require the development of rational load redistribution schemes. It is also apparent that before ceramics are used as structural components in harsh service environments, thoughtful consideration should be given to reliability degradation due to time-dependent phenomena. Thus, issues germane to component life, such as cyclic fatigue and creep behavior, must be addressed analytically. Computational strategies are needed to extend current methods of analysis from subcritical crack growth and creep rupture to laminated CMC materials that are subject to multiaxial states of stress.

An important aspect that has not been addressed in detail is the effect of a rising *R*-curve behavior, where fracture toughness is a function of crack size. Clearly fiber-toughened matrices have process zones around the crack tip. Within this zone, energy dissipates locally, which develops a damage tolerance by increasing the resistance to crack growth with crack extension. Failure of materials exhibiting *R*-curve behavior would depend on the rate at which resistance increases with crack growth. During crack extension this behavior would modify the strength distribution. Modeling efforts by Kendall et al. (1986) and others have accounted for this behavior in monolithic ceramics, and it is reasonable to extend their work to ceramic composite material systems. Furthermore, if ceramic materials mimic ductile failure locally, cyclic fatigue may become a design issue. Under cyclic loads, the process zone advances as the crack tip extends; therefore, brittle fracture mechanics may need to be modified to account for pseudoductile fracture. Hence, application of modified metallic fatigue analyses may be a distinct possibility.

In addition, recent progress in processing ceramic material systems has not been matched by mechanical testing efforts. There is a definite need for experiments that support the development of reliability models. Initially this effort should include experiments that test the fundamental concepts (e.g., quantifying the size effect in the fiber direction) within the framework of current stochastic models. For example, probing experiments could be conducted along various biaxial load paths to establish level surfaces of reliability in a particular two-dimensional stress space (similar to probing yield surfaces in metals). One could then verify such concepts as the maximum stress response, which is often assumed in the noninteractive reliability models proposed for these materials. After establishing a theoretical framework, characterization tests should then be conducted to provide the functional dependence of model parameters with respect to temperature and environment. Finally data from structural tests that are multiaxial (and possibly nonisothermal) would be used to challenge the predictive capabilities of models through comparison to benchmark response data. These tests involve nonhomogeneous fields of stress, deformation, and temperature, and would include two-bar tests as well as plate and shell structures. Results from structural testing provide feedback for subsequent modification, but ad hoc models result in the absence of structured interaction between the experimentalist and the theoretician. The validity of these models is then forever open to question. Furthermore, we cannot overemphasize that this kind of testing supports methods for designing components, not the materials. Currently this effort is hampered by the quality and scarcity of data (note the lack of failure data necessary to estimate composite Weibull parameters). Finally, ceramic properties pertinent to structural design (which include stochastic parameters) vary with test methods. The mechanics research community is beginning to realize this, and a consensus is beginning to form regarding standards. However, we wish to underscore the fundamental need for experimental programs that are relevant to structural mechanics issues.

In closing, we recognize that when failure is less sensitive to imperfections in the material, stochastic methods may not be as essential. Yet, trends in design protocols are moving in the direction of probabilistic analyses (even for metals) and away from the simplistic safety-factor approach. In this sense, brittle ceramics will serve as prototypical materials in the study and development of reliability models that will act as the basis of future design codes.

References

Batdorf, S. B., and Heinisch, H. L., Jr., 1978, "Weakest Link Theory Reformulation for Arbitrary Fracture Criterion," *Journal of the American Ceramic Society*, Vol. 61, pp. 355–358.

Batdorf, S. B., 1982, "Tensile Strength of Unidirectionally Reinforced Composites—I," *Journal of Reinforced Plastics and Composites*, Vol. 1, No. 2, pp. 153–164.

Batdorf, S. B., and Ghaffarian, R., 1984, "Size Effect and Strength Variability of Unidirectional Composites," *International Journal of Fracture*, Vol. 26, pp. 113–123.

Blass, J. J., and Ruggles, M. B., 1990, "Design Methodology Needs for Fiber-Reinforced Ceramic Heat Exchangers," ORNL/TM-11012, Oak Ridge National Lab., TN.

Budiansky, B., Hutchinson, J. W., and Evans, A. G., 1986, "Matrix Fracture in Fiber-Reinforced Ceramics," *Journal of the Mechanics and Physics of Solids*, Vol. 34, No. 2, pp. 167–189.

Cassenti, B. N., 1984, "Probabilistic Static Failure of Composite Material," *AIAA Journal*, Vol. 22, No. 1, pp. 103–110.

Coleman, B. D., 1958, "On the Strength of Classical Fibers and Fiber Bundles," *Journal of the Mechanics and Physics of Solids*, Vol. 7, No. 1, pp. 66–70.

Cooper, N. R., 1988, "Probabilistic Failure Prediction of Rocket Motor Components," PhD Thesis, Royal Military College of Science (Avail. Univ. Microfilms Inc.).

Daniels, H. E., 1945, "The Statistical Theory of the Strength of Bundles of Threads," *Proceedings of the Royal Society of London*, Series A, Vol. 183, No. 995, pp. 405–435.

de Roo, P., and Paluch, B., 1985, "Application of a Multiaxial Probabilistic Failure Criterion to a Unidirectional Composite," *Developments in the Science and Technology of Composite Materials*, A. R. Bunsell, P. Lamicq, and A. Massiah, eds., Association Européenne des Matériaux Composites, Bordeaux, pp. 328–334.

DeSalvo, G. J., 1970, "Theory and Structural Design Applications of Weibull Statistics," WANL-TME-2688, Westinghouse Astronuclear Laboratory.

DiCarlo, J. A., 1989, "CMC's for the Long Run," *Advanced Materials and Processes*, Vol. 135, No. 6, pp. 41–44.

Duffy, S. F., and Arnold, S. M., 1990, "Noninteractive Macroscopic Reliability Model for Whisker Reinforced Ceramic Composites," *Journal of Composite Materials*, Vol. 24, No. 3, pp. 293–308.

Duffy, S. F., and Mandersheid, J. M., 1990, "Noninteractive Macroscopic Reliability Model for Ceramic Matrix Composites With Orthotropic Material Symmetry," ASME JOURNAL OF ENGINEERING FOR GAS TURBINES AND POWER, Vol. 112, No. 4, pp. 507–511.

Duffy, S. F., Wetherhold, R. C., and Jain, L. K., 1990, "Extension of a Noninteractive Reliability Model for Ceramic Matrix Composites," NASA CR-185267.

Harlow, D. G., and Phoenix, S. L., 1978, "The Chain-of-Bundles Probability Model for the Strength of Fibrous Materials—1. Analysis and Conjectures," *Journal of Composite Materials*, Vol. 12, No. 2, pp. 195–214.

Hu, T. G., and Goetschel, D. B., 1989, "The Application of the Weibull Strength Theory to Advanced Composite Materials," *Tomorrow's Materials: Today*, Vol. 1, Proceedings of the 34th International SAMPE Symposium and Exhibition, G. A. Zakrzewski et al., eds., SAMPE, Covina, CA, pp. 585–599.

Jayatilaka, A. S., 1979, *Fracture of Engineering Brittle Materials*, Applied Science Publishers, London, United Kingdom, pp. 249–257.

Kendall, K., Alford, N. M., Tan, S. R., and Birchall, J. D., 1986, "Influence of Toughness on Weibull Modulus of Ceramic Bending Strength," *Journal of Materials Research*, Vol. 1, No. 1, pp. 120–123.

Marshall, D. B., Cox, B. N., and Evans, A. G., 1985, "The Mechanics of Matrix Cracking in Brittle Matrix Fiber Composites," *Acta Metallurgica*, Vol. 33, No. 11, pp. 2013–2021.

Miki, M., Murotsu, Y., Tanaka, T., and Shao, S., 1989, "Reliability of the Strength of Unidirectional Fibrous Composites," *30th Structures, Structural Dynamics and Materials Conference*, Part 2, AIAA, Washington, DC, pp. 1032–1040.

Quinn, G. D., 1989, "Flexure Strength of Advanced Ceramics—A Round Robin Exercise," MTL TR-89-62 (Avail. NTIS, AD-A212101).

Rosen, B. W., 1964, "Tensile Failure of Fibrous Composites," *AIAA Journal*, Vol. 2, No. 11, pp. 1985–1991.

Schneider, D., and Palazotto, A. N., 1979, "A Technique for Evaluating a Unique Set of Three Weibull Parameters Considering Composite Materials," *Fibre Science and Technology*, Vol. 12, No. 4, pp. 269–281.

Sutcu, M., 1989, "Weibull Statistics Applied to Fiber Failure in Ceramic Composites and Work of Fracture," *Acta Metallurgica*, Vol. 37, No. 2, pp. 651–661.

Thomas, D. J., and Wetherhold, R. C., 1990, "Reliability Analysis of Continuous Fiber Composite Laminates," NASA CR-185265.

Thouless, M. D., and Evans, A. G., 1988, "Effects of Pull-Out on the Mechanical Properties of Ceramic-Matrix Composites," *Acta Metallurgica*, Vol. 36, No. 3, pp. 517–522.

Weibull, W. A., 1939, "Statistical Theory of the Strength of Materials," *Ingeniors Vetenskaps Akadamien Handlingar*, No. 151.

Weil, N. A., and Daniel, I. M., 1964, "Analysis of Fracture Probabilities in Nonuniformly Stressed Brittle Materials," *Journal of the American Ceramic Society*, Vol. 47, No. 6, pp. 268–274.

Wetherhold, R. C., 1983, "Statistics of Fracture of Composite Material Under Multiaxial Loading," PhD Dissertation, University of Delaware.

Wu, H. F., 1989, "Statistical Analysis of Tensile Strength of ARALL Laminates," *Journal of Composite Materials*, Vol. 23, No. 10, pp. 1065–1080.

Yang, L., 1989, "Reliability of Composite Laminates," *Mechanics of Structures and Machines*, Vol. 16, No. 4, pp. 523–536.

Zweben, C., 1968, "Tensile Failure of Fiber Composites," *AIAA Journal*, Vol. 6, No. 12, pp. 2325–2331.

S. F. Duffy
NASA Resident Research Associate.

L. M. Powers
NASA Resident Research Associate.

Cleveland State University,
Cleveland, OH 44115

A. Starlinger
National Research Council
NASA Research Associate,
NASA Lewis Research Center,
Cleveland, OH 44135

Reliability Analysis of Structural Ceramic Components Using a Three-Parameter Weibull Distribution

This paper describes nonlinear regression estimators for the three-parameter Weibull distribution. Issues relating to the bias and invariance associated with these estimators are examined numerically using Monte Carlo simulation methods. The estimators were used to extract parameters from sintered silicon nitride failure data. A reliability analysis was performed on a turbopump blade utilizing the three-parameter Weibull distribution and the estimates from the sintered silicon nitride data.

Introduction

To date, most reliability analyses performed on structural components fabricated from ceramic materials have utilized the two-parameter form of the Weibull distribution. The use of a two-parameter Weibull distribution to characterize the random nature of material strength implies a nonzero probability of failure for the full range of applied stress. This represents a conservative design assumption when analyzing structural components. A three-parameter form of the Weibull distribution is available. The additional parameter is a threshold stress that allows for zero probability of failure when applied stress is at or below the threshold value. By employing the concept of a threshold stress, design engineers can effectively tailor the design of a component to optimize structural reliability.

Difficulties in estimating parameters as well as a lack of strength data with corresponding fractographic analysis has limited the use of this distribution. Several authors (including Weibull, 1939; Weil and Daniel, 1964; Schneider and Palazotto, 1979) have proposed estimation methods for the three-parameter distribution. For various reasons these techniques have not been widely utilized. The nonlinear regression method proposed by Margetson and Cooper (1984) is adopted here to establish estimators for the three-parameter Weibull formulation. Estimators are applied using failure data obtained from the open literature. Specifically, Weibull parameters are estimated from failure data reported by Chao and Shetty (1991). The data were generated from test specimens fabricated from a monolithic silicon nitride. Strength tests were conducted on this material using three-point bend, four-point bend, and pressurized-disk specimen geometries. Here the Weibull parameters are estimated from the four-point bend test data, and failure data from the three-point bend tests and pressurized-disk tests are subsequently used to challenge structural reliability predictions made for these latter two geometries. To conduct structural reliability analyses, the three-parameter Weibull distribution was embedded in a reliability model known as the principle of independent action (PIA). We point out that the three-parameter form of the Weibull distribution can be extended to Batdorf's (1974, 1978) model and reliability models proposed for ceramic matrix composites (see Duffy et al., 1993; or Thomas and Wetherhold, 1991). All reliability computations presented here were made utilizing the integrated design program CARES (Ceramic Analysis and Reliability Evaluation of Structures) (Nemeth et al., 1990).

In general, the objective of parameter estimation is the derivation of functions (or estimators) that are dependent on the failure data and that yield, in some sense, optimum estimates of the underlying population parameters. Various performance criteria can be applied to ensure that optimized estimates are obtained consistently. Two important performance criteria are estimate invariance and estimate bias. An estimator is invariant if the bias associated with the estimated value is independent of the true parameters that characterize the underlying population. Bias is a measure of deviation of the estimated parameter from the true population parameter. Here the functional value of an estimator is a point estimate (in contrast to an interval estimate) of the true population parameter. The values of the point estimates computed from a number of samples obtained from a population will vary from sample to sample. A sample is defined as a collection (i.e., more than one) of observations taken from a specified population, and a population represents the totality of all possible observations about which statistical inferences could be made. In this paper, the observations are the failure strengths of test specimens fabricated from ceramic materials. The issues of bias and invariance and their relationship to the functions proposed by

---

Contributed by the International Gas Turbine Institute and presented at the 37th International Gas Turbine and Aeroengine Congress and Exposition, Cologne, Germany, June 1-4, 1992. Manuscript received by the International Gas Turbine Institute, February 24, 1992. Paper No. 92-GT-296. Associate Technical Editor: L. S. Langston.

Margetson and Cooper (1984) are explored numerically. In the numerical studies, distributions of the point estimates are obtained by taking numerous samples from the population and computing point estimates as a function of sample size. If the mean of a distribution of such estimates is equal to the value of the true parameter for a given sample size, the associated estimator is said to be unbiased. If an estimator yields biased results, the value of the individual estimates can be corrected if the estimators are invariant (see Thoman et al., 1969, for the procedure associated with two-parameter maximum-likelihood estimators). The Monte Carolo simulations that are presented later demonstrate that the functions are neither invariant nor unbiased.

Estimating Weibull Distribution Parameters

Weibull (1939, 1951) proposed the first probabilistic model that accounted for scatter in failure strength and the size effect encountered in structural components fabricated from brittle materials. His approach is based on the weakest link theory (WLT) attributed to Midgley and Pierce (1926). This earlier research (sponsored by the textile industry) focused on modeling yarn strength. Unlike Midgely and Pierce, who assumed a Gaussian distribution for yarn strength, Weibull proposed a unique probability density function for failure strength that now bears his name. Weibull's three-parameter probability density function has the following form:

$$f(x) = \left(\frac{\alpha}{\eta}\right)\left(\frac{x-\lambda}{\eta}\right)^{(\alpha-1)} \exp\left(-\left(\frac{x-\lambda}{\eta}\right)^{\alpha}\right) \quad (1)$$

for a continuous random variable x, when $0 \le \lambda < x$, and

$$f(x) = 0 \quad (2)$$

for $x \le \lambda$. The cumulative distribution function is given by the expression

$$F(x) = 1 - \exp\left(-\left(\frac{x-\lambda}{\eta}\right)^{\alpha}\right) \quad (3)$$

for $x > \lambda$, and

$$F(x) = 0 \quad (4)$$

for $x \le \lambda$. Here $\alpha(>0)$ is the Weibull modulus (or the shape parameter), $\eta(>0)$ is the scale parameter, and $\lambda(>0)$ is the threshold parameter. When applied to analyses of structural components, the random variable x usually represents a component of the Cauchy stress tensor or an invariant of this tensor. For a uniaxial stress field in a homogeneous isotropic material, application of Weibull's theory yields the following expression for the probability of failure

$$\mathcal{P} = 1 - \exp(-B) \qquad \sigma > \gamma \quad (5)$$

where

$$B = \int_V \left(\frac{\sigma-\gamma}{\beta}\right)^{\alpha} dV \quad (6)$$

and

$$\mathcal{P} = 0 \qquad \sigma \le \gamma \quad (7)$$

Note that α, β, and γ are material parameters and will not depend on the geometry of the test specimen. In this context β has the dimension of (stress)•(volume)$^{1/\alpha}$, γ has the dimension of stress, and α is dimensionless.

Certain monolithic ceramics have exhibited threshold behavior (e.g., Quinn, 1989; Chao and Shetty, 1991). It is anticipated that ceramic matrix composites will similarly exhibit this behavior (Duffy et al., 1993). Threshold behavior is demonstrated if the failure data display a nonlinear behavior when the ranked probability of failure ($\mathcal{P}_i$) is represented as a function of the corresponding failure values. Careful fractography must yield clear evidence that only one type of defect is causing failure. Thus, the fractographic analysis must demonstrate that the nonlinear behavior of the failure data is not the result of competing failure mechanisms. When experimental data indicate the existence of a threshold stress, a three-parameter Weibull distribution should be employed in the stochastic failure analysis of structural components. However, the three-parameter form of the Weibull distribution has been somewhat ignored as a result of difficulties encountered in extracting estimates of the parameters from experimental data. Margetson and Cooper (1984) proposed a relatively simple nonlinear regression method to estimate the three distribution parameters. Regression analysis postulates a relationship between two variables. In an experiment, typically one variable can be controlled (the independent variable) while the response variable (or dependent variable) is uncontrolled. In simple failure experiments the material dictates the strength at failure, indicating that the failure stress is the response variable. The ranked probability of failure ($\mathcal{P}_i$) can be controlled by the experimentalist since it is functionally dependent on the sample size (N). After numbering the observed failure stresses (σ_1, σ_2, σ_3, . . . , σ_N) in ascending order, and specifying

$$\mathcal{P}_i(\sigma_i) = (i - 0.5)/N \quad (8)$$

then clearly the ranked probability of failure for a given stress level can be influenced by increasing or decreasing the sample size. The procedure proposed by Margetson and Cooper (1984) adopts this philosophy. They assume that the specimen failure stress is the dependent variable, and the associate ranked probability of failure becomes the independent variable.

Using Eq. (5), an expression can be obtained relating the ranked probability of failure ($\mathcal{P}_i$) to an estimate of the failure strength ($\hat{\sigma}_i$). Assuming uniaxial stress conditions in a test specimen with a unit volume, Eq. (5) yields

$$\hat{\sigma}_i = \hat{\gamma} + \hat{\beta}[\ln(1/1-\mathcal{P}_i)]^{1/\hat{\alpha}} \quad (9)$$

where $\hat{\sigma}_i$ is an estimate of the ranked failure stress. In addition, $\hat{\alpha}$, $\hat{\beta}$, and $\hat{\gamma}$ are estimates of the shape parameter (α), the scale parameter (β), and the threshold parameter (γ), respectively. Defining the residual as

$$\delta_i = \hat{\sigma}_i - \sigma_i \quad (10)$$

where σ_i is the ith ranked failure stress obtained from actual test data, then the sum of the squared residuals is expressed as

$$\sum_{i=1}^{N} (\delta_i)^2 = \sum_{i=1}^{N} (\hat{\gamma} + \hat{\beta} W_i^{1/\hat{\alpha}} - \sigma_i)^2 \quad (11)$$

Here the notation of Margetson and Cooper (1984) is adopted where

$$W_i = \ln(1/1 - \mathcal{P}_i) \quad (12)$$

Note that the forms of $\hat{\sigma}_i$ and W_i change with specimen geometry (see the discussion in a later section relating to the four-point bend specimen geometry). It should be apparent that the objective of this method is to obtain parameter estimates that minimize the sum of the squared residuals. Setting the partial derivatives of the sum of the squares of the residuals with respect to $\hat{\alpha}$, $\hat{\beta}$, and $\hat{\gamma}$ equal to zero yields the following three expressions:

$$\hat{\beta} = \frac{N\left(\sum_{i=1}^{N} \sigma_i (W_i)^{1/\hat{\alpha}}\right) - \left(\sum_{i=1}^{N} \sigma_i\right)\left(\sum_{i=1}^{N} (W_i)^{1/\hat{\alpha}}\right)}{N \sum_{i=1}^{N} (W_i)^{2/\hat{\alpha}} - \left(\sum_{i=1}^{N} (W_i)^{1/\hat{\alpha}}\right)\left(\sum_{i=1}^{N} (W_i)^{1/\hat{\alpha}}\right)} \quad (13)$$

$$\hat{\gamma}=\frac{\left(\sum_{i=1}^{N}(W_i)^{2/\hat{\alpha}}\right)\left(\sum_{i=1}^{N}\sigma_i\right)-\left(\sum_{i=1}^{N}\sigma_i(W_i)^{1/\hat{\alpha}}\right)\left(\sum_{i=1}^{N}(W_i)^{1/\hat{\alpha}}\right)}{N\sum_{i=1}^{N}(W_i)^{2/\hat{\alpha}}-\left(\sum_{i=1}^{N}(W_i)^{1/\hat{\alpha}}\right)\left(\sum_{i=1}^{N}(W_i)^{1/\hat{\alpha}}\right)} \tag{14}$$

and

$$\left|\sum_{i=1}^{N}\sigma_i(W_i)^{1/\hat{\alpha}}\ln(W_i)-\hat{\gamma}\sum_{i=1}^{N}(W_i)^{1/\hat{\alpha}}\ln(W_i)-\hat{\beta}\sum_{i=1}^{N}(W_i)^{2/\hat{\alpha}}\ln(W_i)\right|\le\kappa_{\text{conv}} \tag{15}$$

in terms of the parameter estimates. The solution of this system of equations is iterative. The third expression is used to check convergence of the iterative solution. The initial solution vector for this system is determined after assuming $\hat{\alpha} = 1$. Then $\hat{\beta}$ is computed from Eq. (13) and $\hat{\gamma}$ is calculated from Eq. (14). The values of these parameter estimates are then inserted into Eq. (15) to determine if the convergence criterion is satisfied to within some predetermined tolerance (κ_{conv}). If this expression is not satisfied, $\hat{\alpha}$ is updated and a new iteration is conducted. This procedure continues until a set of parameter estimates are determined that satisfy Eq. (15).

Bias and Invarance

Issues relating to estimate bias and invariance are examined numerically using Monte Carlo simulation methods. In this study uniform random numbers are generated in groups of N (which characterizes the sample size), and this is repeated 10,000 times for each value N. Each group of uniform random numbers is generated on the interval 0 to 1 using the Cray random number function RANGET. The uniform random number is converted to a strength observation by employing the inverse of the three-parameter Weibull distribution for failure strength given in Eq. (9). Defining $(S_i)_N$ as the ith random number on the interval 0 to 1 in a sample of size N, then the ith failure strength is

$$(\sigma_i)_N=\gamma+\beta\left[\ln\left(\frac{1}{1-(S_i)_N}\right)\right]^{1/\alpha} \tag{16}$$

where α, β, and γ are the true distribution parameters of an infinite population characterized by a three-parameter Weibull distribution. Again, uniaxial stress conditions are imposed on a specimen of unit volume. However, this method can be extended to other specimen geometries as well.

Once a sample of N random numbers is generated and converted to failure strength observations, the estimators described by Eqs. (13)–(15) are used to obtain the point estimates $\hat{\alpha}$, $\hat{\beta}$, and $\hat{\gamma}$. Percentile distributions of the point estimates, as well as a mean value of the point estimates, can be constructed by repeating this sampling procedure for each value of N. Here the Monte Carlo simulations are carried out 10,000 times for each N. The arithmetic mean of each estimated parameter is a measure of the bias associated with the estimator in determining that parameter, and is usually characterized as a function of the sample size (N). This is depicted graphically in Fig. 1. In this figure the vertical axes represent a ratio of the point estimate value to the parameter true value used to generate the failure observations. The true population parameters are arbitrarily chosen, with α = 1.75, β = 1000, and λ = 300. The horizontal axes represent the sample size N. Note that for all three estimators the mean value of the ratio approaches 1 for large values of N. Thus, each estimator exhibits the attractive property of decreasing bias with increasing sample size. However, the arithmetic mean associated with each parameter is not invariant with respect to the underlying population parameter. This is evident in Fig. 2, which depicts the arithmetic mean values of the parameter estimates from the previous example along with arithmetic mean values from a second example. For the second sample, the true population parameter α has been increased such that α = 2.75, and the other values of the true parameters are unchanged. Clearly the arithmetic means associated with the Weibull modulus (α), the scale parameter (β), and threshold stress (γ) change for sample sizes of less than 100. If the mean values remained invariant, then the three curves in each graph in Fig. 2 would coincide regardless of the values assumed for the true population pa-

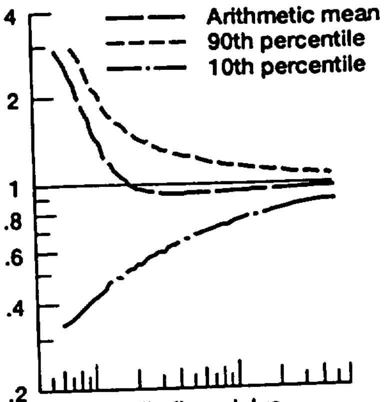

(a) Weibull modulus.

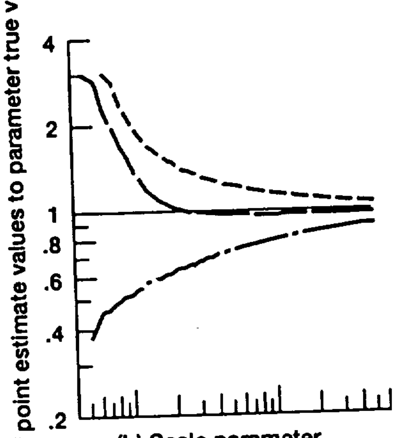

(b) Scale parameter.

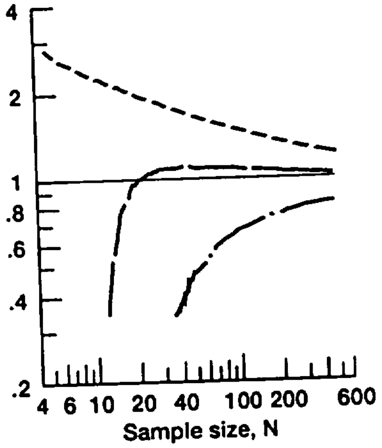

(c) Threshold stress.

Fig. 1 Arithmetic mean values and percentile distributions of the ratio of the point estimate to the true population parameter for each estimator (α = 1.75, β = 1000, γ = 300)

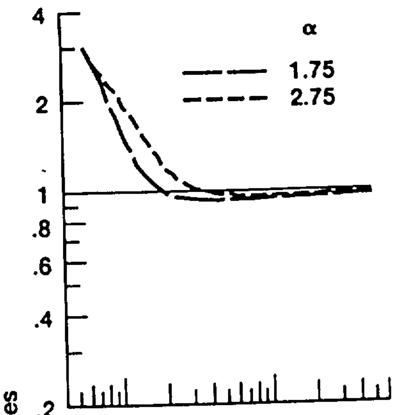

(a) Weibull modulus.

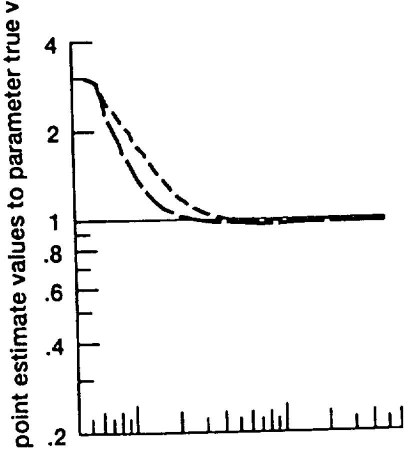

(b) Scale parameter.

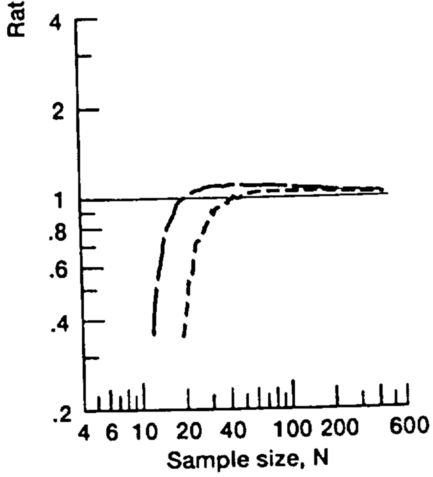

(c) Threshold stress.

Fig. 2 Arithmetic mean values of the ratio of the point estimate to the true population parameter for each estimator (β = 1000, γ = 300)

rameters. This lack of invariance precludes unbiasing the point estimates obtained using this method. If the estimators were invariant, the bias could be removed in a systematic fashion using the method outlined by Thoman et al. (1969) for the maximum-likelihood estimate of the Weibull modulus. The authors indicate that the ratio associated with the two-parameter maximum-likelihood estimator for the scale parameter is also not invariant with respect to the underlying population parameters. However, Thoman et al. (1969) were able to construct a function that contained the ratio associated with the scale parameter and the estimate of the Weibull modulus, but was not dependent on the true population parameters. This function enabled Thoman et al. (1969) to establish unbiasing factors and confidence bounds for the maximum-likelihood estimate of the two-parameter scale parameter. Similar functions for the nonlinear regression estimators discussed in this paper have not been developed. Thus, removing the bias associated with these estimators is not possible, and the design engineer should recognize that the amount of bias may be significant for small sample sizes.

Along with the mean value, the 10th and 90th percentile distributions are depicted for each estimator in Fig. 1. These percentile distributions are related to confidence bounds for a point estimate. The percentile distributions are obtained by ranking in order (from lowest to highest value) the ratios of point estimates to the true value of the distribution parameter. In this case the 10th percentile distribution represents the ratio associated with the 1000th ranked value. Hence, 999 ratios had lesser values. Similarly, the 90th percentile distribution represents the ratio associated with the 9000th ranked value. If the number of samples was increased from 10,000 to infinity, then these ranked values would yield the exact confidence bounds for the estimators. Note that for these estimators the confidence bounds narrow with increasing sample size (N). This is indicated by the decreasing separation in the percentile distributions. However, the percentile distributions are not invariant with respect to the true population parameters. Again, increasing α from 1.75 to 2.75 affected the percentile distributions (Fig. 3). This precludes the computation of confidence bounds on parameter estimates since the value of the true population parameter (the quantity being estimated) would have to be known a priori.

Application—Parameter Estimation and Reliability Analysis

In this section, parameters from the sintered silicon nitride (grade SNW-1000, GTE Wesgo Division) data presented by Chao and Shetty (1991) are estimated. The four-point bend, the three-point bend, and the pressurized-disk data are listed in Table 1. Focusing on the four-point bend specimen, the support span for this text fixture was 40.373 mm and the inner load span was 19.622 mm. The cross sections of the test specimens were 4.0138 mm in width and 3.1106 mm in height.[1] All failures occurred within the 19.6-mm gage section. Thus, each specimen is assumed to be subjected to pure bending. Under this assumption, Eq. (6) becomes (see Weibull and Daniel, 1964)

$$B=\left(\frac{V}{2(\alpha+1)}\right)\left(\frac{\sigma-\gamma}{\sigma}\right)\left(\frac{\sigma-\gamma}{\beta}\right)^{\alpha} \tag{17}$$

where

$$V=bhl=243.0\ \text{mm}^3 \tag{18}$$

and σ ($=Mc/I$) is the outer fiber stress, assuming that the material behaves in a linear elastic fashion. Chao and Shetty examined the fracture surfaces of failed specimens using optical and scanning electron microscopy. These studies indicate that failures were initiated at subsurface pores (i.e., a volume defect). This type of fracture site consistently occurred in all three specimen geometries.

Once again, Eq. (5) can be used to express the functional relationship between the ranked probability of failure ($\mathcal{P}_i$) and the estimate of the failure strength ($\hat{\sigma}_i$). Using the definition of B given in Eq. (17), then the following relationship exists between $\mathcal{P}_i$ and $\hat{\sigma}_i$:

$$\hat{\sigma}_i=\hat{\gamma}^*+\hat{\beta}^*[\hat{\sigma}_i\ln(1/1-\mathcal{P}_i)]^{1/\hat{\alpha}^*} \tag{19}$$

---

[1] All specimen dimensions and failure stresses in Table 1 (including the three-point and the pressurized-disk geometries) were obtained from a personal communication with Chao and Shetty.

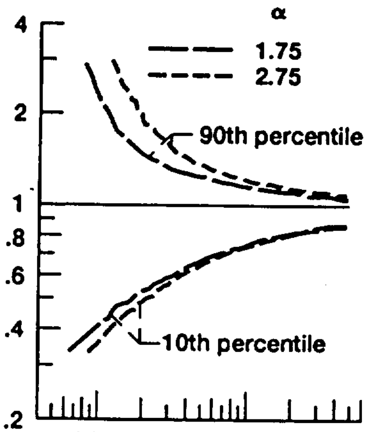

(a) Weibull modulus.

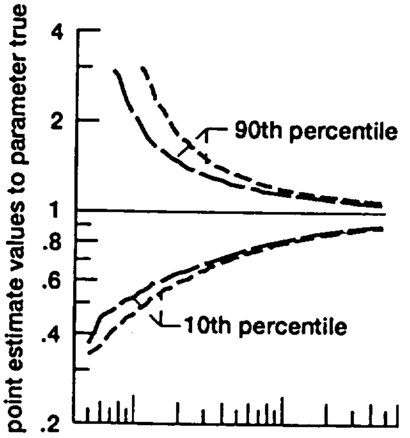

(b) Scale parameter.

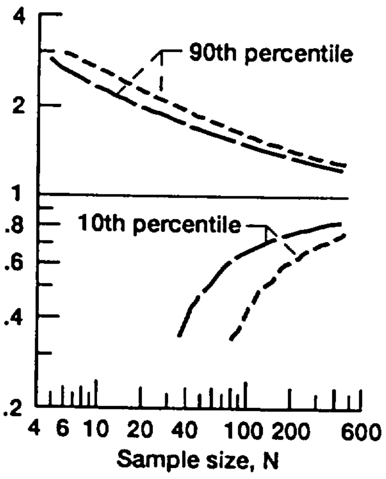

(c) Threshold stress.

Fig. 3 Percentile distributions of the ratio of the point estimate to the true population parameter for each estimator (β = 1000, γ = 300)

Table 1 Estimated parameters for silicon nitride

Specimen number	Strength, MPa		
	Three-point bend	Four-point bend	Pressurized disk
1	715.6	613.9	549.7
2	729.6	623.4	575.5
3	741.0	639.3	587.4
4	758.6	642.1	622.0
5	771.4	653.8	636.7
6	773.1	662.4	639.3
7	824.2	669.5	642.6
8	830.4	672.8	646.3
9	832.8	681.3	659.3
10	863.2	682.0	659.6
11	868.2	699.0	660.4
12	870.9	714.5	661.4
13	878.3	717.4	667.8
14	881.1	725.5	668.9
15	899.4	741.6	670.8
16	900.6	744.9	684.8
17	905.0	751.0	686.2
18	913.8	761.7	691.3
19	916.8	763.9	693.8
20	928.0	774.2	698.1
21	931.0	791.6	706.9
22	934.6	795.2	718.1
23	935.1	829.8	718.8
24	941.1	838.4	726.4
25	941.6	856.4	732.3
26	949.1	868.3	738.1
27	951.6	882.9	748.2
28	953.8	-----	771.5
29	956.5	-----	780.7
30	979.9	-----	786.3
31	-----	-----	796.2
32	-----	-----	811.6

for pure bending conditions. Here

$$\hat{\alpha}^{*}=\hat{\alpha}+1 \tag{20}$$

$$\hat{\beta}^{*}=\left[\left(\frac{2(\hat{\alpha}+1)}{V}\right)(\hat{\beta})^{\hat{\alpha}}\right]^{1/(1+\hat{\alpha})} \tag{21}$$

and

$$\hat{\gamma}^{*}=\hat{\gamma} \tag{22}$$

are introduced. At this point the residual defined by Eq. (10) cannot be formulated since Eq. (19) cannot be solved explicitly for the estimated ranked failure stress ($\hat{\sigma}_i$). However, several alternatives can be pursued to effect a solution. Margetson and Cooper (1984) indicate that the actual ranked failure stress (σ_i) should be substituted for $\hat{\sigma}_i$ on the right-hand side of Eq. (19). Defining

$$W_i=\sigma_i \ln(1/1-\mathcal{P}_i) \tag{23}$$

then Eqs. (13)-(15) can be solved for $\hat{\alpha}^{*}$, $\hat{\beta}^{*}$, and $\hat{\gamma}^{*}$. Estimated values of the material parameters α, β, and γ would then be computed from Eq. (20)-(22). However, once the substitution of

$$\hat{\sigma}_i=\sigma_i \tag{24}$$

is made, Eq. (11) no longer defines the sum of the squared residuals. Exactly what is being minimized is difficult to define (an approximate residual, perhaps). However, this approximate method yields fairly good results (Duffy et al., 1993). This becomes evident in the following discussion in which results of the approximate method are compared to a more rigorous solution.

Note that Eqs. (13)-(15) and Eq. (19) represent N + 3 equations in terms of N + 3 unknowns ($\hat{\alpha}^{*}$, $\hat{\beta}^{*}$, $\hat{\gamma}^{*}$, and $\hat{\sigma}_i$). The alternative solution involves finding an initial estimate of the Weibull parameters using the approach where the estimated failure strengths are substituted with the actual strength data. After computing an initial estimate of the parameters, Eq. (19) is solved numerically (N times) for $\hat{\sigma}_i$. With Eq. (12) redefined as

$$W_i=\hat{\sigma}_i \ln(1/1-\mathcal{P}_i) \tag{25}$$

then Eqs. (13) and (14) are solved for undated values of $\hat{\beta}^{*}$ and $\hat{\gamma}^{*}$ (using the previous value of $\hat{\alpha}^{*}$). The convergence criterion given by Eq. (15) is checked. If the criterion is not satisfied, $\hat{\alpha}^{*}$ is updated, and Eq. (19) is again solved numerically for $\hat{\sigma}_i$. This iterative process is repeated until the convergence criterion is satisfied.

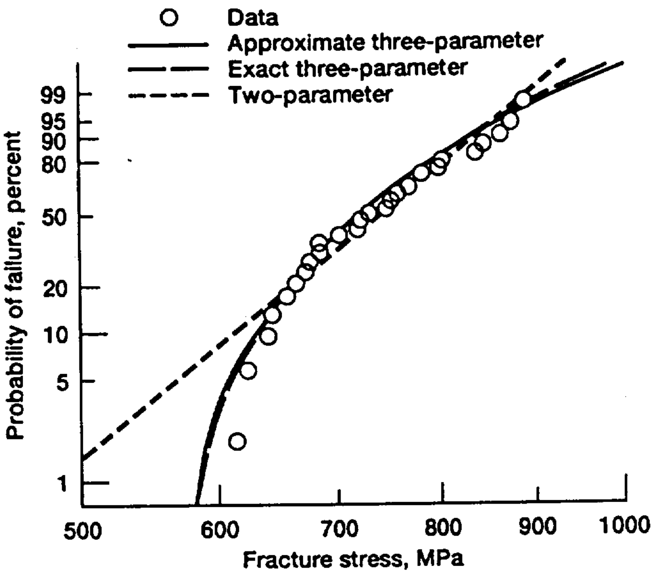

Fig. 4 Comparison of the probability of failure for the four-point specimen using the two- and three-parameter Weibull distribution

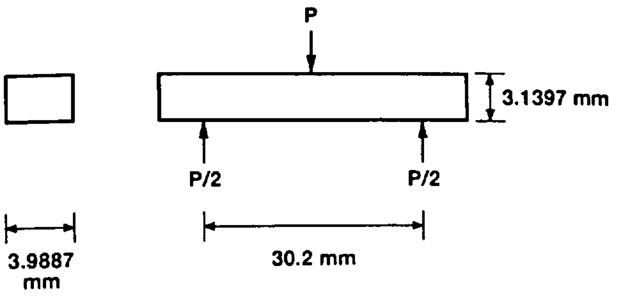

(a) Three-point bend specimen.

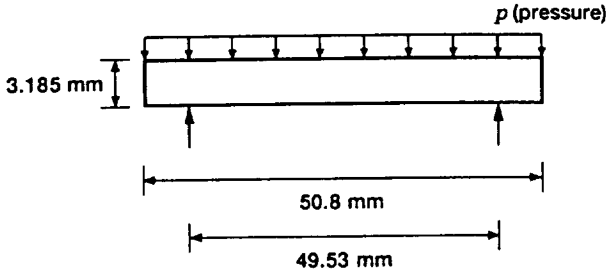

(b) Pressurized disk specimen.

Fig. 5 Geometry of the three-point bend specimen and the pressurized disk specimen

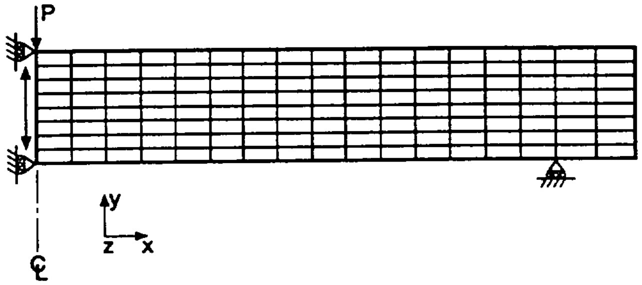

(a) Three-point bend specimen.

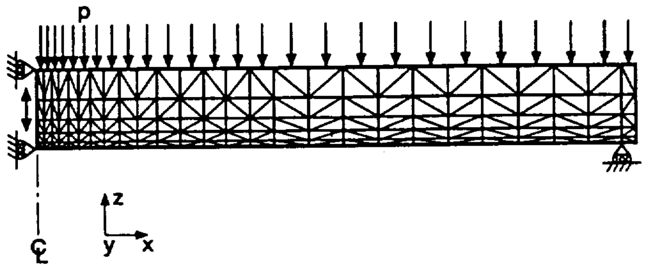

(b) Pressurized disk specimen.

Fig. 6 Finite element discretization

Both procedures are used to estimate parameters from the four-point bend test data listed in Table 1. The approximate method produces estimates of $\hat{\alpha} = 1.55$, $\hat{\beta} = 988.6$, and $\hat{\gamma} = 559.67$. The procedure that includes the solution for $\hat{\sigma}_i$ yields parameter estimates of $\hat{\alpha} = 1.68$, $\hat{\beta} = 861.6$, and $\hat{\gamma} = 558.1$. In addition, maximum-likelihood estimators are used to obtain point estimates for a two-parameter Weibull distribution. This technique gives estimated parameter values of $\hat{\alpha} = 10.2$ and $\hat{\beta} = 978.1$ (with $\hat{\gamma} \equiv 0$). The values obtained from the two-parameter maximum-likelihood estimators differ from the values reported by Chao and Shetty (1991). They used an averaging technique proposed by Batdorf and Sines (1980) that combines data from several test specimens. The pooled data are used to compute estimates from the three and four-point bend data. The estimated scale parameters from both configurations are averaged and, if the method of Batdorf and Sines (1980) is strictly adhered to, then the residuals from two data points are minimized. The authors feel that for this method to yield meaningful results, more than two specimen geometries are needed. The results of the maximum-likelihood estimators and both nonlinear regression methods are presented in Fig. 4, where the probability of failure is plotted as a function of the failure stress; that is, Eq. (5) is graphed using the different parameter estimates. The failure data are included using Eq. (8) to establish the vertical position of each data point. The straight line represents the two-parameter fit to the data. The nonlinear curves represent the three-parameter fit to the data. It is evident that the estimated three-parameter distributions are more efficient in predicting the failure data in the high-reliability region. Also note that there is very little difference between the two procedures used to establish the three-parameter estimates.

With the estimated Weibull parameters obtained using the procedure that includes the solution for $\hat{\sigma}_i$, reliability predictions are made for the three-point bend and the pressurized-disk geometries used in the experimental study by Chao and Shetty (1991). Both specimen geometries are depicted in Fig. 5. The geometries are modeled using MSC/NASTRAN to determine the structural response of the specimens to mechanical loads. The three-point bend geometry is modeled with 136 eight-node elements (MSC/NASTRAN CQUAD8). The mesh for this specimen is shown in Fig. 6. The stress distribution obtained from the finite element analysis is subsequently used as input for the integrated design program CARES (Nemeth et al., 1990). A volume flaw analysis is performed where the volume of a shell element is determined by calculating the midplane area and multiplying this value by the thickness of the element. The probability of failure curve is obtained by scaling (i.e., linearly increasing and decreasing) a single stress distribution a number of times. For each stress distribution a reliability analysis is performed with the CARES algorithm. An appropriate number of reliability computations are made to produce the nonlinear curve in Fig. 7. The linear (two-parameter) curve is established by determining the probability of failure at a single point on the curve and drawing a straight line through this point using the estimated Weibull modulus,

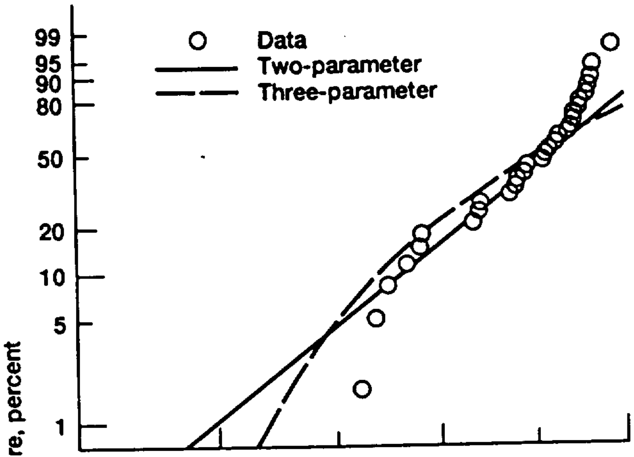

(a) Three-point bend specimen.

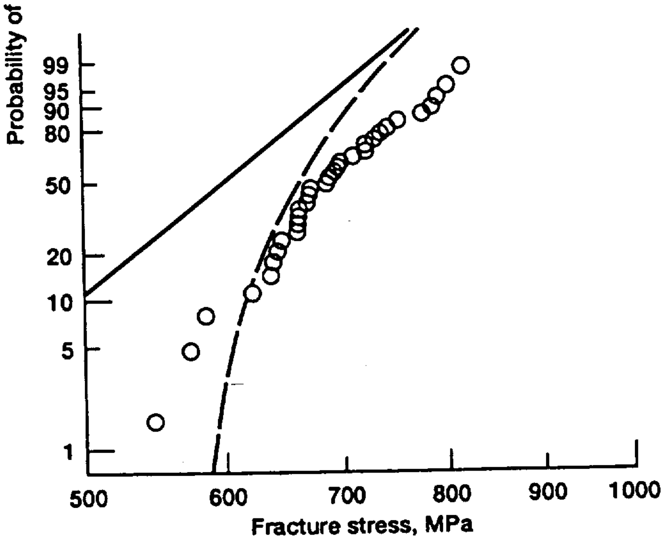

(b) Pressurized-disk specimen.

Fig. 7 CARES probability of failure results and failure data

which coincides with the slope of the linear curve. The data clearly indicate nonlinear behavior; however, both the two- and the three-parameter formulations yield conservative estimates in the high-reliability regions, but nonconservative estimates in the high probability of failure region. Both follow the trend of the data in the 5 to 60 percent probability of failure range of the graph.

The pressurized-disk geometry is modeled with 260 six-node elements (MSC/NASTRAN CTRIAX6). The axisymmetric mesh for this specimen is also shown in Fig. 6. The probability of failure curves are depicted in Fig. 7. All probability of failure curves are generated by computing component reliability from numerous stress distributions that are obtained, once again, by linearly increasing and decreasing a single stress distribution. Here the three-parameter formulation clearly yields a better fit to the data. The two-parameter formulation is distinctly conservative at all stress levels which can lead to overdesigned structural components. To demonstrate this, the parameter estimates obtained from the four-point bend data are used to compute the probability of failure of an aerospace component. Specifically, the component analyzed is a space shuttle main engine (SSME) high-pressure turbopump blade. The finite element mesh used to analyze this turbopump blade is depicted in Fig. 8. Moss and Smith (1987) used this mesh to analyze the dynamic characteristics of the blade. The mesh consists of 1025 brick elements (MSC/NASTRAN CHEXA).

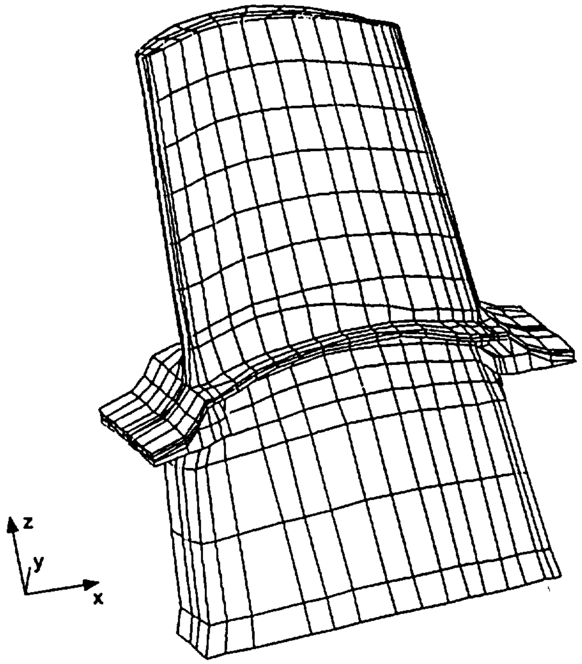

Fig. 8 Finite element discretization of turbopump blade

The shank of the blade is fully constrained. For the purpose of demonstration, it is assumed that the blade is fabricated from the monolithic silicon nitride material discussed in Chao and Shetty (1991). In the analysis Young's modulus is taken as 285.0 GPa and the Poisson ratio is 0.23. The specific load case studied represents a rotational speed of 40,000 rpm at room temperature. At this rotational speed the two-parameter formulation (using the PIA model) results in a component failure probability (P_f) of 75.2 percent. The three-parameter formulation results in a failure probability (P_f) of 0.04 percent. Utilization of the monolithic material would be summarily rejected based on the limited data available and the results of the two-parameter estimates. However, the results from the three-parameter formulation could prompt further consideration. The notable difference in the probability of failure does not indicate conclusively that the underlying population is characterized by a three-parameter Weibull distribution. Additional test data may clearly demonstrate whether the underlying population is characterized by a two- or three-parameter Weibull distribution. In addition, possible design studies could result in a further reduction in the component failure probability. Whether or not further redesign would bring the component failure probability within the stringent limits established for various shuttle components is not the issue here. The authors do not advocate using monolithic silicon nitride in the fabrication of SSME turbopump blades. Rather, this aerospace example emphasizes that the common use of the two-parameter formulation can lead to extremely conservative design decisions.

Conclusions

Enough experimental data exists to suggest threshold behavior (indicated by a nonlinear behavior similar to that displayed in Fig. 4) in certain monolithics. However, whether nonlinear behavior can be attributed to the existence of a threshold stress or competing failure mechanisms is open to question because of the lack of careful fractographic analysis for most data sets (except for the Chao and Shetty data discussed previously and obtained through personal communication). This paper has reviewed a number of aspects related to the simple nonlinear regression technique proposed by Margetson and Cooper (1984). From limited numerical studies it is concluded that the estimators are well-behaved in the sense that bias is minimized, and confidence bounds tighten as the sample size is increased. However, the estimators are not invariant with respect to the underlying parameters that characterize a population. This precludes establishing exact confidence bounds and unbiasing factors.

The estimators perform reasonably well in comparison to the two-parameter maximum-likelihood estimators when both are applied to the silicon nitride data of Chao and Shetty (1991). Using an improved estimator based on the method proposed by Margetson and Cooper (1984), the three-parameter Weibull distribution easily captures the nonlinear trend of the failure data. All reliability computations are made using the simplified PIA model but better correlation to the failure data might be obtained if other more rigorous reliability models were employed. The authors are currently pursuing this analytical approach.

Although the three-parameter formulation obviously provides a better fit to the pressurized-disk data, this may not be readily evident with the three and four-point bend data. Goodness-of-fit statistics such as the Kolmogoroff-Smirnoff statistic and the Anderson-Darling statistic should be used to establish which form of the Weibull distribution would best fit the experimental data. These approaches are currently being studied by the authors.

Finally an aerospace component is analyzed, and the results may indicate the conservativeness of the two-parameter formulation. The authors advocate the use of the three-parameter formulation of the Weibull distribution when experimental data exhibits threshold behavior. Even though the estimates proposed by Margetson and Cooper (1984) are not invariant, additional testing can be conducted to minimize the bias associated with the parameter estimates. As the reliability analysis of the SSME turbopump blade indicates, the costs from additional tests may be well worth the dramatic decrease in a component probability of failure.

References

Batdorf, S. B., and Crose, J. G., 1974, "A Statistical Theory for the Fracture of Brittle Structures Subjected to Nonuniform Polyaxial Stresses," ASME *Journal of Applied Mechanics*, Vol. 41, pp. 459–464.

Batdorf, S. B., and Heinisch, H. L., 1978, "Weakest Link Theory Reformulation for Arbitrary Fracture Criterion," *Journal of the American Ceramic Society*, Vol. 61, No. 7-8, pp. 355-358.

Batdorf, S. B., and Sines, G., 1980, "Combining Data for Improved Weibull Parameter Estimation," *Journal of the American Ceramic Society*, Vol. 63, No. 3-4, pp. 214–218.

Chao, L.-Y., and Shetty, D. K., 1991, "Reliability Analysis of Structural Ceramics Subjected to Biaxial Flexure," *Journal of the American Ceramic Society*, Vol. 74, No. 2, pp. 333-344.

Duffy, S. F., Palko, J. L., and Gyekenyesi, J. P., 1993, "Structural Reliability Analysis of Laminated CMC Components," ASME Journal of Engineering for Gas Turbines and Power, Vol. 115, this issue, pp. 103-108.

Margetson, J., and Cooper, N. R., 1984, "Brittle Material Design Using Three Parameter Weibull Distributions," *Probabilistic Methods in the Mechanics of Solids and Structures*, S. Eggwertz and N. C. Lind, eds., Springer-Verlag, Berlin, pp. 253-262.

Midgley, E., and Pierce, F. T., 1926, "The Weakest Link Theorems on Strength of Long and of Composite Specimens," *Journal of the Textile Institute*, Vol. 17, No. 2, pp. T355-T368.

Moss, L. A., and Smith, T. E., 1987, "Dynamic Characteristics of Singl Crystal SSME Blades," *Structural Integrity and Durability of Reusable Spac Propulsion Systems*, NASA CP-2471, pp. 211-214.

Nemeth, N. N., Manderscheid, J. M., and Gyekenyesi, J. P., 1990, "Ceramic Analysis and Reliability Evaluation of Structures (CARES), Users and Programmers Manual," NASA TP-2916.

Quinn, G. D., 1989, "Flexure Strength of Advanced Ceramics—A Roun Robin Exercise," MTL TR-89-62 (available NTIS, AD-A212101).

Schneider, D., and Palazotto, A. N., 1979, "A Technique for Evaluating Unique Set of Three Weibull Parameters Considering Composite Materials," *Fibre Science and Technology*, Vol. 12, No. 4, pp 296–281.

Thoman, D. R., Bain, L. J., and Antle, C. E., 1969, "Inferences on th Parameters of the Weibull Distribution," *Technometrics*, Vol. 11, No. 3, pp 445–460.

Thomas, D. J., and Wetherhold, R. C., 1991, "Reliability Analysis of Cor tinuous Fiber Composite Laminates," *Composites Structures*, Vol. 18, No. pp. 277-293.

Weibull, W. A., 1939, "A Statistical Theory of the Strength of Materials, *Ingeniors Ventenskaps Akademien Handlinger*, Vol. 151, pp. 5–45.

Weibull, W. A., 1951, "A Statistical Distribution Function of Wide A plicability," ASME *Journal of Applied Mechanics*, Vol. 18, pp. 293-297.

Weil, N. A., and Daniel, I. M., 1964, "Analysis of Fracture Probabilities Nonuniformly Stressed Brittle Materials," *Journal of the American Ceram Society*, Vol. 47, No. 6, pp. 268–274.

NASA Conference Publication 10146

HITEMP Review 1994

Advanced High Temperature Engine Materials Technology Program

Volume II: Compressor/Turbine Materials—Metals and MMC's

NOTICE

This report contains information which falls under the purview of the U.S. Munitions List, as defined in the International Traffic in Arms Regulations. It shall not be transferred to foreign nationals in the U.S., or abroad, without specific approval. Penalty for violations is described in ITAR, Section 127.

Proceedings of the 7th Annual HITEMP Review
held at the Westlake Holiday Inn
sponsored by NASA Lewis Research Center
Cleveland, Ohio
October 24–26, 1994

RELIABILITY ANALYSIS OF SINGLE CRYSTAL NiAl TURBINE BLADES

JOSEPH PALKO[1], Stephen Duffy[1]
Cleveland State University
Cleveland,Ohio

P. Kennard Wright
General Electric Aircraft Engine Co.
Cincinnati, Ohio

Jonathan Salem, Ronald Noebe, Donald R. Wheeler and Fred Holland
NASA Lewis Research Center
Cleveland, Ohio

Introduction

As part of a co-operative agreement with General Electric Aircraft Engines (GEAE), NASA LeRC is modifying and validating the Ceramic Analysis and Reliability Evaluation of Structures (CARES ref. 1) algorithm for use in design of components made of high strength NiAl based intermetallic materials.

NiAl single crystal alloys are being actively investigated by GEAE as a replacement for Ni-based single crystal superalloys for use in high pressure turbine blades and vanes. The driving force for this research lies in the numerous property advantages offered by NiAl alloys (ref. 2) over their superalloy counterparts. These include a reduction of density by as much as a third without significantly sacrificing strength, higher melting point, greater thermal conductivity, better oxidation resistance, and a better response to thermal barrier coatings. The current drawback to high strength NiAl single crystals is their limited ductility. Consequently, significant efforts including the work agreement with GEAE are underway to develop testing and design methodologies for these materials.

The approach to validation and component analysis involves the following steps (Fig. 2): determination of the statistical nature and source of fracture in a high strength, NiAl single crystal turbine blade material; measurement of the failure strength envelope of the material; coding of statistically based reliability models; verification of the code and model; and modeling of turbine blades and vanes for rig testing.

Material Testing and Specimen Design

Brittle materials frequently fail from a single, strength limiting origin due to low toughness. The strength of such a system is thus governed by the weakest-link within the system and is therefore dependent on the surface area and volume stressed during testing. Weibull statistics (ref. 5) are commonly used for reliability analysis of components fabricated from such materials. The calculated failure probability is dependent on the stress state and the material properties of the component.

Several isotropic theories applicable to ceramics and glasses have been incorporated into the public domain CARES (ref. 1) code developed at NASA Lewis. This post-processor code, when combined with a finite element stress analysis, calculates fast fracture probability of a brittle, monolithic structural component. As part of the cooperative agreement with GEAE the code will be modified to model anisotropic materials, such as single crystal NiAl.

The material being considered has limited ductility, is highly anisotropic (Young's modulus varies 95 to 271 GPa; 13.78 E3 ksi to 39.305 E3 ksi) and made in relatively small billets (25 x 50 x 100 mm; 0.98 x 1.96 x 3.94 in.) that will be used individually to produce a vane or blade. Therefore, the statistical nature and

---

[1] Resident research associate at NASA LeRC.

source of fracture is being studied via flexural testing of beam specimens (ref. 3), with statistical analysis of the data and fractography performed on all of the post-tested samples (ref. 4). Flexural testing allows many samples to be removed from a particular region of a given billet, thereby allowing determination of billet-to-billet and within billet consistency. These factors will cause a variation in component reliability. Furthermore, in contrast to tensile testing, flexural testing allows the location of failure to be readily identified because the asymmetry of flexural loading results in a specific fracture pattern.

Two basic types of flaws are typically encountered in brittle materials such as ceramics or glasses: surface defects and volumetric defects. Volumetric defects include large grains, pores, agglomerates and inclusions, while surface defects include exposed volume defects (e.g. a pore machined open) and machining or handling damage that occurs during specimen/component fabrication (ref. 4).

Flexural strength results for the single crystal NiAl indicate the material to exhibit a wide dispersion in strength (Fig. 3) that can be characterized via normal or Weibull statistics. Failure origins were identified in 27 of 29 specimens tested. In all cases failure originated from regions of interdendritic precipitation (Fig. 4). These interdendritic regions always contained a Ni-Al-Hf rich phase (Fig. 5) that was confirmed by x-ray analysis to be the Heusler phase Ni_2AlHf. Roughly half of the initiation sites also contained HfC dendrites within the interdendritic Heusler phase (Fig 6). The HfC phase was identified by Auger electron spectroscopy and confirmed by the shape of the carbon peak (Fig. 7).

Other strength tests planned for verification work include flexure (3 and 4-point), pure tension, pure compression, torsion and biaxial flexure. To date, uniaxial and biaxial flexural tests (Fig. 3) have been conducted, and a torsion specimen is being designed and verified relative to handbook solutions. Verification of a failure theory can be accomplished via measurement of points on the failure envelope and comparison to predictions by the model and code (Fig. 8). Each point on the failure envelope represents a stress state and thus can be measured experimentally for a given material via strength testing with various geometries. As the material exhibits elastic anisotropy and variation in fracture toughness with orientation (ref. 7), several orientations will be considered in strength testing.

For the torsion specimen design, in an effort to conserve time, materials and machining costs, finite element analysis was used to characterize the stress response of several specimens. A baseline model and several variations were analyzed using the ANSYS 5.0 finite element package. The intent was to optimize the stress response of the specimen such that highest stresses would occur in the gage section of the specimen, thus concentrating failure within this section. Upon completion of the stress analysis, a CARES analysis was conducted for each specimen as well.

Each model consisted of three parts: the specimen, a three jaw chuck assembly used to grip the specimen, and a sleeve of surface elements around the volume of the specimen (see Fig. 9). Note that only half of the length of the specimen was modeled to take advantage of symmetry. A desired maximum principal stress of 800 MPa (116.0 ksi) was specified for each specimen. To obtain this stress level, a tangential force in the circumferential direction was applied at third points to the extremities of the chuck assembly.

A total of nine specimen geometries were analyzed. The use of parametric design language within ANSYS facilitated easy manipulation of design variables and model creation. The transition length between the gage section and the grip section of the specimen served as one design parameter. The gage diameter was the other. The different values for these parameters appear in Fig. 10. The intent was to eliminate stress risers in the transition section of the specimen and keep the maximum stress within the gage section. A constant, low stress field was also desirable in the grip section of the specimen. The baseline design satisfied both of these requirements. A plot of the first principal stress for this model is shown in Fig. 11. As the gage section of the specimen became larger, higher stresses began to migrate into the transition section and beyond into the grip section. Also, as the transition length between the grip and gage sections was changed, higher stresses began to migrate into the transition section. Of the nine designs, no model behaved better than the baseline design.

The subsequent reliability analyses reinforced these results. Developing a specimen with high probability of failure in the gage section and low or no probability of failure in the transition and grip sections was the objective. Since it is anticipated that this material will exhibit the so called "size effect" (i.e., decreasing component strength with increasing component size), the overall stressed area of the component would likely affect the reliability results. This factor was monitored as the results of the different models were compared. Again, the various iterations in the design provided no reason to switch from the baseline specimen design.

Component Analysis

As a starting point for the component feasibility study, a two dimensional finite element model of a double tang blade post and disk assembly was obtained from General Electric (see Fig. 12). This was used with the NiAl failure data (Fig. 3) to perform the reliability analysis. Fig. 13 shows the approach used for this type of analysis. Using this approach, the design engineer can concentrate on areas of the component which possess low reliability and modify them accordingly, thus leading to the optimization of the component.

Only the blade dove tail section was considered in the reliability analysis. Two separate analyses were conducted. The first used the entire set of 29 failure data points to calculate the Weibull parameters. The second involved the assumption that through improved processing techniques, the lowest five failure points would be eliminated, hence the Weibull parameters were calculated from the 24 highest failure strength values. The results of the reliability analysis and the respective Weibull parameters appear in Fig. 14. This analysis clearly shows the effect that reduced scatter has on a reliability of a component fabricated from a brittle material system.

This effort was successful in demonstrating the feasibility of such design procedures; however, to fully characterize a component fabricated from this type of material system, a failure criterion has to be developed that captures the anisotropic behavior of the material. This is a subject for future work and is identified as a milestone within the work agreement. Other areas of future work include a more complete characterization of the material's behavior along various crystallographic orientations. Billet to billet strength variation as well as strength variation within each billet will also be monitored.

References

1. N. Nemeth, J. Manderscheid, J. Gyekenyesi, "CARES Users and Programmers Manual," NASA Technical Paper TP2916, 1990.

2. Darolia, R., "NiAl For Turbine Airfoil Applications," in Structural Intermetallics, ed. R. Darolia et al., TMS, Warrendale, PA, 1993, pp. 495-504.

3. ASTM C 1161-90 "Standard Test Method for Flexural Strength of Advanced Ceramics at Ambient Temperature," American Society for Testing and Materials Annual Book of Standards, Vol. 15.01, 1990, pp. 333-339.

4. "Fractography and Characterization of Fracture Origins in Advanced Structural Ceramics," MIL-HDBK-790, (July, 1992).

5. W. Weibull, "A Statistical Theory of the Strength of Materials," Ingeniors Vetenskaps Akademien Handlinger, No. 151, 1939.

6. K. Chang, R, Darolia and H. Lipsitt, "Cleavage Fracture in B2 Aluminides," *Acta Metall.* Vol. 40, No. 10, 1992, pp. 2727-2737.

OBJECTIVE

- Modify and validate the CARES reliability code for use in design of components made from low ductility NiAl based intermetallics.

- This effort is part of a co–operative work agreement between General Electric Aircraft Engines and NASA LeRC.

Fig. 1

CD-94-68043

APPROACH

- Determine the statistical nature and source of fracture in high–strength NiAl single crystal material

- Measure the fracture strength envelope of the material (may involve characterizations in different material directions)

- Develop and code the appropriate failure model to capture both the statistical nature of failure and the anisotropic behavior of the material

- Verify the model and reliability code

- Model turbine vanes and blades for rig testing

Fig. 2

CD-94-68044

WEIBULL PLOT OF FAILURE DATA

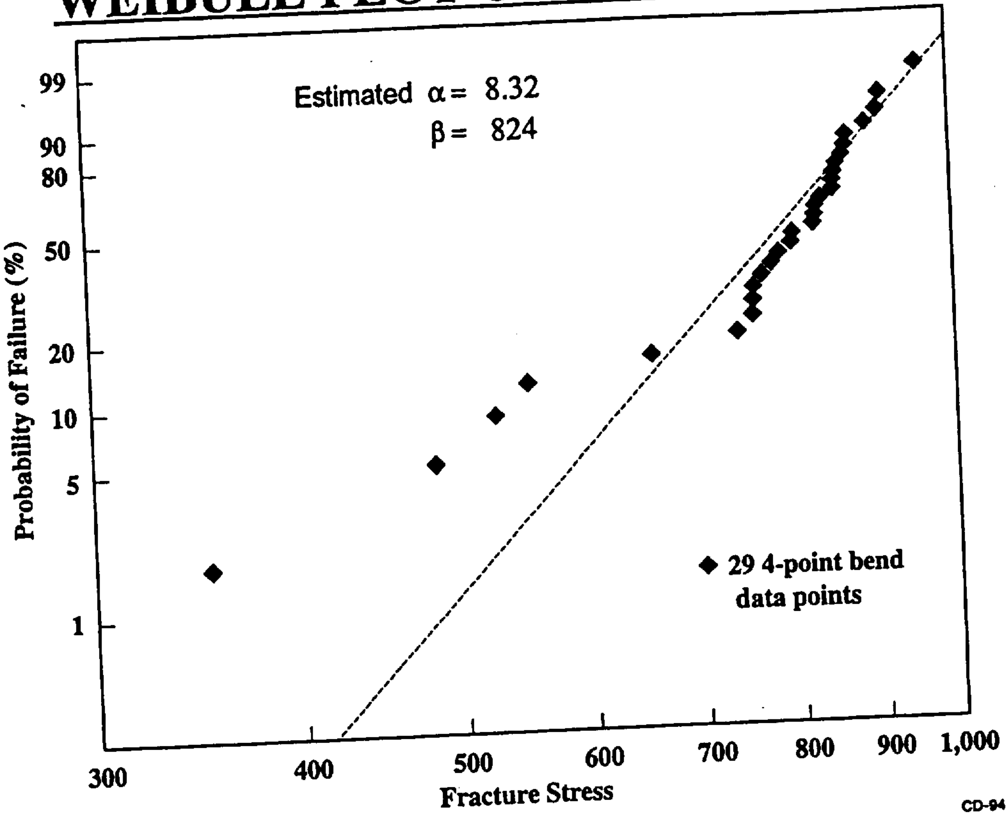

CD-94-68045

Fig. 3

NiAl TEST SPECIMEN FRACTOGRAPHY

- Fractography (SEM/EDS) was performed on 27 of 29 specimens (Origins for 2 were not recovered)
- All had fracture origins at Ni_2AlHf or HfC particles or a combined interdendritic particle

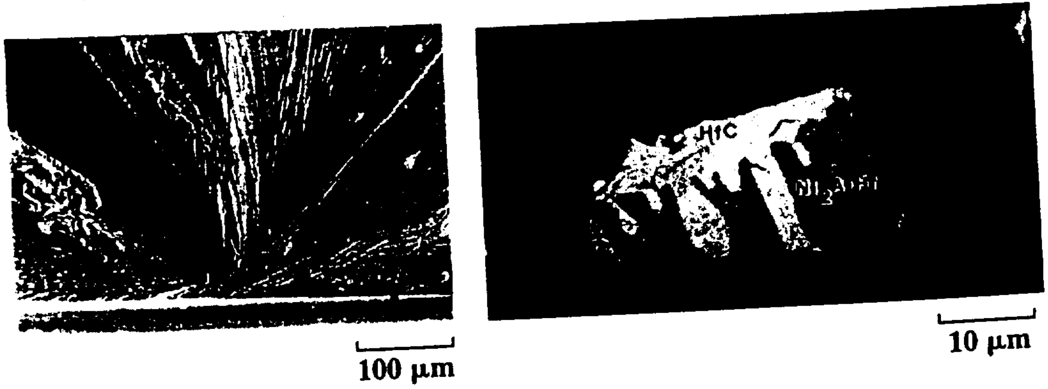

SEM image of failure origin

High mag. image of failure origin

CD-94-68046

Fig. 4

AUGER ANALYSIS SHOWING HEUSLER PHASE

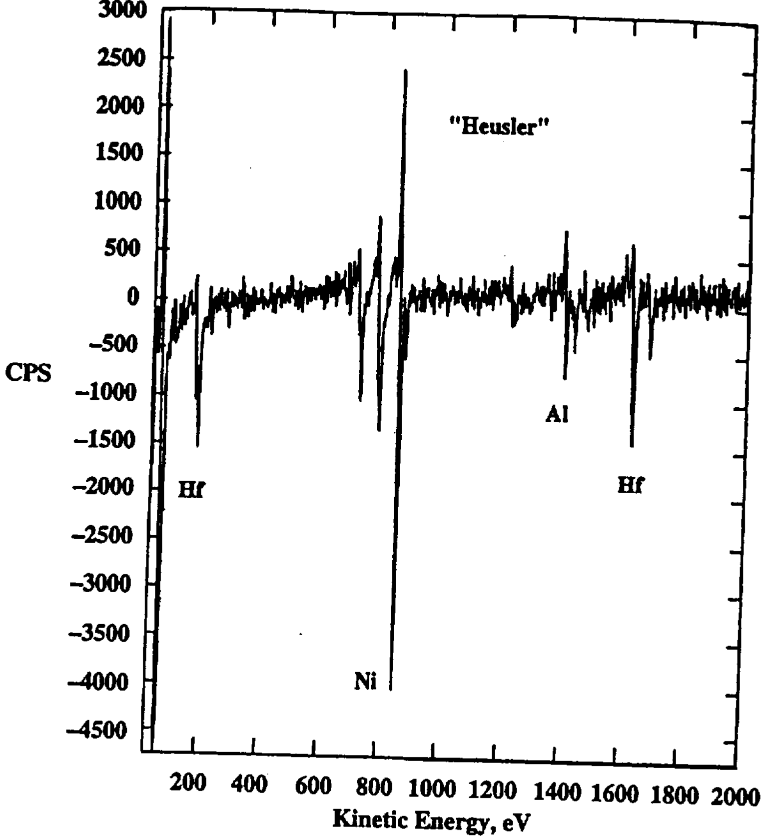

Fig. 5

CD-94-68047

AUGER ANALYSIS SHOWING HfC PHASE

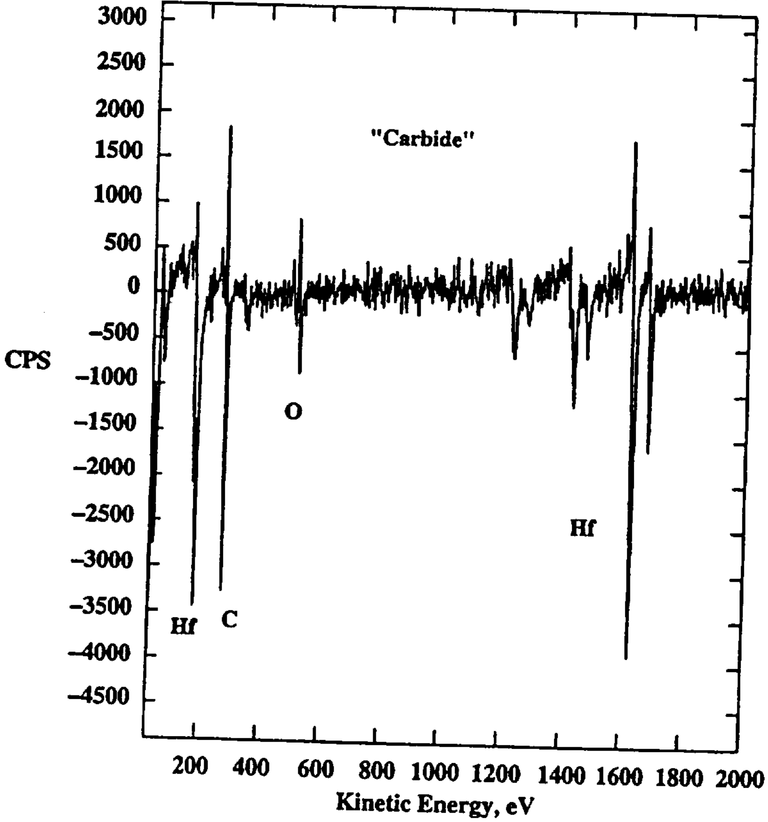

Fig. 6

CD-94-68048

DETAILED AUGER ANALYSIS OF CARBON REGION

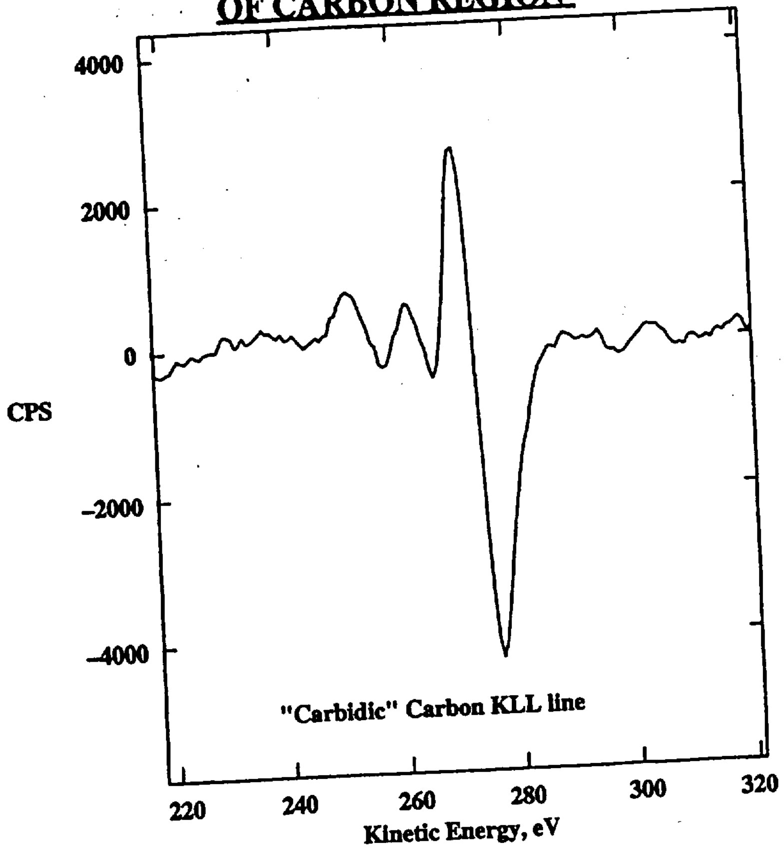

CD-94-68049

Fig. 7

COMPARISON OF FAILURE DATA WITH THEORY

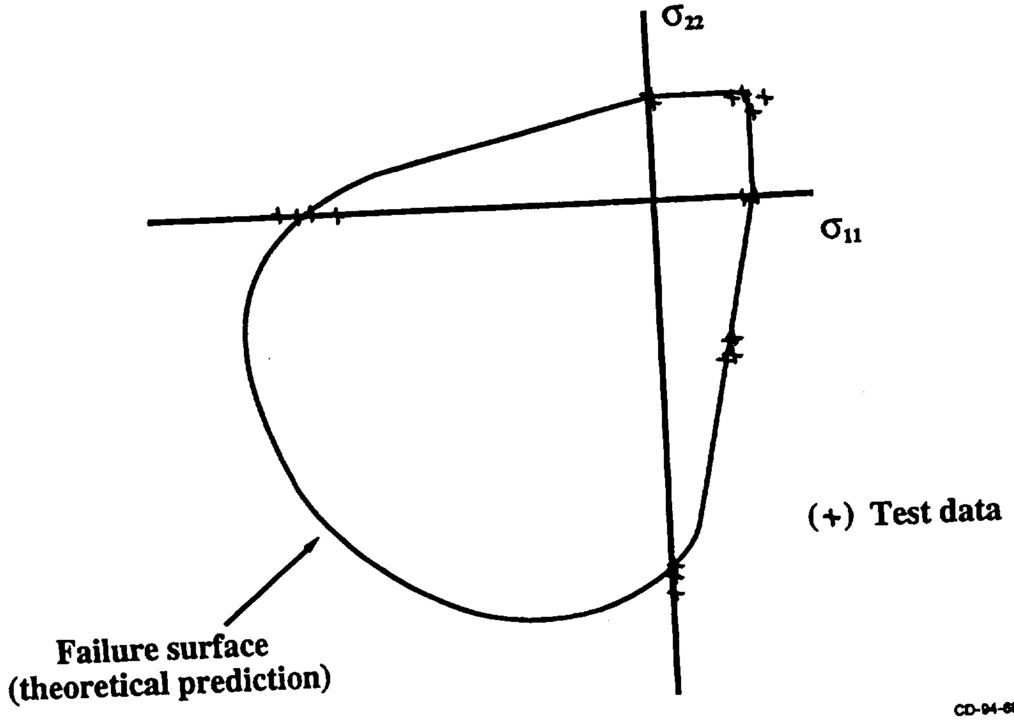

CD-94-68050

Fig. 8

TEST SPECIMEN ANALYSIS

Finite element model of specimen and chucks

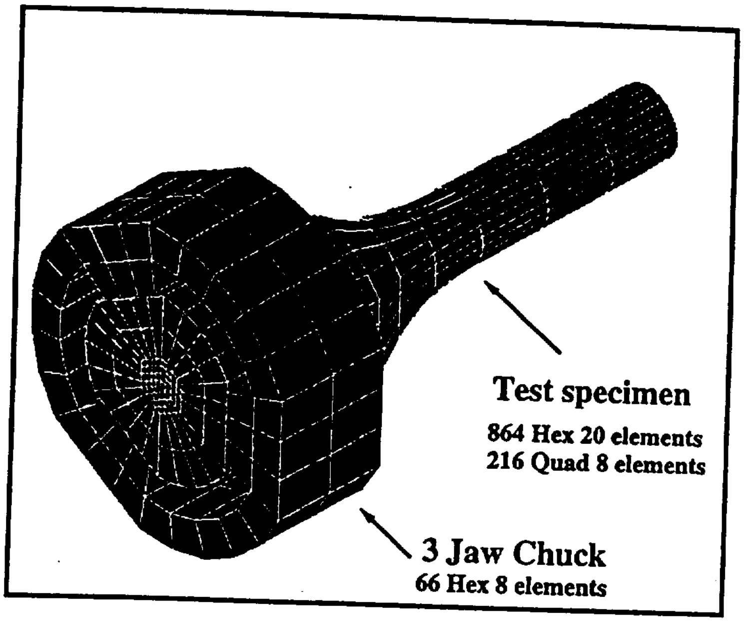

Fig. 9

CD-94-68051

TEST SPECIMEN
(BASE DESIGN)

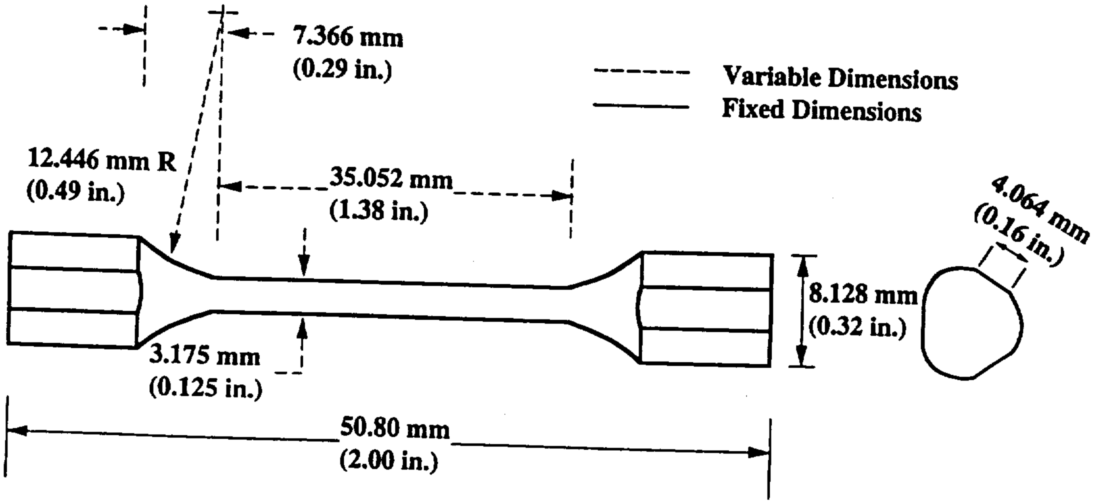

B + ↑

Gage Diameters: 3.175 mm, 3.810 mm, 4.445 mm
(0.125 in.) (0.150 in.) (0.175 in.)

Transition lengths: 7.366 mm, 5.004 mm, 3.505 mm
(0.29 in.) (0.197 in.) (0.138 in.)

Fig. 10

CD-94-68052

PRINCIPAL STRESS PLOT OF BASELINE TORSION SPECIMEN

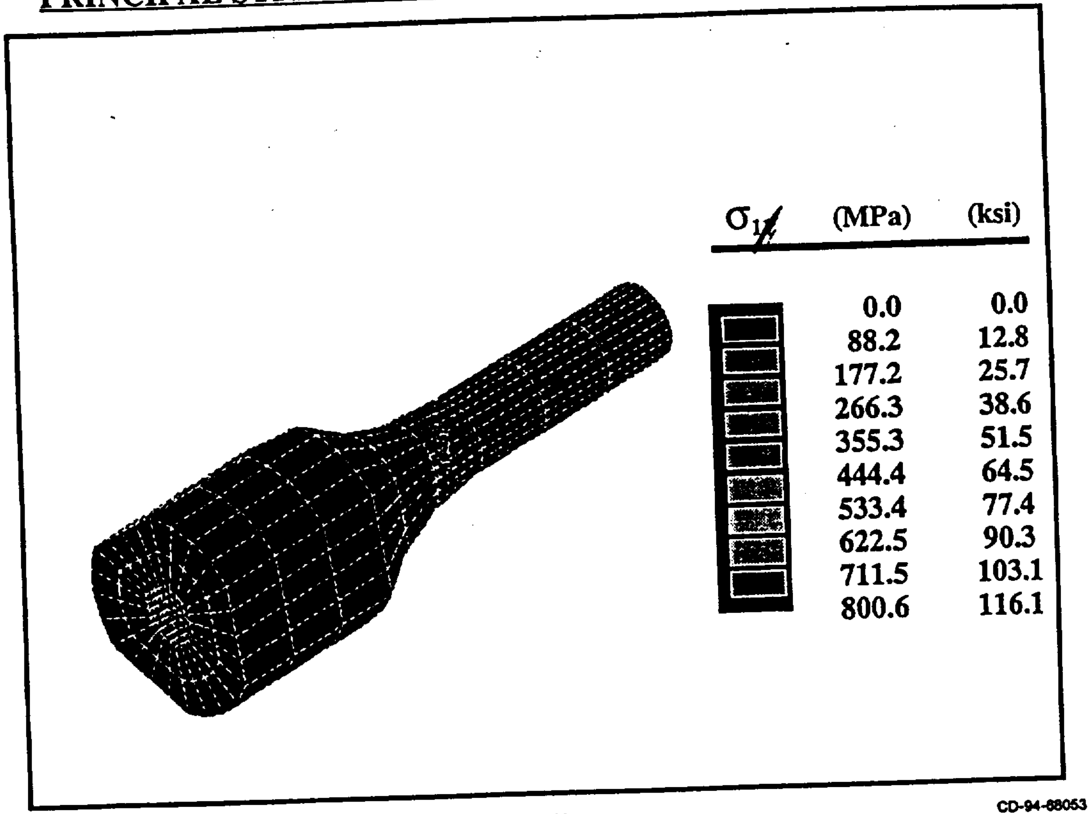

CD-94-68053

Fig. 11

PROBABILISTIC COMPONENT DESIGN PROCEDURE

- **Approach:**

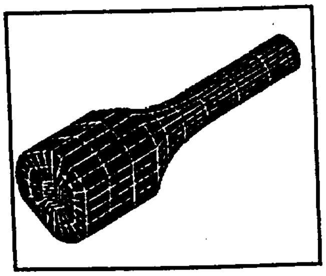

Test Specimen

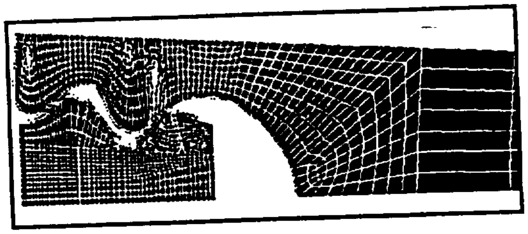

Complex Geometries

—— Material failure characterization

—— Fractographic examination of ruptured specimens

—— Component finite-element analysis

—— Component reliability evaluation

—— Design optimization

Fig. 12

CD-94-68054

BLADE AND DISK ANALYSIS

Finite element model of blade post and disk assembly

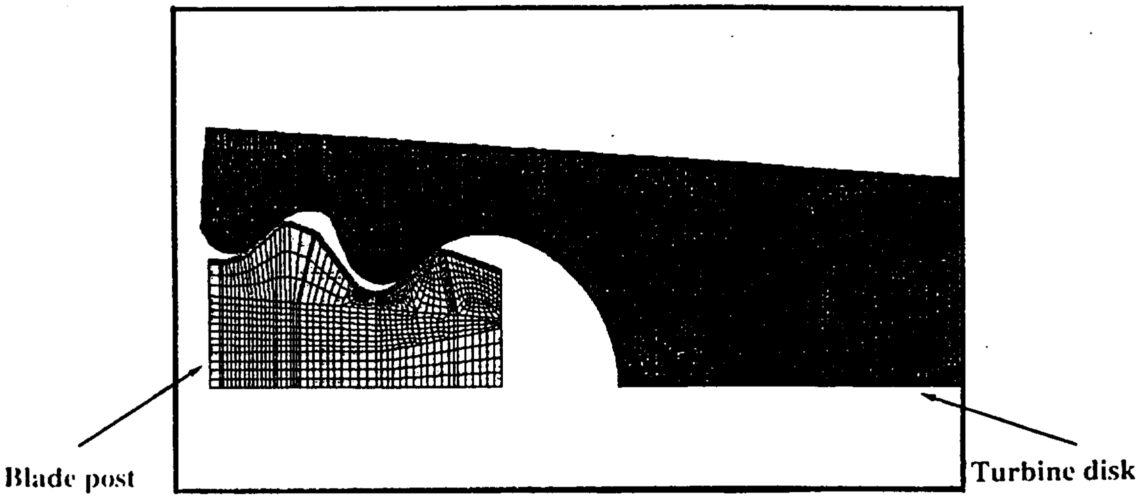

Fig. 13 CD-94-68055

SUMMARY OF CARES ANALYSIS OF BLADE

Two reliability analyses were conducted on blade design

- **Two sets of Weibull parameters were used**

	29 Data points	24 Data points
Alpha	8.32	15.30
Beta $(ksi)^{3/\alpha}$	51,021	74,092
Reliability	99.46%	99.99%

Fig. 14 CD-94-68056

CONCLUSIONS

- Failure origins can be identified in low ductility NiAl's with appropriate testing
- Torsion specimen geometry was verified through FEM and CARES analyses
- Methods in place for component reliability analyses
- Improved processing techniques can be used to improve component reliability

Fig. 15

CD-94-68057

FUTURE WORK

- Test material for billet to billet strength variation
- Test material for strength variation within a billet
- Test for statistical variation along different material directions
- Develop appropriate failure model for this material

Fig. 16

CD-94-68058

Designation: C 1239 - 93

Standard Practice for Reporting Uniaxial Strength Data and Estimating Weibull Distribution Parameters for Advanced Ceramics[1]

1. Scope

1.1 This practice covers the evaluation and subsequent reporting of uniaxial strength data and the estimation of probability distribution parameters for advanced ceramics that fail in a brittle fashion. The failure strength of advanced ceramics is treated as a continuous random variable. Typically, a number of test specimens with well-defined geometry are failed under well-defined isothermal loading conditions. The load at which each specimen fails is recorded. The resulting failure stresses are used to obtain parameter estimates associated with the underlying population distribution. This practice is restricted to the assumption that the distribution underlying the failure strengths is the two-parameter Weibull distribution with size scaling. Furthermore, this practice is restricted to test specimens (tensile, flexural, pressurized ring, etc.) that are primarily subjected to uniaxial stress states. Section 8 outlines methods to correct for bias errors in the estimated Weibull parameters and to calculate confidence bounds on those estimates from data sets where all failures originate from a single flaw population (that is, a single failure mode). In samples where failures originate from multiple independent flaw populations (for example, competing failure modes), the methods outlined in Section 8 for bias correction and confidence bounds are not applicable.

1.2 Measurements of the strength at failure are taken for one of two reasons: either for a comparison of the relative quality of two materials, or the prediction of the probability of failure (or, alternatively, the fracture strength) for a structure of interest. This practice will permit estimates of the distribution parameters that are needed for either. In addition, this practice encourages the integration of mechanical property data and fractographic analysis.

1.3 This practice includes the following:

1.4 The values stated in SI units are to be regarded as the standard.

2. Referenced Documents

2.1 *ASTM Standards:*

C 1145 Terminology of Advanced Ceramics[2]

D 4392 Terminology for Statistically Related Terms[3]

E 6 Terminology Relating to Methods of Mechanical Testing[4]

E 178 Practice for Dealing With Outlying Observations[5]

E 456 Terminology Relating to Quality and Statistics[5]

2.2 *Military Handbook:*

MIL-HDBK-790 Fractography and Characterization of Fracture Origins in Advanced Structural Ceramics[6]

3. Terminology

3.1 Proper use of the following terms and equations will alleviate misunderstanding in the presentation of data and in the calculation of strength distribution parameters.

3.1.1 *censored strength data*—strength measurements (that is, a sample) containing suspended observations such as that produced by multiple competing or concurrent flaw populations.

3.1.1.1 Consider a sample where fractography clearly established the existence of three concurrent flaw distributions (although this discussion is applicable to a sample with any number of concurrent flaw distributions). The three concurrent flaw distributions are referred to here as distributions *A*, *B*, and *C*. Based on fractographic analyses, each specimen strength is assigned to a flaw distribution that initiated failure. In estimating parameters that characterize the strength distribution associated with flaw distribution *A*, all specimens (and not just those that failed from Type A flaws) must be incorporated in the analysis to ensure efficiency and accuracy of the resulting parameter estimates. The strength of a specimen that failed by a Type B (or Type C) flaw is treated as a *right censored* observation relative to the *A* flaw distribution. Failure due to a Type B (or Type C) flaw restricts, or censors, the information concerning Type A

---

[1] This practice is under the jurisdiction of ASTM Committee C-28 on Advanced Ceramics and is the direct responsibility of Subcommittee C28.02 on Design and Evaluation.

Current edition approved April 15, 1993. Published June 1993.

[2] *Annual Book of ASTM Standards*, Vol 15.01.

[3] *Discontinued*—see 1992 *Annual Book of ASTM Standards*, Vol 07.02.

[4] *Annual Book of ASTM Standards*, Vols 03.01 and 08.03.

[5] *Annual Book of ASTM Standards*, Vol 14.02.

[6] Available from Standardization Documents Order Desk, Bldg. 4 Section D, 700 Robbins Ave., Philadelphia, PA 19111-5094, Attn: NPODS.

flaws in a specimen by suspending the test before failure occurred by a Type A flaw (**1**).[7] The strength from the most severe Type A flaw in those specimens that failed from Type B (or Type C) flaws is higher than (and thus to the *right* of) the observed strength. However, no information is provided regarding the magnitude of that difference. Censored data analysis techniques incorporated in this practice utilize this incomplete information to provide efficient and relatively unbiased estimates of the distribution parameters.

3.1.2 *competing failure modes*—distinguishably different types of fracture initiation events that result from concurrent (competing) flaw distributions.

3.1.3 *compound flaw distributions*—any form of multiple flaw distribution that is neither pure concurrent nor pure exclusive. A simple example is where every specimen contains the flaw distribution A, while some fraction of the specimens also contains a second independent flaw distribution B.

3.1.4 *concurrent flaw distributions*—a type of multiple flaw distribution in a homogeneous material where every specimen of that material contains representative flaws from each independent flaw population. Within a given specimen, all flaw populations are then present concurrently and are competing with each other to cause failure. This term is synonymous with "competing flaw distributions."

3.1.5 *effective gage section*—that portion of the test specimen geometry that has been included within the limits of integration (volume, area, or edge length) of the Weibull distribution function. In tensile specimens, the integration may be restricted to the uniformly stressed central gage section, or it may be extended to include transition and shank regions.

3.1.6 *estimator*—a well-defined function that is dependent on the observations in a sample. The resulting value for a given sample may be an estimate of a distribution parameter (a point estimate) associated with the underlying population. The arithmetic average of a sample is, for example, an estimator of the distribution mean.

3.1.7 *exclusive flaw distributions*—a type of multiple flaw distribution created by mixing and randomizing specimens from two or more versions of a material where each version contains a different single flaw population. Thus, each specimen contains flaws exclusively from a single distribution, but the total data set reflects more than one type of strength-controlling flaw. This term is synonymous with "mixtures of flaw distributions."

3.1.8 *extraneous flaws*—strength-controlling flaws observed in some fraction of test specimens that cannot be present in the component being designed. An example is machining flaws in ground bend specimens that will not be present in as-sintered components of the same material.

3.1.9 *fractography*—the analysis and characterization of patterns generated on the fracture surface of a test specimen. Fractography can be used to determine the nature and location of the critical fracture origin causing catastrophic failure in an advanced ceramic test specimen or component.

3.1.10 *population*—the totality of potential observations about which inferences are made.

3.1.11 *population mean*—the average of all potential measurements in a given population weighted by their relative frequencies in the population.

3.1.12 *probability density function*—the function $f(x)$ is a probability density function for the continuous random variable X if:

$$f(x) \geq 0 \tag{1}$$

and

$$\int_{-\infty}^{\infty} f(x)\, dx = 1 \tag{2}$$

The probability that the random variable X assumes a value between a and b is given by the following equation:

$$Pr(a < X < b) = \int_{a}^{b} f(x)\, dx \tag{3}$$

3.1.13 *sample*—a collection of measurements or observations taken from a specified population.

3.1.14 *skewness*—a term relating to the asymmetry of a probability density function. The distribution of failure strength for advanced ceramics is not symmetric with respect to the maximum value of the distribution function but has one tail longer than the other.

3.1.15 *statistical bias*—inherent to most estimates, this is a type of consistent numerical offset in an estimate relative to the true underlying value. The magnitude of the bias error typically decreases as the sample size increases.

3.1.16 *unbiased estimator*—an estimator that has been corrected for statistical bias error.

3.1.17 *Weibull distribution*—the continuous random variable X has a two-parameter Weibull distribution if the probability density function is given by the following equations:

$$f(x) = \left(\frac{m}{\beta}\right)\left(\frac{x}{\beta}\right)^{m-1} \exp\left[-\left(\frac{x}{\beta}\right)^{m}\right] \quad x > 0 \tag{4}$$

$$f(x) = 0 \quad x \leq 0 \tag{5}$$

and the cumulative distribution function is given by the following equations:

$$F(x) = 1 - \exp\left[-\left(\frac{x}{\beta}\right)^{m}\right] \quad x > 0 \tag{6}$$

or

$$F(x) = 0 \quad x \leq 0 \tag{7}$$

where:

m = Weibull modulus (or the shape parameter) (>0), and

β = scale parameter (>0).

3.1.17.1 The random variable representing uniaxial tensile strength of an advanced ceramic will assume only positive values, and the distribution is asymmetrical about the mean. These characteristics rule out the use of the normal distribution (as well as others) and point to the use of the Weibull and similar skewed distributions. If the random variable representing uniaxial tensile strength of an advanced ceramic is characterized by Eqs 4 through 7, then the probability that this advanced ceramic will fail under an applied uniaxial tensile stress σ is given by the cumulative distribution function as follows:

---

[7] The boldface numbers in parentheses refer to the list of references at the end of this practice.

$$P_f = 1 - \exp\left[-\left(\frac{\sigma}{\sigma_\theta}\right)^m\right] \quad \sigma > 0 \tag{8}$$

$$P_f = 0 \quad \sigma \leq 0 \tag{9}$$

where:

P_f = probability of failure, and

σ_θ = Weibull characteristic strength.

Note that the Weibull characteristic strength is dependent on the uniaxial test specimen (tensile, flexural, or pressurized ring) and will change with specimen size and geometry. In addition, the Weibull characteristic strength has units of stress and should be reported using units of megapascals or gigapascals.

3.1.17.2 An alternative expression for the probability of failure is given by the following equation:

$$P_f = 1 - \exp\left[-\int_V \left(\frac{\sigma}{\sigma_0}\right)^m dV\right] \quad \sigma > 0 \tag{10}$$

$$P_f = 0 \quad \sigma \leq 0 \tag{11}$$

The integration in the exponential is performed over all tensile regions of the specimen volume if the strength-controlling flaws are randomly distributed through the volume of the material, or over all tensile regions of the specimen area if flaws are restricted to the specimen surface. The integration is sometimes carried out over an effective gage section instead of over the total volume or area. In Eq 10, σ_0 is the Weibull material scale parameter. The parameter is a material property if the two-parameter Weibull distribution properly describes the strength behavior of the material. In addition, the Weibull material scale parameter can be described as the Weibull characteristic strength of a specimen with unit volume or area loaded in uniform uniaxial tension. The Weibull material scale parameter has units of stress·(volume)$^{1/m}$ and should be reported using units of MPa·(m)$^{3/m}$ or GPa·(m)$^{3/m}$ if the strength-controlling flaws are distributed through the volume of the material. If the strength-controlling flaws are restricted to the surface of the specimens in a sample, then the Weibull material scale parameter should be reported using units of MPa·(m)$^{2/m}$ or GPa·(m)$^{2/m}$. For a given specimen geometry, Eqs 8 and 10 can be equated, which yields an expression relating σ_0 and σ_θ. Further discussion related to this issue can be found in 7.6.

3.2 For definitions of other statistical terms, terms related to mechanical testing, and terms related to advanced ceramics used in this practice, refer to Terminologies D 4392, E 456, C 1145, and E 6 or to appropriate textbooks on statistics (2–5).

3.3 *Symbols:*

A = specimen area (or area of effective gage section, if used).

b = gage section dimension, base of bend test specimen.

d = gage section dimension, depth of bend test specimen.

$F(x)$ = cumulative distribution function.

$f(x)$ = probability density function.

L_i = length of the inner load span for a bend test specimen.

L_o = length of the outer load span for a bend test specimen.

$\mathcal{L}$ = likelihood function.

m = Weibull modulus.

$\hat{m}$ = estimate of the Weibull modulus.

$\hat{m}_U$ = unbiased estimate of the Weibull modulus.

N = number of specimens in a sample.

P_f = probability of failure.

r = number of specimens that failed from the flaw population for which the Weibull estimators are being calculated.

t = intermediate quantity defined by Eq 27, used in calculation of confidence bounds.

V = specimen volume (or volume of effective gage section, if used).

X = random variable.

x = realization of a random variable X.

β = Weibull scale parameter.

ϵ = stopping tolerance in the computer algorithm MAXL.

$\hat{\mu}$ = estimate of mean strength.

σ = uniaxial tensile stress.

σ_i = maximum stress in the *i*th test specimen at failure.

σ_j = maximum stress in the *j*th test specimen at failure.

σ_0 = Weibull material scale parameter (strength relative to unit size) defined in Eq 10.

σ_θ = Weibull characteristic strength (associated with a test specimen) defined in Eq 8.

$\hat{\sigma}_0$ = estimate of the Weibull material scale parameter.

$\hat{\sigma}_\theta$ = estimate of the Weibull characteristic strength.

4. Summary of Practice

4.1 This practice enables the experimentalist to estimate Weibull distribution parameters from failure data. Begin by performing a fractographic examination of each failed specimen (optional, but highly recommended) in order to characterize fracture origins. Usually discrete fracture origins can be grouped by flaw distributions. Screen the data associated with each flaw distribution for outliers. Compute estimates of the biased Weibull modulus and Weibull characteristic strength. If necessary, compute the estimate of the mean strength. If all failures originate from a single flaw distribution, compute an unbiased estimate of the Weibull modulus and compute confidence bounds for both the estimated Weibull modulus and the estimated Weibull characteristic strength. Prepare a graphical representation of the failure data along with a test report.

5. Significance and Use

5.1 Advanced ceramics usually display a linear stress-strain behavior to failure. Lack of ductility combined with flaws that have various sizes and orientations leads to scatter in failure strength. Strength is not a deterministic property but instead reflects an intrinsic fracture toughness and a distribution (size and orientation) of flaws present in the material. This practice is applicable to brittle monolithic ceramics that fail as a result of catastrophic propagation of flaws present in the material. This practice is also applicable to composite ceramics that do not exhibit any appreciable bilinear or nonlinear deformation behavior. In addition, the composite must contain a sufficient quantity of uniformly distributed fibers such that the material is effectively homogeneous. Whisker-toughened ceramic composites may be representative of this type of material.

5.2 Two- and three-parameter formulations exist for the Weibull distribution. This practice is restricted to the two-parameter formulation. An objective of this practice is to obtain point estimates of the unknown parameters by using well-defined functions that incorporate the failure data. These functions are referred to as estimators. It is desirable that an estimator be consistent and efficient. In addition, the estimator should produce unique, unbiased estimates of the distribution parameters (6). Different types of estimators exist, including moment estimators, least-squares estimators, and maximum likelihood estimators. This practice details the use of maximum likelihood estimators due to the efficiency and the ease of application when censored failure populations are encountered.

5.3 Tensile and flexural specimens are the most commonly used test configurations for advanced ceramics. The observed strength values are dependent on specimen size and geometry. Parameter estimates can be computed for a given specimen geometry ($\hat{m}$, $\hat{\sigma}_\theta$), but it is suggested that the parameter estimates be transformed and reported as material-specific parameters ($\hat{m}$, $\hat{\sigma}_0$). In addition, different flaw distributions (for example, failures due to inclusions or machining damage) may be observed, and each will have its own strength distribution parameters. The procedure for transforming parameter estimates for typical specimen geometries and flaw distributions is outlined in 7.6.

5.4 Many factors affect the estimates of the distribution parameters. The total number of test specimens plays a significant role. Initially, the uncertainty associated with parameter estimates decreases significantly as the number of test specimens increases. However, a point of diminishing returns is reached when the cost of performing additional strength tests may not be justified. This suggests that a practical number of strength tests should be performed to obtain a desired level of confidence associated with a parameter estimate. The number of specimens needed depends on the precision required in the resulting parameter estimate. Details relating to the computation of confidence bounds (directly related to the precision of the estimate) are presented in 8.3 and 8.4.

6. Outlying Observations

6.1 Before computing the parameter estimates, the data should be screened for outlying observations (outliers). An outlying observation is one that deviates significantly from other observations in the sample. It should be understood that an apparent outlying observation may be an extreme manifestation of the variability of the strength of an advanced ceramic. If this is the case, the data point should be retained and treated as any other observation in the failure sample. However, the outlying observation may be the result of a gross deviation from prescribed experimental procedure or an error in calculating or recording the numerical value of the data point in question. When the experimentalist is clearly aware that a gross deviation from the prescribed experimental procedure has occurred, the outlying observation may be discarded, unless the observation can be corrected in a rational manner. The procedures for dealing with outlying observations are detailed in Practice E 178.

7. Maximum Likelihood Parameter Estimators for Competing Flaw Distributions

7.1 This practice outlines the application of parameter estimation methods based on the maximum likelihood technique. This technique has certain advantages, especially when parameters must be determined from censored failure populations. When a sample of test specimens yields two or more distinct flaw distributions, the sample is said to contain censored data, and the associated methods for censored data must be employed. The methods described in this practice include censoring techniques that apply to multiple concurrent flaw distributions. However, the techniques for parameter estimation presented in this practice are not directly applicable to data sets that contain exclusive or compound multiple flaw distributions (7). The parameter estimates obtained using the maximum likelihood technique are unique (for a two-parameter Weibull distribution), and as the size of the sample increases, the estimates statistically approach the true values of the population.

7.2 This practice allows failure to be controlled by multiple flaw distributions. Advanced ceramics typically contain two or more active flaw distributions each with an independent set of parameter estimates. The censoring techniques presented herein require positive confirmation of multiple flaw distributions, which necessitates fractographic examination to characterize the fracture origin in each specimen. Multiple flaw distributions may be further evidenced by deviation from the linearity of the data from a single Weibull distribution (for example, Fig. 1). However, since there are many exceptions, observations of approximately linear behavior should not be considered sufficient reason to conclude that only a single flaw distribution is active.

7.2.1 For data sets with multiple active flaw distributions where one flaw distribution (identified by fractographic analysis) occurs in a small number of specimens, it is sufficient to report the existence of this flaw distribution (and the number of occurrences), but it is not necessary to estimate Weibull parameters. Estimates of the Weibull parameters for this flaw distribution would be potentially

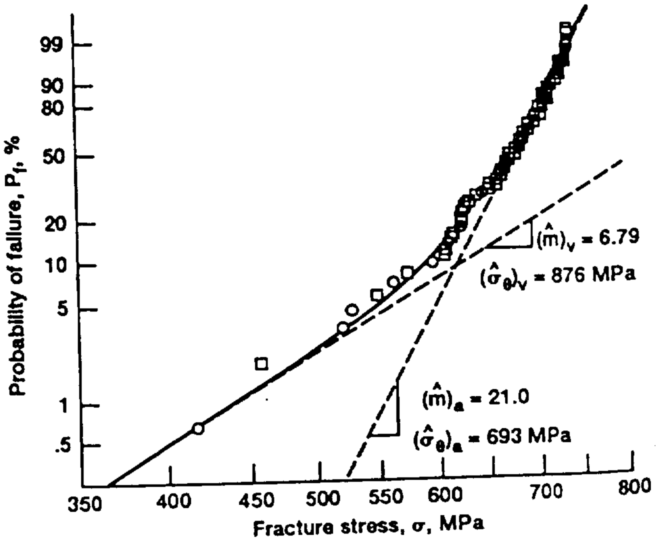

NOTE—The boxes refer to surface flaws; the circles refer to volume flaws.

FIG. 1 Example—Failure Data in Section 10.2

biased with wide confidence bounds (neither of which could be quantified through use of this practice). However, special note should be made in the report if the occurrences of this flaw distribution take place in the upper or lower tail of the sample strength distribution.

7.3 The application of the censoring techniques presented in this practice can be complicated by the presence of test specimens that fail from extraneous flaws, fractures that originate outside the effective gage section, and unidentified fracture origins. If these complications arise, the strength data from these specimens should generally not be discarded. Strength data from specimens with fracture origins outside the effective gage section (**8**), and specimens with fractures that originate from extraneous flaws should be censored; and the maximum likelihood methods presented in this practice are applicable.

7.3.1 Specimens with unidentified fracture origins sometimes occur. It is imperative that the number of unidentified fracture origins, and how they were classified, be stated in the test report. This practice recognizes four options the experimentalist can pursue when unidentified fracture origins are encountered during fractographic examinations. The situation may arise where more than one option will be used within a single data set. Specimens with unidentified fracture origins can be:

7.3.1.1 *Option a*—Assigned a previously identified flaw distribution using inferences based on all available fractographic information,

7.3.1.2 *Option b*—Assigned the same flaw distribution as that of the specimen closest in strength,

7.3.1.3 *Option c*—Assigned a new and as yet unspecified flaw distribution, and

7.3.1.4 *Option d*—Be removed from the sample.

NOTE 1—The user is cautioned that the use of any of the options outlined in 7.3.1 for the classification of specimens with unidentified fracture origins may create a consistent bias error in the parameter estimates. In addition, the magnitude of the bias cannot be determined by the methods presented in 8.2

7.3.2 A discussion of the appropriateness of each option in 7.3.1 is given in Appendix X2. If the strength data and the resulting parameter estimates are used for component design, the engineer must consult with the fractographer before and after performing the fractographic examination. Considerable judgement may be needed to identify the correct option. Whenever partial fractographic information is available, 7.3.1.1 is strongly recommended, especially if the data are used for component design. Conversely, 7.3.1.4 is not recommended by this practice unless there is overwhelming justification.

7.4 The likelihood function for the two-parameter Weibull distribution of a censored sample is defined by the following equation (**9**):

$$\mathcal{L} = \left\{ \prod_{i=1}^{r} \left(\frac{\hat{m}}{\hat{\sigma}_\theta}\right)\left(\frac{\sigma_i}{\hat{\sigma}_\theta}\right)^{\hat{m}-1} \exp\left[-\left(\frac{\sigma_i}{\hat{\sigma}_\theta}\right)^{\hat{m}}\right]\right\} \prod_{j=r+1}^{N} \exp\left[-\left(\frac{\sigma_j}{\hat{\sigma}_\theta}\right)^{\hat{m}}\right] \qquad (12)$$

This expression is applied to a sample where two or more active concurrent flaw distributions have been identified from fractographic inspection. For the purpose of the discussion here, the different distributions will be identified as flaw Types A, B, C, etc. When Eq 12 is used to estimate the parameters associated with the A flaw distribution, then r is the number of specimens where Type A flaws were found at the fracture origin, and i is the associated index in the first summation. The second summation is carried out for all other specimens not failing from type A flaws (that is, Type B flaws, Type C flaws, etc.). Therefore, the sum is carried out from ($j = r + 1$) to N (the total number of specimens) where j is the index in the second summation. Accordingly, σ_i and σ_j are the maximum stress in the ith and jth test specimen at failure. The parameter estimates (the Weibull modulus $\hat{m}$ and the characteristic strength $\hat{\sigma}_\theta$) are determined by taking the partial derivatives of the logarithm of the likelihood function with respect to $\hat{m}$ and $\hat{\sigma}_\theta$ and equating the resulting expressions to zero. Note that $\hat{\sigma}_\theta$ is a function of specimen geometry and the estimate of the Weibull modulus. Expressions that relate $\hat{\sigma}_\theta$ to the Weibull material scale parameter $\hat{\sigma}_0$ for typical specimen geometries are given in 7.6. Finally, the likelihood function for the two-parameter Weibull distribution for a single-flaw population is defined by the following equation:

$$\mathcal{L} = \prod_{i=1}^{N} \left(\frac{\hat{m}}{\hat{\sigma}_\theta}\right)\left(\frac{\sigma_i}{\hat{\sigma}_\theta}\right)^{\hat{m}-1} \exp\left[-\left(\frac{\sigma_i}{\hat{\sigma}_\theta}\right)^{\hat{m}}\right] \qquad (13)$$

where r was taken equal to N in Eq 12.

7.5 The system of equations obtained by maximizing the log likelihood function for a censored sample is given by the following equations (**10**):

$$\frac{\sum_{i=1}^{N} (\sigma_i)^{\hat{m}} \ln(\sigma_i)}{\sum_{i=1}^{N} (\sigma_i)^{\hat{m}}} - \frac{1}{r} \sum_{i=1}^{r} \ln(\sigma_i) - \frac{1}{\hat{m}} = 0 \qquad (14)$$

and

r = N

→ uncensored

$$\hat{\sigma}_\theta = \left[\left(\sum_{i=1}^{N} (\sigma_i)^{\hat{m}}\right)\frac{1}{r}\right]^{1/\hat{m}} \qquad (15)$$

where:

r = number of failed specimens from a particular group of a censored sample.

When a sample does not require censoring, r is replaced by N in Eqs 14 and 15. Equation 14 is solved first for $\hat{m}$. Subsequently $\hat{\sigma}_\theta$ is computed from Eq 15. Obtaining a closed-form solution of Eq 14 for $\hat{m}$ is not possible. This expression must be solved numerically. When there are multiple active flaw populations, Eqs 14 and 15 must be solved for each flaw population. A computer algorithm (entitled MAXL) that calculates the root of Eq 14 is presented as a convenience in Appendix X1.

7.6 The numerical procedure in accordance with 7.5 yields parameter estimates of the Weibull modulus ($\hat{m}$) and the characteristic strength ($\hat{\sigma}_\theta$). Since the characteristic strength also reflects specimen geometry and stress gradients, this standard suggests reporting the estimated Weibull material scale parameter $\hat{\sigma}_0$.

7.6.1 The following equation defines the relationship between the parameters for tensile specimens:

$$(\hat{\sigma}_0)_V = (V)^{1/(\hat{m})_V}(\hat{\sigma}_\theta)_V \qquad (16)$$

where V is the volume of the uniform gage section of the tensile specimen, and the fracture origins are spatially distributed strictly within this volume. The gage section of a tensile specimen is defined herein as the central region of the test specimen with the smallest constant cross-sectional area. However, the experimentalist may include transition regions and the shank regions of the specimen if the volume (or area) integration defined by Eq 10 is analyzed properly. This procedure is discussed in 7.6.3. For tensile specimens in which fracture origins are spatially distributed strictly at the surface of the specimens tested, the following equation applies:

$$(\hat{\sigma}_0)_A = (A)^{1/(\hat{m})_A}(\hat{\sigma}_\theta)_A \tag{17}$$

where A = surface area of the uniform gage section.

7.6.2 For flexural specimen geometries, the relationships become more complex **(11)**. The following relationship is based on the geometry of a flexural specimen found in Fig. 2. For fracture origins spatially distributed strictly within both the volume of a flexural specimen and the outer load span, the following equation applies:

$$(\hat{\sigma}_0)_V = (\hat{\sigma}_\theta)_V \left\{ \frac{V\left[\left(\frac{L_i}{L_o}\right)(\hat{m})_V + 1\right]}{2[(\hat{m})_V + 1]^2} \right\}^{1/(\hat{m})_V} \tag{18}$$

where:

L_i = length of the inner load span,

L_o = length of the outer load span,

V = volume of the gage section defined by the following expression:

$$V = b\,d\,L_o \tag{19}$$

and:

b, d = dimensions identified in Fig. 2.

For fracture origins spatially distributed strictly at the surface of a flexural specimen and within the outer load span, the following equation applies:

$$(\hat{\sigma}_0)_A = (\hat{\sigma}_\theta)_A \left[L_o \left(\frac{d}{(\hat{m})_A + 1} + b \right) \left(\frac{\left(\frac{L_i}{L_o}\right)(\hat{m})_A + 1}{(\hat{m})_A + 1} \right) \right]^{1/(\hat{m})_A} \tag{20}$$

7.6.3 Test specimens other than tensile and flexure specimens may be utilized. Relationships between the estimate of the Weibull characteristic strength and the Weibull material scale parameter for any specimen configuration can be derived by equating the expressions defined by Eqs 8 and 10 with the modifications that follow. Begin by replacing σ (an applied uniaxial tensile stress) in Eq 8 with σ_{max}, which is defined as the maximum tensile stress within the test specimen of interest. Thus:

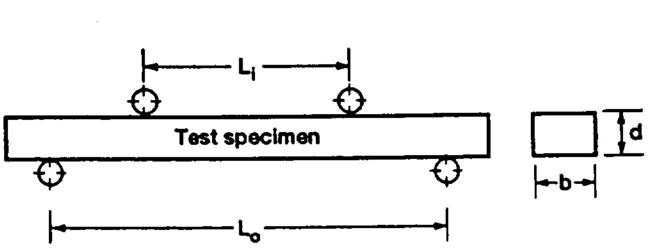

FIG. 2 Flexural Specimen Geometry

$$P_f = 1 - \exp\left[- \left(\frac{\sigma_{max}}{\sigma_\theta} \right)^m \right] \tag{21}$$

Also perform the integration given in Eq 10 such that

$$P_f = 1 - \exp\left[-kV \left(\frac{\sigma_{max}}{\sigma_0} \right)^m \right] \tag{22}$$

where k is a dimensionless constant that accounts for specimen geometry and stress gradients. Note that in general, k is a function of the estimated Weibull modulus $\hat{m}$, and is always less than or equal to unity. The product (kV) is often referred to as the effective volume (with the designation V_E). The effective volume can be interpreted as the size of an equivalent uniaxial tensile specimen that has the same risk of rupture as the test specimen or component. As the term implies, the product represents the volume of material subject to a uniform uniaxial tensile stress **(12)**. Setting Eqs 21 and 22 equal to one another yields the following expression:

$$(\hat{\sigma}_0)_V = (kV)^{1/(\hat{m})_V}(\hat{\sigma}_\theta)_V \tag{23}$$

Thus, for an arbitrary test specimen, the experimentalist evaluates the integral identified in Eq 10 for the effective volume (kV), and utilizes Eq 23 to obtain the estimated Weibull material scale parameter $\hat{\sigma}_0$. A similar procedure can be adopted when fracture origins are spatially distributed at the surface of the test specimen.

7.7 An objective of this practice is the consistent representation of strength data. To this end, the following procedure is the recommended graphical representation of strength data. Begin by ranking the strength data obtained from laboratory testing in ascending order, and assign to each a ranked probability of failure P_f according to the estimator as follows:

$$P_f(\sigma_i) = \frac{i - 0.5}{N} \qquad (24$$

where:

N = number of specimens, and

i = ith datum.

Compute the natural logarithm of the ith failure stress, an the natural logarithm of the natural logarithm of $[1/(1 - P_f)$ (that is, the double logarithm of the quantity in brackets) where P_f is associated with the ith failure stress.

7.8 Create a graph representing the data as shown in Fig 1. Plot $\ln\{\ln[1/(1 - P_f)]\}$ as the ordinate, and $\ln(\sigma)$ as th abscissa. A typical ordinate scale assumes values from +2 t −6. This approximately corresponds to a range in probabilit of failure from 0.25 to 99.9 %. The ordinate axis must b labeled as probability of failure P_f, as depicted in Fig. 1 Similarly, the abscissa must be labeled as failure stres (flexural, tensile, etc.), preferably using units of megapascal or gigapascals.

7.9 Included on the plot should be a line (two or mor lines for concurrent flaw distributions) whose position i fixed by the estimates of the Weibull parameters. The line i defined by the following mathematical equation:

$$P_f = 1 - \exp\left[- \left(\frac{\sigma}{\hat{\sigma}_\theta} \right)^{\hat{m}} \right] \qquad (2$$

The slope of the line, which is the estimate of the Weibu

TEST REPORT

Weibull Parameters Calculated Using Maximum Likelihood Estimators

Material: ________________
Test method: ________________
Specimen size: ________________
Specimens from:
Single billet ☐ ________________
Multiple billets ☐ ________________
Component(s) ☐ ________________
Separately made ☐ ________________
Total number of specimens: ________

FLAW POPULATION 1
Number of specimens: ________
Flaw identity: ________
Spatial dist. ☐ Volume
☐ Surface
☐ ______
Estimates:
$\hat{m}$ = ______
$\hat{\sigma}_\theta$ = ______
$\hat{\sigma}_0$ = ______ (Weibull scale parameter)

Complete the following and report the numbers below if only one flaw population exists:

Correct m for bias (Table 1)
UF = ______ $\hat{m}_u = \hat{m}$ UF = ______

REPORT THESE

90% Confidence bounds:
(Note: Use $\hat{m}$ below, not $\hat{m}_u$.)

m (Table 2)
$q_{0.05}$ = ______ $\hat{m}_{upper} = \hat{m}/q_{0.05}$ = ______
$q_{0.95}$ = ______ $\hat{m}_{lower} = \hat{m}/q_{0.95}$ = ______

σ_θ (Table 3)
$t_{0.05}$ = ______ $\hat{\sigma}_{\theta,upper} = \hat{\sigma}_\theta \exp(-t_{0.05}/\hat{m})$ = ______
$t_{0.95}$ = ______ $\hat{\sigma}_{\theta,lower} = \hat{\sigma}_\theta \exp(-t_{0.95}/\hat{m})$ = ______

FLAW POPULATION 2
Number of specimens: ________
Flaw identity: ________
Spatial dist. ☐ Volume
☐ Surface
☐ ______
Estimates:
$\hat{m}$ = ______
$\hat{\sigma}_\theta$ = ______
$\hat{\sigma}_0$ = ______ (Weibull scale parameter)

FLAW POPULATION 3
Number of specimens: ________
Flaw identity: ________
Spatial dist. ☐ Volume
☐ Surface
☐ ______
Estimates:
$\hat{m}$ = ______
$\hat{\sigma}_\theta$ = ______
$\hat{\sigma}_0$ = ______ (Weibull scale parameter)

How were unidentified specimens treated?
Number of unidentified specimens: ________________

- ☐ Identity estimated by extrapolating fractography
- ☐ Identity assigned arbitrarily to be same as the nearest strength datum
- ☐ Assumed to belong to a distinct population
- ☐ Discarded as random events

FIG. 3 Sample Test Report

modulus $\hat{m}$, should be identified, as shown in Fig. 1. The estimate of the characteristic strength $\hat{\sigma}_\theta$ should also be identified. This corresponds to a P_f of 63.2 %, or a value of zero for $\ln\{\ln[1/1(1 - P_f)]\}$. A test report (that is, a data sheet) that details the type of material characterized, the test procedure (preferably designating an appropriate standard), the number of failed specimens, the flaw type, the maximum likelihood estimates of the Weibull parameters, the unbiasing factor, and the information that allows the construction of 90 % confidence bounds is depicted in Fig. 3. This data sheet should accompany the graph to provide a complete representation of the failure data. Insert a column on the graph (in any convenient location), or alternatively provide a separate table that identifies the individual strength values in ascending order as shown in Fig. 4. This will permit other users to perform alternative analyses (for example, future implementations of bias correction or confidence bounds, or both, on multiple flaw populations). In addition, the experimentalist should include a separate sketch of the specimen geometry that includes all pertinent dimensions. An estimate of mean strength can also be depicted in the graph. The estimate of mean strength $\hat{\mu}$ is calculated by using the arithmetic mean as the estimator in the following equation:

$$\hat{\mu} = \left(\sum_{i=1}^{N} \sigma_i\right)\left(\frac{1}{N}\right) \tag{26}$$

Note that this estimate of the mean strength is not appropriate for samples with multiple failure populations.

8. Unbiasing Factors and Confidence Bounds

8.1 Paragraphs 8.2 through 8.4 outline methods to correct for statistical bias errors in the estimated Weibull parameters and outlines methods to calculate confidence bounds. The procedures described herein to correct for statistical bias errors and to compute confidence bounds are appropriate only for data sets where all failures originate from a single flaw population (that is, an uncensored sample). Procedures for bias correction and confidence bounds in the presence of multiple active flaw populations are not well developed at this time. Note that the statistical bias associated with the estimator $\hat{\sigma}_\theta$ is minimal (<0.3 % for 20 test specimens, as opposed to ≈7 % bias for $\hat{m}$ with the same number of specimens). Therefore, this practice allows the assumption that $\hat{\sigma}_\theta$ is an unbiased estimator of the true population parameter. The parameter estimate of the Weibull modulus ($\hat{m}$) generally exhibits statistical bias. The amount of statistical bias depends on the number of specimens in the sample. An unbiased estimate of m shall be obtained by multiplying $\hat{m}$ by unbiasing factors **(13)**. This procedure is discussed in the following sections. Statistical bias associated with the maximum likelihood estimators presented in this practice can be reduced by increasing the sample size.

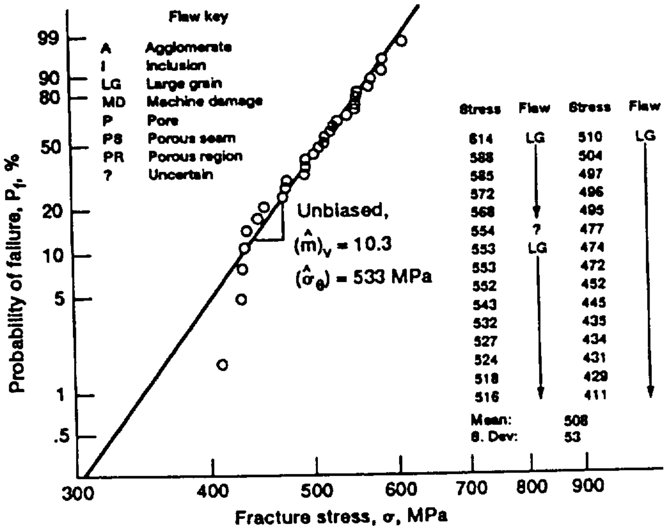

Stress	Flaw	Stress	Flaw
614	LG	510	LG
588		504	
585		497	
572		496	
568		495	
554	?	477	
553	LG	474	
553		472	
552		452	
543		445	
532		435	
527		434	
524		431	
518		429	
516		411	
Mean:		508	
S. Dev:		53	

NOTE—The boxes refer to surface flaws; the circles refer to volume flaws.

FIG. 4 Example—Failure Data with Fractography Information

8.2 An unbiased estimator produces nearly zero statistical bias between the value of the true parameter and the point estimate. The amount of deviation can be quantified either as a percent difference or with unbiasing factors. In keeping with the accepted practice in the open literature, this practice quantifies statistical bias through the use of unbiasing factors, denoted here as *UF*. Depending on the number of specimens in a given sample, the point estimate of the Weibull modulus $\hat{m}$ may exhibit significant statistical bias. An unbiased estimate of the Weibull modulus (denoted as $\hat{m}_U$) is obtained by multiplying the biased estimate with an appropriate unbiasing factor. Unbiasing factors for $\hat{m}$ are listed in Table 1. The example in 11.3 demonstrates the use of Table 1 in correcting a biased estimate of the Weibull modulus. As a final note, this procedure is not appropriate for censored samples. The theoretical approach was developed for uncensored samples where $r = N$.

8.3 Confidence bounds quantify the uncertainty associated with a point estimate of a population parameter. The size of the confidence bounds for maximum likelihood estimates of both Weibull parameters will diminish with increasing sample size. The values used to construct confidence bounds are based on percentile distributions obtained by Monte Carlo simulation. For example, the 90 % confi-

TABLE 1 Unbiasing Factors for the Maximum Likelihood Estimate of the Weibull Modulus

Number of Specimens, *N*	Unbiasing Factor, *UF*	Number of Specimens, *N*	Unbiasing Factor, *UF*
5	0.700	42	0.968
6	0.752	44	0.970
7	0.792	46	0.971
8	0.820	48	0.972
9	0.842	50	0.973
10	0.859	52	0.974
11	0.872	54	0.975
12	0.883	56	0.976
13	0.893	58	0.977
14	0.901	60	0.978
15	0.908	62	0.979
16	0.914	64	0.980
18	0.923	66	0.980
20	0.931	68	0.981
22	0.938	70	0.981
24	0.943	72	0.982
26	0.947	74	0.982
28	0.951	76	0.983
30	0.955	78	0.983
32	0.958	80	0.984
34	0.960	85	0.985
36	0.962	90	0.986
38	0.964	100	0.987
40	0.966	120	0.990

dence bound on the Weibull modulus is obtained from the 5 and 95 percentile distributions of the ratio of $\hat{m}$ to the true population value m. For the point estimate of the Weibull modulus, the normalized values $(\hat{m}/m)$ necessary to construct the 90 % confidence bounds are listed in Table 2. The example in 10.3 demonstrates the use of Table 2 in constructing the upper and lower bounds in $\hat{m}$. Note that the statistical biased estimate of the Weibull modulus must be used here. Again, this procedure is not appropriate for censored statistics.

8.4 Confidence bounds can be constructed for the estimated Weibull characteristic strength. However, the percentile distributions needed to construct the bounds do not involve the same normalized ratios or the same tables as those used for the Weibull modulus. Define the function as follows:

$$t = \hat{m} \ln(\hat{\sigma}_\theta/\sigma_\theta) \tag{27}$$

The 90 % confidence bound on the characteristic strength is obtained from the 5 and 95 percentile distributions of t. For the point estimate of the characteristic strength, these percentile distributions are listed in Table 3. The example in 10.3 demonstrates the use of Table 3 in constructing upper and lower bounds on $\hat{\sigma}_\theta$. Note that the biased estimate of the Weibull modulus must be used here. Again, this procedure is not appropriate for censored statistics. Note that Eq 27 is not applicable for developing confidence bounds on $\hat{\sigma}_0$, therefore the confidence bounds on $\hat{\sigma}_\theta$ should not be converted through the use of Eqs 8 and 10.

9. Fractography

9.1 Fractographic examination of each failed specimen is highly recommended in order to characterize the fracture origins. The strength of advanced ceramics is often limited by discrete fracture origins that may be intrinsic or extrinsic to the material. Porosity, agglomerates, inclusions, and atypical large grains would be considered intrinsic fracture origins. Extrinsic fracture origins are typically on the surface of the specimen and are the result of contact stresses, impact events, or adverse environment. When the means are available to the experimentalist, fractographic methods should be used to locate, identify, and classify the strength limiting fracture origin causing catastrophic failure in an advanced ceramic test specimen. Moreover, for the purpose of parameter estimation, each classification of fracture origin must be identified as a surface fracture origin or a volume fracture origin in order to use the expressions given in 7.6. Thus, there may exist several classifications of fracture origins within the volume (or surface area) of the test specimens in a sample. It should be clearly indicated on the test report (Fig. 3) if a fractographic analysis is not performed. Fractography can be a very subjective analytical method, and the experimentalist is urged to follow the guidelines established in MIL-HDBK-790 concerning fractography.

TABLE 2 Normalized Upper and Lower Bounds on the Maximum Likelihood Estimate of the Weibull Modulus—90 % Confidence Interval

Number of Specimens, N	$q_{0.05}$	$q_{0.95}$	Number of Specimens, N	$q_{0.05}$	$q_{0.95}$
5	0.683	2.779	42	0.842	1.265
6	0.697	2.436	44	0.845	1.256
7	0.709	2.183	46	0.847	1.249
8	0.720	2.015	48	0.850	1.242
9	0.729	1.896	50	0.852	1.235
10	0.738	1.807	52	0.854	1.229
11	0.745	1.738	54	0.857	1.224
12	0.752	1.682	56	0.859	1.218
13	0.759	1.636	58	0.861	1.213
14	0.764	1.597	60	0.863	1.208
15	0.770	1.564	62	0.864	1.204
16	0.775	1.535	64	0.866	1.200
17	0.779	1.510	66	0.868	1.196
18	0.784	1.487	68	0.869	1.192
19	0.788	1.467	70	0.871	1.188
20	0.791	1.449	72	0.872	1.185
22	0.798	1.418	74	0.874	1.182
24	0.805	1.392	76	0.875	1.179
26	0.810	1.370	78	0.876	1.176
28	0.815	1.351	80	0.878	1.173
30	0.820	1.334	85	0.881	1.166
32	0.824	1.319	90	0.883	1.160
34	0.828	1.306	95	0.886	1.155
36	0.832	1.294	100	0.888	1.150
38	0.835	1.283	110	0.893	1.141
40	0.839	1.273	120	0.897	1.133

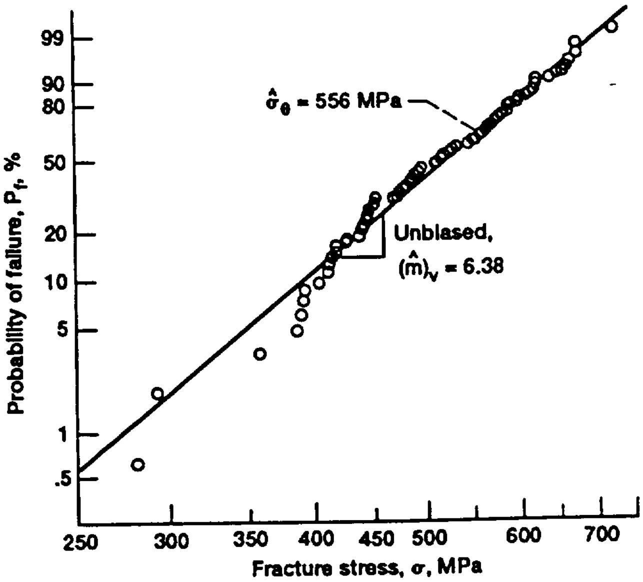

FIG. 5 Example—Failure Data in 10.1

9.2 *Optional*—Perform a fractographic analysis and label each datum with a symbol identifying the type of fracture origin. This can either be a word, an abbreviation, or a different symbol for each type of fracture origin, as depicted in Fig. 4. For example, the abbreviations in LG in Fig. 4 represents failure due to a large grain.

10. Examples

10.1 For the first example, consider the failure data in Table 4. The data represent four-point (¼ point) flexural specimens fabricated from HIP'ed (hot isostatically pressed) silicon carbide (**14**). The solution of Eq 14 requires an iterative numerical scheme. Using the computer algorithm MAXL (see Appendix X1), a parameter estimate of $\hat{m}$ = 6.48 was obtained. (Note that an unbiased value of $\hat{m}$ = 6.38 is shown in Fig. 5; See 10.3 and Eq 31.) Subsequent solution of Eq 15 yields a value of $\hat{\sigma}_\theta$ = 556 MPa. These values for the Weibull parameters were generated by assuming a unimodal failure sample with no censoring (that is, $r = N$). Figure 5 depicts the individual failure data and a curve based on the

TABLE 3 Normalized Upper and Lower Bounds on the Function t—90 % Confidence Interval

Number of Specimens, N	$t_{0.05}$	$t_{0.95}$	Number of Specimens, N	$t_{0.05}$	$t_{0.95}$
5	−1.247	1.107	42	−0.280	0.278
6	−1.007	0.939	44	−0.273	0.271
7	−0.874	0.829	46	−0.266	0.264
8	−0.784	0.751	48	−0.260	0.258
9	−0.717	0.691	50	−0.254	0.253
10	−0.665	0.644	52	−0.249	0.247
11	−0.622	0.605	54	−0.244	0.243
12	−0.587	0.572	56	−0.239	0.238
13	−0.557	0.544	58	−0.234	0.233
14	−0.532	0.520	60	−0.230	0.229
15	−0.509	0.499	62	−0.226	0.225
16	−0.489	0.480	64	−0.222	0.221
17	−0.471	0.463	66	−0.218	0.218
18	−0.455	0.447	68	−0.215	0.214
19	−0.441	0.433	70	−0.211	0.211
20	−0.428	0.421	72	−0.208	0.208
22	−0.404	0.398	74	−0.205	0.205
24	−0.384	0.379	76	−0.202	0.202
26	−0.367	0.362	78	−0.199	0.199
28	−0.352	0.347	80	−0.197	0.197
30	−0.338	0.334	85	−0.190	0.190
32	−0.326	0.323	90	−0.184	0.185
34	−0.315	0.312	95	−0.179	0.179
36	−0.305	0.302	100	−0.174	0.175
38	−0.296	0.293	110	−0.165	0.166
40	−0.288	0.285	120	−0.158	0.159

TABLE 4 Unimodal Failure Stress Data for Hipped (Hot Isostatically Pressed) Silicon Carbide—Example 1

Specimen number, N	Strength, σ_i, MPa	Specimen number, N	Strength, σ_i, MPa
1	281	41	516
2	291	42	520
3	358	43	528
4	385	44	531
5	389	45	531
6	391	46	546
7	392	47	549
8	403	48	553
9	412	49	560
10	413	50	562
11	414	51	563
12	418	52	566
13	418	53	566
14	427	54	570
15	438	55	573
16	440	56	575
17	441	57	576
18	442	58	580
19	444	59	583
20	445	60	588
21	446	61	589
22	452	62	591
23	452	63	591
24	453	64	593
25	470	65	599
26	474	66	600
27	476	67	610
28	476	68	613
29	479	69	620
30	484	70	620
31	485	71	622
32	486	72	622
33	489	73	640
34	492	74	649
35	493	75	657
36	496	76	660
37	506	77	664
38	512	78	674
39	512	79	674
40	514	80	725

estimated values of the parameters. Next, assuming that the failure origins were surface distributed and then inserting the estimated value of $\hat{m}$ and $\hat{\sigma}_\theta$ into Eq 20 along with the specimen geometry (that is, $L_o = 40$ mm, $L_i = 20$ mm, $d = 3.5$ mm, and $b = 4.5$ mm) yields $(\hat{\sigma}_0)_a = 360$ MPa·$(m)^{0.309}$. Note that $(\hat{\sigma}_0)_a$ has units of stress·(area)$^{1/\hat{m}}$; thus, 0.309 = (2./6.48). Alternative, if one were to assume that the failure origins were volume distributed, then the solution of Eq 18 yields $(\hat{\sigma}_0)_v = 37.0$ MPa·$(m)^{0.463}$. Note that $(\hat{\sigma}_0)_v$ has units of stress·(volume)$^{1/\hat{m}}$; thus, 0.463 = (3./6.48). The different values obtained from assuming surface and volume fracture origins underscore the necessity of conducting a fractographic analysis.

10.2 Next, consider a sample that exhibits multiple active flaw distributions (see Table 5). Here each flexural test specimen was subjected to a fractographic analysis. The failure origin was identified as either a volume or a surface fracture origin, and parameter estimates were obtained by using Eqs 14 and 15. For the analysis with volume fracture origins, $r = 13$, and the calculations yielded values of $(\hat{m})_v = 6.79$ and $(\hat{\sigma}_\theta)_v = 876$ MPa. For the analysis with surface fracture origins, $r = 66$, and the calculations yielded values of $(\hat{m})_a = 21.0$ and $(\hat{\sigma}_\theta)_a = 693$ MPa. For the most part, the data as plotted in Fig. 1 fall near the solid curve, which represents the combined probability of failure as follows (15):

$$P_f = 1 - [1 - (P_f)_A][1 - (P_f)_V] \tag{28}$$

where $(P_f)_V$ is calculated by using the following equation:

$$(P_f)_V = 1 - \exp\left[- \left(\frac{\sigma}{(\hat{\sigma}_\theta)_v}\right)^{(\hat{m})_V} \right] \tag{29}$$

and $(P_f)_A$ is calculated by using the following equation:

$$(P_f)_A = 1 - \exp\left[- \left(\frac{\sigma}{(\hat{\sigma}_\theta)_a}\right)^{(\hat{m})_A} \right] \tag{30}$$

The curve obtained from Eq 28 asymptotically approaches the intersecting straight lines that are defined by the estimated parameters and calculated from Eqs 29 and 30. Inserting the estimated Weibull parameters (obtained from the analysis for volume fracture origins) into Eq 18 along with the specimen geometry ($L_o = 40$ mm, $L_i = 20$ mm, $d = 3.5$ mm, and $b = 4.5$ mm) yields $(\hat{\sigma}_0)_v = 65.6$ MPa·$(m)^{0.442}$. Inserting the estimated Weibull parameters (obtained from the analysis for surface fracture origins) into Eq 20 yields $(\hat{\sigma}_0)_a = 446$ MPa·$(m)^{0.95}$.

10.2.1 It must be noted in this example that fractography apparently indicated that all volume failures were initiated from a single distribution of volume flaws, and that all surface failures were initiated from a single distribution of surface flaws. Often, fractography will indicate more complex situations such as two independent distributions of volume flaws (for example, inclusions of foreign material and large voids) in addition to a distribution of surface flaws. Analysis of this type of sample would be very similar to the analysis discussed in 10.1, except that Eqs 14 and 15 would be used three times instead of twice, and the resulting figure would include three straight lines labelled accordingly.

10.3 As an example of computing unbiased estimates of the Weibull modulus, and bounds on both the Weibull

TABLE 5 Bimodal Failure Stress Data—Example 2

Number of Specimens, *N*	Strength, MPa	Fracture Origin type[A]	Number of Specimens, *N*	Strength, MPa	Fracture Origin[A]
1	416	V	41	671	S
2	458	S	42	672	S
3	520	V	43	672	S
4	527	V	44	674	S
5	546	S	45	677	S
6	561	V	46	677	S
7	572	S	47	678	S
8	595	V	48	680	S
9	604	S	49	683	S
10	604	S	50	684	S
11	609	V	51	686	S
12	612	S	52	687	S
13	614	S	53	687	S
14	621	V	54	691	S
15	622	S	55	694	S
16	622	S	56	695	S
17	622	V	57	700	S
18	622	S	58	703	S
19	625	S	59	703	S
20	626	V	60	703	S
21	631	S	61	703	S
22	640	S	62	704	S
23	643	V	63	704	S
24	649	S	64	706	S
25	650	S	65	710	S
26	652	V	66	713	S
27	655	S	67	716	S
28	657	S	68	716	S
29	657	V	69	716	S
30	660	S	70	716	S
31	660	S	71	716	S
32	662	V	72	717	S
33	662	S	73	725	S
34	662	S	74	725	S
35	664	S	75	725	S
36	664	S	76	726	S
37	664	S	77	727	S
38	666	S	78	729	S
39	669	S	79	732	S
40	671	S	...	...	...

[A] Volume fracture origin, *V*; surface flaw origin, *S*

modulus and the Weibull characteristic strength, consider the unimodal failure sample presented in 10.1. The sample contained 80 specimens and the biased estimate of the Weibull modulus was determined to be $\hat{m} = 6.48$. The unbiasing factor corresponding to this sample size is $UF = 0.984$, which is obtained from Table 1. Thus, the unbiased estimate of the Weibull modulus is given as follows:

$$\begin{aligned} \hat{m}_U &= \hat{m} \times UF \\ &= (6.48)(0.984) \\ &= 6.38 \end{aligned} \tag{31}$$

The upper bound on $\hat{m}$ for this example is as follows:

$$\begin{aligned} \hat{m}_{\text{upper}} &= \hat{m}/q_{0.05} \\ &= 6.48/0.878 \\ &= 7.38 \end{aligned} \tag{32}$$

where $q_{0.05}$ is obtained from Table 2 for a sample size of 80 failed specimens. The lower bound is as follows:

$$\begin{aligned} \hat{m}_{\text{lower}} &= \hat{m}/q_{0.95} \\ &= 6.48/1.173 \\ &= 5.52 \end{aligned} \tag{33}$$

where $q_{0.95}$ is obtained from Table 2. Similarly, the upper bound on $\hat{\sigma}_\theta$ is as follows:

$$\begin{aligned} (\hat{\sigma}_\theta)_{\text{upper}} &= \hat{\sigma}_\theta \exp(-t_{0.05}/\hat{m}) \\ &= (556)\exp(0.197/6.48) \\ &= 573 \text{ MPa} \end{aligned} \tag{34}$$

where $t_{0.05}$ is obtained from Table 3 for a sample size of 80 failed specimens. The lower bound on $\hat{\sigma}_\theta$ is as follows:

$$\begin{aligned} (\hat{\sigma}_\theta)_{\text{lower}} &= \hat{\sigma}_\theta \exp(-t_{0.95}/\hat{m}) \\ &= (556)\exp(-0.197/6.48) \\ &= 539 \text{ MPa} \end{aligned} \tag{35}$$

where $t_{0.95}$ is also obtained from Table 3.

11. Keywords

11.1 advanced ceramics; censored data; confidence bounds; fractography; fracture origin; maximum likelihood; strength; unbiasing factors; Weibull characteristic strength; Weibull modulus; Weibull scale parameter; Weibull statistics

APPENDIX

(Nonmandatory Information)

X1. COMPUTER ALGORITHM MAXL

X1.1 Using maximum likelihood estimators to compute estimates of the Weibull parameters requires solving Eqs 14 and 15 for $\hat{m}$ and $\hat{\sigma}_\theta$, respectively. The solution of Eq 15 is straightforward once the estimate of the Weibull modulus $\hat{m}$ is obtained from Eq 14. Obtaining the root of Eq 14 requires an iterative numerical solution. In this appendix, the theoretical approach is presented for the numerical solution of these equations, along with the details of a computer algorithm (optional) that can be used to solve Eqs 14 and 15. A flow chart of the algorithm, which is entitled MAXL, is presented in Fig. X1.1.

X1.2 The MAXL algorithm employs a Newton-Raphson technique **(16)** to find the root of Eq 14. The root of Eq 14 represents a biased estimate of the Weibull modulus. Solution of Eq 15, which depends on the *biased* value of $\hat{m}$, is effectively an *unbiased* estimate of the characteristic strength. The reader is cautioned not to correct $\hat{m}$ for bias prior to computing the characteristic strength. This would yield an incorrect value of $\hat{\sigma}_\theta$. This approach expands Eq 14 in a Taylor series about $\hat{\sigma}_0$;

$$f(\hat{m}) = f(\hat{m}_0) + (\hat{m} - \hat{m}_0)[f'(\hat{m}_0)] + \left[\frac{(\hat{m} - \hat{m}_0)^2}{2}\right] f''(\hat{m}_0) + \ldots \quad \text{(X1.1)}$$

where $f(\hat{m})$ represents the left-hand side of Eq 14, and $\hat{m}_0$ is not a root of $f(\hat{m})$ but is reasonably close. Taking:

$$\Delta\hat{m} = \hat{m} - \hat{m}_0 \quad \text{(X1.2)}$$

and setting Eq X1.1 equal to zero, then:

$$0 = f(\hat{m}_0) + (\Delta\hat{m})[f'(\hat{m}_0)] + \left[\frac{(\Delta\hat{m})^2}{2}\right] f''(\hat{m}_0) + \ldots \quad \text{(X1.3)}$$

If the Taylor series expansion is truncated after the first three terms, the resulting expression is quadratic in $\Delta\hat{m}$. The roots of the quadratic form of Eq X1.3 are as follows:

$$\Delta\hat{m}_{a,b} = -\left[\frac{f'(\hat{m})}{f''(\hat{m})}\right] \pm \left[\left(\frac{f'(\hat{m})}{f''(\hat{m})}\right)^2 - 2\left(\frac{f(\hat{m})}{f''(\hat{m})}\right)\right]^{1/2} \quad \text{(X1.4)}$$

After obtaining $\Delta\hat{m}_{a,b}$ and knowing $\hat{m}_0$, Eq X1.2 is then solved for two values of $\hat{m}$ that represent improved (better than $\hat{m}_0$) estimates of the roots of $f(\hat{m})$, thus

$$\hat{m}_a = \hat{m}_0 + \Delta\hat{m}_a \quad \text{(X1.5)}$$

and

$$\hat{m}_b = \hat{m}_0 + \Delta\hat{m}_b \quad \text{(X1.6)}$$

Eq 14 is evaluated with both values of $\hat{m}$, and the quantity that yields a smaller functional value is accepted as the updated estimate. This updated value of $\hat{m}$ replaces $\hat{m}_0$ in Eq X1.4, and the next iteration is performed. The iterative procedure is terminated when the functional evaluation of Eq 14 becomes less than some predetermined tolerance ϵ.

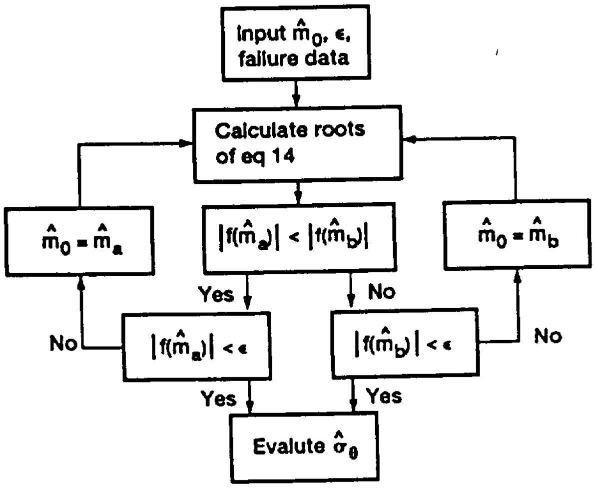

FIG. X1.1 MAXL Flow Chart

X1.3 The following variable name list is provided as a convenience for interpreting the source code of the algorithm MAXL:

DF, DDF—first and second derivatives with respect to $\hat{m}$ of Eq 14.
EPS—predetermined convergence criterion.
F—function defined in Eq 14.
NLIM—maximum numbers of iterations allowed in determining the root of Eq X1.3.
NSUSP—number of suspended (or censored) data ($<NT$).
NT—number of failure stresses.
ST—failure stress; an argument passed to MAXL as input.
STNORM—the largest failure stress; used to normalize all failure stresses to prevent computational overflows.
MO—updated value of $\hat{m}$.
MA, MB—values of the roots $\hat{m}_a$ and $\hat{m}_b$.
WCS—estimated Weibull characteristic strength.
WMT—maximum likelihood estimate of the Weibull modulus.

X1.4 A listing of the FORTRAN source code of the algorithm MAXL is given in Fig. X1.2.

```
C
C    ***************************************************************
C    *                                                             *
C    *                        PROGRAM MAXL                         *
C    *                                                             *
C    *      THIS PROGRAM CALCULATES TWO PARAMETER MAXIMUM          *
C    *      LIKELIHOOD ESTIMATES FROM FAILURE DATA WITH AN         *
C    *      ASSUMED UNDERLYING WEIBULL DISTRIBUTION.  THE          *
C    *      ALGORITHM USES A NONLINEAR NEWTON-RAPHSON METHOD,      *
C    *      AND ACCOMODATES CENSORED DATA.                         *
C    *                                                             *
C    *      REFERENCES:  "ADVANCED CALCULUS FOR APPLICATIONS"      *
C    *                    by HILDEBRAND                            *
C    *                    PRENTICE-HALL, INC.; 1962                *
C    *                                                             *
C    *                   "APPLIED LIFE DATA ANALYSIS"              *
C    *                    by NELSON                                *
C    *                    WILEY & SONS INC.; 1982                  *
C    *                                                             *
C    ***************************************************************
C
      IMPLICIT REAL *8(A-H,O-Z)
      DOUBLE PRECISION ST(1000),ST1(1000)
      DOUBLE PRECISION MO, MA, MB, M1
      COMMON /DATA/ NFAIL, SUM1, NT, ST, ZERO, ONE
      ZERO = 0.D0
      ONE = 1.D0
      TWO = 2.D0
      EPS = 5.0D-10
      NLIM = 500
      MO = 10.08651279857
C
C   --- READ THE FAILURE DATA USING FREE FORMATS;
C         FILE CONTAINING FAILURE DATA IS ALLOCATED TO UNIT 8
C
      DO 10 I = 1,1000
        ST(I) = ZERO
        ST1(I) = ZERO
   10 CONTINUE
      STNORM = ZERO
      READ(8,*) NT
      READ(8,*) NSUSP
      NFAIL = NT - NSUSP
      DO 20 I = 1,NT
        READ(8,*) ST(I)
        STNORM = DMAX1(STNORM,ST(I))
   20 CONTINUE
C
C   --- NORMALIZE FAILURE DATA WITH LARGEST VALUE
C
      DO 30 I = 1,NT
        ST(I) = ST(I)/STNORM
   30 CONTINUE
C
      SUM1 = ZERO
      DO 40 I = 1,NFAIL
        READ(8,*) ST1(I)
        ST1(I) = ST1(I)/STNORM
C         DUFF = DLOG(ST1(I))
        SUM1 = SUM1 + DLOG(ST1(I))
```

FIG. X1.2 FORTRAN Source Code of the Algorithm MAXL

```
   40  CONTINUE
C
C   --- THE FUNCTION F IS DEFINED BY EQ 14 OF ASTM STANDARD XXX
C
C   --- EVALUATE F(MO) AND THE ASSOCIATED SUMS WHICH ARE USED TO CALCULATE
C         THE DERIVATIVES OF F WITH RESPECT TO M
C
      CALL SUM (MO, SUM2, SUM3, F)
C
CCCCCCCCCCCCCCCCCCCCCCCCCCCCCCCCCCCCCCCCCCCCCCCCCCCCCCCCCCCCCCCCCCCCCCCCC
C   ********************************************************************
C   *                      NEWTON-RAPHSON ROOT SOLVER                  *
C   ********************************************************************
C
C   --- USE TAYLOR SERIES SERIES EXPANSION (INCLUDING SECOND DERIVATIVES)
C       FOUND ON PAGE 362 OF "ADVANCED CALCULUS FOR APPLICATIONS BY
C       HILDEBRAND (FIRST EDITION, FIFTH PRINTING) TO DETERMINE THE ROOTS
C       OF THE FOLLOWING EQUATION, WHICH IS QUADRATIC IN DELTA M.
C
C         F(MO+DELTA M) = 0
C                       = F(MO) + DELTA M * F'(MO)
C                           + (DELTA M)**2 * F''(MO)/2
C
C       HERE MO IS THE CURRENT ESTIMATE OF M.
C       THE FORMULA YIELDS TWO ROOTS, DELTA MA AND DELTA MB.
C       MA AND MB ARE THE UPDATED VALUES OF M, WHERE
C
C                 M(A,B) = MO + DELTA M(A,B)
C
C       F(MA) AND F(MB) ARE BOTH EVALUATED.  THE ESTIMATE THAT PRODUCES THE
C       SMALLEST ABSOLUTE VALUE OF F IS CHOSEN FOR THE NEXT ITERATION.
C
C       IF THE QUADRATIC EQUATION DOES NOT HAVE REAL ROOTS, AN
C       APPROXIMATE SOLUTION FOUND ON PAGE 363 OF HILDEBRAND IS USED, I.E.,
C
C            DELTA M = - (F(MO)/F'(MO)) *
C                        (1 + (DELTA M **2) * (F''(MO)/2*F(MO)))
C
C        WHERE ON THE RIGHT-HAND-SIDE OF THE EQN, DELTA M IS TAKEN AS THE
C        FIRST ORDER APPROXIMATION, DELTA M = -F(MO)/F'(MO)
C
CCCCCCCCCCCCCCCCCCCCCCCCCCCCCCCCCCCCCCCCCCCCCCCCCCCCCCCCCCCCCCCCCCCCCCCCC
C
       DO 60 K = 1,NLIM
C
C   --- CALCULATE THE FIRST AND SECOND DERIVATIVES OF THE FUNCTION F
C
        DSUM3 = ZERO
        DDSUM3 = ZERO
        DO 50 I = 1,NT
          DSUM3 = DSUM3+DLOG(ST(I))*(ST(I))**MO*DLOG(ST(I))
          DDSUM3 = DDSUM3 + (DLOG(ST(I)))**3*(ST(I))**MO
   50   CONTINUE
        DSUM2 = SUM3
        DDSUM2 = DSUM3
        DF = (SUM2 * DSUM3 - SUM3 * DSUM2)/(SUM2**2) + ONE/(MO**2)
C
        DDF = ((SUM2 * DDSUM3 - SUM3 * DDSUM2)/SUM2**2)
     $ - (TWO * DSUM2 * (SUM2 * DSUM3 - SUM3 * DSUM2)/SUM2**3)
     $ - TWO/MO**3
```

FIG. X1.2 Continued

```
       RADICAL = (DF/DDF)**2 - TWO*F/DDF
       IF (RADICAL .GE. ZERO) THEN
C
C   --- CALCULATE THE ROOTS OF THE QUADRATIC EQUATION
C
         RADICAL = DSQRT(RADICAL)
         MA = MO - (DF/DDF) + RADICAL
         MB = MO - (DF/DDF) - RADICAL
C
C    --- CALCULATE F(MA), F(MB), AND THE ASSOCIATED SUMS
C
         CALL SUM (MA, SUM2A, SUM3A, FA)
         CALL SUM (MB, SUM2B, SUM3B, FB)
C
C    --- SELECT THE BETTER ROOT BY COMPARING THE ABSOLUTE
C          VALUE OF THE FUNCTION F
C
         IF (DABS(FA) .LE. DABS(FB)) THEN
           MO = MA
           F = FA
           SUM2 = SUM2A
           SUM3 = SUM3A
         ELSE
           MO = MB
           F = FB
           SUM2 = SUM2B
           SUM3 = SUM3B
         END IF
       ELSE
C
C    --- IF THE ROOTS ARE COMPLEX, USE THE APPROXIMATE SOLUTION
C
         M1 = MO - (F/DF)*(ONE+F*DDF/(TWO*DF**2))
C
C    --- CALCULATE F(M1) AND ITS ASSOCIATED SUMS
C
         CALL SUM (M1, SUM2, SUM3, F)
         MO = M1
       END IF
C
C    --- CONVERGENCE CRITERION:
C          COMPARE THE ABSOLUTE VALUE OF THE FUNCTION F
C          WITH A PRESELECTED TOLERANCE
C
       IF (DABS(F) .LE. EPS) GO TO 70
   60 CONTINUE
C
C    --- MAXIMUM NO. OF ITERATIONS REACHED BEFORE SATISFACTORY VALUE OF M FOUND
C
      WRITE(6,100) NLIM
      GO TO 999
C
C    --- SATISFACTORY ESTIMATE OF WEIBULL MODULUS ATTAINED
C
   70 WMT = MO
C
C    --- COMPUTE THE ESTIMATE OF THE WEIBULL CHARACTERISTIC STRENGTH (WCS)
C
      RWMT = 1.0/WMT
```

FIG. X1.2 Continued

```
      WCS = ((SUM2/NFAIL)**RWMT)*STNORM
      WRITE(6,110) WMT
      WRITE(6,120) WCS
100   FORMAT(/,2X,'NO SOLUTION FOUND AFTER ',I4,' ITERATIONS OF THE
     $NEWTON-RAPHSON METHOD',/).
110   FORMAT(/,2X,' THE ESTIMATED WEIBULL MODULUS = ',F8.3,/)
120   FORMAT(/,2X,' THE ESTIMATED CHARACTERISTIC STRENGTH = ',F8.3,/)
999   CONTINUE
      STOP
      END

      SUBROUTINE SUM (M, SUM2, SUM3, F)
      IMPLICIT REAL*8 (A-H, O-Z)
      DOUBLE PRECISION ST(1000), M
      COMMON /DATA/ NFAIL, SUM1, NT, ST, ZERO, ONE
      SUM2 = ZERO
      SUM3 = ZERO
      DO 10 I = 1,NT
        SUM2 = SUM2 + ((ST(I))**M)
        SUM3 = SUM3 + (DLOG(ST(I)) * ((ST(I))**M))
10    CONTINUE
      F = (SUM3/SUM2) - (SUM1/NFAIL) - (ONE/M)
      RETURN
      END
```

FIG. X1.2 Continued

X2. TEST SPECIMENS WITH UNIDENTIFIED FRACTURE ORIGINS

X2.1 Paragraphs 7.3.1.1 to 7.3.1.4 describe four options, (a) through (d), the experimentalist can utilize when unidentified fracture origins are encountered during fractographic examination. The following four subsections further define the four options, and use examples to illustrate appropriate and inappropriate situations for their use.

X2.1.1 Option (a) involves using all available fractographic information to subjectively assign a specimen with an unidentified origin to a previously identified fracture origin classification. Many specimens with unidentified fracture origins have some fractographic information that was judged to be insufficient for positive identification and classification. (It should be noted that the degree of certainty required for "positive identification" of a fracture-initiating flaw varies from one fractographer to another.) In such cases, Option (a) allows the experimentalist the use of the incomplete fractographic information to assign the unidentified fracture origin to a previously identified flaw classification. This option is preferred when partial fractographic information is available. As an example, consider a tensile specimen where fractography was inconclusive. Fractographic markings may have indicated that the origin was located at or very near the specimen surface, but the fracture-initiating flaw could not be positively identified. Other specimens from the sample were positively identified as failing from machining flaws. It is recognized that machining damage is often difficult to discern. Therefore, in this case it would be appropriate to use Option (a) and infer that the origin is machining damage. The test report (see 7.9 and Fig. 3) must clearly indicate each specimen and where this (or any other) option is used for classifying unidentified specimens. The conclusion of machining damage in this example, however, could be erroneous. For instance, the fracture-initiating flaw may have been a "mainstream microstructural feature"[8] (17) (which is also typically difficult to resolve and identify) that happen to be located near the specimen surface. The possibility of erroneous classification such as this are unavoidable in the absence of positive identification of fracture origins.

X2.1.2 Option (b) involves assigning the unidentified fracture origin to the fracture origin classification of the test specimen closest in strength. The specimen closest in strength must have a positively identified fracture origin (not one assigned using Options (a) through (d)). As an example of use of this option, consider a tensile specimen that shattered upon failure such that the fracture origin was damaged and lost, but fracture was clearly initiated from an internal flaw. Other specimens from the sample included positive identification of inclusions and large pores as two active volume-distribution fracture origin classifications. When the fracture strengths from the total data set were ordered, the specimen closest in strength to the specimen with the unidentified fracture origin was the specimen that failed from an inclusion. Use of Option (b) for this test specimen would then allow the unidentified origin to be classified as an inclusion. Justification for Option (b) arises from the tendency of concurrent (competing) flaw distributions to group together specimens with the same origin classification when the test specimens are listed in order of fracture strength. Therefore, the most likely fracture origin classification of a random unidentified specimen is the classification of the specimen closest in strength. The above example can be modified slightly to illustrate a situation where Option (b) would be inappropriate. If the fracture origin classification of the specimen closest in strength was a machining flaw, then Option (b) would lead to a conclusion inconsistent with the fractographic observation that failure occurred from an internal flaw. Fractographic evidence should always supersede conclusions from Option (b).

X2.1.3 Option (c) assumes that the unidentified fracture origins belong to a new, unclassified flaw type and treats these fracture origins as a separate flaw distribution in the censored data analysis. This may occur when the fractographer cannot recognize the flaw type because features of the flaw are particularly subtle and difficult to resolve. In such cases, the fractographer may consistently fail to locate

---

[8] "Mainstream microstructural features" or "ordinary microstructural features" are fracture origins that occur at features such as very large grains that are part of the ordinary distribution of the microstructure, albeit at the large end of the distribution of such features. These are distinguished from abnormal microstructural features such as inclusions or grossly large pores.

and classify the fracture origin. Examples of flaw types that are difficult to identify include: machining damage, zones of atypically high microporosity, and mainstream microstructural features. Option (c) may be appropriate if a set of specimens with unidentified fracture origins have similar and apparently related features. Unfortunately, there are many situations where Option (c) is incorrect and where use of this option could result in substantial errors in parameter estimates. For instance, consider the case where several unidentified specimens are concentrated in the upper tail (high strength) of the strength distribution. These fracture origins may belong to a classification that has been previously identified, but the smaller flaws at the origins were harder to locate, or possibly the origins were lost due to the greater fragmentation associated with high-strength specimens. Use of Option (c) to treat these high-strength specimens as a new flaw classification would create a bias error of unknown magnitude in the parameter estimates of the proper flaw classification.

X2.1.4 Option (d) involves the removal of test specimens with unidentified fracture origins from the sample (that is, the strengths are removed from the list of observed strengths). This option is rarely appropriate, and is not recommended by this practice unless there is clear justification. Option (d) is only valid when test specimens with unidentified fracture origins are randomly distributed through the full range of strengths and flaw classifications. There are few plausible physical processes that create such a random selection. An example where Option (d) is justified is a data set of 50 specimens where the first 10 fractured specimens (in order of testing) were misplaced or destroyed after testing but prior to fractography. The unidentified specimens were therefore created by a process that is random. That is, the 10 strengths are expected to be randomly distributed through the strength distribution of the remaining 40, and the 10 origin classifications are expected to be randomly distributed through the origin types of the remaining 40. (In this example, Option (b) could also be considered.) Option (d) is not appropriate where unidentified fracture origins are a consequence of high-strength test specimens shattering virulently such that the fragment with the origin is lost. This situation occurs with more frequency in the upper tail (high strength) of the strength distribution, and thus the unidentified fracture origins would not occur at random strengths.

X2.2 Paragraphs X2.2.1 to X2.2.6 expand on the proper use and implementation of the four options described in X2.1.

X2.2.1 When partial fractographic information is available, Option (a) is preferred and should be used to incorporate the information as completely as possible into the assignment of fracture origin classification. Option (d) should be used only in unusual situations where a random process for creation of unidentified origins can be justified.

X2.2.2 Situations may arise where more than one option will be used within a single data set. For instance, of five specimens with unidentified origins, three might be classified based on partial fractographic information using Option (a), while the remaining two, which have no fractographic hints, might then be classified using Option (b).

X2.2.3 When specimens with unidentified fracture origins are contained within a data set, the test report (see 7.9) must include a full description of which specimens were unidentified, and which option or options were used to classify the specimens.

X2.2.4 If the unidentified fracture origins occur frequently in the lower tail of the strength distribution, then caution and extra attention is warranted. Strength analyses are typically extrapolated to lower strengths and lower probabilities of failure than those observed in the data set. Proper statistical evaluation and assignment of fracture origin classifications near the lower-strength tail is therefore particularly important because the low-strength distribution typically dominates extrapolations of this type.

X2.2.5 When only a few fracture origins are unidentified, effects of incorrect classification are minimal. When more than 5 or 10 % of the origins are unidentified, substantial statistical bias in estimates of parameters can result. When used for design applications, proper choice of options from X2.1 is critical and should be carefully justified in the test report. In such design applications, it may be prudent to carry out the analysis for more than one option to determine the sensitivity to choice of an improper option. For instance, in a group of 50 specimens with 10 unidentified origins (no partial fractographic information), the analysis could be conducted first using Option (b) then again using Option (c). The results from the two analyses could then be used individually to estimate the behavior of the designed component. If a conservative prediction of component behavior is warranted, the more conservative result of the two analyses should be used.

X2.2.6 Finally, if most or all of the test specimens within a sample contain unidentified fracture origins, then censored data analysis according to this practice is not possible. The strengths should be plotted on Weibull probability axes and, if the data reveal a pronounced bend (concave upwards) which is characteristic of two or more concurrent flaw distributions, then the methods described in this practice cannot be used without further refinements.

REFERENCES

(1) Nelson, W., *Applied Life Data Analysis*, John Wiley & Sons, New York, NY, 1982, pp. 7–9.

(2) Mann, N. R., Schafer, R. E., and Singpurwalla, N.D., *Methods for Statistical Analysis of Reliability and Life Data*, John Wiley & Sons, New York, NY, 1974.

(3) Kalbfleisch, J. D., and Prentice, R. L., *The Statistical Analysis of Failure Time Data*, John Wiley & Sons, New York, NY, 1980.

(4) Lawless, J. F., *Statistical Models and Methods for Lifetime Data*, John Wiley & Sons, New York, NY, 1982.

(5) Nelson, W., *Applied Life Data Analysis*, John Wiley & Sons, New York, NY, 1982.

(6) Mann, N. R., Schafer, R. E., and Singpurwalla, N. D., *Methods for Statistical Analysis of Reliability and Life Data*, John Wiley & Sons, New York, NY, 1974.

(7) Johnson, C. A., "Fracture Statistics of Multiple Flaw Distributions," *Fracture Mechanics of Ceramics*, Vol 5, 1983, pp. 365–386.

(8) Jenkins, M. G., Ferber, M. K., Martin, R. L., Jenkins, V. T., and Tennery, V. J., "Study and Analysis of the Stress State in a Ceramic, Button-Head, Tensile Specimen," ORNL TM-11767, Oak Ridge National Laboratory, 1991.

(9) Nelson, W., *Applied Life Data Analysis*, John Wiley & Sons, New York, NY, 1982, p. 340.

(10) Nelson, W., *Applied Life Data Analysis*, John Wiley & Sons, New York, NY, 1982, p. 341.

(11) Weil, N. A., and Daniel, I. M., "Analysis of Fracture Probabilities in Nonuniformly Stressed Brittle Materials," *Journal of the American Ceramic Society*, Vol 47, No. 6, June 1964, pp. 268–274.

(12) Johnson, C. A., and Tucker, W. T., "Advanced Statistical Concepts of Fracture in Brittle Materials," *Ceramics and Glasses, Engineered Materials Handbook*, Vol 4, 1991, pp. 709–715.

(13) Thoman, D. R., Bain, L. J., and Antle, C. E., "Inferences on the Parameters of the Weibull Distribution," *Technometrics*, Vol 11, No. 3, August 1969, pp. 445–460.

(14) Nemeth, N. N., Manderscheid, J. M., and Gyekenyesi, J. P., "Ceramic Analysis and Reliability Evaluation of Structures (CARES) Users and Programmers Manual," NASA TP-2916, National Aeronautics and Space Administration, 1990.

(15) Johnson, C. A., "Fracture Statistics of Multiple Flaw Distributions," *Fracture Mechanics of Ceramics*, Vol 5, 1983, pp. 365–386.

(16) Hildebrand, F. B., *Advanced Calculus for Applications*, Prentice-Hall, Inc., Englewood Cliffs, NJ, 1962.

(17) Rice, R. W., "Failure in Ceramics: Challenges to NDE and Processing," *Ceramic Developments*, Vols 34–36, C. C. Sorrell and B. Ben-Nissan, Eds., pp. 1057–1064.

Pergamon

Composites Engineering, Vol. 4, No. 8, pp. 787-810, 1994
Elsevier Science Ltd
Printed in Great Britain

0961-9526(94) E00031-X

COMPOSITES RESEARCH AT NASA LEWIS RESEARCH CENTER

Stanley R. Levine, Stephen Duffy,[†] Alex Vary, Michael V. Nathal,
Robert V. Miner, Steven M. Arnold, Michael G. Castelli, Dale A. Hopkins
and Michael A. Meador
National Aeronautics and Space Administration, Lewis Research Center, Cleveland, OH 44135, U.S.A.

(*Received* 25 *March* 1994; *final version accepted* 29 *April* 1994)

Abstract—Composites research at NASA Lewis is focused on their applications in aircraft propulsion, space propulsion and space power, with the first being predominant. Research on polymer-, metal- and ceramic-matrix composites is being carried out from an integrated materials and structures viewpoint. This paper outlines some of the topics being pursued from the standpoint of key technical issues, current status and future directions.

1. INTRODUCTION

Advanced composites are a key to the development of the next generation of civil transport aircraft engines. The driving forces for the development of advanced engines are mission-enabling capabilities and reduced life-cycle costs. An example of a mission-enabling capability is an advanced environmentally friendly engine for a 300 passenger supersonic civil transport intended for entry into service in about 2005. Requirements for this engine include NO_x emissions less than 5 gm kg^{-1} of fuel burned, noise emissions in compliance with FAR 36 Stage III, and low engine weight and acceptable engine performance to make such an aircraft economically attractive to the customer (Stephens *et al.*, 1993). Composites, and other advanced materials, will play a key role in meeting these goals as well as providing us with more economical and efficient subsonic air transportation. An example of potential composites applications in a highly advanced high-bypass ratio turbofan for a subsonic transport is shown in Fig. 1 (Stephens, 1990).

High-temperature composites research at NASA Lewis Research Center is primarily focused on aircraft engines. The effort includes both materials and structures research addressing the materials classes illustrated in Fig. 1, i.e. polymer-matrix composites, metal- and intermetallic-matrix composites, and ceramic-matrix composites. Of necessity, our concerns include constituent development and property characterization; composite fabrication and process modeling; nondestructive evaluation; constituent and composite property models and design codes; and prediction and measurement of performance and life under actual or simulated engine conditions. The purpose of the paper is to provide the reader with an overview of many, but not all, of our composites research efforts. In the brief sections which follow, we will address each area in terms of its key technical issues, current status and future directions.

2. POLYMER MATRIX COMPOSITES[‡]

The use of PMCs in aircraft engines can result in significant weight savings and lead to improved fuel economy, increased payload or increased flight distances. However, the poor thermal and thermal oxidative stability of these materials limits their use to the cooler sections of the engine. Considerable advances have been made over the years to improve the stability of PMCs so that current materials can tolerate extended use at temperatures up to 650°F. While PMCs are the most mature of all composite materials,

---

[†] Cleveland State University.

[‡] Contributed by Michael A. Meador.

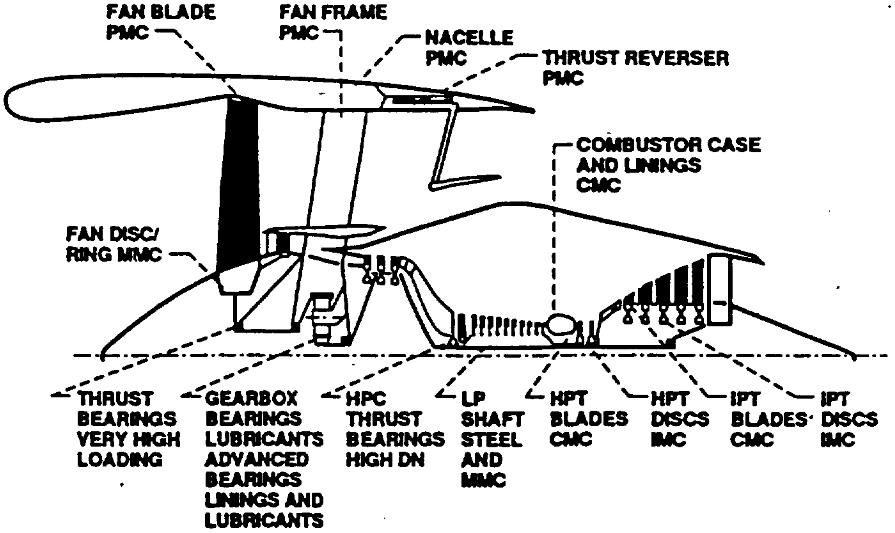

PMC, MMC, IMC, AND CMC = POLYMER, METAL, INTERMETALLIC, AND CERAMIC MATRIX COMPOSITES, RESPECTIVELY. HPC = HIGH PRESSURE COMPRESSOR, LP = LOW PRESSURE, HPT = HIGH PRESSURE TURBINE, IPT = INTERMEDIATE PRESSURE TURBINE.

Fig. 1. Advanced materials applications for an ultra-high-bypass engine (Stephens, 1990).

a number of challenges need to be conquered before they can be fully utilized in both commercial and military aircraft engines. Among these are long-term durability, processability, affordability and repairability.

Over the past two decades, research at the NASA Lewis Research Center has primarily dealt with improving the stability and processability of high-temperature PMCs (Meador *et al.*, 1990). Processability and stability are often mutually exclusive properties for PMCs. Improved thermal oxidative stability in polymers is commonly achieved through the use of stable aromatic groups, e.g. benzene rings. These aromatic groups are rigid, highly planar structures and often render the polymers from which they are made difficult to melt and intractable.

A balance between processability and stability can be achieved by the use of the PMR approach developed at NASA Lewis in the early 1970s (Fig. 2). Molecular weight, and, hence, melt flow and processability, is controlled through the use of a latent reactive endcap (or chain terminating group). At high temperature, this endcap undergoes a cross-linking reaction to provide a material with good stability, high glass transition

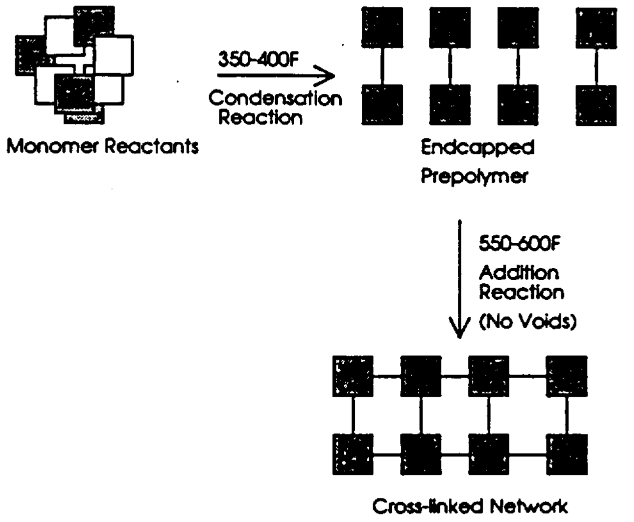

Fig. 2. Reaction scheme for addition polyimides.

temperature, and good mechanical properties (both at room temperature and elevated temperatures). The first polymer developed using this approach was PMR-15 (Serafini *et al.*, 1972), a high-temperature polyimide capable of extended use at temperatures below 500°F.

A variety of high-temperature polyimides have been prepared via this approach (Meador *et al.*, 1991) in an attempt to develop new materials with better stability than PMR-15. Second-generation PMR polyimides, PMR-II, were developed by substituting more thermal-oxidatively stable monomers into the polyimide backbone; this resulted in a 50°F increase in the upper-use temperature (Serafini *et al.*, 1976). Further modifications produced high-molecular-weight versions of PMR-II which showed potential for use at temperatures up to 600°F (Vannucci, 1987).

Recently, efforts have been directed at improving the thermal oxidative stability of PMR-II polyimides via endcap substitution. This has led to the development of styrene-endcapped polyimides, V-CAPs (Vannucci *et al.*, 1990) and paracyclophane-capped polyimides, CyCAPs (Waters *et al.*, 1991). Both systems have better processability than high-molecular-weight versions of PMR-II and can be used at temperatures as high as 650°F.

While these modifications of PMR-15 have resulted in new polyimides with better thermal-oxidative stability, this has been achieved with some sacrifice in processability. This is primarily due to the fact that these formulations have molecular weights 3–5 times that of PMR-15. This results in polyimides with melt viscosities nearly three orders of magnitude higher than PMR-15! Recent efforts have focused on reducing melt viscosities via (1) monomer substitution and (2) reduced cross-link density.

The melt viscosities of polyimides and other polymers can be reduced and their melting points lowered by altering their molecular structure to inhibit crystal packing and other intermolecular interactions in the solid. Since the chemical structures of most polyimides are fairly linear, crystal packing in these systems can be disrupted by using monomers with twists, kinks or other flexible linkages. Considerable reductions in the melt viscosities of PMR-II and V-CAP polyimides can be achieved through the use of a 2,2′-trifluorobenzidine, a diamine with a twisted or noncoplanar geometry (Chuang

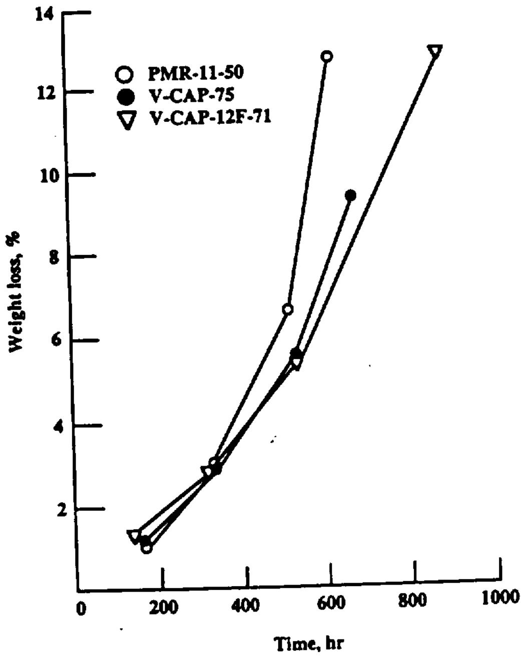

Fig. 3. A comparison of the thermo-oxidative weight losses of G-40-600 reinforced composites prepared with PMR-II-50, V-CAP-75, and a 2,2-bistrifluoromethylbenzidine substituted V-CAP (V-CAP-12F-71) after aging in 1 atm air at 371°C (700°F).

et al., 1992). Polyimides prepared with this diamine have better thermal-oxidative stability than both PMR-II and V-CAP resins (Fig. 3). Another twisted biphenyldiamine has been used to prepare thermoplastic polyimides which have the potential for use in high-temperature synthetic fibers (Chuang *et al.*, 1994). Reduced melt viscosities have also been achieved through the use of a series of flexible multi-ring diamines (Delvigs *et al.*, 1994). However, due to the presence of oxidizable methylene groups, polyimides made with these diamines have stabilities comparable to that of PMR-15.

Reduced cross-link density in addition-cured polyimides can also improve processability; however, this may result in decreased glass transition temperatures and poorer thermal-oxidative stability (Vannucci *et al.*, 1992).

Recent concern over the use of mutagenic diamines, such as methylenedianiline (U.S. Department of Health and Human Services, 1986), has spurred a considerable amount of activity aimed at protecting workers and the environment from potential health risks posed by the use of toxic or carcinogenic diamines. This has led to the search for diamines which do not pose a health risk to materials suppliers and fabricators. A variety of diamines have been examined as replacements for MDA in PMR-15. However, many of these do not provide polyimides with acceptable mechanical properties and thermal-oxidative stability. Polyimides prepared with a mixture of some of these diamines show some promise as MDA replacements (Vannucci and Chriszt, 1993).

The overall performance and durability of PMCs is strongly influenced by the strength of the resin–fiber interface (Bowles, 1990). A variety of graphite fibers are commercially available today. The method of preparation and the surface treatment of each of these fibers is different and information on these processes is usually proprietary. A recent study on a composites prepared with a series of commercially available graphite fibers shows that the nature and strength of the resin–fiber interface is strongly influenced by dipolar interactions occurring between the resin and fiber surface (Serrano *et al.*, 1994) (Fig. 4). These dipolar interactions occur between polar functional groups (hydroxyl, carbonyl and carboxylic acid) present on the fiber surface and the polyimide chain. A strong correlation was found between the polar energy of the fiber surface (measured by both fiber wetting and XPS) and the interlaminar shear strength of PMR-15 composites reinforced with that fiber. A similar correlation was found between composite weight loss and fiber surface polar energy. More work is needed to better characterize these dipolar interactions in order to tailor the fiber surface to improve the strength of the resin–fiber interface.

Oxidation-resistant coatings can also improve the thermal oxidative stability of PMCs. A variety of ceramic coatings have been applied to PMR-15 and PMR-II composites via plasma-assisted chemical-vapor deposition. Silica coatings up to 3500 Å thickness applied to a PMR-15 composite substrate reduced weight losses after 300 h aging in air at 390°C from 20% to nearly 5% (Miller and Gulino, 1994). A five-fold reduction in the weight loss of a PMR-II-50 composite after 300 h at 371°C was achieved with the use of a silicon nitride coating (Harding and Sutter, 1993). This coating survived 1000 thermal cycles from 25 to 371°C without any signs of cracking (Fig. 5). While all of these coatings adhere well to resin-rich surfaces, they do not adhere well to the machined surfaces of composites. Since engine components have bolt holes and machined surfaces, this problem must be solved before oxidation-resistant coatings can be used on PMCs in these applications.

Research in the Polymers Branch at the NASA Lewis Research Center has attempted to overcome some of the technical challenges that prevent the effective utilization of PMCs in aircraft engines. The long-term durability and stability of PMCs can be improved through the use of more stable resin systems, through better understanding and control of the resin–fiber interface, and through the use of oxidation-resistant coatings. Processability in high-temperature polymers can be enhanced by controlling and modifying the polymer's molecular structure. However, further work is needed to develop materials and processes which decrease the manufacturing costs and improve the reliability of high-temperature PMC components. These areas are currently under investigation.

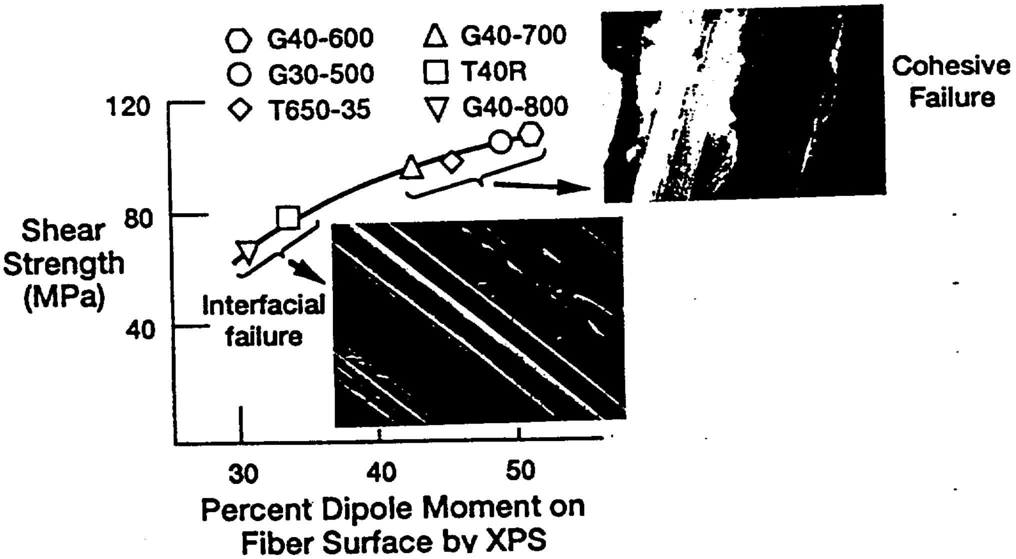

Fig. 4. The effects of fiber surface polarity (per cent dipole moment) on the interlaminar shear strength of PRM-15 composites reinforced with a variety of graphite fibers.

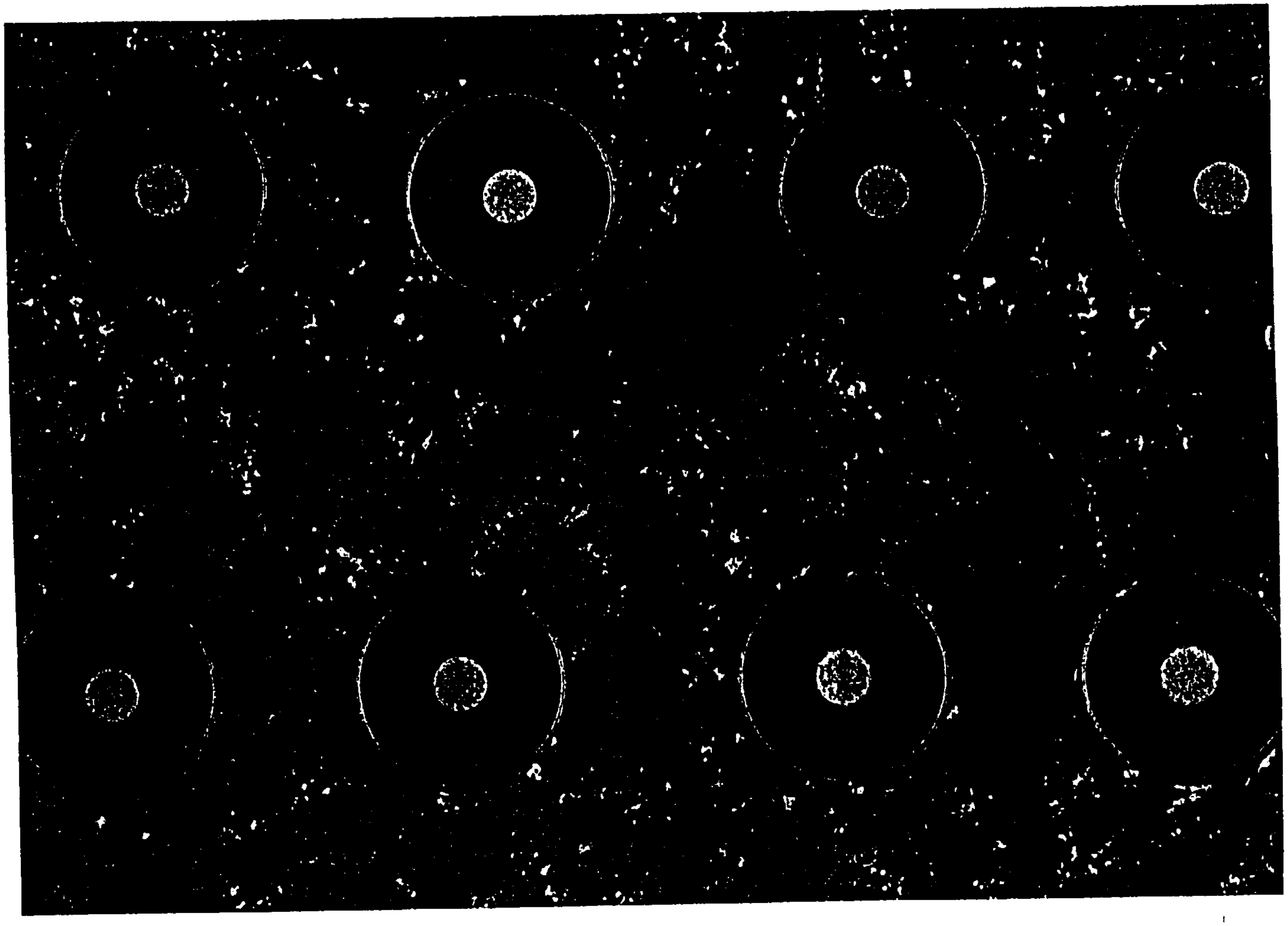

Fig. 9. SCS-6 SiC fiber/reinforced SiC matrix composite formed by reaction forming. The major dispersed matrix phase is $NbSi_2$ (Singh *et al.*, 1994).

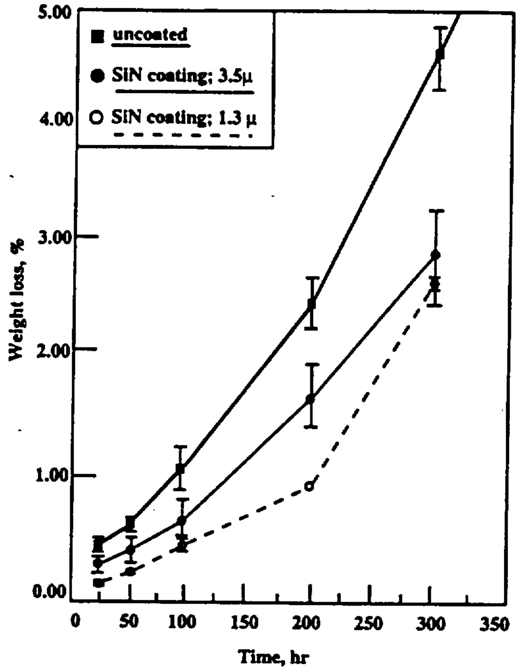

Fig. 5. A comparison of the thermo-oxidative weight losses of uncoated and silicon nitride-coated T-650-42-reinforced PRM-II-50 composites after aging in 1 atm air at 371°C (700°F).

3. METAL-MATRIX COMPOSITES[†]

3.1. *Materials research*

Metal-matrix composites (MMCs), which are defined here to include intermetallic matrices, have received considerable attention as candidates for advanced aerospace applications. These include advanced military and commercial aircraft, the supersonic High-Speed Civil Transport (HSCT), the National Aerospace Plane, and several applications in rocket engines such as those used on the Space Shuttle. These materials can offer higher strength and stiffness at lower weight than current monolithic Ti and Ni alloys. Research at NASA Lewis has focused on Ti-based MMCs for applications in the compressor section of commercial subsonic aircraft, and Fe-and Ni-based MMCs for applications in the turbine section of subsonic aircraft and the exhaust nozzle of the HSCT.

The first MMCs in aircraft gas turbine engines will likely be a Ti-based MMC used in a low-risk static part, but the highest payoffs will be attained with rotating parts such as reinforcing rings in compressor disks. One key issue for these composites is the need for manufacturing technology to produce reliable components at a reasonable cost. Ti-MMCs incorporating SCS-6 fibers produced by the foil/fiber/foil, arc-spray, plasma-spray and powder-cloth processes by various organizations have roughly comparable properties (MacKay *et al.*, 1991; Pickens *et al.*, 1993). Presumably the same may be true for tape casting; however, results have not been published. Because fiber strength dominates the 0° composite strength, distinctions between processes must be made using the same—or an equivalent—strength fiber lot. One of few such studies made has found equivalent 0° strength between composites made by powder cloth and plasma spray (MacKay *et al.*, 1994), two very dissimilar processes. This observation was explained by the fact that equivalent strengths were measured in fibers extracted from the composites, even though plasma spraying had produced some exfoliation of the carbon coating.

Other advantages and disadvantages of these processes in terms of cost, off-axis properties and long time durability are still being assessed. The foil/fiber/foil process is the most mature. It and the arc-spray process, which requires matrix alloy wire, promise lower oxygen levels than the processes using powder, but are limited to formable alloys

---

[†] Contributed by Robert V. Miner and Michael V. Nathal.

and will probably result in higher cost. The two thermal-spray processes, arc and plasma spray, share an advantage in uniform fiber placement, but possible long-time fiber degradation due to some exfoliation of the carbon coating must be explored. Of the powder-based processes, both tape casting and the powder-cloth method utilize polymer binders that must be removed prior to final consolidation, although impurity levels in laboratory coupons have been equal to or lower than those measured in MMCs made by competing processes (MacKay *et al.*, 1994). Tape casting is probably to be favored over the powder-cloth method as a more continuous process. However, yields may be lower and oxygen levels may be higher since a finer powder fraction is required.

Key property issues which will limit the range of application for Ti-MMCs are their environmental resistance and transverse properties. Their low environmental resistance is accentuated in thermomechanical fatigue (TMF) loading. The Ti-MMCs studied to date all exhibit very low lives in TMF cycles having tensile loading at low temperatures (Gabb *et al.*, 1993). TMF behavior in air will likely restrict use to temperatures below about 500°C. Transverse properties of Ti-MMCs are usually found to be lower than those of the monolithic matrix. Transverse tensile strength and ductility (Brindley and Draper, 1993), fatigue resistance in both air and vacuum (Gayda and Gabb, 1992; Lerch, 1990) and TMF resistance (Castelli, 1993) all show this trend. In these studies, it has been shown that failure initiates by debonding of the fiber from the matrix, which can occur in one or more of the C-rich layers of the SCS-6 coating and/or the reaction zone. The limited transverse properties may be overcome by cross-plied fiber architectures, which has been successful in some but not all cases (Lerch, 1990; Larsen *et al.*, 1992). As shown in Fig. 6, the alternative strategy of improving matrix composition also can be very effective in improving transverse composite strength. Both matrix strength and ductility are considered important in determining composite strength, although composite ductility has remained low (Brindley and Draper, 1993).

Despite the property limitations which have been found for Ti-MMCs, applications such as reinforcing rings in the bore of compressor disks show considerable promise because temperatures are limited, direct contact between the MMC and oxygen is excluded, and transverse loads are low. Such components have been successfully engine tested (Kandebo, 1992).

In contrast, the technology for (Fe,Ni)-based MMCs is much less mature, as it is still in the stage of laboratory-scale coupons. These composites have potential to operate in the 1000–1100°C range as turbine and nozzle components. Oxide fibers, particularly Al_2O_3, remain as the best current choice for reinforcement, due to their more favorable

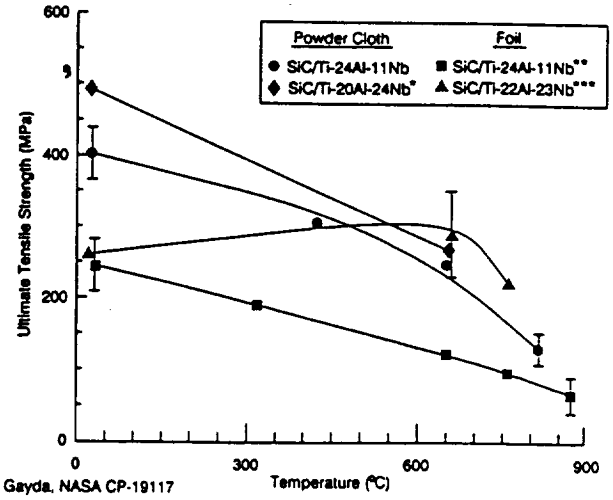

* Gabb and Gayda, NASA CP-19117
** Gambone, WRDC-TR-89-4145
*** Smith et al., WL-TR-92-4035

Fig. 6. Transverse properties of several SCS-6 reinforced titanium aluminide MMCs. By varying composite processing methods and especially matrix composition, the transverse tensile strength has been doubled in the last few years. After Brindley and Draper (1993); reproduced by permission of the U.S. Government.

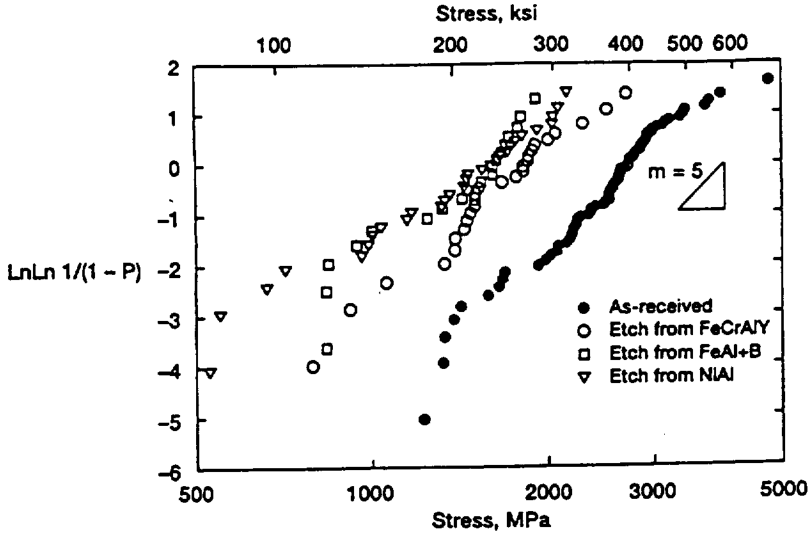

Fig. 7. Weibull probability plots showing strength degradation of sapphire fiber after composite consolidation (Draper and Locci, 1994).

chemical and thermal expansion compatibility with the matrix compared to SiC fibers. Although intermetallics such as NiAl offer the greatest potential due to their light weight and higher-temperature capability (Bowman, 1992), our current focus is on utilization of the more ductile superalloys as nearer-term matrices. Even in the more ductile superalloy matrix composites, however, significant technical challenges need to be resolved. Of prime importance is the need to prevent fiber-strength degradation in Al_2O_3 fibers. Sapphire, the Al_2O_3 fiber with the highest strength potential, has been shown to suffer from strength reductions of the order of 50% when exposed to a variety of matrices at typical composite consolidation cycles (cf. Fig. 7; Draper and Locci, 1994). This strength degradation appears to be caused by the introduction of surface flaws, although degradation has been observed even when the extent of reaction between fiber and matrix is very slight or completely absent. Fiber coatings have been proposed as a solution to this problem. Other oxides such as the Nextel polycrystalline Al_2O_3 fibers are not as attractive for most engine components, primarily because of their low creep strength at high temperatures (Yun and Goldsby, 1993). However, they may compete more effectively if they are less susceptible to strength degradation.

In summary, the future directions for the Ti-MMCs appear to be in the areas addressing actual turbine engine application. Thus, manufacturing technology for lower cost and improved reliability, the methodology needed for efficient design and accurate life prediction, and the accumulation of actual engine test experience should be emphasized. Improved MMC performance through matrix alloy development, environmental protection systems, and the use of alternate fibers are also logical choices. For the less mature superalloy matrix composites, laboratory-scale feasibility demonstrations are still required before engine applications can be seriously considered. The choices for fiber and the development of fiber coatings are currently limiting progress towards the goal of demonstrating mechanical properties which can compete with monolithic superalloys and intermetallics.

3.2. *Deformation and damage of MMC/IMCs*[†]

To fully realize the benefits offered by MMCs, *experimentally verified*, computationally efficient design and life-prediction methods must be developed for the advanced multi-phased materials of interest in advanced engine and propulsion systems. Consequently, these analysis tools must admit physically based, viscoplastic deformation

---

[†] Contributed by Steven M. Arnold and Michael G. Castelli.

life models and be compatible with the finite element method in order to accurately describe the complex thermomechanical load histories typical in the aerospace structures of interest. Furthermore, in order to assist both the structural analyst and the material scientist in developing and utilizing these materials, these tools must encompass the various levels of scale for composite analysis.

To respond to this difficult challenge, parallel approaches wherein the starting point is at the micro- and macroscale have been established at LeRC in deformation and damage modeling and experimental characterization and verification. Clearly, each approach has its realm of applicability, with micromechanics focusing primarily upon applications involving fabrication, material development and life assessment, and the primary usefulness of the macroscale approach[†] being in the design and analysis of structural components. The motivation for pursuing two parallel, yet not mutually exclusive approaches, is heightened by the fact that no one approach is clearly superior, relative to the primary goal of developing accurate, computationally efficient, and experimentally validated analysis tools. For example, the macroscale approach is clearly the most computationally efficient, yet its accuracy may suffer in comparison to its more computationally intense micro counterpart, particularly when highly localized, nonuniform behavior relative to the representative volume element (RVE) dominates.

Significant progress has been made over the past decade in the area of deformation and damage, with regard to experimental, theoretical and computational mechanics of composites (Arnold and Castelli, 1994). However, many issues still remain concerning experimental evaluation and "appropriate" material characterization for this class of materials. To date the vast majority of elevated-temperature experimental fatigue research has been conducted under uniaxial, load-controlled, tension–tension conditions on thin-plate coupons containing partially machined fibers. Great concerns remain within the experimental and modeling communities as to the effects of all of these variables and their relative impact on the data generated to date. Thus, the challenge and ultimate goal is to appropriately control and interpret the experimental evaluations so that accurate input can be provided to guide theoretical modeling efforts and verify their accuracy.

Numerous models both at the micro and macro scales have been proposed (see Arnold and Castelli, 1994, for a more thorough review). However, verification, particularly under thermomechanical multiaxial states of stress, and down selection of these various models is still needed. The dual approach at LeRC, wherein the analysis of structures is viewed both from the micromechanical and macromechanical standpoint, will continue. Ultimately the goal is to develop a hybrid approach for both deformation and damage that is both computationally efficient and accurate under general nonisothermal, multi-axial loadings. Consequently, one future trend will therefore be in the area of symbolic and parallel computations, so as to capitalize on the advances made in software design and computer architecture. Also, for multi-axial verification purposes, benchmark structural testing and analysis will be extremely important and pursued vigorously. It is our expectation that within the next decade accurate and computationally efficient design and analysis techniques will be developed and experimentally verified for a wide range of advanced composite systems with respect to high-temperature, time-dependent deformation and damage, thereby encouraging their assimilation into industry.

4. CERAMIC-MATRIX COMPOSITES

4.1. *Materials research*[‡]

Ceramics offer the potential to operate uncooled or with less cooling and at higher material temperatures than superalloys. This potential plus their low density and good resistance to oxidation make materials such as silicon nitride and silicon carbide extremely attractive. However, their brittle behavior and resultant sensitivity to small flaws that are

---

[†] The macroscale (continuum) approach is where the composite is considered as an isotropic material in its own right, with its own experimentally measurable properties.

[‡] Contributed by Stanley R. Levine.

either inherent in the as-produced material or which develop in service have precluded their reliable use in gas turbines. Recent progress, primarily in Japan and the United states, has demonstrated that fracture toughness, high temperature strength, and statistical reliability can be simultaneously improved. These improvements have resulted in improved functional reliability with durabilities on the order of 100s of hours in prototype automotive gas turbines and the ability to withstand major impact events. However, invariably something unanticipated occurs to cause catastrophic fracture. Thus, the question of the technical feasibility of ceramics for terrestrial engines remains open along with the question of economic viability vis-a-vis more conventional metal engines (Anon, 1993).

Aircraft gas turbine engines require an even higher degree of reliability. It is doubtful that monolithic or *in situ* toughened ceramics can achieve the required functional reliability levels in highly stressed rotating components due to the temporal nature of the flaw population. However, for small, low-stress, static components, they have proven viable (Levine and Herbell, 1992). Because unreinforced ceramics are subject to catastrophic fracture behavior and low reliability due to flaws, NASA Lewis has focused on fiber-reinforced ceramics for about the past 10 years. Our goal has primarily been to identify and develop fiber-reinforced ceramics with performance capabilities beyond those of superalloys in aircraft gas turbines. Therefore we have generally left to the industry, the pursuit of lower-temperature capability systems based on off-the-shelf fibers. We have primarily emphasized the development and characterization of advanced fibers, interphases and systems. Much progress has been made in materials, but many obstacles remain. These are discussed below.

The key to reliable, durable, strong, tough and affordable continuous-fiber-reinforced ceramics resides primarily with the reinforcements. The characteristics we seek are: high strength and stiffness, low density, matrix compatibility both chemically and with respect to thermal expansion match, small diameter for handleability, weaveability and optimum toughening, good thermal and microstructural stability, and, finally, affordable cost. Many of these attributes are also desired in ceramic fibers for reinforcement of metal and intermetallic-matrix composites (DiCarlo, 1991).

To support our interest in fiber development for ceramic-matrix composites (as well as metal- and intermetallic-matrix composites), we have invested considerable effort and resources in the development of fiber-characterization capabilities. Our facilities include equipment for measurement of fiber fast-fracture strength and elastic modulus at room to elevated temperature in air, vacuum and inert environments, and a laser-speckle strain-measurement system for elastic property measurements. The latter is under continued development to provide precision strain measurements for tensile fast fracture and creep. Also in place are systems for measurement of creep and stress rupture in air, vacuum and inert environments. The very simple bend-stress relaxation test (BSR) developed at LeRC has provided the industry with a simple, quick and readily implemented test for assessment of the relative creep resistance of fibers (Morscher and DiCarlo, 1992). Finally, in conjunction with other laboratories, we are contributing to the development of standardization of fiber test methods.

As a frame of reference for discussing fiber status, data will be limited to bend-stress relaxation comparisons. In the BSR test, a straight fiber is constrained to a uniform radius of curvature by tying it into a loop or placing it in a fixture (R_0). After high-temperature heat treatment, the constraint is removed and the radius of curvature is measured (R_A). If the fiber retains the radius of curvature of the constraint, it has fully relaxed (poor creep resistance). For this case, m, the bend-stress relaxation ratio, is 0 ($m = 1 - R_0/R_A = 0$). If it returns to its original straight shape, $R_A = \infty$, and no relaxation (or creep) has occurred ($m = 1 - R_0/R_A = 1$).

Many of the fiber characteristics discussed above for optimum fiber performance are best satisfied by stoichiometric silicon carbide. Several approaches to fabrication for silicon carbide fibers are showing promise for attaining good high-temperature stability and strength. The chemical vapor deposition approach of Textron Specialty Materials has yielded a variety of fiber microstructures and chemistries. The ability to tailor and control the process has yielded a 50 micron fiber with the best combined strength and creep resistance seen to date. Diameter reduction is still an issue. Carborundum has produced creep resistant α-SiC fibers by sintering of extruded green fiber. At this stage of development, the tensile strength is less than desired and the surface roughness and diameter are on the high side. Finally, Dow Corning has produced a near-stoichiometric SiC fiber by the polymeric precursor pyrolysis route. This fiber exhibits good creep resistance, high tensile strength and good handleability. One can conclude from the above that cost and the need for handleability, which is application driven, will be decisive factors in fiber selection. These four fibers along with commercially available fibers are compared in terms of bend-stress relaxation in Fig. 8 (DiCarlo, 1994).

A major concern with SiC fiber-reinforced ceramics is the oxidation resistance of the fiber and the fiber–matrix interface. One approach that can eliminate the interface oxidation issue is the use of oxide fibers and interphases in an oxide matrix. A number of textile-quality multi-filament oxide fibers based on either alumina or aluminosilicate compositions are commercially available. Since the creep of these fibers limits them to low use temperatures (<1100°C), they have not been the focus of our composites research. We have instead sought to identify fibers that have greater capability than single crystal sapphire. We are examining the potential of doped sapphire (Sayir *et al.*, 1993) and various eutectic compositions such as ZrO_2–Al_2O_3 (Farmer *et al.*, 1993) and YAG–Al_2O_3 for potential to offer greater toughness and better high-temperature strength retention and slow crack-growth resistance than sapphire. Exploratory research in the growth of these advanced fibers is being carried out by the laser-heated floating zone approach. Promising fibers are then transitioned to the commercial edge-defined film-fed growth process.

Interfaces with proper weak bonding and oxidative stability are also critical to the satisfactory mechanical performance of fiber-reinforced ceramics. The weak bonding requirement has been achieved with carbon coatings on the fibers in silicon carbide fiber-reinforced systems. However, the oxidation of the carbon interface and SiO_2 formation on the fibers (and matrix if SiC or Si_3N_4) results in bonding of the fibers to the matrix and a loss of strength. Surface coatings of the composite, dense matrices and SiC overlayers on the carbon-coated fibers can alleviate this problem, but do not represent a reliable long-term solution. Other approaches are being pursued at NASA LeRC including Ti–Si–C, BN and porous oxides. Oxide fiber-reinforced systems also require fiber coatings. For single crystal fibers, we have been examining porous oxides and highly anisotropic oxides. Application methods include sol gel, polymeric precursors, and CVD/CVI.

The composite systems being pursued at NASA LeRC can be classified by the type of reinforcement. With SiC reinforcements, we are investigating reaction-bonded silicon nitride (RBSN) and silicon carbide by silicon melt infiltration (Bhatt and Behrendt, 1992). Polymeric precursor fabrication approaches are also being pursued (Hurwitz, 1992). RBSN is attractive because the silicon nitridation process produces essentially no

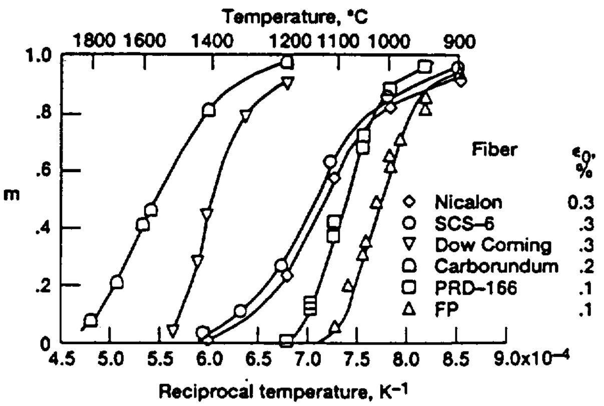

Fig. 8. One hour stress relaxation ratio, *m*, vs reciprocal temperature for several ceramic fibers (Tressler and DiCarlo, 1993).

dimensional change and thus the approach is strain compatible with fiber reinforcement. The polymeric precursor approach is attractive for its complex shape potential. Finally, the melt infiltration approach is attractive because it can yield fully dense matrices.

Our melt infiltration (MI) approach, called reaction forming, is carried out by forming a carbon precursor matrix of controlled porosity and pore size by pyrolysis of a foamed polymer. This allows thorough and uniform silicon melt infiltration and conversion to a silicon carbide plus residual silicon matrix whose microstructure is controlled by the precursor network. Alloying of the silicon with niobium or molybdenum allows the introduction of a third phase for tailoring of toughness, strength and thermal expansion. This capability is illustrated by the photomicrograph in Fig. 9 (Singh *et al.*, 1994). Composites can be produced by resin transfer molding (RTM) or by ply lay-up. However, this process can be combined with chemical vapor infiltration to yield a hybrid processing approach. The basis for this approach is that all SiC fiber-reinforced composites will require an interface coating on the fibers. The most reliable and cost-effective method for placement of this coating would be at the woven preform stage using chemical vapor infiltration (CVI). Furthermore, this coating can be protected by a SiC overlayer coating and the preform rigidized by some additional CVI SiC. From this point, densification can be carried out rapidly and economically by the reaction-formed silicon carbide process. The carbon precursor can be placed by resin transfer molding (RTM), pyrolyzed and converted to SiC by Si melt infiltration (MI). This approach has been dubbed CRM for *C*VI, *R*TM, *M*I.

In the oxide matrix arena, we have been investigating the celsian family of glass-ceramic matrices. Our starting point was barium-aluminosilicate ($BaO-Al_2O_3-2SiO_2$) or BAS. This glass ceramic offers higher temperature capability than other glass ceramics commonly reported as composite matrix materials (e.g. LAS, MAS, BMAS). Bend strength for SCS-6- reinforced BAS is shown in Fig. 10 in comparison to the unreinforced matrix (Bansal, 1994). Strontium substitution for barium in total or in part is being investigated for improved processability, and small-diameter fiber reinforcements are also being investigated. In addition to glass ceramics, we are looking at crystalline matrices such as mullite and alumina combined with either SiC or single-crystal oxide reinforcements.

In summary, the identification of strong, stable and weavable fibers and durable interfaces continue to be very high priority areas for CMC research. Advanced fibers and interfaces are being incorporated into microcomposites and, as sufficient fiber quantities become available, into coupons for assessment of mechanical and environmental durability behavior. The more mature and promising systems are being advanced to rig and engine tests as quickly as possible.

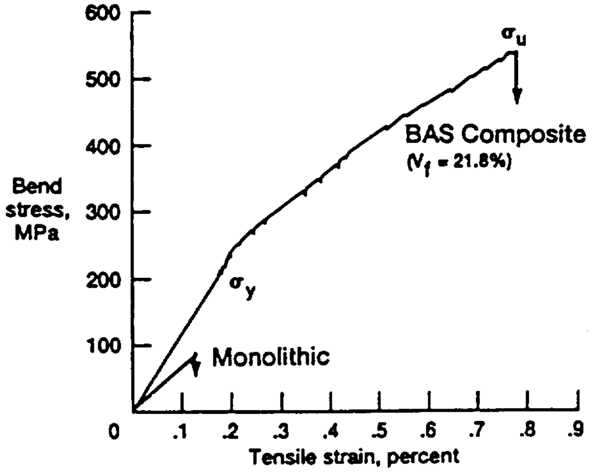

Fig. 10. Bend strength of SCS-6 fiber-reinforced barium-aluminosilicate shows greater strength and strain capability than the monolithic material (Bansal, 1994).

4.2. *Current trends in CMC component analysis*[†]

From an aerospace design engineer's perspective, ceramic composites offer significant potential for raising the thrust/weight ratio and reducing NO_x emissions of gas turbine engines. Considering that these materials will be produced from abundant nonstrategic materials, it is not surprising that research has focused on improving ceramic material properties through processing, as well as establishing protocols for sound design methodology. In particular, continuous ceramic fiber composites exhibit an increase in work of fracture, which allows for "graceful" rather than catastrophic failure. When loaded in the fiber direction, these composites retain substantial strength capacity beyond the initiation of transverse matrix cracking despite the fact that neither of their constituents would exhibit such behavior if tested alone. Indeed, first matrix cracking consistently occurs at strains greater than that in the monolithic matrix material. As additional load is applied beyond first matrix cracking, the matrix tends to break in a series of cracks bridged by the ceramic fibers. Thus any additional load is borne increasingly by the fibers until the ultimate strength of the composite is reached. For most applications the design failure stress will be taken to coincide with the first matrix cracking stress. Matrix cracking usually indicates a loss of component integrity since this phenomenon allows high-temperature oxidation of the interface and fiber, which leads to the strength loss of current composites.

The analysis and design of components fabricated from ceramic composite materials require a departure from the usual deterministic design philosophy (i.e. the factor of safety approach) prevalent in the analysis of metallic structural components, which are more tolerant of flaws and material imperfections. Under applied load, large stress concentrations occur at macroscopic as well as at microscopic flaws, which are unavoidably present in the composite as a result of processing or in-service environmental factors. The observed scatter in component strength is caused by various failure mechanisms, and their corresponding severity leads to composite fracture when the damage-driving force or the effective energy release rate reaches a critical value. This scatter is evident in Fig. 11, where the uniaxial failure data for an oxide-oxide ceramic composite are depicted (Ye, 1994). The data represent the first matrix cracking stress associated with the fiber direction of an alumina matrix reinforced with polycrystalline alumina fibers. Note that the Weibull modulus estimated from this data is 3.68. This value is an indication that significant scatter in composite microcracking strength is present. Observe that the largest stress value in this data set represents over a 330% increase from the lowest level. We should also note that a number of deterministic micromechanical fracture theories exist in the literature that predict a composite's first matrix cracking strength as a function of its constituents. Since all are based on assumed idealistic

---

[†] Contributed by Stephen Duffy.

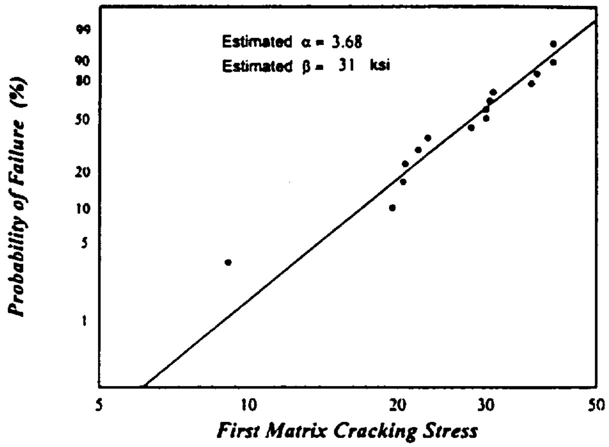

Fig. 11. Uniaxial first matrix cracking stress data for an alumina fiber-reinforced alumina composite.

microstructures, they are typically unable to predict the unavoidable strength variation in current-generation composite materials. In addition, most ceramics exhibit decreasing bulk strength with increasing component volume (the so-called size effect). Since failure is governed by the scatter in strength (ultimate or microcrack yield), statistical design approaches must be employed.

Utilizing structural reliability methods provides a more general accounting of the entire spectrum of values that strength parameters may exhibit. However, the reliability approach demands that the design engineer must tolerate a finite risk of unacceptable performance. This risk of unacceptable performance is identified as a component's probability of failure. The primary concern of the engineer is minimizing this risk in an economical manner. Most quantities that are utilized in engineering designs have, to a greater or lesser extent, some level of uncertainty. This means that if reliability methods are utilized, appropriate analytical tools needed to quantify uncertainty must be readily available. A number of tools and design aids for dealing with uncertainty in a rational fashion have been developed here at NASA Lewis Research Center. These tools include reliability models and computer software that have been tailored to specific composite systems. The reader is directed to the work by Thomas and Wetherhold (1991), Duffy and Arnold (1990), Duffy and Manderscheid (1990) and Duffy *et al.* (1993), regarding the development of reliability models. A number of these reliability models have been incorporated into public-domain computer algorithms such as the T/CARES (Toughened Ceramics Analysis and Reliability Evaluation of Structures) and C/CARES (Composite Ceramics Analysis and Reliability Evaluation of Structures). These computer algorithms are coupled to an assortment of commercially available general-purpose finite element programs. The algorithms yield quasi-static component reliabilities of structures fabricated from ceramic composites; however, work is underway to formulate time-dependent algorithms. Current thought focuses on incorporating the principles of continuum damage mechanics in a similar manner outlined by Duffy and Gyekenyesi (1989).

Focusing attention on the C/CARES algorithm, a noninteractive reliability model has been incorporated where individual uniaxial plies are treated as two-dimensional structures. Each ply (which is discretized in the analysis) is assumed to have five basic strengths or failure modes. The assumption is made that failure is governed by the strength of the weakest link. In essence the component is treated as a series system, and the component probability of failure is evaluated accordingly. Admittedly, the weakest-link concept is a somewhat conservative approach for composites where micro-redundancies exist in certain directions due to parallel arrangements of fibers. However, a macro-level approach to strength measurements should capture this behavior through enhanced distribution parameters. This distinguishes the T/CARES and C/CARES codes from other reliability software where the probability of point failure is usually evaluated. Treating a discretized component as a system allows the design engineer to evaluate size effects, which is not possible when the probability of point failure is evaluated. In addition, the CARES family of software includes parameter-estimation modules that allow the design engineer to evaluate the strength-distribution parameters from failure data. It is assumed that failure strengths can be characterized by either a two- or three-parameter Weibull distribution.

Recent progress in processing ceramic composites has not been matched by mechanical testing efforts. This type of data supports the creation of a complete design data base for a given material. In addition, there is a definite need for experiments that support the development of reliability models. Initially this effort should include experiments that test fundamental concepts (e.g. quantifying size effect in the fiber direction) within the framework of current stochastic models. For example, probing experiments should be conducted along various biaxial load paths to establish level surfaces of reliability in a particular two-dimensional stress space (similar to probing yield surfaces in metals). Concepts such as the maximum stress response which is often assumed in the noninteractive reliability models could be assessed. After establishing a theoretical framework, characterization tests should be conducted to provide the functional dependence of model parameters with respect to temperature. Finally, data from structural tests that are multiaxial (and possibly nonisothermal) could be used to challenge the predictive capabilities of models through comparison to benchmark response data. It cannot be overemphasized that this kind of testing supports design and analysis of components.

5. STRUCTURAL MECHANICS[†]

Achieving the full benefits of composites for aerospace-propulsion and power-system (engine) applications ultimately requires the availability of credible and efficient computer-based tools for component analysis and design. As implied earlier, tools are required which can account for both micromechanical and macromechanical factors affecting critical composite structural performance requirements. Some recent efforts to develop such tools, for a variety of composite materials and structural concepts, are briefly described below.

5.1. *Tools for high-temperature composites*

An important factor affecting the behavior of a CMC is the condition of the interface (or interphase) between fiber and matrix. A distinct interphase can exist as an intentionally applied fiber coating, or can arise due to chemical reaction that occurs between the fiber and matrix during composite fabrication and/or during service at elevated temperatures. The stiffness, strength and thickness of an interphase will influence the overall thermomechanical behavior of a CMC.

One computer-based tool under development at NASA Lewis Research Center, known as CEMCAN (for CEramic Matrix Composite ANalyzer), has recently been used to investigate interface (interphase) effects on CMC behavior. CEMCAN implements a unit cell or representative volume element (RVE) approach with a novel fiber substructuring technique. In this technique the fiber is substructured into multiple layers and the micromechanics equations are formulated at the layer level. The RVE also incorporates a distinct fiber/matrix interphase constituent.

In recent applications of CEMCAN, a unidirectional SiC/RBSN composite (silicon carbide SCS-6 fibers in reaction-bonded silicon nitride matrix) was analyzed for both strong and weak fiber/matrix bond conditions (Mital *et al.*, 1993a). In a strong bond condition, the thermoelastic properties of the distinct interphase constituent are taken to be the same as the matrix (upper bound), whereas in the case of a weak bond, the normal and shear elastic moduli of the interphase are reduced to negligible values (lower bound).

The predicted values of composite effective properties are compared to experimentally measured values, wherever available, and the properties of the interphase are calibrated. The variation of composite properties can also be predicted for varying extent of debond around the fiber circumference or interfacial damage through-the-thickness of the composite.

Results indicate that longitudinal composite properties are rather insensitive to bond conditions, while transverse composite properties are influenced significantly by the bond conditions. Moreover, the comparisons between CEMCAN predictions and experimentally measured values for a SiC/RBSN composite show good agreement as illustrated, for example, in Fig. 12. If the interfacial debonding/damage is limited to a few plies, the degradation in the composite properties is minimal and perhaps difficult to detect by conventional experimental measurements.

The primary advantage of a tool such as CEMCAN is that it provides a simplified, but flexible, capability to represent complex factors such as varying degrees of interfacial bond around the fiber circumference or through-the-thickness, local matrix cracking and fiber breaks (Mital *et al.*, 1993b), different fiber shapes, etc., and the integrated effect of all these aspects on the composite effective properties and thermomechanical behavior. The fiber substructuring technique also permits more accurate (in a piece-wise sense) resolution of local stress distributions in the composite constituents (fiber, interphase and matrix).

[†] Contributed by Dale A. Hopkins.

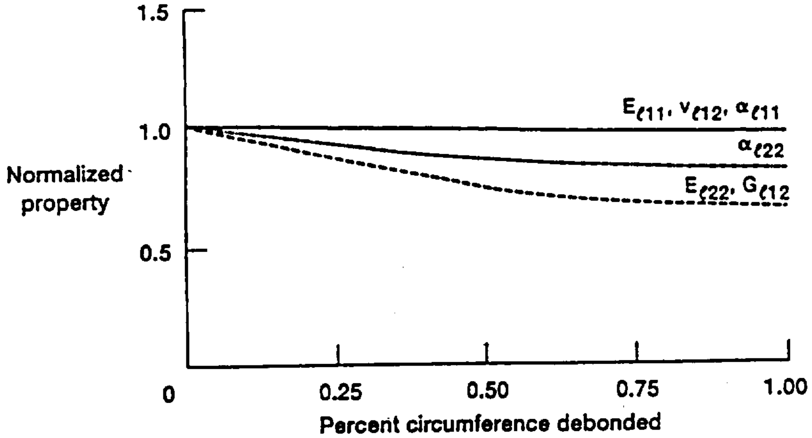

Fig. 12. Unit-cell model and effective elastic properties for [0] SiC/RBSN composite with simulated effect of incomplete fiber/matrix bond.

Another computer-based tool under development at NASA Lewis Research Center, known as BEST—CMS (for *B*oundary *E*lement *S*olution *T*echnique—*C*omposite *M*odeling *S*ystem), has also recently been used to investigate interface effects on CMC behavior. As the name implies, BEST—CMS employs an innovative discrete boundary element methodology and provides sophisticated capabilities for modeling arbitrary fiber architectures, complex fiber/matrix interface conditions, and complex material constitutive behaviors.

The above notwithstanding, a major advantage of BEST—CMS lies in its extremely simple discretization requirements. Specifically, a BEST—CMS model of the composite entails discretizing only the exterior surface of the matrix (with 2-D surface elements) and the centerlines of fibers (with 1-D line elements). The fiber/matrix interface condition is specified merely by entering the type (perfect bond, linear spring, nonlinear spring, or frictional sliding) and the corresponding spring parameters and/or friction coefficient. No explicit discretization of the fiber/matrix interface is required, as the interface behavior is incorporated through the underlying boundary integral equation formulation.

The modeling simplicity advantages of BEST—CMS are more apparent when contrasted to what would be required to create an equivalent finite element model. In the latter case, the entire volume of fibers and matrix must be discretized with 3-D solid elements, and the complex fiber/matrix interfaces must be explicitly modeled using special techniques such as gap elements.

The benefits alluded to above are illustrated in Fig. 13 which shows a sample BEST—CMS model of a unidirectional laminate and computed stress-strain behavior resulting from a linear stress analysis (Goldberg and Hopkins, 1993). The stress-strain results are for a $[90]_2$ SiC/RBSN composite, with fiber/matrix interface conditions specified to simulate both perfect and imperfect bonding. The computed results are compared to experimentally observed behavior, with the simulated imperfect bond case showing better agreement.

In summary, two alternative computer-based tools and their use for micromechanical analyses of CMCs have been described. The capabilities of these tools to model complex factors such as fiber/matrix interface conditions have been demonstrated, and some degree of credibility has been established through comparisons with experimental observations. Whereas the previous focus has been on straight-fiber laminated composites, future emphasis will shift toward more complex composite architectures such as weaves and braids. Indeed, woven and braided PMCs and CMCs are already being pursued for potential engine applications. Accordingly, more sophisticated tools will be needed to enable credible and efficient engine component analysis and design procedures. The BEST—CMS tool, for example, shows particularly good promise in this domain.

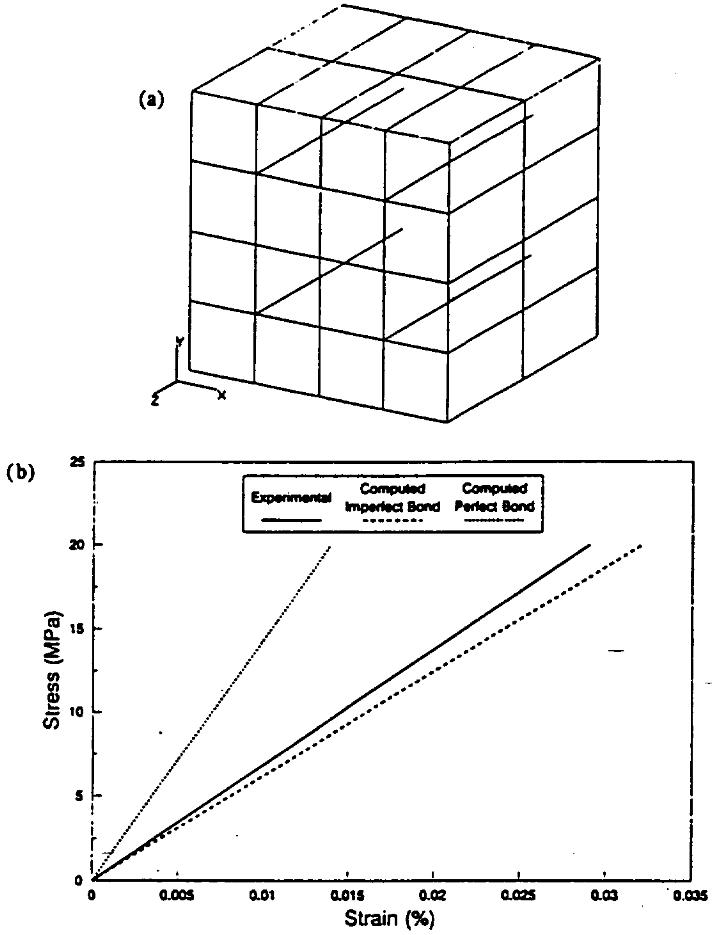

Fig. 13. Boundary element model and effective stress–strain results for $[90]_2$ SiC/RBSN composite with simulated fiber/matrix interface conditions of perfect and imperfect bond.

5.2. *Tools for sensory/active composites*

Sensory/active composites are beginning to receive serious consideration for various smart structures applications in aeropropulsion systems. Applications include, for example, position/clearance control, vibration damping and noise suppression. Very recent progress has occurred in the development of composite mechanics and structural analysis models which is leading toward computer-based tools for the analysis and design of smart engine components.

A unified composite mechanics theory was developed with the capability to model laminated composite structures with embedded piezoelectric layers for both sensory and active modes of behavior (Heyliger and Saravanos, 1993). Using a discrete-layer representation for both displacement and electric potential fields, the theory can accurately model global as well as local electromechanical response. The inclusion of electric potential into the state variables allows representation of general electromechanical boundary conditions and facilitates integration with controller models or other electronic components. Moreover, the formulation includes all energy contributions from elastic, piezoelectric and dielectric components.

The formulations for static and dynamic response of smart composite beam and plate structures with embedded sensors and actuators have also been completed, and specialty finite elements were developed for this purpose. Evaluations have demonstrated the capability of these formulations to represent either sensory (see Fig. 14) or active structures, and to model the complicated stress–stain fields including interactions between passive and active layers (see Fig. 15), interfacial phenomena between sensors and

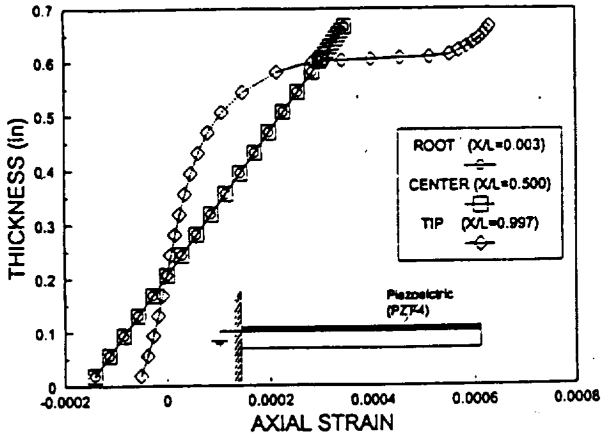

Fig. 14. Through-the-thickness variations of axial strain in active T300/934 composite beam with single piezoceramic layer.

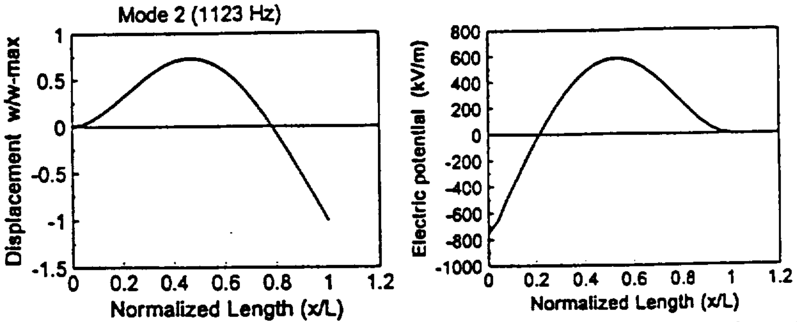

Fig. 15. Typical mode shape and associated electric potential in top surface of sensory beam (2nd bending mode).

composite plies, and critical damage modes in the material. Furthermore, the capability to predict dynamic characteristics under various electric circuit configurations has been demonstrated.

The analytical foundations have also been developed to enable the application of sensory composite structures with delamination-failure detection capabilities by monitoring changes in their dynamic characteristics (Saravanos, 1993). Such non-destructive, real-time health-monitoring capabilities may dramatically improve the reliability of aerospace structural composites. In this work admissible composite mechanics were formulated enabling representations of the effects of delamination cracks and disbonds on the laminate properties such as stiffness, damping, inertia, stresses, etc. An exact analytical procedure was further developed for the prediction of natural frequencies, mode shapes and modal damping in composite beams with an interlaminar delamination.

Evaluations for various cantilever beams with a central delamination have been completed. Correlations with limited reported experimental results show excellent agreement (see Fig. 16). The results indicate that natural frequencies are rather insensitive to small delamination cracks. On the other hand, modal damping seems to be a superior indicator of delamination damage, yet the effects of delamination on damping may vary based on crack size, laminate configuration and mode order. Thus, the combination in changes in both damping and natural frequencies seems to provide a damage signature which may lead to the detection of delamination cracks.

Overall, the mechanics have provided valuable insight into the problem, have facilitated the interpretation of experimental results, and have demonstrated the feasibility of smart composite structures with health-monitoring capabilities. More importantly, the mechanics models have provided the missing link which will enable real-time, in-service detection of delamination presence, size and location from changes in the dynamic signature of the composite structure.

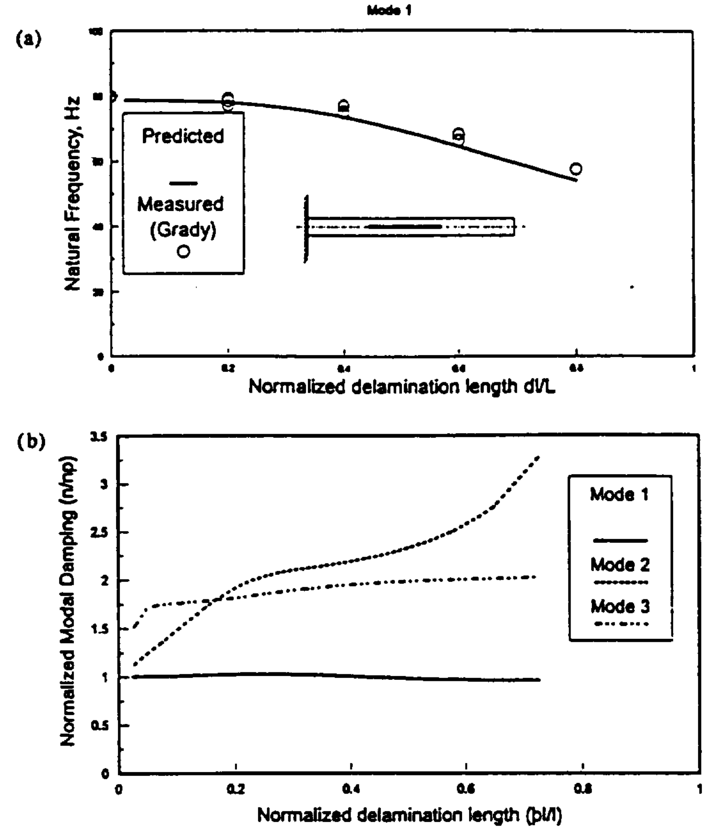

Fig. 16. Effect of delamination size on: (a) fundamental natural frequency of $[0/90]_{3S}$ T300/934; (b) and modal damping of a $[45/-45/90/0]_S$ T300/934 beam.

In summary, considerable progress has been made to develop the fundamental mechanics and structural analysis models necessary to confidently predict the response of sensory/active smart composites. Future efforts will examine other issues, such as digital control systems, power requirements, operating limits, etc., necessary to establish the practical feasibility of smart composite structures in engines.

6. NONDESTRUCTIVE EVALUATION (NDE)[†]

Composites for advanced high-temperature, high-efficiency engines pose new and special challenges for NDE. The engine components will consist of a variety of polymeric-, intermetallic- and ceramic-matrix composite structures. The complex nature of these structures creates strong incentives for advanced nondestructive interrogation and evaluation methods. NDE must range from detection of individual flaws to global imaging of fiber architecture and probabilistic assessment of diffuse flaw populations (Vary, 1992).

At NASA Lewis Research Center, we approach structural composites from the viewpoint that the detection and resolution of individual *micro*-flaws may be unnecessary. This does not mean that individual *macro*-flaws such as delaminations, cracks and similar discontinuities may be ignored. However, it should be recognized that composites may contain a profusion of minute defects that have no discernable effect on reliability or performance unless they are in close proximity and interact massively or encourage degradation in service environments. Then, the challenge is to characterize the collective effect of several kinds of subcritical flaws on mechanical integrity and strength. This is in addition to the detection of overt, dominant defects or global aberrations that would have adverse effects on structural integrity.

[†] Contributed by Alex Vary.

Our view is that NDE methods should be applied concurrently in engineering design, process modeling and structural life analysis. This is in addition to NDE (a) during raw material processing to assure quality, (b) in early stages of component fabrication to screen out defective parts, (c) after fabrication to verify structural integrity, and (d) following service to assess thermomechanical degradation and residual life. NDE methods also provide powerful tools for materials characterization and, as indicated below, we are exploiting these methods in materials testing research to help develop fracture- and life-prediction codes.

The LeRC Structural Integrity Branch investigates and develops methods for nondestructive materials interrogation and flaw characterization. The Branch concentrates on radiographic and ultrasonic techniques including micro-focus radiography, computed tomography, scanning acoustic microscopy, and laser ultrasonics. LeRC researchers pioneered the acousto-ultrasonic (AU) technique which is a practical, sensitive NDE method for assessing variations and degradations of mechanical properties of composites (Vary, 1990). A **Standard Guide for Acousto-ultrasonic Assessment of Composites, Laminates and Bonded Joints** was adopted by ASTM's Committee E-7 on Nondestructive Testing (Anon, 1993).

LeRC researchers are currently exploring *in situ* NDE monitoring of damage accumulation processes in ceramic-matrix composites during mechanical destructive testing. This work combines conventional load frame instrumentation with nondestructive interrogation methods. The *in situ* NDE methods involve adaptations of radiographic, acoustic emission, acousto-ultrasonic, thermographic, and laser imaging techniques. The idea is to apply NDE methods during destructive testing to better understand materials response and to validate fracture prediction and damage accumulation models. This can enhance the various inspection opportunities mentioned previously and the reliability assessment of advanced composite structures before and following service.

An example of *in situ* NDE is our use of radiographic images to determine matrix crack spacing from which one can calculate interfacial shear strengths on the basis of the Aveston–Cooper–Kelly (ACK) theory (Chulya *et al.*, 1991). The *in situ* X-ray method is superior to the conventional optical method for determining crack spacing. The X-ray method provides full-field images of matrix cracking through the entire volume of the gauge section. This NDE method is preferable for materials characterization in that it does not require unloading and removing specimens which would result in crack closure and errors in determining crack spacing.

We apply acoustic emission (AE) and acousto-ultrasonic (AU) methods *in situ* during tensile loading of fiber-reinforced ceramics, i.e. ceramic-matrix composites (CMCs), to identify and discriminate among various failure mechanisms. The objective is to validate "first fracture" and life-prediction models. Our work has identified fracture mechanisms via AE and AU parameters. For example, AU parameters provide relations between stress levels and the onset and saturation of matrix cracking (Tiwari and Hennecke, 1993). AU was is also useful in determining an "effective ultrasonic modulus". We found that this modulus provides a good measure of interfacial shear strength and correlates with modulus values determined from tensile tests. These results confirm that AU can provide a viable approach to nondestructive monitoring of mechanical property changes in composites.

LeRC has installed facilities for experimental study of composite fracture, mechanical response and durability under extreme environmental conditions. The strength, stiffness, toughness and fatigue crack-growth parameters can be evaluated at temperatures to 3000°F (1650°C) in inert, air and other gaseous environments. These test facilities meet the challenges associated with establishing mechanical test methods, sample specifications, and characterization of high-temperature composites over a wide range of thermomechanical conditions. Probabilistic models and algorithms are being developed for sensitivity analyses needed for identifying and predicting the effects of defects and constitutive parameters on the behavior of composites. We expect these latter efforts to provide foundations for guiding NDE for reliability assessment and life prediction.

7. CONCLUDING REMARKS

Historically, most new materials have established viable markets and found commercial success through a linear product-development cycle. In the past the materials scientist would develop a new material system, prototypical components were then fabricated and tested, data bases would be established, and design methodologies were developed in a sequential process. This linear product-development approach was adequate during the cold-war era when large research and development budgets spawned a number of successful high-technology material systems (e.g. smart materials, the utilization of composite materials in the air frames of jet fighters, etc.). However, as American industry continues the struggle to constantly reinvent itself in the post-cold-war era, artifacts such as the linear material-development cycle are being discarded. The current political climate, reduced budgets, and the need to develop dual-use technology all demand that economic issues (and not national defense needs) will dominate the direction of materials research and development. The materials community, which includes material scientists and product design engineers (both at the national research labs and within American industry), must adopt new integrated product-development teams that utilize an assortment of multi-disciplinary skills. In addition, these integrated product-development teams must involve end-users early in the development cycle to ensure economic viability. A primary goal of the integrated product-development teams must be a reduction in the material development cycle. The competitiveness of American material suppliers and their product end-users demands that the cycle for product development be shortened. If a reduction in time-to-market is achieved, the direct results are more American jobs and an improved economic position for American industries in today's global market.

A reduction in the development cycle requires that the concepts of concurrent engineering be embraced. Moreover, to establish a concurrent engineering infrastructure for composites, design guidelines must be established early through codes and standards organizations such as ASTM and ASME. Unless there is a tremendous cost saving or system enhancement (e.g. the NO_x emission reduction in jet engines mentioned previously), product engineers will not utilize a new material until they are comfortable knowing that an appropriate design practice has been codified. The reader need only study the commercialization (or lack thereof) of polymer-matrix composites and carbon–carbon composites to find the evidence to support this last statement.

At NASA Lewis, we have adopted this philosophy in the execution of technology programs for an advanced subsonic transport (AST) and high-speed civil transport (HSCT) and will continue to apply it in developing new initiatives. These programs are being carried out by integrated teams of industry, university, and NASA researchers focused on the needs of the end-use customer. In addition, as the aerospace industry continues to down-size, the longer-term and more research-oriented aspects of the business are being cut to the bone. As a result, there is a strong dependence on NASA to support longer-term research and technology-base efforts as well as near-term focused research.

REFERENCES

Anon (1992). *Proc. Annual Automotive Technology Development Contractors Coordination Meeting*, p.265. Society of Automotive Engines.

Anon (1993). Standard guide for acousto-ultrasonic assessment of composites, laminates, and bonded joints. *Annual Book of ASTM Standards*, 03.03, *Nondestructive Testing*, pp. 760–767. ASTM, Philadelphia, PA.

Arnold, S. M. and Castelli, M. G. (1994). Continuum-based theoretical and experimental studies in deformation and damage of MMCs at NASA-Lewis: progress and trends. *Compos. Engng* 4(8), 811–828 (this issue).

Bansal, N. P. (1994). Method of producing a cermic fiber-reinforced glass-cermic matrix composite. U. S. Patent 5,281,559.

Bhatt, R. T. and Behrendt, D. R. (1992). Reaction-bonded Si_3N_4 and SiC matrix composites. Chapter 6 of *Flight-vehicle Materials, Structures, and Dynamics—Assessment and Future Directions*, Vol. 3, *Ceramics and Ceramic-matrix Composites*, pp. 101–111. ASME, New York.

Bowles, K. J. (1990). Thermo-oxidative stability studies of PMR-15 polymer matrix composites reinforced with various continuous fibers. *SAMPE Q.* 21, 6013.

Bowman, R. R. (1992). Influence of interfacial characteristics on the mechanical properties of continuous fiber reinforced NiAR composites. In *MRS Symp. Proc.* no. 273, *Intermetallic Matrix Composites* Vol. II (Edited by D. B. Miracle, D. L. Anton and J. A. Graves), pp. 145-156. Materials Research Society.

Brindley, P. K. and Draper, S. L. (1993). Failure mechanisms of 0° and 90° SiC/Ti-24Al-11Nb composites under various loading conditions. In *Structural Intermetallics* (Edited by R. Darolia, J. J. Lewandowski, C. T. Liu, P. L. Martin, D. B. Miracle and M. V. Nathal), pp. 727-737. TMS, Warrandale, PA.

Castelli, M. G. (1993). Thermomechanical and isothermal fatigue behavior of a $[90]_8$ titanium matrix composite. *Proc. 8th Tech. Conf. on Composite Materials, Mechanics, and Processing*, pp. 884-892. American Society for Composites.

Chuang, K. C., Kinder, J. D., Hull, D. L. and Youngs, W. Y. (1994). Rodlike polyimides. *Polymer Preprints* 35(1), 341-342.

Chuang, K. C., Vannucci, R. D. and Moore, B. W. (1992). Effects of a noncoplanar biphenyldiamine on the processing and properties of addition polyimides. *Polymer Preprints* 33(1), 435-436.

Chulya, A., Gyekenyesi, J. P. and Bhatt, R. T. (1991). Mechanical behavior of fiber reinforced SiC/RBSN ceramic matrix composites: Theory and experiment. *ASME Pamphlet 91-GT-209*. ASME, New York (also NASA TM 103688).

Delvigs, P., Klopotek, D. L. and Cavano, P. J. (1994). Graphite fiber/polyimide composites with improved processability. In *MRS Symp. Proc.* no. 305, *High Performance Polymers and Polymer Matrix Composites* (Edited by R. K. Eby, R. C. Evers, M. A. Meador and D. Wilson), pp. 33-39. Materials Research Society.

DiCarlo, J. A. (1991). High temperature structural fibers—status and needs. NASA TM 105174.

Dicarlo, J. A. (1994). Creep limitations of current polycrystalline ceramic fibers, composites science and technology. *Compos. Sci. Technol.* 51, 213-222.

Draper, S. L. and Locci, I. E. (1994). Al_2O_3 fiber strength degradation in metal and intermetallic matrix composites. *J. Mater. Res.*, in press.

Duffy, S. F. and Arnold, S. M. (1990). Noninteractive macroscopic statistical failure theory for whisker reinforced ceramic composites. *J. Compos. Mater.* 24, 293-308.

Duffy, S. F. and Gyekenyesi, J. P. (1989). Time-dependent reliability model incorporating continuum damage mechanics for high-temperature ceramics. NASA TM-102046.

Duffy, S. F. and Manderscheid, J. A. (1990). Noninteractive macroscopic reliability model for ceramic matrix composites with orthotropic material symmetry. *Trans. ASME, J. Engng for Gas.Turbines and Power* 112, 507-511 (also published as NASA TM-101414).

Duffy, S. F., Palko, J. L. and Gyekenyesi, J. P. (1993). Structural reliability analysis of laminated CMC components. *Trans. ASME, J. Engng for Gas Turbines and Power* 115, 103-108 (also published as NASA TM-103685).

Farmer, S. C., Sayir, A. and Dickerson, P. O. (1993). Mechanical and microstructural characterization of directionally-solidified alumina-zirconia eutectic fibers. *Proc. Symp.* In Situ *Composites, Science & Technology*, pp. 167-182. TMS, Warrendale, PA.

Gabb, T. P., J. Gayda, Bartolotta, P. A. and Castelli, M. G. (1991). A review of thermomechanical fatigue damage mechanisms in two titanium and titanium aluminide matrix composites. *Int. J. Fatigue* 14(1), 413-422.

Gayda, T. P. and Gabb, J. (1992). Isothermal fatigue behavior of a $[90°]_8$ SiC/Ti-15-3 composite at 436°C. *Int. J. Fatigue* 14, 14-20.

Goldberg, R. K. and Hopkins, D. A. (1993). Micromechanical modeling of laminated composites with interfaces and woven composites using the boundary element method. NASA TM 106280.

Harding, D. R. and Sutter, J. K. (1993). Oxidation barrier coatings for high temperature PMCs. NASA CP-19117, 17-1-17-8.

Heyliger, P. R. *.noand Saravanos, D. A. (1993). On discrete-layer mechanics for health monitoring applications in smart composite structures. In Adaptive Structures and Material Systems* (Edited by G. P. Carman and E. Garcia), ASME Winter Annual Meeting, AD-Vol. 35, pp. 303-312. ASME, New York.

Hurwitz, F. I. (1992). Polymeric precursors for fibers and matrices. Chapter 4 of *Flight-vehicle Materials, Structures, and Dynamics—Assessment and Future Directions*, Vol. 3, *Ceramics and Ceramic-matrix Composites*, pp. 59-77. ASME, New York.

Kandebo, S. W. (1992). Allison tests variable cycle fighter/attack core engine. *Av. week and Space Tech.* 24 Feb., 130-131.

Larsen, J. M., Revelos W. C. and Gambone, M. L. (1992). Possibilities and pitfalls in aerospace applications of titanium matrix composites. In *MRS Symp. Proc.* no. 273, *Intermetallic Matrix Composites* Vol. II (Edited by D. B. Miracle, D. L. Anton and J. A. Graves), pp. 3-16. Materials Research Society.

Lerch, B. A. (1990). Fatigue behavior of SiC/Ti-15-3 laminates. NASA CP-10051, 35.1-35.9.

Levine, S. R. and Herbell, T. P. (1992). Aerospace applications. In *Engineered Materials Handbook*, Vol. 4, *Ceramic and Glasses*, pp. 1003-1006. ASM, Metals Park, OH.

MacKay, R. A., Brindley, P. K. and Froes, F. H. (1991). Continuous fiber-reinforced titanium aluminide composite. *J. Metals* 43(5), 23-29.

MacKay, R. A., Draper, S. L., Ritter and Siemers, P. A. (1994). A comparison of the mechanical properties and micro structures of intermetallic matrix composites fabricated by two different methods. *Met. Trans.*, in press.

Meador, M. A., Cavano, P. J. and Malarik, D. C. (1990). High temperature polymer matrix composites for extreme environments. In *Structural Composites: Design and Processing Technologies, Proc. 6th Annual ASM/ESD Advanced Composites Conf.*, pp. 529-539. ASM, Metals Park, OH.

Miller, L. M. and Gulino, D. A. (1994). Aluminum oxide films for thermo-oxidative protection of polyimide-based composites. In *MRS Symp. Proc.* no. 305, *High Performance Polymers and Polymer Matrix Composites* (Edited by R. K. Eby, R. C. Evers, M. A. Meador and D. Wilson), pp. 191-196. Materials Research Society.

Mital, S. K., Murthy, P. L. N. and Chamis, C. C. (1993a). Ceramic matrix composites properties/microstresses with complete and partial interphase bond. NASA TM 106136.

Mital, S. K., Murthy, P. L. N. and Chamis, C. C. (1993b). Ceramic matrix composites: effect of local damage on composite response. NASA CP 19117, Vol. III, pp. 76.1-76.11.

Morscher, G. N. and DiCarlo, J. A. (1992). A simple test for thermomechanical evaluation of ceramic fibers. *J. Am. Ceramic Soc.* 75(1), 136–140.

Pickens, J. W. Smith, J. W. and Lerch B. W. (1993). Relationships among processing surface structure, and properties of arc sprayed fibers and composites. NASA CP-10104, 31.1- 31.17.

Saravanos, D. A. (1993). Mechanics for the effects of delaminations on the dynamic characteristics of composite laminates. In *Dynamic Characteristics of Advanced Materials* (Edited by P. K. Raju and R. F. Gibson), ASME Winter Annual Meeting, NCA-16/AMD-172, pp. 11-21. ASME, New York.

Sayir, H., Sayir, A. and Lagerlzöf, K. P. D. (1993). Temperature-dependent brittle fracture of undoped and impurity-doped sapphire fibers. *Ceramic Engng Sci. Proc.* 14, 581–590.

Serafini, T. T., Delvigs, P. and Lightsey, G. R. (1972). Thermally stable polyimides from solutions of monomeric reactants. *J. Appl. Polymer Sci.* 16, 905.

Serafini, T. T., Vannucci, R. D. and Alston, W. B. (1976). Second generation PMR polyimides. NASA TMX-71984.

Serrano, A. M., Jangchud, I., Eby, R. K., Bowles, K. J and Jayne, D. T.(1994). Interfacial bonding mechanisms in carbon fiber/PMR-15 composites. In *MRS Symp. Proc.* no. 305, *High Performance Polymers and Polymer Matrix Composites* (Edited by R. K. Eby, R. C. Evers, M. A. Meador and D. Wilson), pp. 105–111. Materials Research Society.

Singh, M., Dickerson, R. M. and Behrendt, D. R. (1994). Characterization of silicon carbide fiber reinforced reaction-formed silicon carbide matrix composites. *18th Annual Conf. on Advanced Ceramics and Composites*, Cocoa Beach, FL. To be submitted for publication in *Ceramic Engng Sci. Proc.*

Stephens, J. R. (1990). NASA's HITEMP program for UHBR engines. AIAA-902395.

Stephens, J. R., Hecht, R. J. and Johnson, A. M. (1993). Material requirements for the high speed civil transport. *AIAA Conf. Proc., International Symp. on Air Breathing Engines*, Japan. AIAA, Washington, DC.

Thomas, D. J. and Wetherhold, R. C. (1991). Reliability analysis of laminates with load sharing. *J. Compos. Mater.* 25, 1459–1475.

Tiwari, A. and Henneke, E. G., II (1993). Real time acousto-ultrasonic NDE technique for monitoring damage in SiC/CAS ceramic composites. *Proc. 2nd International Conf. on Acousto-ultrasonics: Acousto-ultrasonic Materials Characterization* (Edited by A. Vary), pp. 273-283. American Society for Nondestructive Testing.

U. S. Department of Health and Human Services (1986). Methylenedianiline. *Current Intelligence Bulletin* 47.

Vannucci, R. D. (1987). PMR polymide compositions for improved performace at 371°C. *SAMPE Q.* 19, 31.

Vannucci, R. D. and Chriszt, J. K. (1993). Properties of MDA-free polyimide composites. NASA CP-19117, 12-1-12-11.

Vannucci, R. D., Malarik, D. C. and Waters, J. F. (1990). Autoclavable addition polyimides for 371°C composite applications. *Proc. 22nd International SAMPE Technical Conf.*, Boston, MA. SAMPE, Covina, CA.

Vannucci, R. D., Olshavsky, M. A. and Chriszt, J. K. (1992). Processability and properties of blocked PMR polyimide resins and composites. NASA CP-10104, 9-1-9-15.

Vary, A. (1990). Acousto-ultrasonics. In *Non-destructive Testing of Fiber Reinforced Plastics Composites* (Edited by J. Summerscales), Vol. 2, pp. 18–54. Elsevier Applied Science, Barking.

Vary, A. (1992). NDE standards for high temperature materials. In *Nondestructive Testing Standards—Present and Future*, ASTM STP 1151 (Edited by H. Berger and L. Mordfin), pp. 211–224. ASTM, Philadelphia, PA.

Waters, J. F., Sutter, J. K., Meador, M. A. B., Baldwin, L. J. and Meador, M. A. (1991). Addition curing thermosets endcapped with 4-Amino[2.2]paracyclophane. *J. Polymer Sci.*: Part A: *Polymer Chem.* 29, 1917–1924.

Ye, P. (1994). The failure statistics of an oxide-oxide ceramic composite. M. S. Thesis, Cleveland State University.

Yun, H. M. and Goldsby, J. C. (1993). Tensile creep behavior of polycrystalline alumina fibers. NASA TM 106269.

AN OVERVIEW OF ENGINEERING CONCEPTS AND CURRENT DESIGN ALGORITHMS FOR PROBABILISTIC STRUCTURAL ANALYSIS

S.F. Duffy[1], **J.Hu**[2]
Civil Engineering Department
Cleveland State University
Cleveland, Ohio

D.A. Hopkins[3]
Structural Mechanics Branch
NASA Lewis Research Center
Cleveland, Ohio

ABSTRACT

The article begins by examining the fundamentals of traditional deterministic design philosophy. The initial section outlines the concepts of failure criteria and limit state functions, two traditional notions that are embedded in deterministic design philosophy. This is followed by a discussion regarding safety factors (a possible limit state function) and the common utilization of statistical concepts in deterministic engineering design approaches. Next, the fundamental aspects of a probabilistic failure analysis are explored, and it is shown that deterministic design concepts mentioned in the initial portion of the article are embedded in probabilistic design methods. For components fabricated from ceramic materials (and other similarly brittle materials) the probabilistic design approach yields the widely used Weibull analysis after suitable assumptions are incorporated. The authors point out that Weibull analysis provides the rare instance where closed form solutions are available for a probabilistic failure analysis. Since numerical methods are usually required to evaluate component reliabilities, a section on Monte Carlo methods is included to introduce the concept. The article concludes with a presentation of the technical aspects that support the numerical method known as fast probability integration (FPI). This includes a discussion of the Hasofer-Lind and Rackwitz-Fiessler approximations.

INTRODUCTION

Most parameters that are incorporated into engineering analyses have to a greater, or lesser extent, some level of uncertainty. In order to achieve a general accounting of the entire spectrum of values that design parameters exhibit (especially for those cases where one or more of the design parameters exhibits substantial scatter) a design engineer should utilize probabilistic methods. However, a reliability approach to engineering design demands that an engineer must tolerate a finite risk of unacceptable performance. This risk of unacceptable performance is identified as a component's probability of failure. The primary concern of the engineer is minimizing this risk in an economical manner. To accomplish this requires analytical tools that quantify uncertainty in a rational fashion. The tools for dealing with uncertainty in a rational fashion have been developed in a field of mathematics known as probability theory. Since entire texts are dedicated to this field, only those concepts that are applicable to the design of engineered components are presented here.

In order to meet the numerical needs that accompany a probabilistic analysis several research teams sponsored by NASA Lewis Research Center (LeRC) have focused on the development and application of reliability design algorithms. Two of these groups have produced program deliverables that include reliability models and computer software. Specifically, one program focuses on the engineering analysis of components fabricated from ceramic materials. A number of reliability models developed for ceramic materials (see Duffy et al., 1992, for an overview) have been incorporated into public domain computer algorithms such as the CARES (Ceramics Analysis and Reliability Evaluation of Structures), T/CARES (Toughened Ceramics Analysis and Reliability Evaluation of Structures) and C/CARES (Composite Ceramics Analysis and Reliability Evaluation of Structures). These computer algorithms are coupled to an

---

[1] Associate Professor, [2] Graduate Assistant, [3] Acting Branch Chief

assortment of commercially available general purpose finite element programs. The algorithms yield quasi-static component reliability. In addition the CARES family of software includes parameter estimation modules that allow the design engineer to evaluate the strength distribution parameters from failure data. It is assumed that for this type of reliability analysis the failure strength of the material can be characterized by either a two- or three-parameter Weibull distribution.

The second program that has developed probabilistic tools for design engineers is the Probabilistic Structural Analysis Methods (PSAM) program. This endeavor takes on a more global perspective and deals with the stochastic nature of design parameters in a general fashion. In a manner similar to the structural ceramics effort mentioned above, this program integrates probabilistic algorithms with structural analysis methods. The primary result is the NESSUS (Numerical Evaluation of Stochastic Structures Under Stress) computer software.

This article presents the underlying engineering concepts that support the technical aspects of both the CARES and PSAM programs. In addition, the authors outline the commonality between the programs by demonstrating the shared technical principles. Specific details regarding the CARES family of software algorithms and the NESSUS software are incorporated into the conference presentation that accompanies this article.

FAILURE CRITERION & LIMIT STATE FUNCTION

The success of a structural analysis hinges on the appropriate choice of design variables used to describe the overall thermo-mechanical behavior of a component. The design variables can include, but are not limited to, strength parameters, external loads, allowable deformations at predetermined locations in the component, cycles-to-failure, and material stiffness properties. After the engineer has determined what design variables are pertinent to a given class of design problems, they can be assembled in an N-dimensional vector. This vector of design parameters can be identified as

$$y_a = (y_1, y_2, \dots y_N) \tag{1}$$

Design variables can easily interact with one another, thus a functional relationship is needed to describe any interaction. This function is most commonly referred to as a failure criterion. Common examples include strength based criterion such as the maximum distortional energy criterion and the Mohr-Coulomb criterion; fatigue failure criterion are represented by Miner's rule; and fracture criterion include the critical strain energy release rate method and the stress intensity factor methods. Usually a failure criterion represents the first step in defining a limit state. If an operational state for a structural component falls within the boundaries of a limit state, the performance of the structural component is acceptable. An operational state for a component that falls on the boundary of a limit state denotes failure. For the failure criterion just cited a delineation between acceptable performance and failure is made at a point in the component.

A failure criterion and a limit state function can be expressed by the general formulation

$$g = g(y_a) \tag{2}$$

Note that g defines a surface in an N-dimensional design variable space. Once again this function must stipulate how each design variable interacts in producing failure. Here values of $g > 0$ indicate a *safe* structure, whereas values of $g \leq 0$ correspond to a *failed* structure. The failure criterion (or a limit state function) can be defined by either a complete loss of load carrying capacity, or alternatively by a loss in serviceability. The conceptual distinction between a limit state function and a failure criterion is based on scale. It was indicated above that a failure criterion focuses on a point. Limit state functions focus on the component or structure. Often times there is no difference between the two since failure at a point constitutes failure of the component. In contrast, consider a structural component where plastic yield is a possible failure mode. If yielding (failure) at a point is described by a yield function, then this function represents the failure criterion for this particular mode of failure. Yet a structural component may not fail if yielding has occurred only at a point. In fact the component may continue to function safely until a sufficient number of plastic hinges have formed and the structure collapses. The formation of a sufficient number of plastic hinges is described mathematically by a limit state function. The reader is directed to the extensive literature that followed Drucker's initial work (1952) in establishing bounds on limit state functions for this type of failure analysis. However, the point is that for a plasticity analysis the failure criterion (i.e., the yield criterion) is different from the limit state function.

As a prelude to the discussion that follows later concerning Weibull analysis, a structural component fabricated from a ceramic material is treated as a weakest-link system. If one link in the chain fails, the entire chain fails. This assumption gives rise to a particular modeling approach in calculating component reliability. It also infers that failure at a point constitutes component failure. In this sense the failure criterion and the limit state function will be one in the same.

SAFETY FACTORS & DETERMINISTIC FAILURE ANALYSIS

To begin contrasting the difference between deterministic and probabilistic failure analyses the discussion in this section is focused on a specific failure mode, i.e., the exhaustion of strength capacity. A structural component can fail when it encounters an extreme load, or when a combination of loads reaches a critical collective magnitude, and the ability to withstand the applied load is exhausted. With the design algorithms presented in this article the engineer can easily quantify the magnitude of the extreme load event leading to failure, and account for the frequency at which this extreme event occurs. In addition, the strength (or capacity) of the material and any variation in this design parameter can be quantified. A brief discussion regarding safety factors (as well as safety margins) follows. This discussion underscores the need to account for variability of design parameters in a coherent manner. These quantities are typically utilized in deterministic designs, and are easily incorporated into probabilistic designs.

In the field of structural mechanics it is customary to define safety factors (and sometimes safety margins) in order to ascertain how "close" a component is to failing. If L represents the load on a component, and R represents the resistance (or capacity) of the material, then the safety factor is defined as

$$S.\,F. = \frac{R}{L} \tag{3}$$

Alternatively, the safety margin can be utilized, and this measure is defined as

$$S.\,M. = R - L \tag{4}$$

Failure occurs when the safety factor falls below one, or when the safety margin falls below zero. These two expressions represent the simplest and most fundamental definition of a limit state. In the following section where the principles of probabilistic failure analysis are outlined, these two expressions are utilized to explain basic concepts. However, to employ either safety factors or safety margins the design engineer must quantify parameters R and L. Data must be collected and a single "most-likely" value must be assigned for each parameter. If the typical structural engineer has been exposed to statistical methods, these concepts were encountered in quantifying material properties from experimental data. Thus the design engineer is familiar with the concept of a central location parameter for experimental data defined by the sample mean, i.e.,

$$\bar{x} = \left(\frac{1}{N}\right) \sum_{i=1}^{N} x_i \tag{5}$$

A second parameter, the sample variance, serves as a measure of data dispersion. It is defined as

$$S^2 = \left(\frac{1}{N-1}\right) \sum_{i=1}^{N} [\,x_i - \bar{x}\,]^2 \tag{6}$$

In the expressions for the sample mean and variance,x_i represents the i^{th} observation in an experiment with N observations. Other sample descriptors exist (e.g., skewness and kurtosis); however, the mean and the variance are more widely recognized and understood. Usually the sample mean is used to identify a single "most-likely" value for a design parameter. The variance is most often utilized in a simple minded fashion to indicate how well the experiment is being performed, i.e., a small variance indicates good experimental technique. However, this attitude tends to minimize the fact that some design parameters inherently behave in a random fashion. Variation in experimental data can easily be a fundamental property of a particular design parameter, not a commentary on experimental technique.

Often the engineer is not required to determine values for design parameters directly from experiments. Values for resistance parameters can be obtained from handbooks or existing corporate data bases. Either source of information may concurrently list values for the standard deviation (defined as the square root of the sample variance) but this information is too often ignored in a deterministic failure analysis where the sample mean is used to represent the "most-likely" value of the design parameter. Increasing the mean value of the load parameter by a multiple (usually three) of standard deviations, and decreasing the mean value of resistance parameter by the same multiple of standard deviations is one way of including information regarding data dispersion in a safety factor design . This method, referred to as the three-sigma approach, yields the following definition for the factor of safety

$$S.\,F. = \frac{\bar{x}_R - 3\,(S_R)^{1/2}}{\bar{x}_L + 3\,(S_L)^{1/2}} \tag{7}$$

Clearly this definition of the safety factor admits information concerning the data dispersion for both the load and resistance parameters.

However, if either of the design parameters exhibits a significant scatter, as evidenced by a relatively large sample standard deviation, then the design engineer must compensate in some manner to maintain a prescribed safety factor for a component. Thus, in an effort to maintain a given level for the safety factor, analyses predicated on equation (7) may easily lead to uneconomical designs. Utilizing probabilistic methods can readily compensate for parameter variation, enabling an engineer to further pursue a design that would be otherwise rejected based on traditional methods. In addition, for materials that exhibit size effects where the average strength decreases with specimen size (e.g., ceramic materials) the three-sigma approach leads to a fundamental problem in identifying what value to use for the resistance random variable.

FUNDAMENTALS OF PROBABILISTIC FAILURE ANALYSIS

Utilization of equation (7) represents an attempt to include more information regarding the true characteristics of design parameters. Momentarily focusing on the resistance parameter, equation (7) implies that the resistance design parameter is inherently multi-valued. If this multi-valued resistance parameter assumes different values at random during strength-to-failure experiments, then the parameter should be treated as a random variable. This holds for the load design parameter as well. Specifically note that if the load and resistance design parameters are treated as random variables, then equation (7) does not include any information on the underlying distribution (e.g., normal, log-normal, Weibull, exponential, etc.) that characterizes the design parameter. As the discussion unfolds in this section the reader will see that reliability methods attempt to overcome this inadequacy.

Consider a component fabricated from a material with a resistance described by the random variable R. A single load, represented by the random variable L, is applied to the component. Both random variables are represented mathematically by distinctly different probability density functions (e.g., normal, log-normal, exponential, Weibull, Rayleigh, etc.). The load and resistance random variables can be described by the same type of probability density function as long as the distribution parameters are different.

However, in this discussion the distributions for the random variables are left unspecified. This is intentional in order to simplify and emphasize several issues. Making use of the concept of a safety factor, the probability of failure for a component where a single load is applied is given by the expression

$$P_f = Probability\,(R/L \leq 1) \tag{8}$$

Alternatively, the probability of failure can be defined using the safety margin. Here

$$P_f = Probability\,(R - L \leq 0) \tag{9}$$

For either definition, P_f is the product of two finite probabilities summed over all possible outcomes. Each probability is associated with an event and a random variable. The first event is defined by the random variable L taking on a value in the range

$$\left(x - \frac{dx}{2}\right) \leq L \leq \left(x + \frac{dx}{2}\right) \tag{10}$$

The probability associated with this event is the area under the probability density function for the load random variable over this interval, i.e.,

$$P_1 = f_L(x)\;dx \tag{11}$$

The second event is associated with the probability that the random variable R is less than or equal to x. This is the area under the probability density function for the resistance random variable over the range from minus infinity (or an appropriate lower limit defined by the range of the resistance random variable) to x. This second probability is given by the cumulative distribution function evaluated at x, i.e.,

$$P_2 = F_R(x) \tag{12}$$

With the probability of failure defined as the product of these two probabilities, summed over all possible values of x, then

$$P_f = \int_{-\infty}^{+\infty} F_R(x)\;f_L(x)\;dx \tag{13}$$

To interpret this integral expression, consider Figure 1. This figure contains a graph of an arbitrary probability density function (f_R) for the resistance random variable superimposed on the graph of an arbitrary probability density function (f_L) for the load random variable. Note that R and L must have the same dimensions to plot these two quantities on the same graph. A common misconception is that P_f is the area of overlap encompassed by the two probability density functions. Scrutiny of equation (13) leads to the appropriate conclusion that the probability of failure is the area under the composite function

$$\eta_{RL}(x) = F_R(x)\,f_L(x) \tag{14}$$

Due to the complexities introduced by specifying $F_R(x)$ and $f_L(x)$ a closed form solution rarely exists for equation (13). One exception is the application of equation (13) to ceramic materials, which is discussed in the next section.

CERAMIC MATERIALS AND SYSTEM RELIABILITY

Even though variations in loads and strength can be readily accommodated by the concepts presented in the previous section, for components fabricated from ceramic materials it is the variation in material strength that dominates the design. Lack of ductility combined with flaws, defects, or inclusions that have various sizes and orientations leads to scatter in failure strength. Thus the strength associated with these ceramic materials reflects an intrinsic fracture toughness and a homogeneous distribution of flaws present in the materials. The analytical concepts presented in this section will accommodate this singular focus on strength variation.

Experimental data indicates that the continuous random

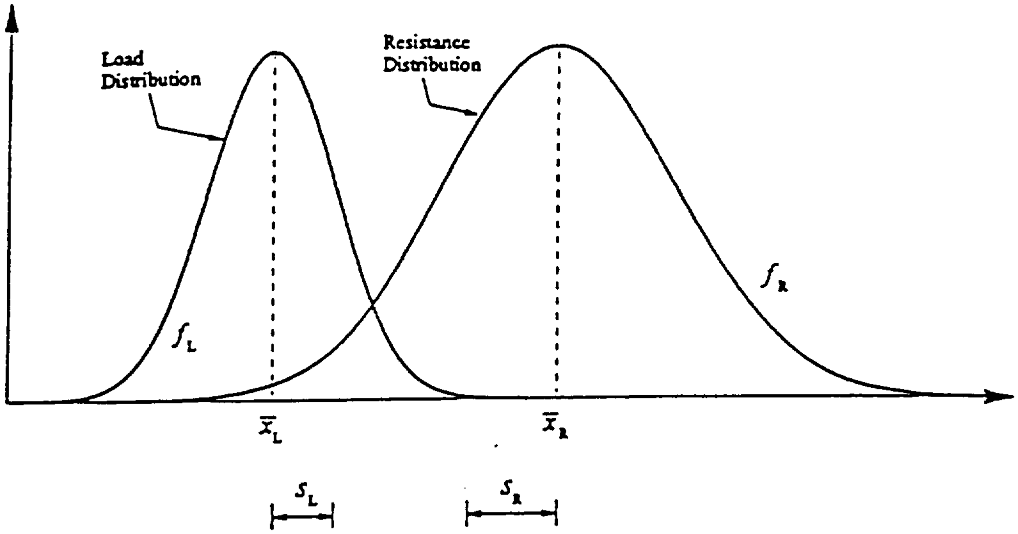

Figure 1 An arbitrary load - resistance interference graph

variable representing uniaxial tensile strength (a resistance design parameter) of monolithic ceramics is asymmetrical about the mean and will assume only positive values. These characteristics rule out the use of the normal distribution (as well as others) and point to the use of the Weibull distribution or a similarly skewed distribution. The three-parameter Weibull probability density function for a continuous random strength variable, denoted as Σ, is given by the expression

$$f_\Sigma(\sigma) = \left[\frac{\alpha}{\beta}\right]\left[\frac{\sigma-\gamma}{\beta}\right]^{(\alpha-1)} \exp\left[-\left[\frac{\sigma-\gamma}{\beta}\right]^{\alpha}\right] \qquad (15)$$

for $\sigma > \gamma$, and

$$f_\Sigma(\sigma) = 0 \qquad (16)$$

for $\sigma \leq \gamma$. In equation (15) α is the Weibull modulus (or the shape parameter), β is the Weibull scale parameter, and γ is a threshold parameter. If the value of the random variable is below the threshold parameter, the probability density function is zero. Often the value of the threshold parameter is taken to be zero. In component design this represents a conservative assumption, and yields the more widely used two-parameter Weibull formulation.

If the resistance design parameter is characterized by the Weibull distribution and the load design parameter is assumed deterministic, then the following probability density function

$$f_L(x) = \delta\,(x - x_o) \qquad (17)$$

is utilized in equation (13) for the load random variable. Here δ is the Dirac delta function defined as

$$\delta\,(x - x_o) = \begin{cases} \infty & x = x_o \\ 0 & x \neq x_o \end{cases} \qquad (18)$$

Note that the Dirac delta function satisfies the classical definition of a probability density functions. This function represents the scenario where the standard deviation of a distribution approaches zero in the limit, and the random variable takes on a central value (identified here as x_o). Insertion of equation (17) into equation (13) yields the following expression for the probability of failure:

$$P_f = \int_{-\infty}^{\infty} F_R(x)\, \delta(x - x_o)\, dx \qquad (19)$$

However, with the Dirac delta function embedded in the integral expression, the probability of failure simplifies to

$$P_f = F_R(x_\bullet) \tag{20}$$

Thus the probability of failure is governed by the cumulative distribution function that characterizes the resistance random variable. This expression (with modification) is a fundamental concept associated with Weibull analysis.

Equation (20) yields the probability of failure (after an appropriate distribution has been specified for the random variable R) for a simple component with a single deterministic load which is identified as $x_\bullet$. However, a unique property of ceramic materials is an apparent decreasing trend in strength with an increase in the size of the component. This is the so called size effect. As an example, consider that the simple component represents a uniaxial tensile specimen. Now suppose that two groups of these simple components exist. Each group is identical with the exception that the size of the specimens in the first group is uniformly smaller than the specimens in the second group. For ceramic materials the sample mean from the first group would be consistently and distinctly larger in a manner that can not be accounted for by randomness. Thus equation (20) must be transformed in some fashion to admit a size dependence. This is accomplished through the use of system reliability concepts. It should be understood that the expression given in equation (20) represents the probability of failure *for a uniform set of boundary conditions*. If the boundary conditions are modified in any fashion, or the geometry of the component changes, equation (20) is no longer valid. To account for size effects and deal with the probability of failure for a component in a general manner, the component should be treated as a system, and the focus must be directed on the probability of failure of the system.

Typically, for a structural component with a varying stress field, the component is discretized, and the stress field is characterized using finite element methods. Since component failure may initiate in any of the discrete elements, it is easy to consider the discretized component from a systems viewpoint. A discretized component is a series system if it fails when one of the discrete elements fail. This concept gives rise to weakest-link reliability theories. A discretized component is a parallel system when failure of a single element does not necessarily cause the component to fail, since the remaining elements may sustain the load through redistribution. Parallel systems lead to what has been referred to in the literature as "bundle theories." These two types of systems represent the extremes of failure behavior and suggest more complex systems such as "r out of n" systems. Here a component (system) of n elements functions if at least r elements have not failed. However, the failure behavior of monolithic ceramic materials is brittle and catastrophic. This type of behavior fits within the description of a series system, thus ceramic materials are modeled as a weakest-link reliability system.

Now the focus is directed to the probability of failure of a discrete element and how this failure relates to the overall probability of failure of the component. If the failure of an individual element is considered a statistical event, and if these events are independent, then the probability of failure of a discretized component that acts as a series system is given by

$$P_f = 1 - \prod_{i=1}^{N} \left(1 - \mathcal{P}_i\right) \tag{21}$$

where N is the number of discrete finite elements for a given component. Here the probability of failure of the i^{th} discrete element ($\mathcal{P}_i$) is given by the expression

$$\mathcal{P}_i = \psi \, \Delta V_i \tag{22}$$

where V denotes volume and ψ is a failure function per unit volume of material. This introduces the requisite size scaling that is associated with ceramic materials. Adopting an argument used by Weibull (1939) where the norm of the ΔV_i's tends to zero in the limit as N goes to infinity, then the component probability of failure is given by the following expression

$$P_f = 1 - \exp\left(-\int_V \psi \, dV \right) \tag{23}$$

What remains is the specification of the failure function ψ. The most basic formulation for ψ is given by the principle of independent action (PIA). For this reliability model

$$\psi = \left(\frac{\sigma_1}{\beta}\right)^\alpha + \left(\frac{\sigma_2}{\beta}\right)^\alpha + \left(\frac{\sigma_3}{\beta}\right)^\alpha \tag{24}$$

where σ_1, σ_2 and σ_3 are principle stresses. Equation (23) is the essence of Weibull analysis. The issue of other possible forms for ψ has been discussed in detail in articles by Duffy and Arnold (1990), Duffy and Manderscheid (1990), Thomas and Wetherhold (1991), and Duffy et al. (1993).

As a final note, equations (20) and (23) can be equated once a distribution function is specified for the resistance random variable. As was indicated earlier, the distribution of choice is the Weibull distribution. There is a fundamental reason for this choice that goes beyond the fact that the Weibull distribution usually provides a good fit to the data. Often times the log-normal distribution provides an adequate fit to failure data representing ceramic materials. However, the log-normal distribution precludes any accounting of size effects. The reader is directed to work by Hu (1995) for a detailed discussion on this matter. As it turns out, once a conscious choice is made to utilize the Weibull distribution, equations (20) and (23) provides a convenient formulation for parameter estimation. The details for accomplishing this are provided in Duffy (1995).

The next issue the design engineer is confronted with concerns the numerical evaluation of equation (13) when a closed form solution is not readily available. The remainder of this article is dedicated to this important issue. However, before proceeding on to the next section the reader is reminded that probabilistic concepts were introduced by adopting a very simple failure criterion. In the sections that follow the failure criterion is left unspecified and the details of the numerical techniques are highlighted.

MONTE CARLO METHODS

In this section the authors expand the scope of the discussion beyond simple failure criterion represented by safety factors and safety margins. This discussion begins with the observation that most structural components are designed based on the results obtained from a finite element analysis. This analysis can incorporate a mechanical analysis, a thermal analysis, or both. In all cases the design engineer seeks to predict, and most times minimize, the stress field throughout the component in an economical fashion. The stress field is approximated by the stress state obtained from each discrete element. Once again the focus of the design algorithms presented here is on individual (discrete) elements. In general the reliability of an individual finite element is computed from the expression

$$R = \mathit{Probability}[g(y_a) > 0] \tag{25}$$

when a failure criterion is used to define point failure. Note that the failure criterion is left unspecified thus equation (25) is a general, fundamental relationship. The discussion that follows outlines specific details that must be embedded in this relationship.

To evaluate equation (25) the design space must be defined. In addition, the relevant joint probability density function that represents the design variables must be established. As was indicated earlier if there are N random variables associated with a limit state function, then the design space is an N-dimensional space (a hyperspace) that represents the entire domain of possible values of the design variables. In order to transform a limit state function into a reliability model a joint probability density function must be utilized. This function establishes the relative frequency of occurrence for a specific combination of values (realizations) of the design random variables. Keep in mind that the limit state function is used to determine which area of the design space (a region that represents all possible outcomes of the design random variables) will result in a successful event. Thus according to equation (25) the *safe* domain of the design space should satisfy $g(y_a) > 0$. Obviously, the portion of the design space that satisfies $g(y_a) \leq 0$ is the *failure* domain for the finite element. Thus the reliability of a finite element is the integration of the joint probability density function over the *safe* design space defined by the failure criterion. This integration takes the form

$$R = \int_{\delta_s} f(y_a)\, dy_a \tag{26}$$

where $f(y_a)$ is the joint density function of the random variables, and δ_s is the *safe* domain of the design space. This concept is simplified to a two-dimensional design variable space depicted in Figure 2.

Unfortunately, the integral in equation (26) does not usually have a closed form solution. An exception to this was presented in the section where the principles of Weibull analysis are examined. Thus in general, numerical techniques must be utilized to evaluate the reliability of a finite element. Two numerical techniques are discussed in this article that provide approximate solutions of equation (26). They are the conventional Monte Carlo method, and the fast probability integration (FPI) method. Other methods exist (the reader is referred to Hu (1995) for an overview) but only these two methods are presented here due to limitations placed on the length of this article. The reader is referred to Wu (1994) for a more comprehensive development of the numerical techniques associated with the FPI method. In addition, Hu's thesis (1995) presents details regarding a Monte Carlo method with an extremely efficient sampling approach.

The conventional Monte Carlo simulation is conceptually simple, very general, and relatively straightforward to implement. Thus it is commonly used to numerically estimate the probability of failure when a closed form solution to equation (26) is unavailable. In general the probability of failure of a structural component can be expressed as

$$P_f = \int_{\delta_f} f(y_a)\, dy_a \tag{27}$$

where δ_f is the failure domain that satisfies the expression

$$g(y_a) \leq 0 \tag{28}$$

Equation (27) is an alternative expression to equation (26) since

$$P_f = 1 - R \tag{29}$$

Now define an indicator function I such that

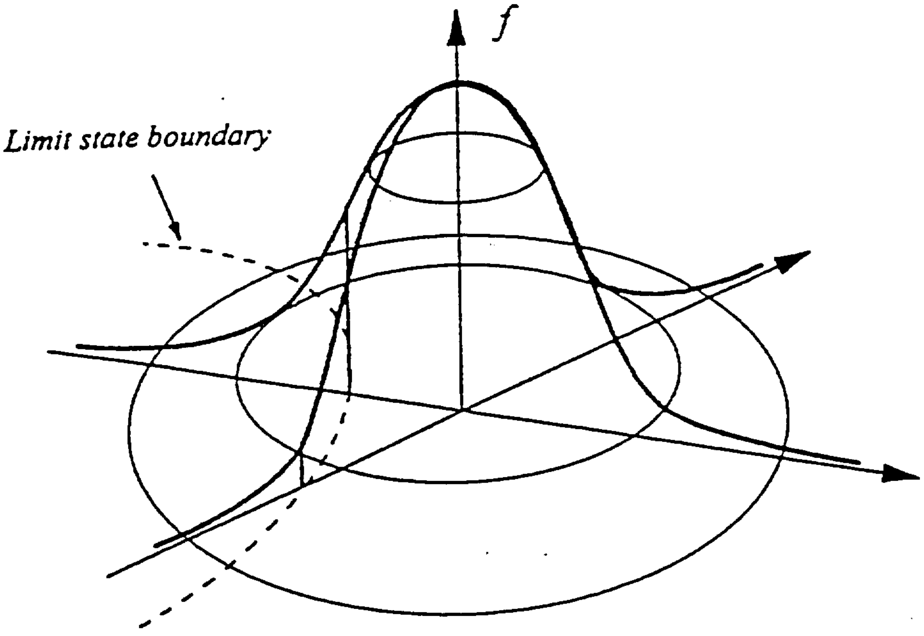

Figure 2 Two-dimensional joint PDF with limit state

$$I = \begin{cases} 1 & g(y_a) \le 0 \\ 0 & g(y_a) > 0 \end{cases} \qquad (30)$$

This indicator function can be included in the integral defined by equation (27) if the integration range is expanded to include the range of the design space, i.e.,

$$P_f = \int_{\theta_s+\theta_f} I\, f(y_a)\, dy_a \qquad (31)$$

The integral on the right side of this expression defines the expectation of the indicator function, i.e.,

$$E\,[I] = \int_{\theta_s+\theta_f} I\, f(y_a)\, dy_a \qquad (32)$$

Recall from statistics that the definition of the mean (μ) of a random variable is the expectation of the variable. Thus

$$\mu_x = \int_{-\infty}^{\infty} x f(x)\, dx \qquad (33)$$

Also recall that the mean associated with a random variable can be estimated from a sample taken from the population that is being characterized by the distribution function $f(x)$. The estimated value of the mean is given by the simple expression

$$\bar{x} = \frac{1}{N} \sum_{j=1}^{N} x_j \qquad (34)$$

Where x_j is the jth observation in a random sample taken from the population. In a similar fashion the probability of failure (P_f) represents the expected value, of the indicator function. Thus equation (31) can be expressed as

$$P_f = \lim_{N \to \infty} \left\{ \frac{1}{N} \sum_{j=1}^{N} I_j \right\} \qquad (35)$$

Here it is implied that a random sample of *successes* ($I=1$) and *failures* ($I=0$) has been generated. Thus I_j is the jth evaluation of the limit state function where the random observations have been generated from the cumulative distribution function F_{Y_n}.

The simulation method defined by equation (35) is referred to as a conventional Monte Carlo simulation. The objective is to generate a sufficiently large set of observations (i.e., large N) in order to reproduce the statistical characteristics of the underlying population that the observations are taken from. The concept of the conventional Monte Carlo method is shown in Figure 3, where the solid circles represent a *success*, i.e., $I=1$ and $g(y_n) \leq 0$. The open circles are observations that do not pass the failure criterion. Here $I=0$ and $g(y_n) > 0$. While this approach may not be the most efficient numerical technique, eventually it will converge to the correct solution, i.e., the solution approaches P_f in the limit as N approaches infinity.

THE FAST PROBABILITY INTEGRATION METHOD

This section presents the details of obtaining component reliabilities from fast probability integration (FPI) methods. These details are presented in terms of the simplified failure criterion defined by safety factors or safety margins. This is done to merely clarify technical concepts. At the end of the section the details are provided that allows the application of this method to arbitrary failure criterion.

Thus the probability of failure for a structural component can be expressed as

$$P_f = Probability(R - L \leq 0) \tag{36}$$

where R is the resistance random variable and L is the load random variable (both of which were stipulated as design variables). Define the safety margin as

$$M = R - L \tag{37}$$

The expectation of the safety margin is

$$\mu_M = \mu_R - \mu_L \tag{38}$$

where μ_M is the mean of M, μ_R is the mean of R and μ_L is the mean of L. Similarly, the variance of the safety margin is given by the expression

$$\delta_M^2 = \delta_R^2 + \delta_L^2 - 2cov[R, L] \tag{39}$$

where "*cov*" represents the covariance function, δ_R^2 is the variance of R, and δ_L^2 is the variance of L. However, if R and L are independent random variables, then

$$cov[R, L] = 0 \tag{40}$$

and

$$\delta_M^2 = \delta_R^2 + \delta_L^2 \tag{41}$$

Making use of the definition of the safety margin, the probability of failure can be expressed as

$$P_f = Probability(-\infty \leq M \leq 0) \tag{42}$$

If R and L are normal random variables, then M (which is also a limit state function) becomes a linear combination of two normally distributed random variables. Thus M is a normally distributed random variable. Making use of the standard normal CDF (Φ), the probability of failure is given by the expression

$$P_f = \Phi\left(-\frac{\mu_M}{\delta_M}\right) \tag{43}$$

Substitution yields

$$P_f = \Phi\left[\frac{\mu_L - \mu_R}{(\delta_R^2 + \delta_L^2)^{1/2}}\right] \tag{44}$$

Now define the reliability index β such that

$$\beta = \frac{\mu_R - \mu_L}{(\delta_R^2 + \delta_L^2)^{1/2}} \tag{45}$$

then

$$P_f = \Phi(-\beta) \tag{46}$$

This is equivalent to the integral expression given in equation (19), i.e.,

$$P_f = \int_{\delta_f} f\,(R,L)\; dR\; dL \tag{47}$$

Thus equation (46) represents a "fast integration" of equation (47), hence the origin of term "fast probability integration" (FPI) for the approach that utilizes the reliability index. The expression

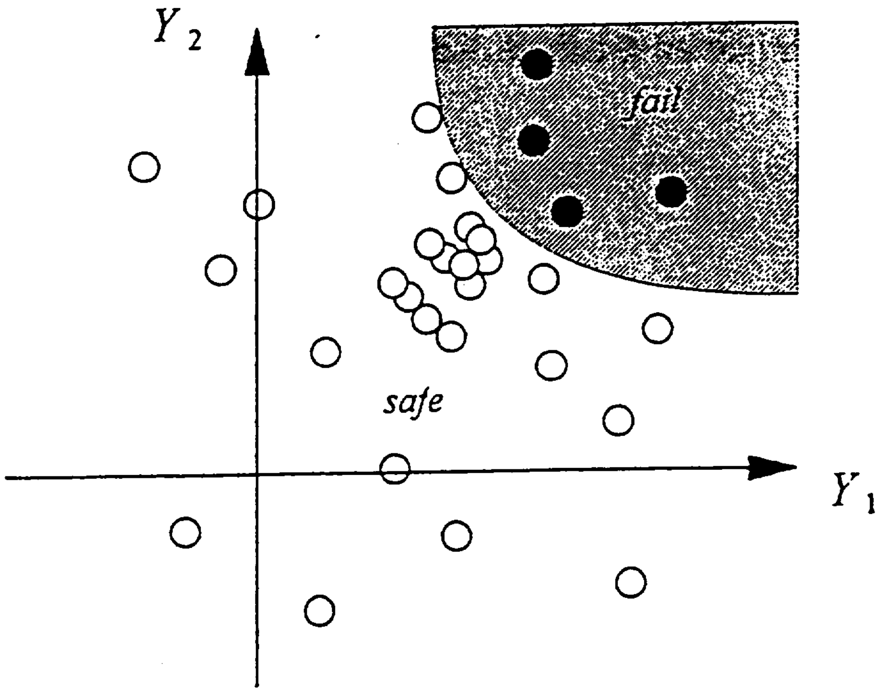

Figure 3 Conventional Monte Carlo methods

for the reliability index was derived based on the special case where the safety margin serves as the limit state function. More generally, other expressions for β can be derived by adopting different limit state functions. However, in general, the straightforward relationship between the reliability index and the probability of failure expressed above no longer holds. If the limit state function is a non-linear function of the design variables or the design variables are not normally distributed, then equation (46) will not hold. Yet for either case there are approximations that can be utilized which yield good results, provided the limit state functions and the design variables are suitably restricted.

Before the discussion on how the relationship between the probability of failure and the reliability index can be approximated, a geometric interpretation of the reliability index is given using the simple definition of the safety margin expressed in equation (38). If R and L are normally distributed, they can be transformed to standard normal variables. By definition the transformed resistance variable is

$$R' = \frac{R-\mu_R}{\delta_R} \tag{48}$$

and the transformed load variable is

$$L' = \frac{L-\mu_L}{\delta_L} \tag{49}$$

Thus the resistance variable can be expressed as

$$R = R'\delta_R + \mu_R \tag{51}$$

and the load variable can be expressed as

$$L = L'\delta_L + \mu_L \tag{51}$$

In terms of the transformed random variables the safety margin becomes

$$M = \delta_R R' - \delta_L L' + (\mu_R - \mu_L) \tag{52}$$

Now the reliability index can be interpreted as the shortest distance from the origin in the transformed variable space to the failure surface, which is defined by M. This is depicted in Figure 4 where the failure surface associated with this particular safety margin is shown in both the original and the transformed design variable space. The point on the failure surface that is

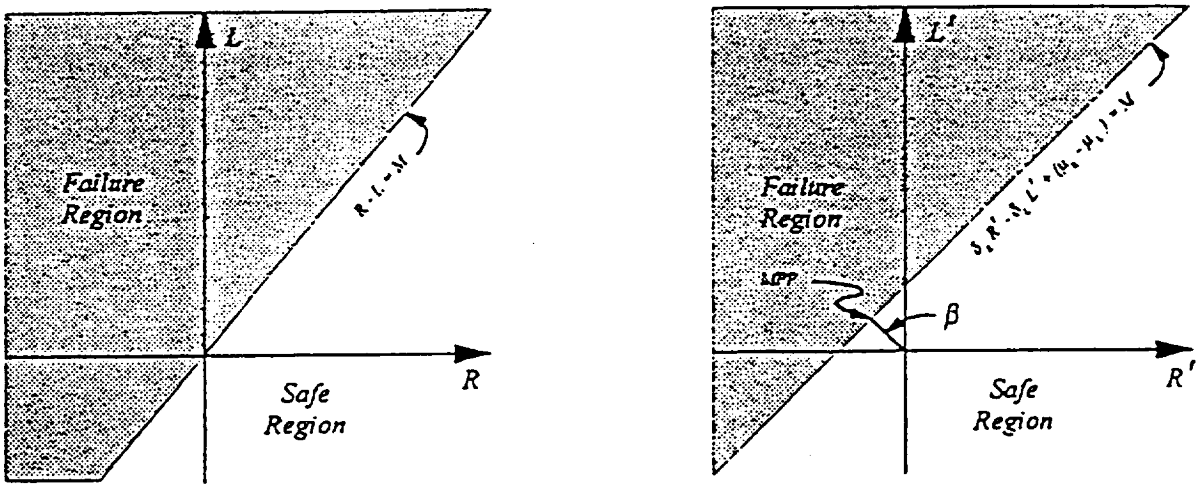

Figure 4 a) Failure surface in the standard variable space. b) Failure surface and MPP in the transformed variable space

nearest to the origin is referred to as the most probable point (MPP) in structural reliability literature. The reader can easily verify that equation (45) can be derived from the geometry presented in Figure 4. This last figure is important. If

- the limit state function can be linearized, and
- the design variables can be transformed to standard normal variables,

then β can be determined using analytic geometry concepts. Once β has been found, the probability of failure is calculated directly using equation (46).

Finally, before discussing approximate methods associated with linearizing the limit state function and normalizing the design variables, a brief discussion is necessary concerning the extension of equation (46) to N design variables. The preceding discussion focused on two independent, normally distributed, random variables. Equation (47) holds for N independent, normally distributed random variables, if the limit state function (g) is a linear function of the random variables. Under these circumstances

$$\beta = \frac{\mu_g}{\delta_g} \tag{53}$$

where

$$g = 1 - \sum_{i=1}^{N} a_i y_i \tag{54}$$

$$\mu_g = E[g] \tag{55}$$

and

$$\delta_g^2 = VAR[g] \tag{56}$$

Note that a_i is the coefficient of the i'th term of the limit state function and depends on the particular limit state function utilized.

THE HASOFER-LIND APPROXIMATION

Hasofer and Lind (1974) proposed a technique (identified here as the H-L method) that approximates the failure surface for those cases where the limit state function is not a linear combination of the design variables. The failure surface (a hyper-surface in the N-dimensional design variable space) is approximated by a hyper-plane tangent to the failure surface at the MPP (see Figure 4). This approximation is accomplished by utilizing the first term of a Taylor series expansion of the limit state function at the MPP. Thus

$$g(z_a) = g(z_a^*) + \sum_{i=1}^{N} \left(\frac{\partial g}{\partial z_i}\right)_* (z_i - z_i^*) \qquad (57)$$

where z_a is the vector of standard normal variables which are related to the design variables in the following manner

$$z_a = \frac{(y_a - \mu_{Y_a})}{\delta_{Y_a}} \qquad (59)$$

Here z_a^* is the vector representing the location of the MPP, and the asterisk associated with the partial derivative indicates the vector and the associated derivatives are being evaluated at the MPP.

Since the limit state function is approximated by the first term of a Taylor series expansion, the H-L method is referred to as a "first order" method. Keep in mind that the H-L approximation will be *exact* if the design variables are normally distributed, and the true limit state function is linear. The reader should question how good the approximation is if the actual limit state function is not linear (a hyper-plane) in the transformed standard normal variable space. The joint probability density function tends to decay exponentially with a relative increase in distance from the mean (i.e., the "peak" of the joint PDF in Figure 2). For large values of β (i.e., low probability of failure) the main contribution to the probability integral, i.e., equation (28), usually comes from regions near the MPP, since the relevant functional values of the joint PDF will assume their largest values in the near vicinity of the MPP. Therefore, provided that the actual limit state surface is well-behaved and does not exhibit significant deviations from the tangent hyper-plane approximation in the neighborhood of the MPP, a reasonably accurate estimate of the actual probability of failure (P_f) can still be obtained from equation (46) by this first order approximation.

Since β represents the shortest distance from the origin to the failure surface in standard normal variable space, and the location of the MPP is not known a priori, a search algorithm must be employed. An optimization method making use of Lagrange multipliers is utilized here. The following steps represent the details of this search algorithm:

(1) Assume initial values for the normal design variables y_i^*, and transform these values to standard normal values z_i^* using equation (58).

(2) Transform the limit state function $g(y_a)$ to $g(z_a)$ using equation (57). This requires the evaluation of the partial derivatives at the corresponding values of z_i^*.

(3) Evaluate the Lagrange multipliers

$$\alpha_i^* = \left\{ \frac{\left(\frac{\partial g}{\partial z_i}\right)}{\left[\sum_{i=1}^{n}\left(\frac{\partial g}{\partial z_i}\right)^2\right]^{1/2}} \right\}_* \qquad (60)$$

(4) Assemble the vector z_i^* using

$$z_i^* = -\alpha_i^* \beta \qquad (60)$$

where β is unknown at this point.

(5) Substitute z_i^* into the following expression

$$g(z_a) = 0 \qquad (61)$$

and solve for β. Note that this last expression is a scalar valued function. Hence one equation is solved for one unknown (β).

(6) With β known, update values of z_i^* and repeat steps (3) to (5) until a suitable convergence criterion is met. This convergence criterion can be easily related to the change in β from one iteration to the next.

The geometric interpretation of the algorithm above is shown in Figure 5. Note that the rate of convergence for the H-L algorithm will depend on the following

- the nature of the true limit state function,
- the starting point,
- the characteristics of the random variables, and
- the correlation between the random variables.

These issues have been discussed thoroughly in the open literature and will not be revisited here.

THE RACKWITZ-FIESSLER APPROXIMATION

If the random variables that are utilized in the limit state function are not normally distributed, a second approximation must be employed. Based on a concept suggested by Paloheimo and Hannus (1974), Rackwitz and Fiessler (1978) proposed a modification of the FPI method to account for design variables

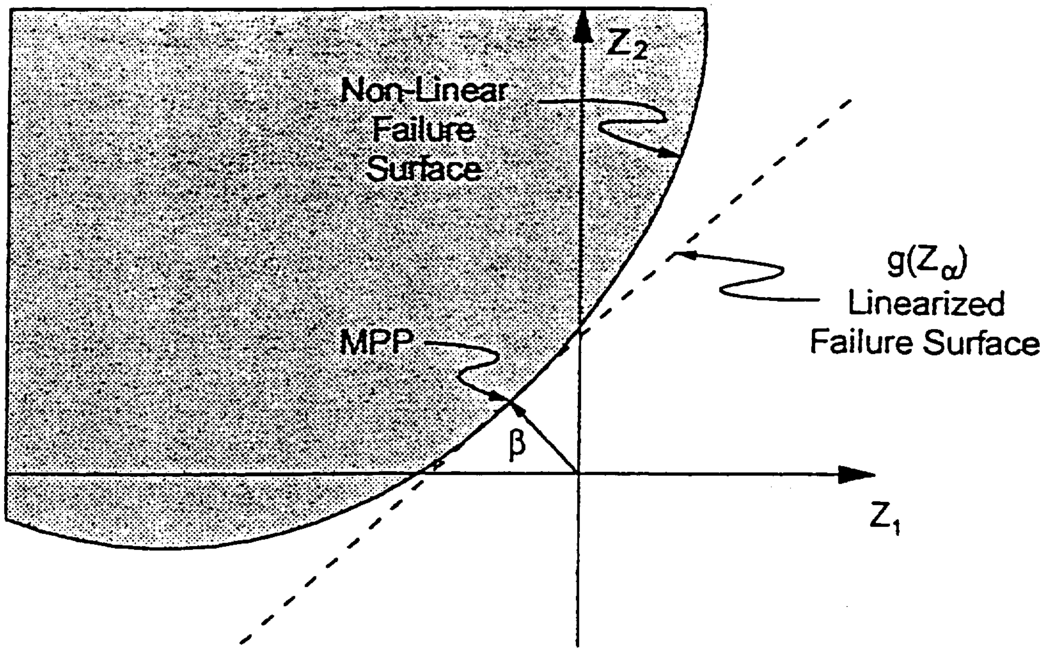

Figure 5 Schematic of the Hasofer-Lind approximation where a non-linear failure surface is approximated by a linear tangent hyper-plane

with non-normal distributions. The technique (referred to here as the R-F method) converts non-normal random variables into standard normal variables by first equating the CDFs of the standard normal and non-normal distributions, i.e.,

$$\Phi\left(\frac{y_i^* - \mu_{Y_i}^{\tilde N}}{\delta_{Y_i}^{\tilde N}}\right) = F_{Y_i}(y_i^*) \tag{63}$$

Here F_{Y_i} represents the non-normal cumulative distribution function (e.g., the two-parameter Weibull distribution) and Φ is the standard normal cumulative distribution function. In addition the PDFs of the standard normal and non-normal distributions are equated leading to the expression

$$\frac{1}{\delta_{Y_i}^{\tilde N}}\,\phi\left(\frac{y_i^* - \mu_{Y_i}^{\tilde N}}{\delta_{Y_i}^{\tilde N}}\right) = f_{Y_i}(y_i^*) \tag{64}$$

Here f_{Y_i} represents the non-normal probability density function and ϕ is the standard normal probability density function. These last two expressions must be evaluated at every approximated MPP. The character $\tilde N$ signifies the normal distribution in both expressions. Thus, the equivalent normal mean ($\mu_{Y_i}^{\tilde N}$) and equivalent normal standard deviation ($\delta_{Y_i}^{\tilde N}$) of non-normal variables can be derived from equations (62) and (63). Specifically

$$\mu_{Y_i}^{\tilde N} = y_i^* - \delta_{Y_i}^{\tilde N}\,\Phi^{-1}[F_{Y_i}(y_i^*)] \tag{65}$$

and

$$\delta_{Y_i}^{\tilde N} = \frac{\phi[\Phi^{-1}[F_{Y_i}(y_i^*)]]}{f_{Y_i}(y_i^*)} \tag{66}$$

SUMMARY

An overview is given of engineering concepts and computational algorithms which have been developed enabling probabilistic design approaches to structural analysis. Probabilistic design approaches are shown to have evolved as a natural extension of traditional deterministic design approaches.

The well established Weibull analysis approach, commonly utilized for the design of components fabricated of brittle materials such as ceramics, is shown to be a special case of the more general probabilistic design problem formulation. Substantial developments have occurred to extend the Weibull analysis approach to more complex failure mechanisms and for the approximate numerical solution of more realistic component design problems using finite element analysis techniques. These efforts have produced comprehensive design tools, such as is embodied in the CARES family of software developed at NASA Lewis Research Center.

In the more general case, much of the development effort has focused on efficient numerical algorithms to achieve accurate approximate solutions of probabilistic design problems involving complex and nonlinear failure or limit state functions and design parameters described by non-normal distributions. Several specific algorithms are described which are extensions of the fast probability integration approaches originally developed by Hasofer and Lind, and Rackwitz and Feissler, as well as extensions of Monte Carlo simulation approaches allowing for more selective sampling. Again, these efforts have produced comprehensive design tools, such as is embodied in the NESSUS family of software developed at Southwest Research Institute under the sponsorship of NASA Lewis Research Center.

The various methods presented provide a quantitative basis to account for design uncertainties inherent to physical systems. The ultimate benefit of probabilistic design approaches is a more rational basis for making design decisions that balance component or system efficiency with reliability or safety. This benefit is especially important in the design of high-performance and/or life-critical systems.

REFERENCES

Drucker, D.C., Greenberg, W. and Greenberg, H.J., "Extended Limit Design Theorems for Continuous Media," *Quart. Appl. Math.*, Vol. 9, pp. 381-389, 1952.

Duffy, S.F. and Arnold, S.M., "Noninteractive Macroscopic Statistical Failure Theory for Whisker Reinforced Ceramic Composites," *Journal of Composite Materials*, Vol. 24, No. 3, pp. 293-308, 1990.

Duffy, S.F. and Manderscheid, J.M., "Noninteractive Macroscopic Reliability Model for Ceramic Matrix Composites with Orthotropic Material Symmetry," *Journal of Engineering for Gas Turbines and Power*, Vol. 112, No. 4, pp. 507-511, 1990.

Duffy, S.F., Chulya, A. and Gyekenyesi, J.P., "Structural Design Methodologies for Ceramic Based Material Systems," Chapter 14 in Flight-Vehicle Materials, Structures and Dynamics Technologies - Assessment and Future Directions, eds. A.K. Noor and S.L. Venneri, The American Society of Mechanical Engineers, pp. 265-285, 1992.

Duffy, S.F., Palko, J.L. and Gyekenyesi, J.P., "Structural Reliability Analysis of Laminated CMC Components," *Journal of Engineering for Gas Turbines and Power*, Vol. 115, No. 1, pp. 103-108, 1993.

Duffy, S.F., "Issues Relating to Reliability Based Design Component Design," to appear in Handbook on Whisker and Particulate Reinforced Ceramic Matrix Composites, K. Bowman, S.K. El-Rahaiby, and J. Wachtman eds., to be published by DoD Ceramics Information Analysis Center.

Hasofer, A.M., and Lind, N.C., "An Exact and Invariant First Order Reliability Format," *Journal of the Engineering Mechanics Division*, Vol. 100, No. EM1, pp. 111-121, 1974.

Hu, J., "Modeling Size Effects and Numerical Techniques in Structural Reliability Analysis," *Masters Thesis*, Cleveland State University, 1995.

Paloheimo, E. and Hannus, M., "Structural Design Based on Weighted Fractiles," *Journal of the Structural Division*, Vol. 100, No. ST7, pp. 661-676, 1974.

Rackwitz, R. and Fiessler, B., "Structural Reliability Under Combined Random Load Sequences," *Journal of Composite Structures*, Vol. 9, pp. 489-494, 1978.

Thomas, D.J. and Wetherhold, R.C., "Reliability Analysis of Laminates with Load Sharing," *Journal of Composite Materials*, Vol. 25, pp. 1459-1475, 1991.

Weibull, W., "A Statistical Theory of the Strength of Materials," *Ingeniors Vetenskaps Akademien Handlinger*, No. 151, 1939.

Wu, Y.-T., "Computational Methods for Efficient Structural Reliability and Reliability Sensitivity Analysis," *AIAA Journal*, Vol. 32, No. 8, pp. 1717-1723, 1994.

STP 1201

Life Prediction Methodologies and Data for Ceramic Materials

C. R. Brinkman and S. F. Duffy, editors

ASTM Publication Code Number (PCN)
04-012010-09

ASTM
1916 Race Street
Philadelphia, PA 19103

Sung R. Choi[1], Jonathan A. Salem[2], and Joseph L. Palko[1]

COMPARISON OF TENSION AND FLEXURE TO DETERMINE FATIGUE LIFE PREDICTION PARAMETERS AT ELEVATED TEMPERATURES

REFERENCE: Choi, S. R., Salem, J. A., and Palko, J. L., "Comparison of Tension and Flexure to Determine Fatigue Life Prediction Parameters at Elevated Temperatures," Life Prediction Methodologies and Data for Ceramic Materials, ASTM STP 1201, C. R. Brinkman and S. F. Duffy, Eds., American Society for Testing and Materials, Philadelphia, 1994.

ABSTRACT: High temperature slow crack growth of a hot-pressed silicon nitride (NCX 34) was determined at temperatures of 1200 and 1300°C in air. Three different testing methods were utilized: dynamic and static fatigue with bend specimens, and static fatigue with dog-bone-shaped tensile specimens. Good agreement exists between the dynamic and static fatigue results under bending. However, fatigue susceptibility in uniaxial tensile loading was greater than in bending. This result suggests that high temperature fatigue behavior should be measured with a variety of specimen configuration and loading cycles so that adequate lifetime prediction parameters are obtained.

KEYWORDS: silicon nitride, slow crack growth, dynamic fatigue, static fatigue, tensile fatigue, lifetime prediction

Silicon nitride ceramics are candidate materials for high temperature structural applications in advanced heat engines and heat recovery systems. The major limitation of this material in high temperature applications is fatigue-associated failure, where slow crack growth of inherent defects or flaws can occur until a critical size for catastrophic failure is reached. Therefore, it is very important to evaluate fatigue behavior with specified loading condition so that accurate lifetime prediction of ceramic components is ensured.

There are several ways of determining fatigue parameters. Dynamic, static or cyclic fatigue loading can be applied to smooth specimens with inherent flaws or to precracked fracture mechanics specimens in which the crack velocity measurements are made directly. A considerable number of studies have been carried out to characterize fatigue behavior of silicon nitride ceramics using the testing methods

---

[1] Research Associates, Cleveland State University, Cleveland, OH 44115; Resident Research Associates, NASA Lewis Research Center, Cleveland, OH 44135.

[2] Research Engineer, NASA Lewis Research Center, Cleveland, OH 44135.

L. Palko[1]

NE FATIGUE
RATURES

alko, J. L., "Comparison of
e Prediction Parameters at
odologies and Data for
kman and S. F. Duffy, Eds.,
Philadelphia, 1994.

of a hot-pressed silicon
es of 1200 and 1300°C in
ilized: dynamic and static
gue with dog-bone-shaped
ween the dynamic and static
gue susceptibility in
bending. This result
or should be measured with
ng cycles so that adequate

, dynamic fatigue, static

materials for high
ed heat engines and heat
is material in high
d failure, where slow crack
until a critical size for
it is very important to
ing condition so that
nents is ensured.

atigue parameters.
be applied to smooth
d fracture mechanics
ments are made directly. A
ied out to characterize
using the testing methods

iversity, Cleveland, OH
is Research Center,

Center, Cleveland, OH

---

mentioned above [1-7]. Although the reported results agree to some degree, there remains uncertainty and disagreement among the testing methodologies, depending on test materials and even on researchers.

In this study, high temperature fatigue behavior of a hot-pressed silicon nitride was determined at 1200 and 1300°C in air using three different loading conditions: dynamic and static loading for flexure beam specimens and static loading for dog-bone-shaped uniaxial tensile specimens. Finite element analysis was carried out for the tensile specimens to obtain stress distributions and to assure the appropriateness of the specimen configurations designed. The material was chosen because it exhibited moderate fatigue susceptibilities at high temperatures, enabling the comparison of fatigue lifetime prediction results from various testing methods. This material has been previously used under bending loading to study high-temperature structural reliability [8], long term environmental exposure [9] and effects of oxidation on strength distribution [10].

EXPERIMENTAL METHOD

Material

The material[#] used in this study was a hot-pressed silicon nitride containing 8% Y_2O_3. The room temperature basic physical and mechanical properties of the material are shown in Table 1. The material exhibited a slightly bimodal grain structure of large elongated and fine equiaxed grains. This bimodal grain structure resulted in a high fracture toughness ($K_{IC} \approx 7$ MPa√m) as well as a rising R-curve [11], typical to most in-situ toughened silicon nitrides with elongated grain structure.

Test Procedures

Dynamic and static fatigue testing for the as-machined flexure beam specimens was conducted in ambient air at 1200 and 1300°C using a SiC four-point bend fixture in an electromechanical testing machine. The inner and outer span of the test fixture were 10 mm and 30 mm, respectively. The nominal dimensions of the rectangular test specimens were 3 mm by 7 mm by 35 mm, respectively, in height, width, and length. Four loading rates of 4.2 to 4200 N/min were used in the dynamic fatigue

TABLE 1--Physical and mechanical properties of NCX 34 silicon nitride at room temperature [11,12]

Young's[1] Modulus, E (GPa) [11]	Hardness[2] H(GPa) [11]	Density[3] (g/cm^3) [11]	Fracture Toughness[4] K_{IC}(MPa√m) [11]	RT Strength[5] (MPa) [12]
296	14.5±0.6	3.37	6.90±0.56	805±50

Notes:
1. By strain gaging; 2. By Vickers microhardness indenter;
3. By buoyancy method; 4. By SEPB method; 5. With specimens of 6.35 mm (width) by 3.17 mm (height) using a four-point fixture with 9.525/19.05 mm- inner and outer spans [12].

[#] NCX 34, fabricated in 1979, Norton Co. Northboro, MA.

testing, resulting in the corresponding stressing rates of 2 to 2000 MPa/min. Stress levels applied in the static fatigue tests were 250 to 500 MPa at 1200°C, and 75 to 400 MPa at 1300°C, respectively. The number of the test specimens in the dynamic fatigue testing was four at each loading rate per temperature; whereas, the total number of the test specimens in the static fatigue testing was 14 and 21, respectively, at 1200 and 1300°C. Each test specimen was preloaded with 20 N to maintain good alignment relative to the test fixture, and held at the test temperature for 20 min prior to testing.

The tensile fatigue behavior was investigated at temperatures of 1200 and 1300°C in air. The dog-bone-shaped tensile test specimens, similar to those used in creep testing measurements by Wiederhorn et al. [13], were utilized for this testing. A test specimen with strain gages attached is shown in Fig. 1. The dimensions of the test specimens were 2.5 mm by 2.5 mm by 20 mm in cross section and gage length, respectively. To minimize the degree of misalignment of the tensile test specimen, the loading pin holes of each test specimen were tapered toward the center so that load was applied to the center of the specimen, as suggested by Carroll et al [14]. With this tapered pin hole configuration and careful specimen mounting, it was possible to achieve less than two percent misalignment at a stress of 150 MPa.

The tensile specimens were preloaded with 35 N at room temperature and heated to the test temperature. Each test specimen was kept at the test temperature for about 20 min prior to applying the full test load. The testing was conducted in dead weight creep machines. A total of 14 test specimens were used at 1200°C with a nominal applied stress range of 80 to 200 MPa; whereas, at 1300°C a total of 15 were used with applied stresses from 50 to 100 MPa. A finite element analysis of the test specimen has shown that high stress, similar in magnitude to those occurring in the gage section, occurred around the loading pin hole due to the stress concentration. Hence, particular care was taken to minimize the possibility of machining-induced damage around the tapered pin-hole. Every pin hole was carefully diamond polished with a specially designed hand tool. Also, all the surfaces and edges of each as-machined test specimen were carefully hand-sanded to minimize any machining damage.

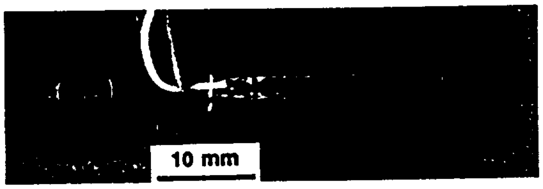

FIG. 1--A dog-bone-shaped tensile test specimen with strain gages attached.

sing rates of 2 to 2000
fatigue tests were 250 to
:, respectively. The
atigue testing was four at
he total number of the test
4 and 21, respectively, at
oaded with 20 N to maintain
and held at the test

igated at temperatures of
ensile test specimens,
ements by Wiederhorn et al.
specimen with strain gages
of the test specimens were
d gage length,
lignment of the tensile
test specimen were tapered
the center of the
With this tapered pin
ing, it was possible to
a stress of 150 MPa.

ch 35 N at room temperature
specimen was kept at the
plying the full test load.
machines. A total of 14
nal applied stress range
f 15 were used with
element analysis of the
lar in magnitude to those
the loading pin hole due
r care was taken to
damage around the tapered
d polished with a
urfaces and edges of each
sanded to minimize any

n with strain gages

Finite Element Analysis of Tensile Specimens

The finite element model for the tensile test specimen consisted of 1040 HEX/20 elements with a total of 5747 nodes. The model was analyzed using the MSC/NASTRAN finite element package. Linear static analysis was employed, with one eighth symmetry for simplicity. The specimen was loaded such that a specified uniform uniaxial tensile stress was present in the gage section. Three FORCE cards were used to apply the load. The load was applied to the one side of one element through the thickness. Since HEX/20 elements were used for the analysis, the load was divided into four parts. The outer nodes of the element received one part of the load each and the center node received two parts of the load. This load scheme was used to remain consistent with the element shape function formulations employed for the 20 node element [15].

Typical stress contours thus obtained are shown in Fig. 2, where σ_{zz} (principal stress along the specimen length) is plotted for one eighth symmetry of the specimen. This figure indicates that the maximum stress is present both at the gage section and at the pin hole (in the nine o'clock direction) due to the stress concentration. Note that the stresses in the neck region are always lower than that occurring in the gage section. Although the maximum stress occurs at the pin hole as well as at the gage section, the probability of failure is considerably higher at the gage section than at the pin hole since the volume or surface area stressed under the maximum stress is much greater at the gage section than at the pin hole. However, every attempt was made to minimize machining-induced damage.

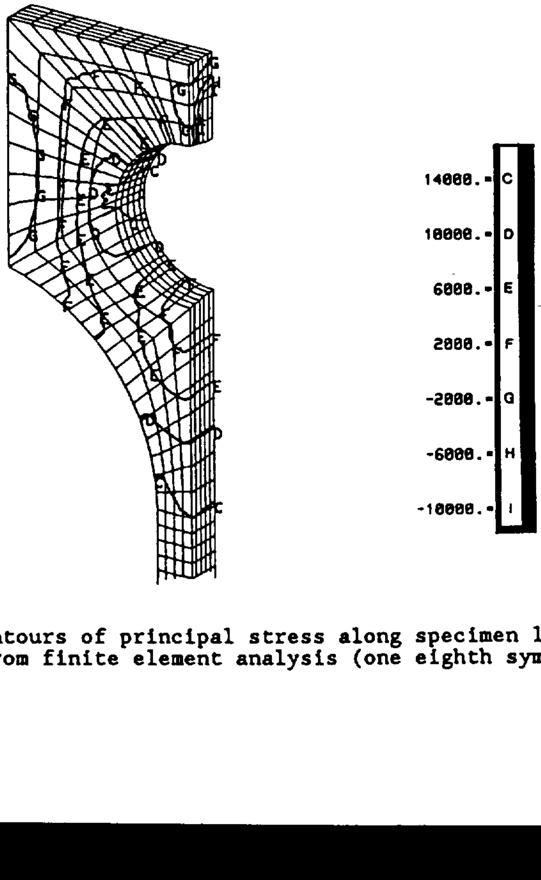

FIG. 2--Contours of principal stress along specimen length obtained from finite element analysis (one eighth symmetry).

RESULTS AND DISCUSSION

For most ceramics and glasses, slow crack growth can be expressed by the empirical relation

$$v = A\ [K_I/K_{IC}]^n \tag{1}$$

where A and n are the fatigue parameters associated with material and environment, K_I is the mode I stress intensity factor, and K_{IC} is fracture toughness. For dynamic fatigue testing which employs constant loading rate ($\dot{P}$) or constant stressing rate ($\dot{\sigma}$), the corresponding fatigue strength, σ_f, is expressed [16]

$$\sigma_f = [B\ (n+1)\ S_i^{n-2}]^{1/n+1}\ \dot{\sigma}^{1/n+1} \tag{2}$$

where $B = 2/[AY^2(n-2)K_{IC}^{n-2}]$ with Y being the crack geometry factor and S_i is the inert strength. The fatigue constants n, B and A can be obtained from the intercept and slope, respectively, of the linear fit of Log σ_f versus Log $\dot{\sigma}$. In the same way, for static fatigue testing where constant stress is applied, the time to failure (t_{fs}) can be derived easily in terms of applied stress (σ) as follows [1]

$$t_{fs} = [B\ S_i^{n-2}]\ \sigma^{-n} \tag{3}$$

Likewise, static fatigue parameters B and n can be evaluated by a linear regression analysis of the static fatigue curve when time to failure (Log t_{fs}) is plotted against applied stress (Log σ). However, it should be noted that there are several statistical approaches to estimate the fatigue parameters from dynamic and static fatigue data [17].

The relationship in fatigue life between dynamic and static fatigue is [18]

$$t_{fs} = t_{fd}/(n+1) \tag{4}$$

where t_{fd} is the time to failure in dynamic fatigue, which corresponds to $t_{fd} = \sigma_f/\dot{\sigma}$. By substituting t_{fs} in Eq. (4) into Eq. (3) with $\sigma = \sigma_f$, the dynamic fatigue curve can be converted into an equivalent static fatigue curve as follows:

$$t_{fd} = \alpha\ \sigma_f^{-n} \tag{5}$$

where α is the value associated with B, n and S_i.

Dynamic and Static Fatigue in Bending

A summary of the dynamic fatigue results at 1200 and 1300°C in air is presented in Fig. 3. The solid lines in the figure represent the best-fit lines based on Eq. (2). The decrease in fatigue strength with decreasing stressing rate, which represents fatigue susceptibility, was evident at both temperatures. The fatigue parameter (n) was determined to be $n = 16.0$ and 15.0 at 1200 and 1300°C, respectively, from a linear regression of Log σ_f versus Log $\dot{\sigma}$. Fractographic analysis of the failure surfaces revealed the presence of slow crack growth zones at the lower stressing rates, while no appreciable slow crack growth was obtained at higher stress rates.

The results obtained from the static fatigue tests at 1200 and 1300°C in air are shown in Fig. 4. The arrow marks in the figure represent the specimens that did not break before about 600 hr. Also, the solid lines in the figure represent the best-fit lines based on Eq. (3). The fatigue constant n was evaluated to be $n = 20.7$ and 15.0 at 1200 and 1300°C, respectively. The fatigue constant $n = 15\text{-}21$ thus owth can be expressed

(1)

d with material and
.or, and K_{IC} is
hich employs constant
he corresponding

(2)

eometry factor and S_i
and A can be obtained
linear fit of Log σ_f
testing where
$_s$) can be derived
1]

(3)

evaluated by a linear
en time to failure
. However, it should
ches to estimate the
data [17].

amic and static

(4)

, which corresponds to
(3) with $\sigma = \sigma_f$, the
ivalent static fatigue

(5)

1200 and 1300°C in
e figure represent the
fatigue strength with
e susceptibility, was
er (n) was determined
:ively, from a linear
nalysis of the
:k growth zones at the
rack growth was

tests at 1200 and
; in the figure
about 600 hr. Also,
it lines based on Eq.
= 20.7 and 15.0 at
it n = 15-21 thus

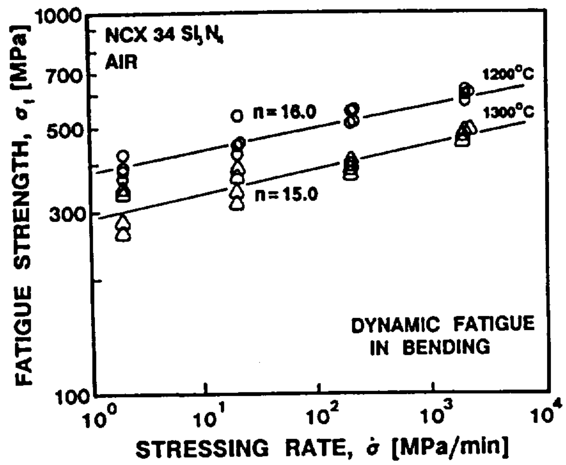

FIG. 3--Results of dynamic fatigue testing in bending of NCX 34 silicon nitride at 1200 and 1300°C in air.

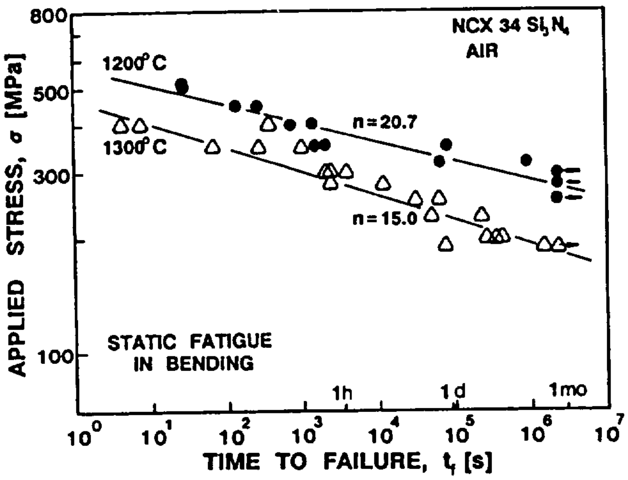

FIG. 4--Results of static fatigue testing in bending of NCX 34 silicon nitride at 1200 and 1300°C in air.

obtained agrees reasonably well with the value of n = 15-16 determined from the dynamic fatigue testing. A value of n = 12 was reported previously, obtained from static fatigue with MOR bars at 1400°C in air [19].

It is interesting to compare the static fatigue results obtained in this study with those obtained by previous researchers. Particularly at 1200°C, the stress rupture data of Quinn [9] is very different from those reported in this study. Similarly, Wiederhorn and Tighe [8] observed almost no failure at 1200°C at 400 MPa, even with specimen containing Knoop indents. The data in Fig. 4, however, indicates that they all should have failed at about 1000 seconds. This is due to the fact that there are billet to billet variations in the material, as pointed out previously [8]. Similarly, Quinn [9] reported bands of nonuniform material which cracked and crept differently. Thus, NCX 34 silicon nitride seems to be a such a material that some subtle chemistry or microstructural variation leads to radically different behavior.

It is important to note that appreciable creep deformation occurred for the specimens subjected at 1300°C to the lowest stressing rate in the dynamic fatigue testing and to the lowest applied stress in the static fatigue testing. Fracture surfaces of the specimens tested at different stressing rates or applied stresses showed that slow crack growth zones dominate failure as stressing rate or applied stress decreases. One complication evident from the fractography is the shape of the crack developed, especially in the specimens subjected to long time to failure. The cracks, though initially half-pennies in configuration, develop into corner and straight-through cracks as the crack size approaches the specimen size, as shown in Fig. 5. This may affect the values of the measured fatigue parameters, due to changes in crack geometry and net section stress. Further, enhanced creep at high temperature can result in neutral axis shift attributed to asymmetric creep behavior between the compression and tension sides of a flexure beam specimen [20]. This neutral axis shift may affect the stress distribution and possibly change the fatigue parameters.

Static Fatigue in Tension

Some of the uniaxial tensile specimens failed from the loading pin holes. This undesirable pin-hole failure was found to be associated with machining damage, which was minimized later by careful hand polishing with diamond compound around the tapered pin holes. Another undesirable failure associated with machining damage occurred at the intersection of the straight gage section and the radius of curvature of the neck region, where a small surface discontinuity (damage) existed. The typical gage section and intersection failures are shown in Fig. 6. This neck region failure was also minimized by careful hand polishing around the intersections with SiC sand paper.

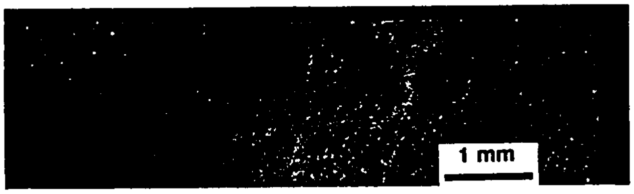

FIG. 5--Fracture surface of a specimen subjected to static fatigue in bending at 1300°C; σ = 190 MPa and t_f = 456 hr.

: fatigue results obtained
: researchers. Particularly
9] is very different from
derhorn and Tighe [8]
Pa, even with specimen
, however, indicates that
onds. This is due to the
ns in the material, as
[9] reported bands of
ifferently. Thus, NCX 34
that some subtle chemistry
ly different behavior.

e creep deformation
C to the lowest stressing
e lowest applied stress in
s of the specimens tested
ses showed that slow crack
te or applied stress
fractography is the shape
cimens subjected to long
y half-pennies in
ht-through cracks as the
hown in Fig. 5. This may
ameters, due to changes in
er, enhanced creep at high
attributed to asymmetric
nsion sides of a flexure
may affect the stress
parameters.

failed from the loading pin
found to be associated
ter by careful hand
pered pin holes. Another
damage occurred at the
the radius of curvature of
tinuity (damage) existed.
lures are shown in Fig. 6.
careful hand polishing

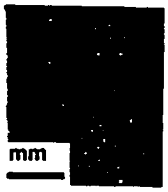

ed to static fatigue in

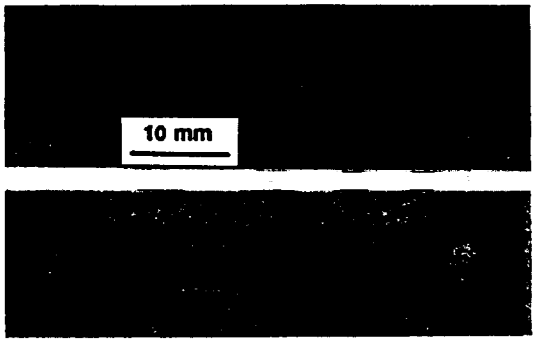

(a)

(b)

FIG. 6--Fractured uniaxial tensile test specimens: (a) desirable gage section failure; (b) undesirable neck region failure.

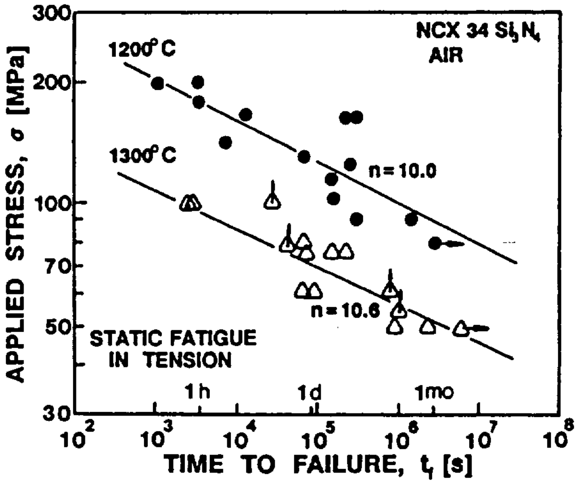

FIG. 7--Results of static fatigue testing in uniaxial tension of NCX 34 silicon nitride at 1200 and 1300°C in air.

A summary of the uniaxial tensile fatigue results obtained at 1200 and 1300°C in air is presented in Fig. 7. The solid lines in the figure represent the best-fit lines obtained by a linear regression analysis of Log t_f versus Log σ. It should be noted that specimens failed from the pin holes and neck region (marked with vertical arrows) were excluded in the regression analysis. The horizontal arrow marks in the figure represent the test specimens that did not break before 600 hr. The fatigue parameter n was determined to be n = 10.0 and 10.6 at 1200 and 1300°C, respectively. This fatigue parameter of n ≈ 10 is somewhat lower than that (n ≈ 15-21) from the dynamic and static fatigue testing with the flexure beam specimens. By contrast, the parameter of n ≈ 10

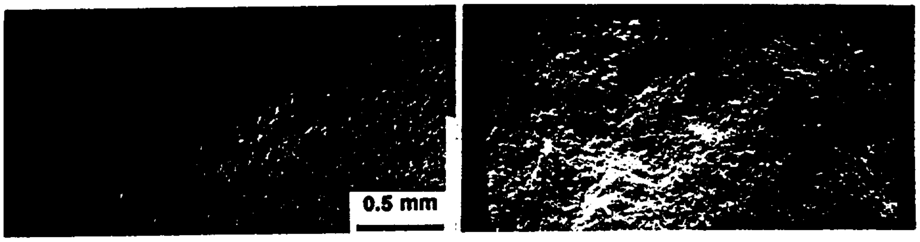

(a) (b)

Fig. 8--Fracture surfaces of specimens subjected to static fatigue in uniaxial tension at 1300°C: (a) $\sigma = 100$ MPa; $t_f = 42$ min; (b) $\sigma = 50$ MPa; $t_f = 682$ h.

determined for the smooth (as-machined) specimens is higher than the value of $n = 5.2$ obtained for the uniaxial tensile specimens with Knoop indent cracks by Henager and Jones [21].

At high applied stress, failure was usually (but not always clearly) associated with slow crack growth; whereas, at lower applied stress creep-induced failure was dominant at both temperatures. Multiple creep crack formation in the gage section was typically observed for the specimens failed at lower stresses. Fig. 8 shows the fracture surfaces of specimens failed at 1300°C at two different applied stresses of $\sigma = 100$ and 50 MPa. The formation of a dominant crack is evident for the specimen failed at 100 MPa with $t_f = 42$ min (volume failure). However, a clear fracture origin was not readily discernable from the specimen failed at 50 MPa with $t_f = 682$ hr, suggesting that crack coalescence associated with creep damage caused specimen failure.

Comparison of Fatigue Parameters

Comparison of dynamic and static fatigue behavior in bending can be evaluated by converting the dynamic fatigue data into a corresponding static fatigue curve via Eqs. (4) and (5). The resulting plots are shown in Fig. 9, where the converted dynamic fatigue data are compared with the static fatigue data. Also included in the figure are the data obtained from the uniaxial tensile fatigue testing.

Overall agreement between dynamic and static fatigue in bending is reasonably good, notwithstanding a little variation, especially at 1200°C. Therefore, based on these results it is possible to obtain slow crack growth parameters from either static or dynamic fatigue testing techniques, as observed previously for Ceralloy 147A silicon nitride [22]. The dynamic fatigue testing is preferable since the time to failure is shorter in dynamic fatigue than in static fatigue. Care should be taken when an extrapolation based on the dynamic fatigue data is made to predict slow crack growth behavior in the low applied stress regime.

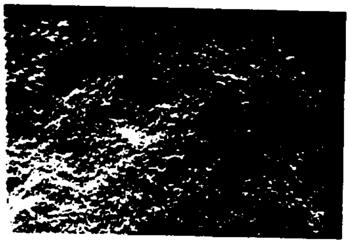

(b)

ted to static fatigue in
$_f$ = 42 min;

nens is higher than the
nsile specimens with Knoop

lly (but not always
hereas, at lower applied
oth temperatures.
tion was typically
esses. Fig. 8 shows the
C at two different applied
of a dominant crack is
h t_f = 42 min (volume
s not readily discernable
32 hr, suggesting that
caused specimen failure.

behavior in bending can
data into a corresponding
e resulting plots are
atigue data are compared
n the figure are the data
ting.

atic fatigue in bending is
ation, especially at
s possible to obtain slow
dynamic fatigue testing
147A silicon nitride
le since the time to
static fatigue. Care
the dynamic fatigue data
n the low applied stress

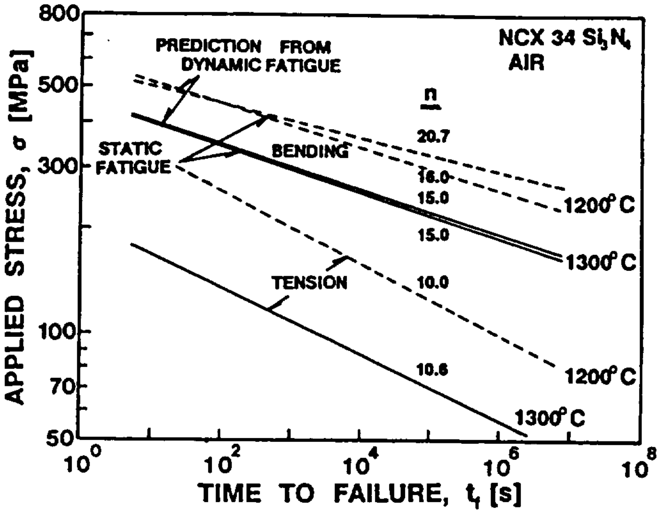

FIG. 9--Comparison of fatigue life curves obtained from dynamic and static bend fatigue and tensile static fatigue for NCX 34 silicon nitride at 1200 and 1300°C in air.

The difference between the tensile static fatigue and the dynamic or static bend fatigue is much larger as seen in Fig. 9. The difference in fatigue strength between the tensile and bend loading is probably due to the difference in effective volume or surface area between the two specimen configurations (dog-bone-shaped tensile specimens and flexure beam specimens). The ratio of bending strength to tensile strength can be calculated using the following equation

$$\sigma_T/\sigma_B = [A_{effB}/A_{effT}]^{1/m} \quad \text{or}$$
$$= [V_{effB}/V_{effT}]^{1/m} \qquad (6)$$

where A_{eff} and V_{eff} are effective surface area and effective volume, respectively, and m is the Weibull modulus. Since the Weibull modulus at 1200 and 1300°C were not known, a value of $m \approx 10$ was arbitrarily chosen. By assuming that failure is controlled by volume-associated failure, and taking $V_{effB} = 11.28$ mm^3 and $V_{effT} = 62.5$ mm^3 based on the fixture and specimen geometry, a value of $\sigma_T/\sigma_B = 0.786$ is obtained. This ratio of 0.786 is a reasonable estimate at 1200°C, but a poor one at 1300°C since the ratios of the tensile fatigue strength to the bend fatigue strength (dynamic or static) at $t_f = 1$ s (assuming little fatigue) are 0.7 and 0.4, respectively.

Using the experimental data and the appropriate equation and assuming $K_{IC} \approx 5$ MPa$\sqrt{m}$ at 1200 to 1300°C, the fatigue parameter A was calculated and tabulated in Table 2. By using the A value, the fatigue life curve (Fig. 9) was converted into a crack velocity curve, Fig. 10, where crack velocity is plotted, based on Eq. (1), as a function of normalized stress intensity factor K_I/K_{IC}. The crack velocity curve obtained at 1300°C from the uniaxial tensile fatigue with Knoop indent crack [18] was also included in the figure for comparison. As already

TABLE 2--Summary of fatigue parameters of NCX 34 silicon nitride at 1200 and 1300°C in air under various loading.

Loading and geometry	Temp (°C)	n	B (MPa^{2}min)	A (m/min)
Dynamic in Bending	1200 1300	16.0 15.0	14.702 10.269	0.194 0.300
Static in Bending	1200 1300	20.7 15.0	11.148 11.697	0.191 0.262
Static in Tension	1200 1300	10.0 10.6	16.242 11.126	0.319 0.417
Static in Tension with Indents [21]	1300	5.2	-	-

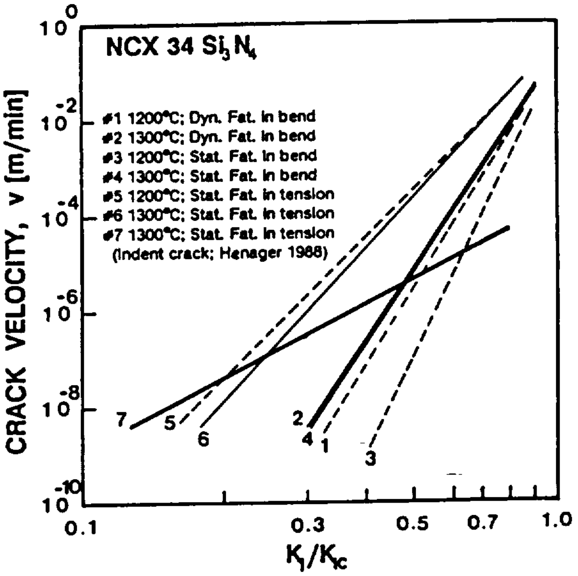

FIG. 10--Summary of crack velocity curves obtained from different testing methods for NCX 34 silicon nitride at 1200 and 1300°C in air.

shown in the fatigue life curve (Fig. 9), there is reasonably good agreement between the dynamic and static fatigue in bending, but a large discrepancy between the uniaxial tension and bend fatigue data. Fig. 10 also shows that in uniaxial tensile loading the fatigue susceptibility of the indent cracks was much greater than that of the smooth (as-machined) specimens, as observed previously for the GN-10 silicon nitride material at 1200°C [5].

34 silicon nitride at

β ?a min)	A (m/min)
14.702	0.194
10.269	0.300
11.148	0.191
11.697	0.262
16.242	0.319
1.126	0.417
-	-

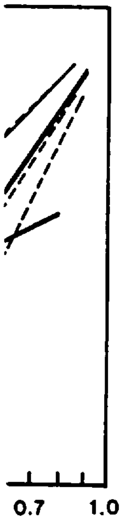

ined from different
1200 and 1300°C in air.

is reasonably good
ie in bending, but a large
and fatigue data. Fig. 10
fatigue susceptibility
of the smooth (as-
the GN-10 silicon

The difference in fatigue susceptibility of smooth and Knoop precracked specimens may be due to the nature of the cracks used or the method of parameter estimation: The dynamic and static methods determine parameters empirically from stress and time-to-failure data that results from inherent defects that develop into cracks, grow and cause failure; whereas fracture mechanics methods, such as the Knoop indent, attempt to directly observe and track the length of an initially sharp, well developed crack.

These results indicate that there is no unique fatigue testing methodology, implying that a variety of fatigue loading cycles, specimen configurations and flaw systems should be used to thoroughly characterize fatigue behavior of ceramic components that will have multiaxial stresses. An important result obtained from this fatigue testing study is that the dog-bone-shaped tensile specimens that have been used primarily in creep studies of ceramics can be applied to high-temperature tensile fatigue life (stress rupture) testing.

CONCLUSIONS

(1). The high-temperature fatigue parameters for this material determined from dynamic and static fatigue bend data are in good agreement. Fatigue parameters were n = 15 to 20.

(2). A discrepancy exists between bend (dynamic or static) fatigue and uniaxial tensile fatigue, resulting in more fatigue susceptibility for uniaxial tension. The discrepancy is presumably due to creep associated mechanism, different in bending and tension primarily attributed to neutral axis shift occurring in the bend specimens.

(3). Creep-associated failure became dominant as applied stress or stressing rate decreased. In this case, neutral axis shift via asymmetric creep deformation may have affected the stress distribution of flexure specimens, and presumably changed the fatigue parameters, which were based on an elastic stress solution. The use of tensile specimens is thus strongly preferable in this case.

(4). Fatigue behavior should be evaluated with a variety of stress states, loading cycles and flaw (inherent or artificial) configurations to ensure accurate life prediction parameters.

ACKNOWLEDGEMENTS

This research was sponsored in part by the Ceramic Technology Project, DOE Office of Transportation Technologies, under contract DE-AC05-84OR21400 with Martin Marietta Energy Systems, Inc. The authors are grateful to R. Pawlik at NASA Lewis for his experimental and SEM work.

REFERENCES

[1] Ritter, J. E., "Engineering Design and Fatigue Failure of Brittle Materials," pp 661-686 in Fracture Mechanics of Ceramics, Vol. 4, Bradt, R. C., Hasselman, D. P. H., and Lange, F. F. Eds., Plenum Publishing Co., NY, 1978.

[2] Trantina, G. G., "Strength and Life Prediction for Hot-Pressed Silicon Nitride," Journal of American Ceramic Society, Vol. 62, 1979, pp 377-380.

[3] Govila, R. K., "Uniaxial Tensile and Flexural Stress Rupture

Strength of Hot-Pressed Si_3N_4," Journal of American Ceramic Society, Vol. 65, 1982, pp 15-21.

[4] Quinn, G. D., and Quinn, J. B., "Slow Crack Growth in Hot-Pressed Silicon Nitride," pp 603-636 in Fracture Mechanics of Ceramics, Vol. 6, Bradt, R. C., et al. Eds., Plenum Press, NY, 1983.

[5] Choi, S. R., and Salem, J. A., "Comparison of Dynamic Fatigue Behavior Between SiC Whisker-Reinforced Composite and Monolithic Silicon Nitrides," NASA TM 103707, NASA Lewis Research Center, Cleveland, OH, 1991.

[6] Chuck, L., McCullum, D. E., Hecht, N. L., and Goodrich, S. M., "High-Temperature Tension-Tension Cyclic Fatigue for a Hipped Silicon Nitride," Ceramic Engineering and Science Proceedings, Vol. 12, 1991, pp 1509-1523.

[7] Evans, A. G., and Wiederhorn, S. M., "Crack Propagation and Failure Prediction in Silicon Nitride at Elevated Temperatures," Journal of Material Science Vol. 9, 1974, pp 270-278.

[8] Wiederhorn, S. M., and Tighe, N. J., "Structural Reliability of Yttria Doped Hot Pressed Silicon Nitride at Elevated Temperatures," Journal of American Ceramic Society, Vol. 66, 1983, pp 884-889.

[9] Quinn, G. D., "Characterization of Turbine Ceramics After Long Term Environmental Exposure," U.S. Army Tech. Report TR 80-15, U.S Army Materials and Mechanics Research Center, Watertown, MA, 1980.

[10] Easler, T.E., Bradt, R. C., and Tressler, R. E., "Effect of Oxidation and Oxidation Under Load on Strength Distribution of Silicon Nitride," Journal of American Ceramic Society, Vol. 65, 1982, pp 317-319.

[11] Choi, S. R. and Salem, J. A., Bimonthly Progress Report, Ceramic Technology for Advanced Heat Engines Project, W.B.S. Element 3.2.1.7., November-December/1991, Oak Ridge National Laboratory, Oak Ridge, TN, 1991.

[12] Sanders, W. A., unpublished work, NASA Lewis Research Center.

[13] Wiederhorn, S. M., Roberts, D. E., Chuang, T.-Z., and Chuck, L., "Damage-Enhanced Creep in a Siliconized Silicon Carbide: Phenomenology," Journal of American Ceramic Society, Vol. 71, 1988, pp 602-608.

[14] Carroll, D. F., Wiederhorn, S. M., and Roberts, D. E., "Technique for Tensile Creep Testing of Ceramics," Journal of American Ceramic Society, Vol. 72, 1989, pp 1610-1614.

[15] Bathe, K. J., Finite Element Procedures in Engineering Analysis, Prentice-Hall, Englewood Cliffs, NJ, 1982.

[16] Evans, A. G., "Slow Crack Growth in Brittle Materials under Dynamic Loading Conditions," International Journal of Fracture, Vol. 10, 1974, pp 1699-1705.

[17] Jakus, K., Coyne, D. C., and Ritter, J. E., "Analysis of Fatigue Data for Lifetime Prediction for Ceramic Materials," Journal of Materials Science, Vol. 13, 1978, pp 2071-2080.

[18] Davidge, R. W., McLaren, J. R., and Tappin, G., "Strength-Probability-Time (SPT) Relationship in Ceramics," Journal of

f *American Ceramic*

ck Growth in Hot-Pressed
Mechanics of Ceramics,
Press, NY, 1983.

n of Dynamic Fatigue
omposite and Monolithic
Lewis Research Center,

and Goodrich, S. M.,
Fatigue for a Hipped
d Science Proceedings,

ck Propagation and Failure
Temperatures," *Journal*
-278.

ructural Reliability of
at Elevated
ic Society, Vol. 66, 1983,

e Ceramics After Long Term
Report TR 80-15, U.S Army
Watertown, MA, 1980.

R. E., "Effect of
ength Distribution of
ramic Society, Vol. 65,

rogress Report, Ceramic
ect, W.B.S. Element
ge National Laboratory,

wis Research Center.

, T.-Z., and Chuck, L.,
licon Carbide:
mic Society, Vol. 71,

berts, D. E., "Technique
ournal of American Ceramic

in Engineering Analysis,
.

le Materials under Dynamic
al of Fracture, Vol. 10,

., "Analysis of Fatigue
aterials," *Journal of*
-2080.

, G., "Strength-
amics," *Journal of*

Materials Science, Vol. 8, 1973, pp 1699-1705.

[19] Larsen, D. C., and Adams, J. W., "Property Screening and Evaluation of Ceramic Turbine Materials," AFWAL-TR- 83-4141, Wright Aeronautical Laboratories, Wright-Patterson AFB, OH, 1984.

[20] Chuang, T.-J., and Wiederhorn, S. M., "Damage-Enhanced Creep in a Siliconized Silicon Carbide: Mechanics of Deformation," *Journal of American Ceramic Society*, Vol. 71, 1988, pp 595-601.

[21] Henager, C. H., and Jones, R. H., "Environmental Effects on Slow Crack Growth in Silicon Nitride," *Ceramic Engineering and Science Proceedings*, Vol. 9, 1988, pp 1525-1530.

[22] Salem, J. A., and Choi, S. R., Ceramic Technology Project Semiannual Progress Report for April 1991 through September 1991, pp 305-319, ORNL/TM-11984, Oak Ridge National Laboratory, Oak Ridge, TN, 1992.

A Viscoplastic Constitutive Theory for Monolithic Ceramics—I

L. A. Janosik
NASA Lewis Research Center,
Cleveland, OH 44135

S. F. Duffy
Cleveland State University,
Cleveland, OH 44115

This paper, which is the first of two in a series, provides an overview of a viscoplastic constitutive model that accounts for time-dependent material deformation (e.g., creep, stress relaxation, etc.) in monolithic ceramics. Using continuum principles of engineering mechanics, the complete theory is derived from a scalar dissipative potential function first proposed by Robinson (1978), and later utilized by Duffy (1988). Derivations based on a flow potential function provide an assurance that the inelastic boundary value problem is well posed, and solutions obtained are unique. The specific formulation used here for the threshold function (a component of the flow potential function) was originally proposed by Willam and Warnke (1975) in order to formulate constitutive equations for time-independent classical plasticity behavior observed in cement and unreinforced concrete. Here constitutive equations formulated for the flow law (strain rate) and evolutionary law employ stress invariants to define the functional dependence on the Cauchy stress and a tensorial state variable. This particular formulation of the viscoplastic model exhibits a sensitivity to hydrostatic stress, and allows different behavior in tension and compression.

Introduction

With increasing use of ceramic materials in high-temperature applications, the need arises to predict thermomechanical behavior accurately. This paper will focus on inelastic deformation behavior associated with these service conditions. A number of constitutive theories for materials that exhibit sensitivity to the hydrostatic component of stress have been proposed that characterize deformation using time-independent classical plasticity as a foundation. Corapcioglu and Uz (1978) reviewed several of these theories by focusing on the proposed form of the individual yield function. The review includes the works of Kuhn and Downey (1971), Shima and Oyane (1976) and Green (1972). Not included is the work by Gurson (1977) who not only developed yield criteria and a flow rule, but also discussed the role of void nucleation. Subsequent work by Mear and Hutchinson (1985) extended Gurson's work to include kinematic hardening of the yield surfaces. Although the previously mentioned theories admit a dependence on the hydrostatic component of stress, none of these theories allow different behavior in tension and compression. Willam and Warnke (1975) proposed a yield criterion for concrete that admits a dependence on the hydrostatic component of stress and explicitly allows different material responses in tension and compression. Several formulations of their model exist, i.e., a three-parameter formulation and a five-parameter formulation. For simplicity the work presented here builds on the three-parameter formulation.

The aforementioned theories are somewhat lacking in that they are unable to capture creep, relaxation, and rate-sensitive phenomena exhibited by ceramic materials at high temperature. A noted exception is the recent work by Ding et al. (1994), as well as the work by White and Hazime (1995). Another exception is a paper by Liu et al. (1997), which is an extension of the work presented by Ding and co-workers. As these authors point out, when subjected to elevated service temperatures, ceramic materials exhibit complex thermomechanical behavior that is inherently time dependent, and hereditary in the sense that current behavior depends not only on current conditions, but also on thermomechanical history. This paper presents the formulation of a macroscopic continuum theory that captures these time-dependent phenomena. Specifically, the overview contained in this paper focuses on the complete multiaxial derivation of the constitutive model, and examines the attending geometric implications when the Willam–Warnke (1975) yield function is utilized as a scalar threshold function. A second paper, which will appear shortly, examines specific time-dependent stress–strain behavior that can be modeled with the constitutive relationship presented in this article. No attempt is made here to assess the accuracy of the model in comparison to experiment. A quantitative assessment is reserved for a later date, after the material constants have been suitably characterized for a specific ceramic material. The quantitative assessment could easily dovetail with the nascent efforts of White and co-workers.

Flow Potential

Early work in the field of metal plasticity indicated that inelastic deformations are essentially unaffected by hydrostatic stress. This is not the case for ceramic-based material systems, unless the ceramic is fully dense. The theory presented here allows for fully dense material behavior as a limiting case. In addition, as Chuang and Duffy (1994) point out, ceramic materials exhibit different time-dependent behavior in tension and compression. Thus inelastic deformation models for ceramics must be constructed in a fashion that admits sensitivity to hydrostatic stress and differing behavior in tension and compression. This will be accomplished here by developing an extension of a J_2 model first proposed by Robinson (1978) and later extended to sintered powder metals by Duffy (1988). Although the viscoplastic model presented by Duffy (1988) admitted a sensitivity to hydrostatic stress, it did not allow for different material behavior in tension and compression.

The complete theory is derivable from a scalar dissipative potential function identified here as Ω. Under isothermal conditions this function is dependent upon the applied stress (σ_{ij}) and internal state variable (α_{ij}), i.e.,

$$\Omega = \Omega(\sigma_{ij}, \alpha_{ij}) \tag{1}$$

Contributed by the International Gas Turbine Institute and presented at the 41st International Gas Turbine and Aeroengine Congress and Exhibition, Birmingham, United Kingdom, June 10–13, 1996. Manuscript received at ASME Headquarters February 1996. Paper No. 96-GT-368. Associate Technical Editor: J. N. Shinn.

The stress dependence for a J_2 plasticity model or a J_2 viscoplasticity model is usually stipulated in terms of the deviatoric components of the applied stress, i.e.,

$$S_{ij} = \sigma_{ij} - (1/3)\sigma_{kk}\delta_{ij} \tag{2}$$

and a deviatoric state variable

$$a_{ij} = \alpha_{ij} - (1/3)\alpha_{kk}\delta_{ij} \tag{3}$$

For the viscoplasticity model presented here these deviatoric tensors are incorporated, along with the effective stress

$$\eta_{ij} = \sigma_{ij} - \alpha_{ij} \tag{4}$$

and an effective deviatoric stress, identified as

$$\Sigma_{ij} = S_{ij} - a_{ij} \tag{5}$$

Both tensors, i.e., η_{ij} and Σ_{ij}, are utilized for notational convenience.

The potential nature of Ω is exhibited by the manner in which the flow and evolutionary laws are derived. The flow law is derived from Ω by taking the partial derivative with respect to the applied stress, i.e.,

$$\dot{\epsilon}_{ij} = \frac{\partial\Omega}{\partial\sigma_{ij}} \tag{6}$$

The adoption of a flow potential and the concept of normality, as expressed in Eq. (6), were introduced by Rice (1970). In his work the relationship above was established using thermodynamic arguments. The authors wish to point out that Eq. (6) holds for each individual inelastic state.

The evolutionary law is similarly derived from the flow potential. The rate of change of the internal stress is expressed as

$$\dot{\alpha}_{ij} = -h\,\frac{\partial\Omega}{\partial\alpha_{ij}} \tag{7}$$

where h is a scalar function of the inelastic state variable (i.e., the internal stress) only. Using arguments similar to Rice's, Ponter and Leckie (1976) have demonstrated the appropriateness of this type of evolutionary law.

To give the flow potential a specific form, the following integral format proposed by Robinson (1978) is adopted:

$$\Omega = K^2\left[\left(\frac{1}{2\mu}\right)\int F^n dF + \left(\frac{R}{H}\right)\int G^m dG\right] \tag{8}$$

where μ, R, H, and K are material constants. In this formulation μ is a viscosity constant, H is a hardening constant, n and m are unitless exponents, and R is associated with recovery. The octahedral threshold shear stress K appearing in Eq. (8) is generally considered a scalar state variable that accounts for isotropic hardening (or softening). However, since isotropic hardening is often negligible at high homologous temperatures (≥ 0.5), to a first approximation K is taken to be a constant for metals. This assumption will be adopted in the present work regarding ceramic materials. The reader is directed to the work by Janosik (1998) for specific details regarding the experimental test matrix needed to characterize these parameters.

Several of the quantities identified as material constants in the theory are strongly temperature dependent in a nonisothermal environment. However, for simplicity, the present work is restricted to isothermal conditions. A paper by Robinson and Swindeman (1982) provides the approach by which an extension can be made to nonisothermal conditions. The present article concentrates on representing the complexities associated with establishing an inelastic constitutive model that will satisfy the assumptions stipulated herein for ceramic materials.

The dependence upon the effective stress Σ_{ij} and the deviatoric internal stress a_{ij} are introduced through the scalar functions

$$F = F(\Sigma_{ij}, \eta_{ij}) \tag{9}$$

and

$$G = G(a_{ij}, \alpha_{ij}) \tag{10}$$

Inclusion of η_{ij} and α_{ij} will account for sensitivity to hydrostatic stress. The concept of a threshold function was introduced by Bingham (1922) and later generalized by Hohenemser and Prager (1932). Correspondingly, F will be referred to as a

Nomenclature

a_{ij} = deviatoric component of the state variable tensor
B = constant (in general polynomial form of F)
C = coefficient used to simplify expressions for flow and evolutionary laws
F = Bingham–Prager threshold function
G = scalar state function
H = hardening constant
h = scalar hardening function dependent on the inelastic state variable
I_1, J_2, J_3 = invariants associated with the Willam–Warnke threshold function F
$\mathcal{J}_1$, $\mathcal{J}_2$, $\mathcal{J}_3$ = invariants associated with the scalar function G
K = octahedral threshold shear stress
m, n = unitless exponents
R = recovery constant
r = position vector in Π-plane representing deviatoric component of a stress state
S_{ij} = deviatoric component of applied stress tensor
u, v = component of position vector r
Y = normalized threshold stress
α_{ij} = internal state variable tensor
$\dot{\alpha}_{ij}$ = state variable evolutionary law
δ_{ij} = Kronecker delta
ϵ_{ij} = flow law (inelastic strain rate)
η_{ij} = effective stress tensor
θ = angle of similitude measured in the Π-plane
λ = scalar function in general polynomial form of F; dependent on J_3 through the angle of similitude θ
μ = viscosity constant
Π = plane perpendicular to the hydrostatic stress line in the Haigh–Westergaard stress space (i.e., the Π-plane)
π = 3.14159 . . .
ρ = Willam–Warnke hydrostatic threshold parameter
Σ_{ij} = effective deviatoric stress tensor
σ = threshold stress
σ_{ij} = applied Cauchy stress tensor
Ω = scalar dissipative potential function
$\hat{}$ = denotes parameters associated with scalar function F
$\tilde{}$ = denotes parameters associated with scalar function G
$\dot{}$ = rate

Subscripts

bc = equal biaxial compressive
c = compressive
i, j, k = tensorial components
m, n = tensorial components
q, u, v = tensorial components
t = tensile

Bingham–Prager threshold function. Inelastic deformation occurs only for those stress states where

$$F(\Sigma_{ij}, \eta_{ij}) > 0 \tag{11}$$

For frame indifference, the scalar functions F and G (and hence Ω) must be form invariant under all proper orthogonal transformations. This condition is ensured if the functions depend only on the principal invariants of Σ_{ij}, a_{ij}, η_{ij}, and α_{ij}, that is

$$F = F(I_1, J_2, J_3) \tag{12}$$

and

$$G = G(\mathcal{I}_1, \mathcal{J}_2, \mathcal{J}_3) \tag{13}$$

where

$$I_1 = \eta_{ii} \tag{14}$$

$$J_2 = (\tfrac{1}{2})\Sigma_{ij}\Sigma_{ij} \tag{15}$$

$$J_3 = (\tfrac{1}{3})\Sigma_{ij}\Sigma_{jk}\Sigma_{ki} \tag{16}$$

and

$$\mathcal{I}_1 = \alpha_{ii} \tag{17}$$

$$\mathcal{J}_2 = (\tfrac{1}{2})a_{ij}a_{ij} \tag{18}$$

$$\mathcal{J}_3 = (\tfrac{1}{3})a_{ij}a_{jk}a_{ki} \tag{19}$$

These scalar quantities are elements of what is known in invariant theory as an integrity basis for the functions F and G.

A three parameter flow criterion proposed by Willam and Warnke (1975) will serve as the Bingham–Prager threshold function, F. The Willam–Warnke criterion uses the previously mentioned stress invariants to define the functional dependence on the Cauchy stress (σ_{ij}) and internal state variable (α_{ij}). In general, this flow criterion can be constructed from the following general polynomial:

$$F = \lambda\left(\frac{\sqrt{J_2}}{\sigma_c}\right) + B\left(\frac{I_1}{\sigma_c}\right) - 1 \tag{20}$$

where σ_c is the uniaxial threshold flow stress in compression and B is a constant determined by considering homogeneously stressed elements in the virgin inelastic state, i.e.,

$$\alpha_{ij} = 0 \tag{21}$$

Note that a threshold flow stress is similar in nature to a yield stress in classical plasticity. In addition, λ is a function dependent on the invariant J_3 and other threshold stress parameters that are defined momentarily. The specific details in deriving the final form of the function F can be found from Willam and Warnke (1975), and this final formulation is stated here as

$$F(I_1, J_2, J_3) = \frac{1}{\sigma_c}\left[\frac{1}{r(\vartheta)}\right]\left[\frac{2J_2}{5}\right]^{1/2} + \frac{I_1}{3\rho\sigma_c} - 1 \tag{22}$$

for brevity. The function F is implicitly dependent on J_3 through the function r, which is characterized in the next section. This function is dependent on the angle of similitude ϑ, which is defined by the expression

$$\cos(3\vartheta) = \frac{(3\sqrt{3})J_3}{2(J_2)^{3/2}} \tag{23}$$

The invariant I_1 in Eq. (22) admits a sensitivity to hydrostatic stress. The invariant J_3 in Eq. (23) accounts for different behavior in tension and compression, since this invariant changes sign when the direction of a stress component is reversed. The parameter ρ characterizes the tensile hydrostatic threshold flow stress. This parameter will also be considered in more detail in the next section.

A similar functional form is adopted for the scalar state function G, i.e.,

$$G(\mathcal{I}_1, \mathcal{J}_2, \mathcal{J}_3) = \frac{1}{\sigma_c}\frac{1}{r(\hat{\vartheta})}\left[\frac{2\mathcal{J}_2}{5}\right]^{1/2} + \frac{\mathcal{I}_1}{3\rho\sigma_c} \tag{24}$$

The function G stipulated in the expression above is implicitly dependent on $\mathcal{J}_3$ through a second angle of similitude, $\hat{\vartheta}$, which is defined by the expression

$$\cos(3\hat{\vartheta}) = \frac{(3\sqrt{3})\mathcal{J}_3}{2(\mathcal{J}_2)^{3/2}} \tag{25}$$

This formulation assumes a threshold does not exist for the scalar function G, and follows the framework of previously proposed constitutive models based on Robinson's (1978) viscoplastic law.

Threshold Parameters

For the Willam–Warnke three-parameter formulation, the model parameters include σ_t, the tensile uniaxial threshold stress, σ_c, the compressive uniaxial threshold stress, and σ_{bc}, the equal biaxial compressive threshold stress. The function $r(\vartheta)$ appearing in Eq. (22) and the function $r(\hat{\vartheta})$ appearing in Eq. (24) depend implicitly on these parameters. This is demonstrated later in this section.

To explore the nature of the potential function, level surfaces of Ω are projected onto various stress subspaces for the virgin inelastic state. Restricting our view to the virgin inelastic state implies surfaces of Ω = const are also surfaces of F = const. As noted previously, F plays the role of a Bingham–Prager threshold function. Since there are an infinite family of surfaces F = const, each associated with a particular magnitude of the inelastic strain rate, we restrict the scope of this discussion to threshold surfaces to gain an understanding of the physical nature of the current model.

The parameters σ_t and σ_c are depicted in Fig. 1 where a threshold surface ($F = 0$) has been projected onto the σ_{11}–σ_{22} stress subspace. For illustration, a set of threshold flow stress

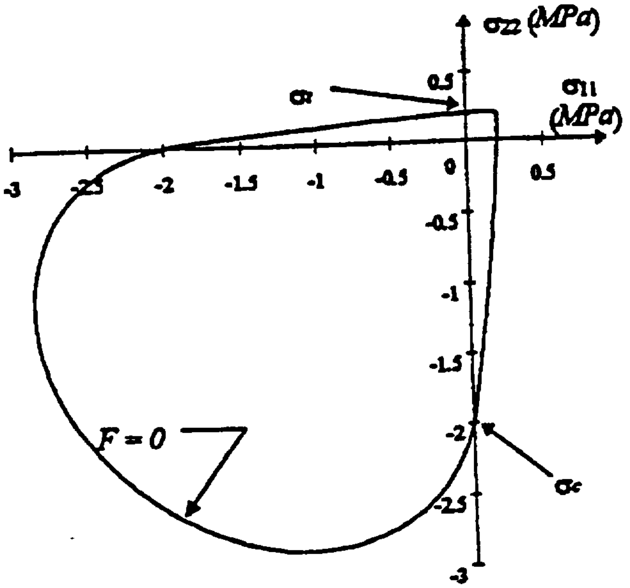

Fig. 1 Threshold function projected onto the σ_{11}–σ_{22} stress plane

values has been adopted that roughly corresponds to values anticipated for isotropic monolithic ceramics. Specifically, the compressive uniaxial threshold stress value is $\sigma_c = 2.00$ MPa. The tensile uniaxial threshold stress value is $\sigma_t = 0.20$ MPa, and the equal biaxial compressive threshold stress value is $\sigma_{bc} = 2.32$ MPa. Using these stress threshold values, the flow function in Fig. 1 defines a smooth flow surface for any combination of stresses. States of stress lying within the flow surface depicted in this figure represent elastic states of stress. Inelastic flow occurs when any load path reaches this surface, or other surfaces beyond (i.e., surfaces where $F > 0$). It is readily discerned from this figure that the constitutive model allows different flow behavior in tension and compression.

The threshold parameter σ_{bc} can be seen when a cutting plane is passed through the flow surface ($F = 0$) in the Haigh–Westergaard stress space. Specifically the cutting plane contains the hydrostatic stress line and it intersects the conic surface ($F = 0$) along two lines (see Fig. 2). By convention, these lines of intersection are termed meridians. The relative position of each meridian is defined by the angle of similitude $\tilde{\theta}$ (which is depicted in Fig. 3). For the tensile meridian $\tilde{\theta} = 0$, and for the compressive meridian $\tilde{\theta} = \pi$. The tensile and compressive meridians, depicted in Fig. 2, are linear for the three-parameter Willam–Warnke criterion. Meridians are nonlinear for the five-parameter formulation. In Fig. 2 all three parameters, i.e., σ_t, σ_c, and σ_{bc} are visible. These parameters are defined by the intersection of load paths with the flow surface. This characterization of the threshold flow stresses is described in detail by Palko (1992). Also note that this formulation of the Bingham–Prager flow function introduces a dependence on the hydrostatic component of the stress state. Combining views from Figs. 2 and 3 in the Haigh–Westergaard stress space yields a flow surface in the shape of a pyramid with a triangular base. As a reference, typical J_2 plasticity models have yield surfaces that are right circular cylinders in the Haigh–Westergaard stress space.

In lieu of the previously mentioned three threshold stress parameters, the threshold parameters

$$\rho = \frac{Y_{bc} Y_t}{Y_{bc} - Y_t} \tag{26}$$

$$r_t = \left(\frac{6}{5}\right)^{1/2} \frac{Y_{bc} Y_t}{2Y_{bc} + Y_t} \tag{27}$$

and

$$r_c = \left(\frac{6}{5}\right)^{1/2} \left[\frac{Y_{bc} Y_t}{3Y_{bc} Y_t + Y_{bc} - Y_t}\right] \tag{28}$$

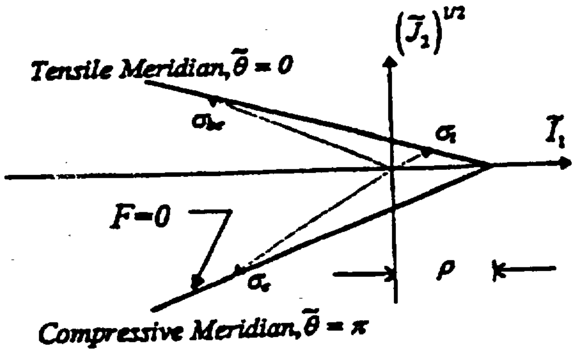

Fig. 2 Threshold flow stresses defined by the tensile and compressive meridians

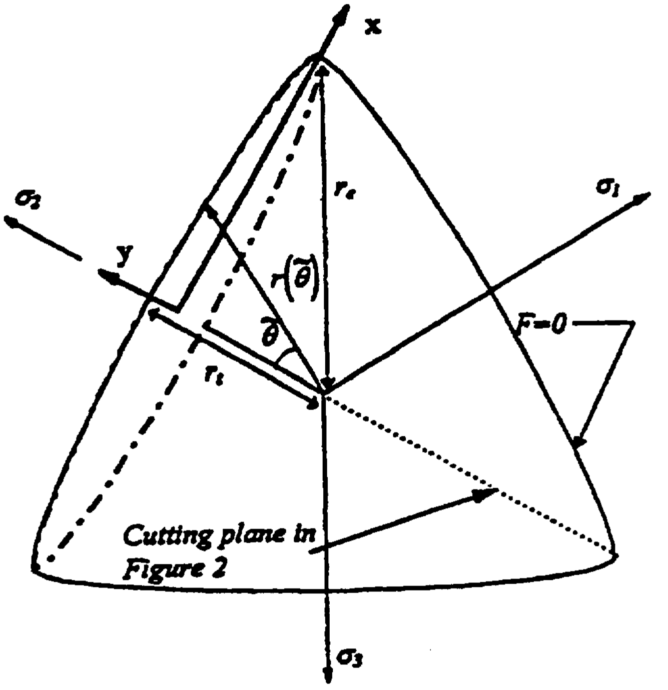

Fig. 3 Flow surface projected onto the Π-plane in the Haigh–Westergaard stress space

are utilized in order to simplify the expression presented later for the function r. These alternative threshold stress parameters are dependent on the parameters σ_t, σ_c, and σ_{bc}. Specifically, the normalized threshold stresses

$$Y_t = \frac{\sigma_t}{\sigma_c} \tag{29}$$

and

$$Y_{bc} = \frac{\sigma_{bc}}{\sigma_c} \tag{30}$$

are introduced to simplify Eqs. (26)–(28). Details of the derivations for the parameters appearing in Eqs. (26)–(28) can be found from either Palko (1992) or Chen (1982).

The parameter ρ is depicted graphically in Fig. 2. As noted earlier, this parameter is the tensile threshold hydrostatic flow stress. Willam and Warnke postulated that a single sector ($-\pi/3 \leq \theta \leq \pi/3$) of the flow surface in the Π-plane could be represented as a segment of an ellipse. The major and minor axes of the ellipse are formulated as functions of the intercepts r_c and r_t (see Fig. 3). The minor axis of the ellipse is assumed to coincide with a tensile axis. However, the center of the ellipse does not necessarily coincide with the hydrostatic axis, either for a material in the virgin state, or for a material that has been subjected to a service history. The reader should consult Palko (1992) for the complete derivation. With the function $r(\tilde{\theta})$ defined flow surface can be completely mapped in a Π-plane, as depicted in Fig. 3.

For either $\tilde{\theta}$ or $\bar{\theta}$ the function $r(\theta)$ is defined as

$$r(\theta) = \frac{u(\theta)}{v(\theta)} \tag{31}$$

where

$$u(\theta) = 2r_c(r_c^2 - r_t^2)\cos(\theta) + r_c(2r_t - r_c)[4(r_c^2 - r_t^2) \times \cos^2(\theta) + 5r_t^2 - 4r_t r_c]^{1/2} \tag{32}$$

and

$$v(\theta) = 4(r_c^2 - r_t^2)\cos^2(\theta) + (r_c - 2r_t)^2 \qquad (33)$$

For the definitions expressed in Eqs. (31)–(33)

$$-\frac{\pi}{3} \le \theta \le \frac{\pi}{3} \qquad (34)$$

Physically, $r(\tilde{\theta})$ represents the deviatoric component of a stress state, since this vector lies in the Π-plane. Note that Eq. (31) yields $r(\tilde{\theta}) = r_t$ for the special case of $\tilde{\theta} = 0$. Similarly, $r(\tilde{\theta}) = r_c$ for $\tilde{\theta} = \pi/3$.

Flow Surfaces: Interpretation

As in Robinson's original theory, the current model is closely tied to the concepts of a potential function and normality. It is this potential-normality structure that provides a consistent framework. According to the stability postulate of Drucker (1959), the concepts of normality and convexity are important requirements, which must be imposed on the development of a flow or yield surface. Constitutive relationships developed on the basis of these requirements assure that the inelastic boundary-value problem is well posed, and solutions obtained are unique. Experimental work by Robinson and Ellis (1985) has demonstrated the validity of the potential-normality structure relative to an isotropic J_2 alloy (i.e., type 316 stainless steel). With this structure, the direction of the inelastic strain rate vector for each stress point on a given surface is directed normal to the flow surface F = const (see Fig. 4). Without experimental evidence to the contrary, it is postulated that this structure is similarly valid for isotropic monolithic ceramic materials.

For constitutive models based on Robinson's (1978) original framework flow surfaces generated by nonzero values of F are associated with different inelastic strain rates. Figure 4 illustrates a typical family of level surfaces generated by monotonically increasing the magnitude of F ($\alpha_{ij} = 0$). The family is projected onto the $\sigma_{11}-\sigma_{22}$ stress plane. Large values of F = const correspond to flow surfaces that eventually cluster, forming a limiting surface. This implies large changes in inelastic strain rate for only small stress changes, analogous to the yield condition of classical plasticity. This feature was pointed out originally by Rice (1970) for constitutive models based on Eq. (6).

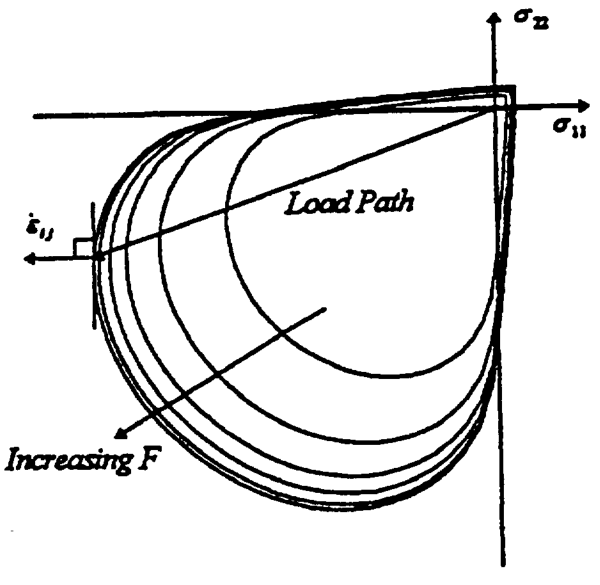

Fig. 4 Flow surfaces associated with a monotonically increasing value of the flow function F

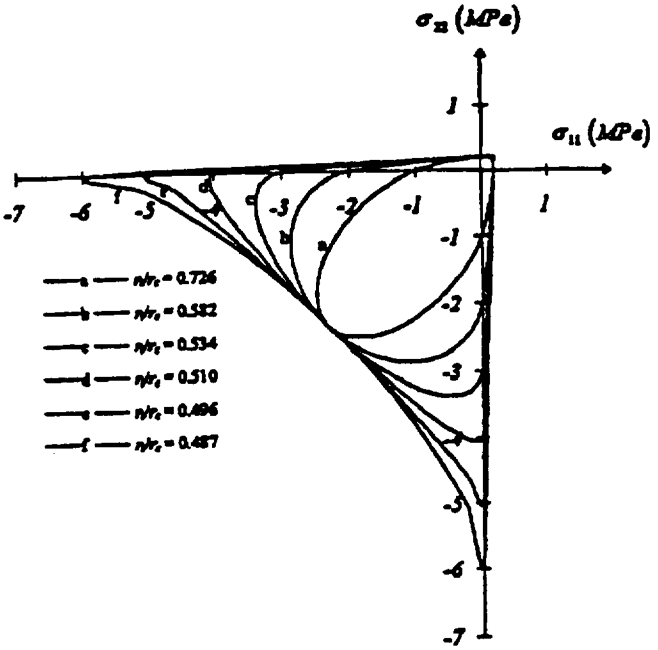

Fig. 5 Flow surfaces as a function of the ratio r_t/r_c

The convexity of the proposed flow surface assures stable material behavior, i.e., positive dissipation of inelastic work, which is based on thermodynamic principles. The convexity requirement also implies that level surfaces of a function are closed surfaces, since an open region of the flow surface allows the existence of a load path along which failure will never occur. For the Willam–Warnke model, convexity is assured if the ratio of the intercepts in the Π-plane satisfies the condition $1.0 \ge r_t/r_c > 0.5$. The family of surfaces shown in Fig. 5 illustrates the concept of convexity for surfaces having various r_t/r_c ratios. Here the values of the ratio vary from 0.726 to 0.487. Notice the surfaces identified as "e" and "f" violate the convexity condition.

Finally, the Willam–Warnke flow criterion (and the constitutive theory presented herein) degenerates to simpler models under special limiting conditions. For the case of $r_c = r_t = r_o$, where r_o is the same for any angle $\tilde{\theta}$, the model degenerates to a two-parameter formulation, i.e., the Drucker–Prager flow criterion. When projected onto the $\sigma_{11}-\sigma_{22}$ stress plane under these conditions, the flow surface depicted in Fig. 1 degenerates to an ellipse (see Fig. 6). Note that the major axis of this ellipse

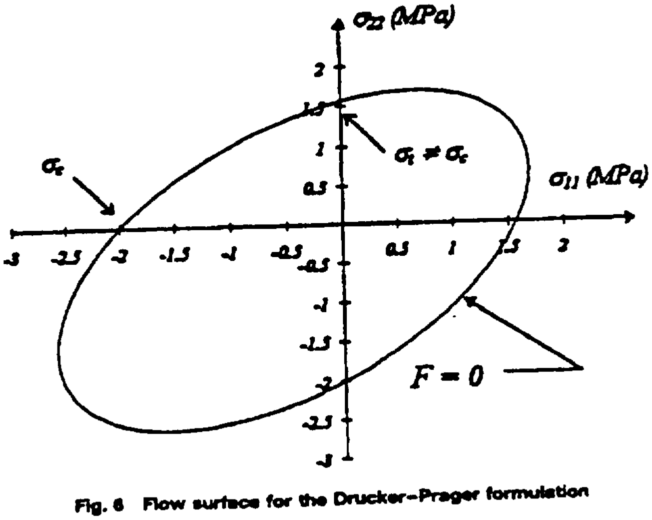

Fig. 6 Flow surface for the Drucker–Prager formulation

is aligned with the bisector of the first and third quadrants, and the intercepts along the σ_{11} and σ_{22} axes represent uniaxial tensile and compressive threshold stresses that are not equal in magnitude, even though the flow surface degenerates to a circle in the Π-plane. The Drucker–Prager formulation yields different tensile and compressive threshold stresses because the formulation produces a right circular cone in the three-dimensional Haigh–Westergaard stress space. For the special case where $r_c = r_t = r_o$ and $\rho = \infty$, the Willam–Warnke model reduces to the single-parameter Von Mises criterion. For this case, the flow surface degenerates to a circle in the Π-plane (a right circular cylinder in the three-dimensional Haigh–Westergaard stress space) and an ellipse in $\sigma_{11}-\sigma_{22}$ stress space, which is depicted in Fig. 7.

Stress–Strain Relationship

Employing the chain rule for differentiation and taking the partial derivative of Ω with respect to σ_{ij}, as indicated in Eq. (6), yields

$$\dot{\epsilon}_{ij} = \left(\frac{\partial \Omega}{\partial F}\right)\left[\frac{\partial F}{\partial I_1}\frac{\partial I_1}{\partial \eta_{kk}}\frac{\partial \eta_{kk}}{\partial \sigma_{ij}} + \frac{\partial F}{\partial J_2}\frac{\partial J_2}{\partial \Sigma_{mn}}\frac{\partial \Sigma_{mn}}{\partial S_{mn}}\frac{\partial S_{mn}}{\partial \sigma_{ij}} + \frac{\partial F}{\partial J_3}\frac{\partial J_3}{\partial \Sigma_{mn}}\frac{\partial \Sigma_{mn}}{\partial S_{mn}}\frac{\partial S_{mn}}{\partial \sigma_{ij}}\right] \quad (35)$$

where Eq. (8) has been utilized to define Ω.

Evaluating the partial derivative terms in Eq. (35) yields the following expression for the flow law

$$\dot{\epsilon}_{ij} = C_0\left[C_1\delta_{ij} + C_2\Sigma_{ij} + C_3\left(\Sigma_{jq}\Sigma_{qi} - \frac{2J_2\delta_{ij}}{3}\right)\right] \quad (36)$$

where the magnitudes of the coefficients C_0, C_1, C_2, and C_3 are dependent on the invariants defined in Eqs. (14)–(16) (i.e., I_1, J_2, and J_3), the three threshold parameters (i.e., σ_t, σ_c, and σ_{bc}), and the flow potential parameters utilized in Eq. (8) (i.e., μ, K, and n). The first coefficient is defined by the expression

$$C_0 = \frac{K^2F^n}{2\mu} \quad (37)$$

The remaining three coefficients are defined as

$$C_1 = \frac{1}{3\rho\sigma_c} \quad (38)$$

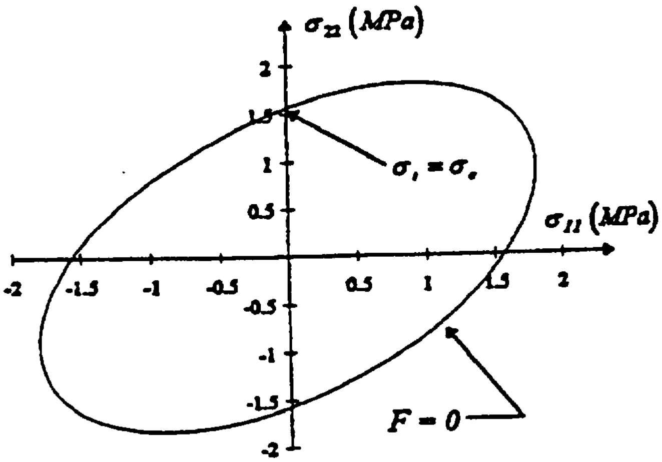

Fig. 7 Flow surface for the Von Mises formulation

$$C_2 = \left[\frac{1}{2r(\tilde{\theta})\sigma_c}\right]\left[\frac{2}{5J_2}\right]^{1/2} - \frac{1}{\sigma_c}\left[\frac{1}{r(\tilde{\theta})}\right]^2\left[\frac{2J_2}{5}\right]^{1/2}\left[\frac{\partial r(\tilde{\theta})}{\partial J_2}\right] \quad (39)$$

and

$$C_3 = -\frac{1}{\sigma_c}\left[\frac{2J_2}{5}\right]^{1/2}\left[\frac{\partial r(\tilde{\theta})}{\partial J_3}\right]\left[\frac{1}{r(\tilde{\theta})}\right]^2 \quad (40)$$

Note that the partial derivatives of $r(\tilde{\theta})$ appearing in Eqs. (39) and (40) are defined as

$$\frac{\partial r(\tilde{\theta})}{\partial J_2} = \left\{\frac{1}{v(\tilde{\theta})}\left[\frac{du(\tilde{\theta})}{d\tilde{\theta}}\right] - \frac{u(\tilde{\theta})}{v^2(\tilde{\theta})}\left[\frac{dv(\tilde{\theta})}{d\tilde{\theta}}\right]\right\} \times \left\{\frac{3\sqrt{3}J_3}{2J_2[4(J_2)^3 - 27(J_3)^2]^{1/2}}\right\} \quad (41)$$

and

$$\frac{\partial r(\tilde{\theta})}{\partial J_3} = -\left\{\frac{1}{v(\tilde{\theta})}\left[\frac{du(\tilde{\theta})}{d\tilde{\theta}}\right] - \frac{u(\tilde{\theta})}{v^2(\tilde{\theta})}\left[\frac{dv(\tilde{\theta})}{d\tilde{\theta}}\right]\right\} \times \left\{\frac{\sqrt{3}}{[4(J_2)^3 - 27(J_3)^2]^{1/2}}\right\} \quad (42)$$

where

$$\frac{du(\tilde{\theta})}{d\tilde{\theta}} = 2r_c(r_t^2 - r_c^2)\sin(\tilde{\theta}) + \frac{4r_c(2r_t - r_c)(r_t^2 - r_c^2)\sin(\tilde{\theta})\cos(\tilde{\theta})}{[4(r_c^2 - r_t^2)\cos^2(\tilde{\theta}) + 5r_t^2 - 4r_tr_c]^{1/2}} \quad (43)$$

and

$$\frac{dv(\tilde{\theta})}{d\tilde{\theta}} = 8(r_t^2 - r_c^2)\sin(\tilde{\theta})\cos(\tilde{\theta}) \quad (44)$$

Similarly, utilizing the chain rule for differentiation and taking the partial derivative of Ω with respect to the internal stress α_{ij} as indicated in Eq. (7) yields

$$\begin{aligned}\dot{\alpha}_{ij} &= -h\left(\frac{\partial \Omega}{\partial F}\frac{\partial F}{\partial \alpha_{ij}} + \frac{\partial \Omega}{\partial G}\frac{\partial G}{\partial \alpha_{ij}}\right)\\ &= -h\left\{\left(\frac{\partial \Omega}{\partial F}\right)\left[\frac{\partial F}{\partial I_1}\frac{\partial I_1}{\partial \eta_{kk}}\frac{\partial \eta_{kk}}{\partial \alpha_{ij}} + \frac{\partial F}{\partial J_2}\frac{\partial J_2}{\partial \Sigma_{mn}}\frac{\partial \Sigma_{mn}}{\partial a_{mn}}\frac{\partial a_{mn}}{\partial \alpha_{ij}} + \frac{\partial F}{\partial J_3}\frac{\partial J_3}{\partial \Sigma_{mn}}\frac{\partial \Sigma_{mn}}{\partial a_{mn}}\frac{\partial a_{mn}}{\partial \alpha_{ij}}\right] + \left(\frac{\partial \Omega}{\partial G}\right)\left[\frac{\partial G}{\partial \mathcal{I}_1}\frac{\partial \mathcal{I}_1}{\partial \alpha_{ij}} + \frac{\partial G}{\partial \mathcal{J}_2}\frac{\partial \mathcal{J}_2}{\partial a_{mn}}\frac{\partial a_{mn}}{\partial \alpha_{ij}} + \frac{\partial G}{\partial \mathcal{J}_3}\frac{\partial \mathcal{J}_3}{\partial a_{mn}}\frac{\partial a_{mn}}{\partial \alpha_{ij}}\right]\right\}\end{aligned} \quad (45)$$

Evaluating the partial derivative terms in Eq. (43) yields the following expression for the evolutionary law:

$$\dot{\alpha}_{ij} = h\left\{\dot{\epsilon}_{ij} - C_4\left[C_1\delta_{ij} + C_5a_{ij} + C_6\left(a_{jq}a_{qi} - \frac{2\mathcal{J}_2\delta_{ij}}{3}\right)\right]\right\} \quad (46)$$

where $\dot{\epsilon}_{ij}$ is given in Eq. (36). The magnitudes of the coefficients C_4, C_5, and C_6 are dependent on the invariants defined in Eqs. (17)–(19) (i.e., $\mathcal{I}_1$, $\mathcal{J}_2$, and $\mathcal{J}_3$), the three threshold parameters (i.e., σ_t, σ_c, and σ_{bc}), and the flow potential parameters utilized in equation (8) (i.e., R, H, K, and m). The first coefficient is defined by the expression

$$C_4 = \frac{K^2 R G^m}{H} \tag{47}$$

The remaining two coefficients are defined as

$$C_5 = \left[\frac{1}{2r(\hat{\theta})\sigma_c}\right]\left[\frac{2}{5\mathcal{J}_2}\right]^{1/2} - \frac{1}{\sigma_c}\left[\frac{1}{r(\hat{\theta})}\right]^2\left[\frac{2\mathcal{J}_2}{5}\right]^{1/2}\left[\frac{\partial r(\hat{\theta})}{\partial \mathcal{J}_2}\right] \tag{48}$$

and

$$C_6 = -\frac{1}{\sigma_c}\left[\frac{2\mathcal{J}_2}{5}\right]^{1/2}\left[\frac{\partial r(\hat{\theta})}{\partial \mathcal{J}_3}\right]\left[\frac{1}{r(\hat{\theta})}\right]^2 \tag{49}$$

Note that the partial derivatives of $r(\hat{\theta})$ appearing in Eqs. (48) and (49) are defined as

$$\frac{\partial r(\hat{\theta})}{\partial \mathcal{J}_2} = \left\{\frac{1}{v(\hat{\theta})}\left[\frac{du(\hat{\theta})}{d\hat{\theta}}\right] - \frac{u(\hat{\theta})}{v^2(\hat{\theta})}\left[\frac{dv(\hat{\theta})}{d\hat{\theta}}\right]\right\} \times \left\{\frac{3\sqrt{3}\,\mathcal{J}_3}{2\,\mathcal{J}_2[4(\mathcal{J}_2)^3 - 27(\mathcal{J}_3)^2]^{1/2}}\right\} \tag{50}$$

and

$$\frac{\partial r(\hat{\theta})}{\partial \mathcal{J}_3} = -\left\{\frac{1}{v(\hat{\theta})}\left[\frac{du(\hat{\theta})}{d\hat{\theta}}\right] - \frac{u(\hat{\theta})}{v^2(\hat{\theta})}\left[\frac{dv(\hat{\theta})}{d\hat{\theta}}\right]\right\} \times \left\{\frac{\sqrt{3}}{[4(\mathcal{J}_2)^3 - 27(\mathcal{J}_3)^2]^{1/2}}\right\} \tag{51}$$

Equations (36) and (46) constitute a multiaxial statement of a constitutive theory for isotropic materials. In the present and subsequent developments, it will serve as an inelastic deformation model for ceramic materials.

Summary and Conclusions

A multiaxial continuum theory was presented for predicting the inelastic response of isotropic monolithic ceramic materials. The viscoplastic constitutive model was derived from a single scalar dissipative function, which has similar geometric interpretations (e.g., convexity and normality) to the yield function encountered in classical plasticity. By adopting a flow potential to derive the theory, certain required continuum properties can be demonstrated, thereby ensuring that the resulting inelastic boundary value problem is well-posed, and solutions obtained are unique.

Constitutive equations for the flow law (strain rate) and evolutionary law are formulated based on a threshold function, which exhibits a sensitivity to hydrostatic stress and allows different behavior in tension and compression. Further, inelastic deformation is treated as inherently time dependent. A rate of inelastic strain is associated with every state of stress. As a result, creep, stress relaxation, and rate sensitivity are phenomena resulting from applied boundary conditions and are not treated separately in an ad hoc fashion.

The overview presented in this paper has provided a qualitative assessment of the capabilities of this viscoplastic model in capturing the complex thermomechanical behavior exhibited by ceramic materials at elevated service temperatures. Incorporating this model into a nonlinear finite element code would provide industry the means to numerically simulate the inherently time-dependent and hereditary phenomena exhibited by these materials in service.

References

Bingham, E. C., 1922, *Fluidity and Plasticity*, McGraw-Hill, New York.

Chen, W. F., 1982, *Plasticity in Reinforced Concrete*, McGraw-Hill, New York.

Chuang, T.-J., and Duffy, S. F., 1994, "A Methodology to Predict Creep Life for Advanced Ceramics Using Continuum Damage Mechanics," *Life Prediction Methodologies and Data for Ceramic Materials*, ASTM STP 1201, C. R. Brinkman and S. F. Duffy, eds., American Society for Testing and Materials, Philadelphia, pp. 207–227.

Corapcioglu, Y., and Uz, T., 1978, "Constitutive Equations for Plastic Deformation of Porous Materials," *Powder Technology*, Vol. 21, pp. 269–274.

Ding, J.-L., Liu, K. C., and Brinkman, C. R., 1994, "A Comparative Study of Existing and Newly Proposed Models for Creep Deformation and Life Prediction of Si3N4," in: *Life Prediction Methodologies and Data for Ceramic Materials*, ASTM STP 1201, C. R. Brinkman and S. F. Duffy, eds., American Society for Testing and Materials, Philadelphia, pp. 62–83.

Drucker, D. C., 1959, "A Definition of Stable Inelastic Material," ASME *Journal of Applied Mechanics*, Vol. 26, pp. 101–106.

Duffy, S. F., 1988, "A Unified Inelastic Constitutive Theory for Sintered Powder Metals," *Mechanics of Materials*, Vol. 7, pp. 245–254.

Green, R. J., 1972, "A Plasticity Theory for Porous Solids," *International Journal for Mechanical Sciences*, Vol. 14, pp. 215.

Gurson, A. L., 1977, "Continuum Theory of Ductile Rupture by Void Nucleation and Growth: Part I—Yield Criteria and Flow Rules for Porous Ductile Media," ASME *Journal of Engineering Materials and Technology*, Vol. 99, pp. 2–15.

Hohenemser, K., and Prager, W., 1932, "Ueber die Ansaetze der Mechanik Isotroper Kontinua," *Zeit fuer angewandte Mathematik und Mechanik*, Vol. 12.

Janosik, L. A., 1998, "A Unified Viscoplastic Constitutive Theory for Monolithic Ceramics," Master's Thesis, Cleveland State University, Cleveland, OH.

Kuhn, H. A., and Downey, C. L., 1971, "Deformation Characteristics and Plasticity Theory of Sintered Powder Metals," *International Journal of Powder Metallurgy*, Vol. 7, pp. 15–25.

Liu, K. C., Brinkman, C. R., Ding, J.-L., and Liu, S., 1997, "Predictions of Tensile Behavior and Strengths of Si_3N_4 Ceramic at High Temperatures Based on a Viscoplastic Model," ASME Journal of Engineering for Gas Turbines and Power, Vol. 119, pp. 200–204.

Mear, M. E., and Hutchinson, J. W., 1985, "Influence of Yield Surface Curvature on Flow Localization in Dilatant Plasticity," *Mechanics of Materials*, Vol. 4, pp. 395–407.

Palko, J. L., 1992, "Interactive Reliability Model for Whisker-Toughened Ceramics," Master's Thesis, Cleveland State University, Cleveland, OH.

Ponter, A. R. S., and Leckie, F. A., 1976, "Constitutive Relationships for Time-Dependent Deformation of Metals," ASME *Journal of Engineering Materials and Technology*, Vol. 98.

Rice, J. R., 1970, "On the Structure of Stress-Strain Relations for Time-Dependent Plastic Deformation in Metals," ASME *Journal of Applied Mechanics*, Vol. 37, p. 728.

Robinson, D. N., 1978, "A Unified Creep-Plasticity Model for Structural Metals at High Temperature," ORNL/TM 5969.

Robinson, D. N., and Swindeman, R. W., 1982, "Unified Creep-Plasticity Constitutive Equations for 2-1/4 CR-1 Mo Steel at Elevated Temperature," ORNL/TM 8444.

Robinson, D. N., and Ellis, J. R., 1985, "Experimental Determination of Flow Potential Surfaces Supporting a Multiaxial Formulation of Viscoplasticity," *Proc. 5th International Seminar on Inelastic Analysis and Life Prediction in High Temperature Environments*, Paris, France.

Shima, S., and Oyane, M., 1976, "Plasticity Theory for Porous Metals," *International Journal of Mechanical Sciences*, Vol. 18, p. 285.

White, C. S., and Hazime, R. M., 1995, "Internal Variable Modeling of the Creep of Monolithic Ceramics," *Proc. 11th Biennial Conference on Reliability, Stress Analysis, and Failure Prevention*, O. Jadaan, ed., The American Society of Mechanical Engineers, Philadelphia, PA.

Willam, K. J., and Warnke, E. P., 1975, "Constitutive Model for the Triaxial Behaviour of Concrete," *Int. Assoc. Bridge Struct. Eng. Proc.*, Vol. 19, pp. 1–30.

Design with Brittle Materials

Stephen F. Duffy, Cleveland State University
Lesley A. Janosik, NASA Lewis Research Center

BRITTLE MATERIALS (e.g., ceramics, intermetallics, and graphites) are increasingly being used in the fabrication of lightweight components. From a design engineer's perspective, brittle materials often exhibit attractive high-strength properties at service temperatures that are well beyond use temperatures of conventional ductile materials. For advanced diesel and turbine engines, ceramic components have already demonstrated functional abilities at temperatures reaching 1370 °C (2500 °F), which is well beyond the operational limits of most conventional metal alloys. However, a penalty is paid in that these materials typically exhibit low fracture toughness, which is usually defined by a critical stress intensity factor, and typically quantified by K_{Ic}. This inherent undesirable property must be considered when designing components. Lack of ductility (i.e., lack of fracture toughness) leads to low strain tolerance and large variations in observed fracture strength. When a load is applied, the absence of significant plastic deformation or microcracking causes large stress concentrations to occur at microscopic flaws. These flaws are unavoidably present as a result of fabrication or in-service environmental factors. Note that nondestructive evaluation (NDE) inspection programs cannot be successfully implemented during fabrication. The combination of high strength and low fracture toughness leads to relatively small critical defect sizes that cannot be detected by current NDE methods. As a result, components with a distribution of defects (characterized by various sizes and orientations) are produced, which leads to an observed scatter in component strength. Catastrophic crack growth for brittle materials occurs when the crack driving force or energy release rate reaches a critical value and the resulting component failure proceeds in a catastrophic manner.

The emphasis in this article is placed on design methodologies and characterization of certain material properties. Of particular interest to the design engineer is the inherent scatter in strength noted above. Accounting for this phenomenon requires a change in philosophy on the design engineer's part that leads to a reduced focus on the use of safety factors in favor of reliability analyses. If a brittle material with an obvious scatter in tensile strength is selected for its high-strength attributes, or inert behavior, then components should be designed using an appropriate design methodology rooted in statistical analysis. However, the reliability approach presented in this chapter demands that the design engineer must tolerate a finite risk of unacceptable performance. This risk of unacceptable performance is identified as the probability of failure of a component (or alternatively, component reliability). The primary concern of the engineer is minimizing this risk in an economical manner.

This article presents fundamental concepts and models associated with performing time-independent and time-dependent reliability analyses for brittle materials exhibiting scatter in ultimate strength. However, the discussion contained within this article is not limited to materials exposed to elevated service temperatures. The concepts can be easily extended to more mundane applications where brittle materials such as glass or cements are used. Specific applications that have utilized ceramic materials at near-ambient temperatures include wear parts (nozzles, valves, seals, etc.), cutting tools, grinding wheels, bearings, coatings, electronics, and human prostheses. Other brittle materials, such as glass and graphite materials, have been used in the fabrication of infrared transmission windows, glass skyscraper panels, television cathode ray tubes (CRTs), and high-temperature graphite bearings. Thus, in this article the design methodologies used to analyze these types of components, as well as components exposed to elevated service temperatures, are presented. Reliability algorithms are outlined, and several applications are presented to further illustrate the utilization of these reliability algorithms in structural applications. For further background material on statistical methods, see the article "Statistical Aspects of Design" in this Volume.

Time-Independent Reliability Analyses

An engineer is trained to quantify component failure through the use of a safety factor. By definition, the safety factor for a component subjected to a single load L is given by the ratio:

$$\text{Safety factor} = \frac{R}{L} \qquad \text{(Eq 1)}$$

where R is the resistance (or strength) of the material from which the component is fabricated. Making use of the concept of a safety factor, the probability of failure (P_f) for the component where a single load is applied is given by the expression:

$$P_f = \text{Probability}\left(\frac{R}{L} \geq 1\right) \qquad \text{(Eq 2)}$$

In making the transition from a deterministic safety factor for a component to a probability of failure, for the most general case, the assumption is made that both R and L are random variables. Under this assumption P_f is the product of two finite probabilities summed over all possible outcomes. Both probabilities are associated with an event and a random variable.

The first event is defined by the random variable L taking on a value in the range:

$$\left(x - \frac{dx}{2}\right) \leq L \leq \left(x + \frac{dx}{2}\right) \qquad \text{(Eq 3)}$$

The probability associated with this event is the area under the probability density function (PDF) for the load random variable (f_L) over this interval, i.e.,

$$P_1 = f_L(x)\,dx \qquad \text{(Eq 4)}$$

The second event is associated with the probability that the random variable R is less than or equal to x. This is the area under the probability density function for the resistance random variable (f_R) from $-\infty$ (or an appropriate lower limit defined by the range of the resistance random variable) to x. This second probability is given by the cumulative distribution function (CDF) for the resistance random variable (F_R) evaluated at x, that is:

$$P_2 = F_R(x) \qquad \text{(Eq 5)}$$

With the probability of failure defined as the product of these two probabilities, summed over all possible values of x, then:

$$P_f = P_1 P_2 = \int_{-\infty}^{+\infty} F_R(x) f_L(x) dx \qquad \text{(Eq 6)}$$

To interpret this integral expression, consider the graphs in Fig. 1. In this figure, the graph of an arbitrary PDF for the resistance random variable is superimposed on the graph of an arbitrary PDF for the load random variable. Note that R and L must have the same dimensional units (e.g., force or stress) to superimpose their graphs in the same figure. A common misconception is that P_f is the area of overlap encompassed by the two probability density functions. Scrutiny of Eq 6 leads to the appropriate conclusion that the probability of failure is really the area under the composite function:

$$g_{RL}(x) = F_R(x) f_L(x) \qquad \text{(Eq 7)}$$

which is also illustrated in Fig. 1.

Next, consider the situation where the load random variable has very little scatter relative to the resistance random variable. For example, if a number of test specimens were fabricated from a brittle material (a monolithic ceramic), the ultimate tensile strength can easily vary by more than 100%. That is, the highest strength value in the group tested can easily be twice as large as the lowest value. Variations of this magnitude are not typical for the load design variable, and the engineer could easily conclude that load is a deterministic design variable while strength is a random design variable. This assumption can be accommodated in this development by allowing the PDF for the load random variable to be defined by the expression:

$$f_L(x) = \delta(x - x_0) \qquad \text{(Eq 8)}$$

Here δ is the Dirac delta function defined as:

$$\delta(x - x_0) = \begin{cases} \infty & x = x_0 \\ 0 & x \neq x_0 \end{cases} \qquad \text{(Eq 9)}$$

Note that the Dirac delta function satisfies the definition for a PDF; that is, the area under the curve is equal to 1, and the function is greater than or equal to 0 for all values of x. The Dirac delta function represents the scenario where the standard deviation of a random variable approaches 0 in the limit, and the random variable takes on a single value, that is, the central value identified here as x_0. Because the Dirac delta function is being used to represent the load random variable, then x_0 represents the deterministic magnitude of the applied load. Keep in mind that the applied load can have units of force or stress. However, load and resistance are commonly represented with units of stress. Thus x_0 is replaced with σ, an applied stress, and the probability of failure is given by the expression:

$$P_f = \int_{-\infty}^{+\infty} F_R(x) \delta(x - \sigma) dx \qquad \text{(Eq 10)}$$

However, with the Dirac delta function embedded in the integral expression, the probability of failure simplifies to:

$$P_f = F_R(\sigma) \qquad \text{(Eq 11)}$$

Thus the probability of failure is equal to the CDF of the resistance random variable evaluated at the applied load, σ. The use of the Dirac delta function in representing the load design variable provides justification for the use of the Weibull CDF (or a similarly skewed distribution) in quantifying the probability of failure for components fabricated from ceramics or glass.

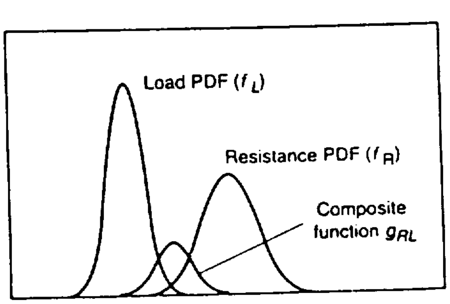

Fig. 1 Interference plot for load and resistance random variables

System Reliability

A unique property of most brittle materials is an apparent decrease in tensile strength as the size of the component increases. This is the so-called size effect. As an example, consider a simple component such as a uniaxial tensile specimen. Now suppose that two groups of these simple components have been fabricated. Each group is identical with the exception that the size of the specimens in the first group is uniformly smaller than the specimens in the second group. The mean sample strength from the first group would be consistently and distinctly larger in a manner that cannot be accounted for by randomness. Thus Eq 11 must be transformed in some manner to admit a size dependence. This is accomplished through the use of system reliability concepts. (See the article "Reliability in Design" in this Volume for details on formulating the basic equations for system reliability.) After the following discussion the reader should be cognizant that the expression given in Eq 11 represents the probability of failure for a specified set of boundary conditions. If the boundary conditions are modified in any way, Eq 11 is no longer valid. To account for size effects and to deal with the probability of failure for a component in a general manner, the component should be treated as a system, and the focus must be directed on the probability of failure of the system.

The typical approach to designing structural components with varying stress fields involves discretizing the component in order to characterize the stress field using finite element mc ods. Because component failure may initiate any of the discrete elements, it is convenien consider a component as a system and uti system reliability theories. A component is a ries system if it fails when one discrete elem fails. This type of failure can be modeled us weakest-link reliability theories. A componer a parallel system when failure of a single elem does not cause the component to fail. In this c the remaining elements sustain load through distribution. This type of failure can be mod with what has been referred to in the literatur "bundle theories." Weakest-link theories bundle theories represent the extremes of fai behavior modeled by reliability analysis. T suggest more complex systems such as "r ou n" systems. Here a component (system) elements functions if at least r elements have failed. This type of system model has not f widespread application in structural reliab analysis. The assumption in this article is tha failure behavior of the brittle materials is su and catastrophic. This type of behavior fits w the description of a series system, thus a wea link reliability system is adopted.

Now the probability of failure of a dis element must be related to the overall proba of failure of the component. If the failure individual element is considered a stati event, and if these events are independent, the probability of failure of a discretized co nent that acts as a series system is given b expression:

$$P_f = 1 - \prod_{i=1}^{N} (1 - p_i) \qquad ($$

where N is the number of finite elements for a component analysis. Here p_i is the probabi failure of the ith discrete element.

In the next section an expression is sp for the probability of failure (or alternative reliability) of the ith discrete element for a s fied state of stress, that is, a uniaxial tensile This expression allows the introduction scaling. Once size-scaling relationships are lished for a simple state of stress, the re ships are extended to multiaxial states of s

Two-Parameter Weibull Distribution and Size Effects

In the ceramic and glass industry the distribution is universally accepted as th bution of choice in representing the unc PDF for tensile strength. A two-parameter lation and a three-parameter formulat available for the Weibull distribution. H the two-parameter formulation usually le more conservative estimate for the co probability of failure. The two-parameter PDF for a continuous random strength denoted as Σ, is given by the expression

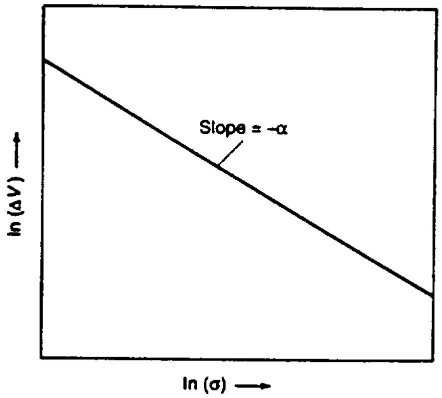

Fig. 2 Specimen gage volume plotted as a function of failure stress

$$f_\Sigma(\sigma) = \left(\frac{\alpha}{\beta}\right)\left(\frac{\sigma}{\beta}\right)^{(\alpha-1)} \exp\left[-\left(\frac{\sigma}{\beta}\right)^{\alpha}\right] \qquad \text{(Eq 13)}$$

for $\sigma > 0$, and

$$f_\Sigma(\sigma) = 0 \qquad \text{(Eq 14)}$$

for $\sigma \leq 0$. The cumulative distribution is given by the expression:

$$F_\Sigma(\sigma) = 1 - \exp\left[-\left(\frac{\sigma}{\beta}\right)^{\alpha}\right] \qquad \text{(Eq 15)}$$

for $\sigma > 0$, and

$$F_\Sigma(\sigma) = 0 \qquad \text{(Eq 16)}$$

for $\sigma \leq 0$. Here α (a scatter parameter, or Weibull modulus) and β (a central location parameter, or typically referred to as the Weibull scale parameter) are distribution parameters that define the Weibull distribution in much the same way as the mean (a central location parameter) and standard deviation (a scatter parameter) are parameters that define the Gaussian (normal) distribution. Note that in the ceramics and glass literature when the two-parameter Weibull formulation is adopted then "m" is used for the Weibull modulus α, and either σ_0 or σ_θ (see the discussion in the parameter estimation section regarding the difference between σ_0 and σ_θ) is used for the Weibull scale parameter. In this article, the (α, β) notation is used exclusively and reference is made to the typical notation adopted in the ceramics literature. The reason for this is the tendency to overuse the "σ" symbol (e.g., σ_θ, σ_0, σ_i-failure observation, and σ_t-threshold stress, etc.). Throughout this discussion the symbol "σ" implies applied stress.

If the random variable representing uniaxial tensile strength of an advanced ceramic is characterized by a two-parameter Weibull distribution, that is, the random strength parameter is governed by Eq 13 and 14, then the probability that a uniaxial test specimen fabricated from an advanced ceramic will fail can be expressed by the CDF:

$$P_f = 1 - \exp\left[-\left(\frac{\sigma_{\max}}{\beta_\theta}\right)^{\alpha}\right] \qquad \text{(Eq 17)}$$

Note that $\sigma_{\max}$ is the maximum normal stress in the component. When used in the context of characterizing the strength of ceramics and glasses, the central location parameter is referred to as the Weibull characteristic strength (β_θ). In the ceramic literature, this parameter can either be identified as the Weibull characteristic strength or the Weibull scale parameter. Because tensile strength is the random variable of interest, this parameter is referred to as a strength parameter throughout the rest of this article. The characteristic strength is dependent on the uniaxial test specimen (tensile, flexural, pressurized ring, etc.) used to generate the failure data. For a given material, this parameter will change in magnitude with specimen geometry (the so-called size effect alluded to earlier). The Weibull characteristic strength typically has units of stress. The scatter parameter α is dimensionless.

With the tensile strength characterized by the two-parameter Weibull distribution, the discussion returns to the weakest-link expression for component probability of failure defined by Eq 12. Let $\Re_i$ represent the reliability of the ith continuum element where:

$$\Re_i = 1 - p_i \qquad \text{(Eq 18)}$$

The reliability of this continuum element is then governed by the following expression:

$$\Re_i = \exp\left(-\left(\frac{\sigma}{\beta_0}\right)^{\alpha} \Delta V\right) \qquad \text{(Eq 19)}$$

where σ is the principal tensile stress applied to the continuum element. The volume of this arbitrary continuum element is identified by ΔV. In this expression β_0 is the Weibull material scale parameter and can be described as the Weibull characteristic strength of a specimen with unit volume loaded in uniform uniaxial tension. This is a material specific parameter that is utilized in the component reliability analyses that follow. The dimensions of this parameter are stress × (volume)$^{1/\alpha}$.

The requisite size scaling discussed earlier is introduced by Eq 19. To demonstrate this, take the natural logarithm of Eq 19 twice, that is:

$$\ln \ln (\Re_i) = \ln\left(-\left(\frac{\sigma}{\beta_0}\right)^{\alpha} \Delta V\right) \qquad \text{(Eq 20)}$$

Manipulation of Eq 20 yields:

$$\ln(\Delta V) = -\alpha \ln(\sigma) + \ln \ln (\Re_i) + \alpha \ln(-\beta_0) \qquad \text{(Eq 21)}$$

with

$$y = \ln(\Delta V) \qquad \text{(Eq 22)}$$

$$x = \ln(\sigma) \qquad \text{(Eq 23)}$$

$$m = -\alpha \qquad \text{(Eq 24)}$$

and

$$b = \ln \ln (\Re_i) + \alpha \ln(-\beta_0) \qquad \text{(Eq 25)}$$

then it is apparent that Eq 21 has the form of a straight line, that is, $y = mx + b$.

Once again consider the two groups of test specimens fabricated from the same material mentioned at the beginning of the section on system reliability. Recall that the specimens in each group are identical with each other, but the two groups have different gage sections such that ΔV (which is now identified as the gage section volume) is different for each group. Estimate Weibull parameters α and β_0 from the failure data obtained from either group (parameter estimation is discussed in detail in a following section). After the Weibull parameters are estimated the straight line in Fig. 2 is located by setting $\Re_i$ equal to 0.5 (i.e., the 50th percentile) in Eq 21. This value for $\Re_i$ should establish a line that correlates well with the median values in each group.

Now return to the data sets mentioned above and establish the stress value associated with the median in each group. Plot the gage volumes (ΔV) of each group as a function of the median stress values in Fig. 2. If no size effect is present, the median failure strengths of the groups will fall close to a horizontal line. This would indicate no correlation between gage volume and the median strength value. Keep in mind that the discussion here could proceed using any percentile value, not just the 50th percentile. A systematic variation away from a horizontal line indicates a size effect exists that must be considered in engineering design. If the median values for each group follows the trend indicated by the solid line in Fig. 2 the design engineer should have no apprehensions using Weibull analysis with size scaling. Figures 1 and 3 in Ref 1 are two excellent examples of these types of graphs with actual data.

The ability to account for size effects of individual elements is introduced through the expression for $\Re_i$ given by Eq 19. A rational approach for justifying this expression is outlined above. Now a general expression for the probability of failure for a component (i.e., a general form for Eq 17) is derived based on Eq 19. Under the assumptions that the component consists of an infinite number of elements (i.e., the continuum assumption) and that the component is best represented by a series system, then:

$$P_f = 1 - \lim_{k \to \infty}\left(\prod_{i=1}^{k} \Re_i\right) \qquad \text{(Eq 26)}$$

Substituting for $\Re_i$ yields:

$$P_f = 1 - \exp\left(-\lim_{k \to \infty} \sum_{i=1}^{k} \left(\left(\frac{\sigma}{\beta_0}\right)^{\alpha} \Delta V\right)_i\right) \qquad \text{(Eq 27)}$$

Here ΔV once again represents the volume of an element. The limit inside the bracket is a Riemann sum. Thus:

$$P_f = 1 - \exp\left[-\int \left(\frac{\sigma}{\beta_0}\right)^{\alpha} dV\right] \qquad \text{(Eq 28)}$$

Weibull (Ref 2) first proposed this integral representation for the probability of failure. The expression is integrated over all tensile regions of the specimen volume if the strength-controlling flaws are randomly distributed through the volume of the material, or over all tensile regions of the specimen area if flaws are restricted to the specimen surface. For failures caused by surface defects, the probability of failure is given by the expression:

$$P_f = 1 - \exp\left[-\int \left(\frac{\sigma}{\beta_0}\right)^{\alpha} dA\right] \qquad \text{(Eq 29)}$$

which is derived in a manner similar to Eq 28. The segregation of defect populations into volume and surface-distributed flaws hints at the possibility of multiple defect populations. Reference 3 presents an in-depth treatment of this topic as it relates to ceramic materials.

The Weibull material scale parameter β_0 has units of stress × $(\text{volume})^{1/\alpha}$. If the strength-controlling flaws are restricted to the surface of the specimens in a sample, then the Weibull material scale parameter has units of stress × $(\text{area})^{1/\alpha}$. For a given specimen geometry, Eq 17 and 28 can be equated, yielding an expression relating β_0 and β_θ. Methods for converting β_θ to an equivalent β_0 value are addressed in ASTM Standard Practice C 1239-95.

Three-Parameter Weibull Distribution

The three-parameter Weibull PDF for a continuous random strength variable, denoted as Σ, is given by the expression:

$$f_\Sigma(\sigma) = \left(\frac{\alpha}{\beta}\right)\left(\frac{\sigma-\gamma}{\beta}\right)^{(\alpha-1)} \exp\left[-\left(\frac{\sigma-\gamma}{\beta}\right)^{\alpha}\right] \qquad \text{(Eq 30)}$$

for $\sigma > \gamma$, and

$$f_\Sigma(\sigma) = 0 \qquad \text{(Eq 31)}$$

for $\sigma \le \gamma$. In Eq 30 α is once again the Weibull modulus (or the shape parameter), β is the Weibull scale parameter, and γ is a threshold parameter. The cumulative distribution is given by the expression

$$F_\Sigma(\sigma) = 1 - \exp\left[-\left(\frac{\sigma-\gamma}{\beta}\right)^{\alpha}\right] \qquad \text{(Eq 32)}$$

for $\sigma > \gamma$, and

$$F_\Sigma(\sigma) = 0 \qquad \text{(Eq 33)}$$

for $\sigma \le \gamma$. The same reasoning presented in the previous section on size scaling utilizing a two-parameter formulation can be applied using the three-parameter formulation. The resulting expression for the probability of failure of a component subjected to a single applied stress σ is:

$$P_f = 1 - \exp\left[-\int \left(\frac{\sigma-\gamma}{\beta_0}\right)^{\alpha} dV\right] \qquad \text{(Eq 34)}$$

if the defect population is spatially distributed throughout the volume. A similar expression exists for failures caused by area defects. The focus of the discussion in the next section turns to accommodating multiaxial stress states in Eq 28 and Eq 34. This involves the development of multiaxial reliability models.

The approach outlined in this section and previous sections to account for the scatter in failure strength and the size effect of brittle materials was first introduced by Weibull (Ref 2 and 4). The concepts were based on the principles of weakest-link theory presented earlier. A number of authors including Pierce (Ref 5), Kontorova (Ref 6), as well as Frenkel and Kontorova (Ref 7) have made contributions in this area. In fact, Pierce first proposed the weakest-link concept while modeling yarn failure. However, Pierce assumed a Gaussian distribution for the strength random variable of yarn, and Weibull developed the unique PDF for his work that now bears his name. Hu (Ref 8) explored the difficulties associated with parameter estimation when a Gaussian or log normal distribution is adopted for the strength random variable. Shih (Ref 9) has shown that the three-parameter Weibull distribution is a more accurate approximation of brittle material behavior (specifically monolithic ceramics) than the Gaussian or other distributions. However, most analyses incorporate a two-parameter Weibull PDF where the threshold stress (the value of applied stress below which the failure probability is 0) is taken as 0. The reliability predictions obtained using the two-parameter function are more conservative than those obtained with the three-parameter model.

Multiaxial Reliability Models

Over the years a number of reliability models have been presented that extend the uniaxial format of Eq 28 and 34 to multiaxial states of stress. Only models associated with isotropic brittle materials are presented here. Anisotropic reliability models are beyond the scope of this article. References 10 and 11 contain information pertaining to reliability models for brittle composites. The monolithic models highlighted here include the principle of independent action (PIA) model, the normal stress averaging (NSA) model, and Batdorf's model. A brief discussion is presented for each. A detailed development is omitted for the sake of brevity. In order to simplify the present tion of each model, recast Eq 28 as:

$$P_f = 1 - \exp\left[-\int \psi\, dV\right] \qquad \text{(Eq 3}$$

where ψ is identified as a failure function per un volume. What remains is the specification of th failure function ψ for each reliability model.

Phenomenological Models (NSA and PIA To predict the time-independent (also referred t as fast-fracture) material response under mu tiaxial stress states Weibull (Ref 2) proposed ca culating a failure function per unit volum (Weibull identified the function as the risk o rupture) by averaging the tensile normal stre raised to an exponent in all directions over th area of a unit radius sphere for volume flaws. Th is known as the NSA model where:

$$\psi = k\,\bar{\sigma}_n^{\alpha} \qquad \text{(Eq 3}$$

where

$$\bar{\sigma}_n^{\alpha} = \frac{\int_A \sigma_n^{\alpha}\, dA}{\int_A dA} \qquad \text{(Eq 3}$$

and

$$k = \frac{(2\alpha+1)}{(\beta_0)^{\alpha}} \qquad \text{(Eq 3}$$

The area integration in Eq 37 is performed over th region of a unit sphere where σ_n (the Cauchy norm stress) is tensile. The reader is directed to Ref 12 f an in-depth explanation of the constants appeari in the equations above. Gross (Ref 13) demo strated that for surface flaws this same averagi technique can be executed over the contour of circle with a unit radius. Although the surface fla technique is intuitively plausible for the NS model, the approach is somewhat arbitrary. In ad tion, it lacks a closed-form solution, and therefo requires computationally intensive numerical mo eling.

Barnett et al. (Ref 14) and Freudenthal (Ref 1 proposed an alternative approach usually refer to as the PIA model. Here:

$$\psi = \left(\frac{\sigma_1}{\beta_0}\right)^{\alpha} + \left(\frac{\sigma_2}{\beta_0}\right)^{\alpha} + \left(\frac{\sigma_3}{\beta_0}\right)^{\alpha} \qquad \text{(Eq 3}$$

where σ_1, σ_2, and σ_3 are the three principal stres at a given point. The PIA model is the probabilis equivalent to the deterministic maximum stress f ure theory.

The NSA model, and in particular the P model, have been widely applied in brittle ma rial design. The reader is directed to Ref 16 to for a more in-depth development and discussi of the merits of these two models. Historica the NSA and the PIA models have been popu methods for multiaxial stress state analysis. Ho ever, the NSA and PIA models are in essence phenomenological and do not specify the nature of the defect causing failure. As a consequence, no foundation exists for extrapolating predictions made by these models to conditions different from the original test conditions. Other models that are rooted in the principles of fracture mechanics are discussed in the next section.

Batdorf's Theory—Mechanistic Model. The concepts proposed by Batdorf (Ref 21), and later refined by Batdorf and Crose (Ref 22), are important in that the approach incorporates a mechanistic basis for the effect of multiaxial states of stress into the weakest-link theory. Here material defects distributed throughout the volume (and/or over the surface) are assumed to have a random orientation. In addition, the defects are assumed to be noninteracting discontinuities (cracks) with an assumed regular geometry. Failure is assumed to occur when a far-field effective stress associated with the weakest flaw reaches a critical level. The effective stress is a predefined combination of the far-field normal stress and the far-field shear stress. It is also a function of the assumed crack configuration, the existing stress state, and the fracture criterion employed (hence the claim that the approach captures the physics of fracture). Accounting for the presence of a far-field shear stress reduces the far-field normal stress needed for fracture. This model is identified by taking:

$$\Psi = \alpha k_B \int_0^{(\sigma_e)_{\max}} \frac{\Phi(\Sigma, \sigma_{cr})}{4\pi} \sigma_{cr}^{\alpha-1} \, d\sigma_{cr} \qquad \text{(Eq 40)}$$

where Φ is a solid angle that is dependent on the fracture criterion selected, the crack configuration, and the applied stress state. The maximum effective stress $(\sigma_e)_{max}$ is defined as an equivalent mode I fracture stress for mixed-mode loading. The crack-density coefficient k_B is obtained from the following expression:

$$k_B = \frac{\eta_v(\sigma_{cr})}{(\sigma_{cr})^u} \qquad \text{(Eq 41)}$$

Here σ_{cr} is defined as the critical far-field normal stress for a given crack configuration under mode I loading. Once again Ref 12 can provide a detailed interpretation of the parameters appearing in Eq 40. For the most part, the Batdorf model yields more accurate reliability analyses than those produced by either the NSA or PIA models.

Numerous authors have discussed the stress distribution around cracks of various types under different loading conditions and proposed numerous criteria to describe impending fracture. Specifically, investigators such as Giovan and Sines (Ref 23), Batdorf (Ref 21), Stout and Petrovic (Ref 24), as well as Petrovic and Stout (Ref 25) have compared results from the most widely accepted mixed-mode fracture criteria with each other and with selected experimental data. The semiempirical equation developed by Palaniswamy and Knauss (Ref 26) and Shetty (Ref 27) seemingly provides enough flexibility to fit to experimental data. In addition, Shetty's criterion can account for the out-of-plane crack growth that is observed under mixed-mode loadings. However, several issues must be noted. No prevailing consensus has emerged regarding a best probabilistic fracture theory. Most of the available criteria predict somewhat similar results, despite the divergence of initial assumptions. Moreover, one must approach the mechanistic models with some caution. The reliability models based on fracture mechanics incorporate the assumptions made in developing the fracture models on which they are based. One of the fundamental assumptions made in the derivation of fracture mechanics criteria is that the crack length is much larger than the characteristic length of the microstructure. This is sometimes referred to as the continuum principle in engineering mechanics. For the brittle materials discussed here, that characteristic length is the grain size (or diameter). If one contemplates the fact that most brittle materials are high strength with an attending low fracture toughness, then the critical defect size can be quite small. If the critical defect size approaches the grain size of the material, then the phenomenological models discussed above may be more appropriate than the mechanistic models.

Parameter Estimation

As indicated earlier, the distribution of choice for characterizing the tensile strength of brittle materials is the Weibull distribution. One fundamental reason for this choice goes beyond the fact that the Weibull distribution usually provides a good fit to the data. While the log-normal distribution often provides an adequate fit, it precludes any accounting of size effects. Reference 8 provides a detailed discussion on this matter. As it turns out, once a conscious choice is made to utilize the Weibull distribution, Eq 17 provides a convenient formulation for parameter estimation. However, one cannot extract the fundamental distribution parameters needed for general component analysis from this expression, unless the test specimen has the same geometry and applied loads as the component. The fundamental distribution parameters (identified previously as material specific parameters) were embedded in Eq 28. Thus, together Eq 17 and 28 provide a convenient method for extracting material specific parameters from failure data.

Tensile strength measurements are taken for one of two reasons: either for a comparison of the relative quality of two materials or for the prediction of the failure probability for a structural component. The latter is the focus of this article, although the analytical details provided here allow for either. To obtain point estimates of the unknown Weibull distribution parameters, well-defined functions are utilized that incorporate the failure data and specimen geometry. These functions are referred to as estimators. It is desirable that an estimator be consistent and efficient. In addition, the estimator should produce unique, unbiased estimates of the distribution parameters. Different types of estimators exist, including: moment estimators, least squares estimators, and maximum likelihood estimators. This discussion initially focuses on maximum likelihood estimators (MLE) due to the efficiency and the ease of application when censored failure populations are encountered. The likelihood estimators are used to compute parameters from failure populations characterized by a two-parameter Weibull distribution. Alternatively, nonlinear regression estimators (discussed later) are utilized to calculate unknown distribution parameters for a three-parameter Weibull distribution.

Many factors affect the estimates of the distribution parameters. The total number of test specimens plays a significant role. Initially, the uncertainty associated with parameter estimates decreases significantly as the number of test specimens increases. However, a point of diminishing returns occurs when the cost associated with performing additional strength tests may not be justified by improvements in the estimated values of the distribution parameters. This suggests that a practical number of strength tests should be performed to obtain a desired level of confidence associated with a parameter estimate. This point cannot be overemphasized. However, quite often 30 specimens (a widely cited rule-of-thumb) is deemed a sufficient quantity of test specimens when estimating Weibull parameters. One should immediately ask why 29 specimens would not suffice. Or more importantly, why is 30 specimens sufficient? The answer to this is addressed in ASTM Standard Practice C 1239-95 where the details of computing confidence bounds for the maximum likelihood estimates (these bounds are directly related to the precision of the estimate) are presented. Duffy et al. (Ref 28) discusses the reasons why these same confidence bounds are not available for the nonlinear regression estimators.

Tensile and flexural specimens are the most commonly used test configurations in determining ultimate strength values for brittle materials. However, as noted earlier, most brittle material systems exhibit a decreasing trend in material strength as the test specimen geometry is increased. Thus, the observed strength values are dependent on specimen size and geometry. Parameter estimates can be computed based on a given specimen geometry; however, the parameter estimates should be transformed and utilized in a component reliability analysis as material-specific parameters. The procedure for transforming parameter estimates for the typical specimen geometries just cited is outlined in ASTM Standard Practice C 1239-95. The reader should be aware that the parameters estimated using nonlinear regression estimators are material-specific parameters. Therefore, no transformation is necessary after these parameters have been estimated.

Brittle materials can easily contain two or more active flaw distributions (e.g., failures due to inclusions or machining damage) and each will have its own strength distribution parameters. The censoring techniques for the two-parameter Weibull distribution require positive confirmation of multiple-flaw distributions, which neces-

Table 1 Alumina fracture stress data

Specimen No.	Stress, MPa	Specimen No.	Stress, MPa	Specimen No.	Stress, MPa
1	307	13	347	25	376
2	308	14	350	26	376
3	322	15	352	27	381
4	328	16	353	28	385
5	328	17	355	29	388
6	329	18	356	30	395
7	331	19	357	31	402
8	332	20	364	32	411
9	335	21	371	33	413
10	337	22	373	34	415
11	343	23	374	35	456
12	345	24	375		

sitates fractographic examination to characterize the fracture origin in each specimen. Multiple-flaw distributions may also be indicated by a deviation from the linearity of the data from a single Weibull distribution (see Fig. 3). However, observations of approximately linear behavior should not be considered a sufficient reason to conclude a single flaw distribution is active. The reader is strongly encouraged to integrate mechanical failure data and fractographic analysis.

As was just noted, discrete fracture origins are quite often grouped by flaw distributions. The data for each flaw distribution can also be screened for outliers. An outlying observation is one that deviates significantly from other observations in the sample. However, an apparent outlying observation may be an extreme manifestation of the variability in strength. If this is the case, the data point should be retained and treated as any other observation in the failure sample. Yet the outlying observation can be the result of a gross deviation from prescribed experimental procedure, or possibly an error in calculating or recording the numerical value of the data point in question. When the experimentalist is clearly aware that either of these situations has occurred, the outlying observation may be discarded, unless the observation (i.e., the strength value) can be corrected in a rational manner. For the sake of brevity, this discussion omits any discussion on the performance of fractographic analyses and omits any discussion concerning outlier tests.

Two-Parameter MLEs. With the above discussion serving as background, attention is now focused on obtaining estimated values of the Weibull parameters α and β_θ. This discussion focuses on MLEs because of their efficiency and ease of application when censored failure populations are encountered. When a sample containing ultimate strength observations yields two or more distinct flaw distributions, the sample is said to contain censored data. The maximum likelihood methodology accounts for censored data in a rational, straightforward manner. Other estimation techniques (specifically linear regression estimators) must appeal to ad hoc reranking schemes in the presence of censored data.

Johnson and Tucker (Ref 1), as well as others, have shown that the MLE method is more efficient in estimating parameters. Here, efficiency is measured through the use of confidence bounds.

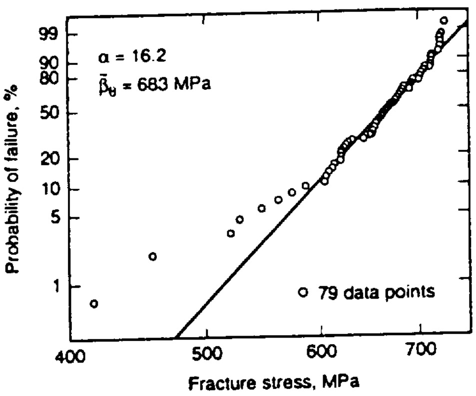

Fig. 3 Sample with multiple failure populations

For an equivalent confidence level, the authors of these works have demonstrated that the confidence bounds for an MLE is always smaller than the confidence bound obtained using linear regression. For this reason the likelihood estimators should be used to compute parameters from failure populations characterized by a two-parameter Weibull distribution.

The parameter estimates obtained using the maximum likelihood technique are unique (for a two-parameter Weibull distribution), and as the size of the sample increases, the estimates statistically approach the expected values of the true population parameter. Let $\sigma_1, \sigma_2, \ldots, \sigma_N$ represent realizations of the ultimate tensile strength (a random variable) in a given sample, where it is assumed that the ultimate tensile strength is characterized by the two-parameter Weibull distribution. The likelihood function associated with this sample is the joint probability density of the N random variables and thus is a function of t unknown Weibull distribution parameters (α, β The likelihood function for an uncensored sa ple under these assumptions is given by the e pression:

$$L = \prod_{i=1}^{N} \left(\frac{\tilde{\alpha}}{\tilde{\beta}_\theta}\right)\left(\frac{\sigma_i}{\tilde{\beta}_\theta}\right)^{\tilde{\alpha}-1} \exp\left[-\left(\frac{\sigma_i}{\tilde{\beta}_\theta}\right)^{\tilde{\alpha}}\right] \qquad \text{(Eq}$$

The parameter estimates (the Weibull modulus and the characteristic strength $\tilde{\beta}_\theta$) are determined taking the partial derivatives of the logarithm of likelihood function with respect to $\tilde{\alpha}$ and $\tilde{\beta}_\theta$, equating the resulting expressions to 0. Note that tildes distinguish a parameter estimate from its c responding true value. The system of equati obtained by differentiating the log likelihood fu tion for a censored sample is given by:

$$\frac{\sum_{i=1}^{N} (\sigma_i)^{\tilde{\alpha}} \ln(\sigma_i)}{\sum_{i=1}^{N} (\sigma_i)^{\tilde{\alpha}}} - \frac{1}{N}\sum_{i=1}^{N} \ln(\sigma_i) - \frac{1}{\tilde{\alpha}} = 0 \qquad \text{(Eq}$$

and

$$\tilde{\beta}_\theta = \left[\left(\sum_{i=1}^{N} (\sigma_i)^{\tilde{\alpha}}\right)\frac{1}{N}\right]^{1/\tilde{\alpha}} \qquad \text{(Eq}$$

Equation 43 is solved numerically, becaus closed-form solution for $\tilde{\alpha}$ cannot be obtained f this expression. Once $\tilde{\alpha}$ is determined this val inserted into Eq 44 and $\tilde{\beta}_\theta$ is calculated directly.

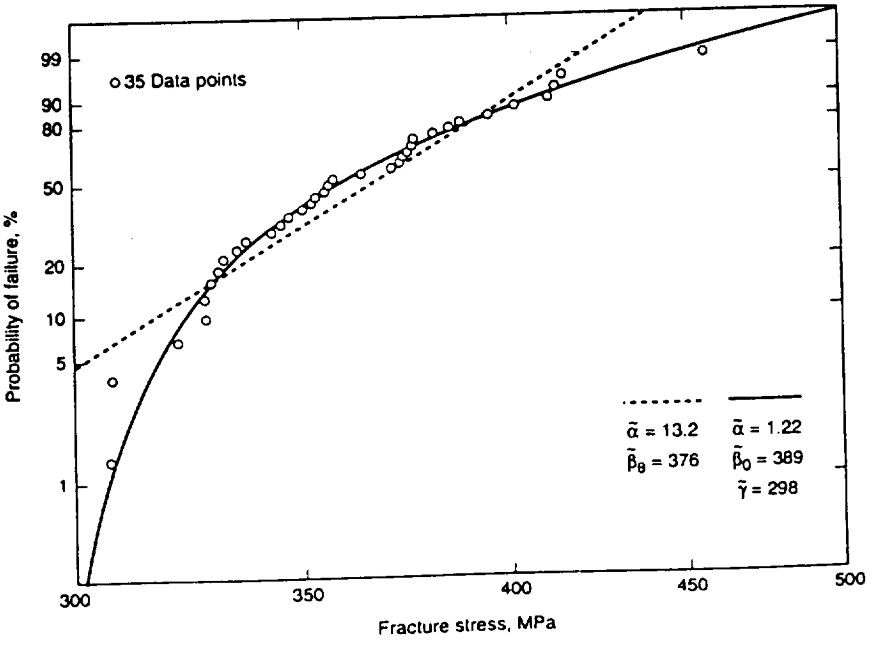

Fig. 4 Alumina failure data (see Table 1) and probability of failure curves based on estimated parameters for the tw three-parameter Weibull distributions

reader is once again directed to ASTM Standard Practice C 1239-95 for the expressions corresponding to samples with censored data.

Three-Parameter Linear Regression. To date, most reliability analyses performed on structural components fabricated from ceramic materials have utilized the two-parameter form of the Weibull distribution. The use of a two-parameter Weibull distribution to characterize the random nature of material strength implies a nonzero probability of failure for the full range of applied tensile stress. This represents a conservative design assumption when analyzing structural components. The three-parameter form of the Weibull distribution was presented earlier in Eq 30 and 31. The additional parameter is a threshold stress (γ) that allows for zero probability of failure when the applied stress is at or below the threshold value. Certain monolithic ceramics have exhibited threshold behavior. The reader is directed to an extensive database assembled in Ref 29, the silicon nitride data in Ref 30, as well as data (with supporting fractography) presented in Ref 31 that was analyzed later in Ref 28.

When strength data indicates the existence of a threshold stress, a three-parameter Weibull distribution should be employed in the stochastic failure analysis of structural components. By employing the concept of a threshold stress, an engineer can effectively tailor the design of a component to optimize structural reliability. To illustrate the approach, Duffy et al. (Ref 28) embedded the three-parameter Weibull distribution in a reliability model that utilized PIA. Analysis of a space-shuttle main engine (SSME) turbopump blade predicted a substantial improvement in component reliability when the three-parameter Weibull distribution was utilized in place of the two-parameter Weibull distribution. Note that the three-parameter form of the Weibull distribution can easily be extended to Batdorf's (Ref 21, 22) model, reliability models proposed for ceramic composites by Duffy et al. (Ref 32), or Thomas and Wetherhold (Ref 33), as well as the interactive reliability models proposed by Palko (Ref 34).

The nonlinear regression method presented here was first proposed by Margetson and Cooper (Ref 35). However, these estimators maintain certain disadvantages relative to bias and invariance, and these issues were explored numerically in Ref 28. The Monte Carlo simulations in Ref 28 demonstrated that the functions proposed in Ref 35 are neither invariant nor unbiased. However, they are asymptotically well behaved in that bias decreases and confidence intervals contract as the sample size increases. Thus, even though bias and confidence bounds may never be quantified using these nonlinear regression techniques, the user is guaranteed that estimated values improve as the sample size is increased.

Regression analysis postulates a relationship between two variables. In an experiment typically one variable can be controlled (the independent variable), while the response variable (or dependent variable) is not. In simple failure experiments the material dictates the strength at failure, indicating that the failure stress is the response variable. The ranked probability of failure (P_i) can be controlled by the experimentalist, because it is functionally dependent on the sample size (N). After arranging the observed failure stresses ($\sigma_1, \sigma_2, \sigma_3, \ldots, \sigma_N$) in ascending order, and specifying:

$$P_i = \frac{(i - 0.5)}{N} \qquad \text{(Eq 45)}$$

then clearly the ranked probability of failure for a given stress level can be influenced by increasing or decreasing the sample size. The procedure proposed in Ref 35 adopts this philosophy. They assume that the specimen failure stress is the dependent variable, and the associated ranked probability of failure becomes the independent variable.

Using the three-parameter version of Eq 34, an expression can be obtained relating the ranked probability of failure (P_i), to an estimate of the failure strength ($\tilde{\sigma}_i$). Assuming uniaxial stress conditions in a test specimen with a unit volume, Eq 34 yields:

$$\tilde{\sigma}_i = \tilde{\gamma} + \tilde{\beta}_0 \left[\ln \left(\frac{1}{1 - P_i} \right) \right]^{1/\tilde{\alpha}} \qquad \text{(Eq 46)}$$

where $\tilde{\alpha}$, $\tilde{\beta}_0$, and $\tilde{\gamma}$ are estimates of the shape parameter (α), the scale parameter (β_0), and threshold parameter (γ), respectively. Expressions for the evaluation of these parameters for a test specimen subjected to pure bending are found in Ref 28. Defining the residual as:

$$\delta_i = \tilde{\sigma}_i - \sigma_i \qquad \text{(Eq 47)}$$

where σ_i is the ith ranked failure stress obtained from actual test data, then the sum of the squared residuals is expressed as:

$$\sum_{i=1}^{N} (\delta_i)^2 = \sum_{i=1}^{N} \left[\tilde{\gamma} + \tilde{\beta}_0 (W_i)^{1/\tilde{\alpha}} - \sigma_i \right]^2 \qquad \text{(Eq 48)}$$

Here the notation of Ref 35 has been adopted where:

$$W_i = \ln \left(\frac{1}{1 - P_i} \right) \qquad \text{(Eq 49)}$$

Note that the forms of $\tilde{\sigma}_i$ and W_i change with specimen geometry. This is discussed in more detail in Ref 28.

It should be apparent that the objective of this method is to obtain parameter estimates that minimize the sum of the squared residuals. Setting the partial derivatives of the sum of the squared residuals with respect to $\tilde{\alpha}$, $\tilde{\beta}_0$, and $\tilde{\gamma}$ equal to zero yields the following three expressions:

$$\tilde{\beta}_0 = \frac{N \left[\sum_{i=1}^{N} \sigma_i (W_i)^{1/\hat{\alpha}} \right] - \left[\sum_{i=1}^{N} \sigma_i \right] \left[\sum_{i=1}^{N} (W_i)^{1/\hat{\alpha}} \right]}{N \sum_{i=1}^{N} (W_i)^{2/\hat{\alpha}} - \left[\sum_{i=1}^{N} (W_i)^{1/\hat{\alpha}} \right] \left[\sum_{i=1}^{N} (W_i)^{1/\hat{\alpha}} \right]} \qquad \text{(Eq 50)}$$

$$\begin{aligned} \tilde{\gamma} = & \left\{ \left[\sum_{i=1}^{N} \sigma_i \right] \left[\sum_{i=1}^{N} (W_i)^{2/\hat{\alpha}} \right] \right. \\ & \left. - \left[\sum_{i=1}^{N} \sigma_i (W_i)^{1/\hat{\alpha}} \right] \left[\sum_{i=1}^{N} (W_i)^{1/\hat{\alpha}} \right] \right\} \\ & \times \left\{ N \sum_{i=1}^{N} (W_i)^{2/\hat{\alpha}} - \left[\sum_{i=1}^{N} (W_i)^{1/\hat{\alpha}} \right] \left[\sum_{i=1}^{N} (W_i)^{1/\hat{\alpha}} \right] \right\}^{-1} \end{aligned} \qquad \text{(Eq 51)}$$

and

$$\begin{aligned} & \left| \sum_{i=1}^{N} \sigma_i (W_i)^{1/\tilde{\alpha}} \ln (W_i) - \tilde{\gamma} \sum_{i=1}^{N} \sigma_i (W_i)^{1/\tilde{\alpha}} \ln (W_i) \right. \\ & \left. - \tilde{\beta}_0 \sum_{i=1}^{N} \sigma_i (W_i)^{2/\tilde{\alpha}} \ln (W_i) \right| \le \kappa_{\text{conv}} \end{aligned} \qquad \text{(Eq 52)}$$

in terms of the parameter estimates. The solution of this system of equations is iterative, where the third expression is used to check convergence of an iteration. The initial solution vector for this system is determined after assuming a convenient value for $\tilde{\alpha}$, say $\tilde{\alpha} = 1$. Then β_0 is computed from Eq 50 and $\tilde{\gamma}$ is calculated from Eq 51. The values of these parameter estimates are then inserted into Eq 52 to determine if the convergence criterion is satisfied to within some predetermined tolerance (κ_{conv}). If this expression is not satisfied, $\tilde{\alpha}$ is updated and a new iteration is conducted. This procedure continues until a set of parameter estimates is determined that satisfy Eq 52.

The estimators perform reasonably well in comparison to estimates of the two-parameter Weibull distribution for the alumina data found in Table 1. Figure 4 is a plot of probability of failure versus failure stress for this data. The straight line represents the two-parameter fit to the data where $\tilde{\alpha} = 143.2$, $\beta_\theta = 395$ ($\tilde{\gamma} \equiv 0$) using values from Ref 29 for the shape and scale parameters. The nonlinear curve represents the three-parameter fit to the data where $\tilde{\alpha} = 1.22$, $\tilde{\beta}_0 = 389$, and $\tilde{\gamma} = 298$. Note that the three-parameter distribution appears more efficient in predicting the failure data in the high-reliability region of the graph. This is a qualitative assessment. Goodness-of-fit statistics such as the Kolmogorov-Smirnov statistic, the Anderson-Darling statistic, and likelihood ratio tests could provide quantitative measures to establish which form of the Weibull distribution would best fit the experimental data. These statistics are utilized in conjunction with hypothesis testing to assess the significance level at which the null hypothesis can be rejected. Comparisons can then be made based on the value of the significance level.

Time-Independent Reliability Algorithms

After a reliability model has been adopted and the failure function ψ has been specified, the primary task is the evaluation of the integral given in Eq 35. Closed-form solutions exist for only the simplest of component geometries and boundary conditions. Therefore, integrated computer algorithms have been developed that enable the design engineer to predict the time-independent (fast-fracture) reliability of components subjected to thermomechanical loading. Two algorithms are discussed here. One algorithm has been developed at the NASA Lewis Research Center and has been given the acronym CARES (Ceramics Analysis and Reliability Evaluation of Structures). This algorithm is widely discussed in Ref 12 and 36 to 38. The second computer algorithm, given the acronym ERICA, was developed by AlliedSignal (Ref 39, 40) with funding provided by the U.S. Department of Energy. Both algorithms are discussed briefly, and design examples are illustrated.

CARES Algorithm. The NASA Lewis Research Center CARES algorithm couples commercially available finite element programs, such as MSC/NASTRAN, ANSYS, or ABAQUS, with the probabilistic design models discussed previously. The algorithm contains three software modules that:

- Perform parameter estimation using experimental data obtained from standard laboratory specimens
- Generate a neutral database from MSC/NASTRAN, ABAQUS, and ANSYS finite element results files
- Evaluate the reliability of thermomechanically loaded components

Heat-transfer and linear-elastic finite element analyses are used to determine the temperature field and stress field. The component reliability analysis module of CARES uses the thermoelastic or isothermal elastostatic results to calculate the time-independent reliability for each element using a specified reliability model. Each element can be made arbitrarily small, such that the stress field in an element can be approximated as constant throughout the element (or subelement). The algorithm is compatible with most (but not all) two-dimensional elements, three-dimensional elements, axisymmetric elements, and shell elements for the commercial finite element algorithms mentioned above. Reliability calculations are performed at the Gaussian integration points of the element or, optionally, at the element centroid. Using the element integration points enables the element to be divided into subelements, where integration point subvolumes, subareas, and subtemperatures are calculated. The location of the Gaussian integration point in the finite element and the corresponding weight functions are considered when the subelement volume and/or area is calculated. The number of subelements in each element depends on the integration order chosen and the element type. If the probability of survival for each element is assumed to be a mutually exclusive event, the overall component reliability is the product of all the calculated element (or subelement) survival probabilities. The CARES algorithm produces an optional PATRAN file containing risk-of-rupture intensities (a local measure of reliability) for graphical rendering of the critical regions of the structure.

ERICA Algorithm. Unlike CARES, the AlliedSignal algorithm ERICA has a software architecture with a single module. Currently, only one finite element program interface exists for the algorithm, that is, an interface with the ANSYS finite element program. Once again stress and temperature information from the solution of a discretized component are used in conjunction with a specified reliability model to assess component reliability. ERICA admits multiple flaw distributions that can be spatially distributed through the volume, along the surface, and along the edges of a component. Both isotropic material behavior, and to a limited extent, anisotropic material behavior (for surface calculations) are taken into account. This anisotropic surface option allows the user to account for various types of surface finish on a component (e.g., ground, as fired, etc.). The ERICA algorithm can function on any platform that supports ANSYS. A limited number of element types are supported that offer the user some flexibility in modeling a component. Note that neither CARES nor ERICA support a full suite of elements for any of the commercial finite element algorithms.

Time-Independent Design Examples

Reliability analyses are typically segreg
into two categories: time-independent and ti
dependent. This classification is rooted bot
the historic development of the reliability mo
presented here and also in a practical approac
the analysis of a component. Yet in many
stances, a component must perform in an
quate fashion over a predetermined service
To accomplish this design goal, the compo
must survive the initial load cycle. Thus,
calculated time-independent reliability valu
used as a screening criterion and can also be
as an initial value for the time-dependent anal
discussed later. A fundamental premise of p
abilistic analysis dictates that if the reliabili
a component varies with time then it should n
exceed the initial value (unless there exists s
physical mechanism such as flaw healing tha
account for this phenomenon). Typically, m
als deteriorate with time, and this assumpti
incorporated throughout this chapter. From
torical perspective, the authors simply poin
that the time-independent models were d
oped first (hence they are presented first her
addition, the time-independent approach
been rigorously exercised over the years. E
sive design experience and databases have
established prior to proposal of the tim
pendent modeling efforts outlined later ir
chapter.

Both the CARES and ERICA reliability
rithms have been used in the design and an
of numerous structural components. Of the
the NASA CARES algorithm has been
widely utilized for proprietary reasons.
CARES reliability algorithm has been us
design glass and ceramic parts for a wide ra
applications. These include hot section co
nents for turbine and internal combustio
gines, bearings, laser windows on test rig
domes, radiant heater tubes, spacecraft acti
valves and platforms, CRTs, rocket lau
tubes, and ceramic packaging for microp
sors. Illustrated below are some typical
and analysis applications that have utiliz
CARES software. In the interest of bre
complete example problem cannot be inclu

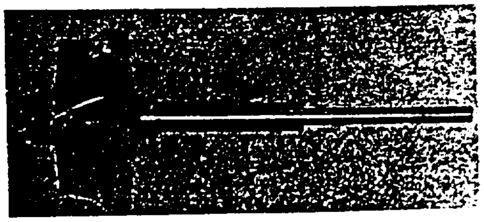

Fig. 5 Ceramic automotive turbocharger wheel. Courtesy of AlliedSignal Turbocharging and Truck Brake Systems

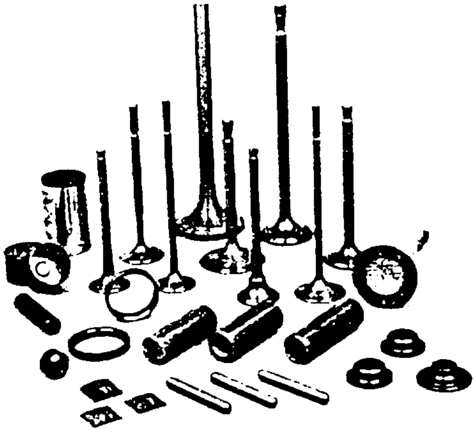

Fig. 6 Automotive valves and engine components. Courtesy of TRW Automotive Valve Division

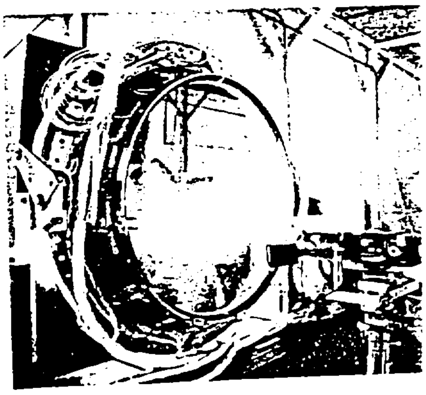

Fig. 7 The largest known ZnSe window manufac
a cryogenic vacuum chamber. Courtesy o
Danbury Optical Systems

this article. For a complete step-by-step procedure on conducting a time-independent component reliability analysis, the reader is directed to Ref 12.

The CARES algorithm has been successfully used in the development of ceramic turbocharger wheels (Ref 41). Specifically, the CARES algorithm was utilized to design the CTV7301 silicon nitride turbocharger rotor, depicted in Fig. 5, which was implemented in the Caterpillar 3406E diesel engine. The reduced rotational inertia of the silicon nitride ceramic rotor compared to a metallic rotor significantly enhanced the turbocharger transient performance and reduced emissions. Note that this was a joint effort involving AlliedSignal and Caterpillar and represents the first design and large-scale deployment of ceramic turbochargers in the United States. More than 1700 units have been supplied to Caterpillar Tractor Company for on-highway truck engines. These units together have accumulated a total of over 120 million miles of service.

Extensive work has been performed to analyze graphite and ceramic structural components such as high-temperature valves, test fixtures, and turbine wheels using CARES. A silicon nitride turbine wheel has been designed as a retrofit to replace components fabricated from Waspaloy in a military cartridge-mode air turbine starter (Ref 42). The silicon nitride component reduced cost and weight while increasing resistance to temperature, erosion, and corrosion.

The CARES algorithm has been used to analyze a ceramic-to-metal brazed joint for automotive gas turbine engines (Ref 43, 44). A major design hurdle in ceramic-to-metal joining is the thermal expansion mismatch between the two different materials. This results in high residual stresses that increase the likelihood of ceramic failure. One of the goals of this work was to improve the capability of the metal shaft to transmit power by reducing concentrated tensile stresses. The results confirmed the importance of probabilistic failure analysis for assessing the performance of various brazed joint designs.

A monolithic graphite spacecraft activation valve was designed (Ref 45) to direct reaction control gases for fine tuning the trajectory of a high-performance kinetic energy kill vehicle during the last 9 s of flight. Utilizing the CARES software, the valve was designed to withstand a gas pressure of 11.4 MPa (1.6 ksi) at 1930 °C (3506 °F).

A design study (Ref 46) demonstrated the viability of an uncooled silicon nitride combustor for commercial application in a 300 kW engine with a turbine inlet temperature of 1370 °C (2498 °F). Using the CARES algorithm, an analysis identified the most severe transient thermal stress in an emergency shutdown. The most critical area was found to be around the dilution port.

Ceramic poppet valves for spark ignition engines have been designed (Ref 47). These parts, depicted with other engine components in Fig. 6, have been field tested in passenger cars with excellent results. Potential advantages offered by these valves include reduced seat insert and valve guide wear, improved valve train dynamics, increased engine output, and reduced friction loss using lower spring loads.

The largest known zinc-selenide (ZnSe) containment window (depicted in Fig. 7) was designed using the CARES algorithm. The window formed a pressure barrier between a cryogenic vacuum chamber containing optical equipment and a sensor chamber. The window measured 79 cm (31 in.) in diameter by 2.5 cm (1 in.) thick and was used in a test facility for long-range infrared sensors.

The previous examples cited successful applications of the reliability algorithms in the design and analysis of commercial applications. In many cases, the algorithms have been an integral component of research and development efforts in government-supported programs. A specific example of this is the use of the CARES algorithm by participating organizations in the Advanced Turbine Technology Applications Program (ATTAP) to determine the reliability of structural component designs. The ATTAP program (Ref 48) is intended to advance the technological readiness of the ceramic automotive gas turbine engine. Structural ceramic components represent the greatest technical challenge facing the commercialization of such an engine and are thus the prime project focus. Cooperative efforts have been developed between industry, key national facilities, and academia to capitalize on the unique capabilities and facilities developed for ceramic materials characterization and processing technology. Figure 8 depicts engine components, including structural, combustion, regeneration, and insulation applications designed using the NASA-developed CARES software.

Life Prediction Using Reliability Analyses

The discussions in the previous sections assumed all failures were independent of time and history of previous thermomechanical loadings. However, as design protocols emerge for brittle material systems, designers must be aware of several innate characteristics exhibited by these materials. When subjected to elevated service temperatures, they exhibit complex thermomechanical behavior that is both inherently time dependent and hereditary in the sense that current behavior depends not only on current conditions, but also on thermomechanical history. The design engineer must also be cognizant that the ability of a component to sustain load degrades over time due to a variety of effects such as oxidation, creep, stress corrosion, and cyclic fatigue. Stress corrosion and cyclic fatigue result

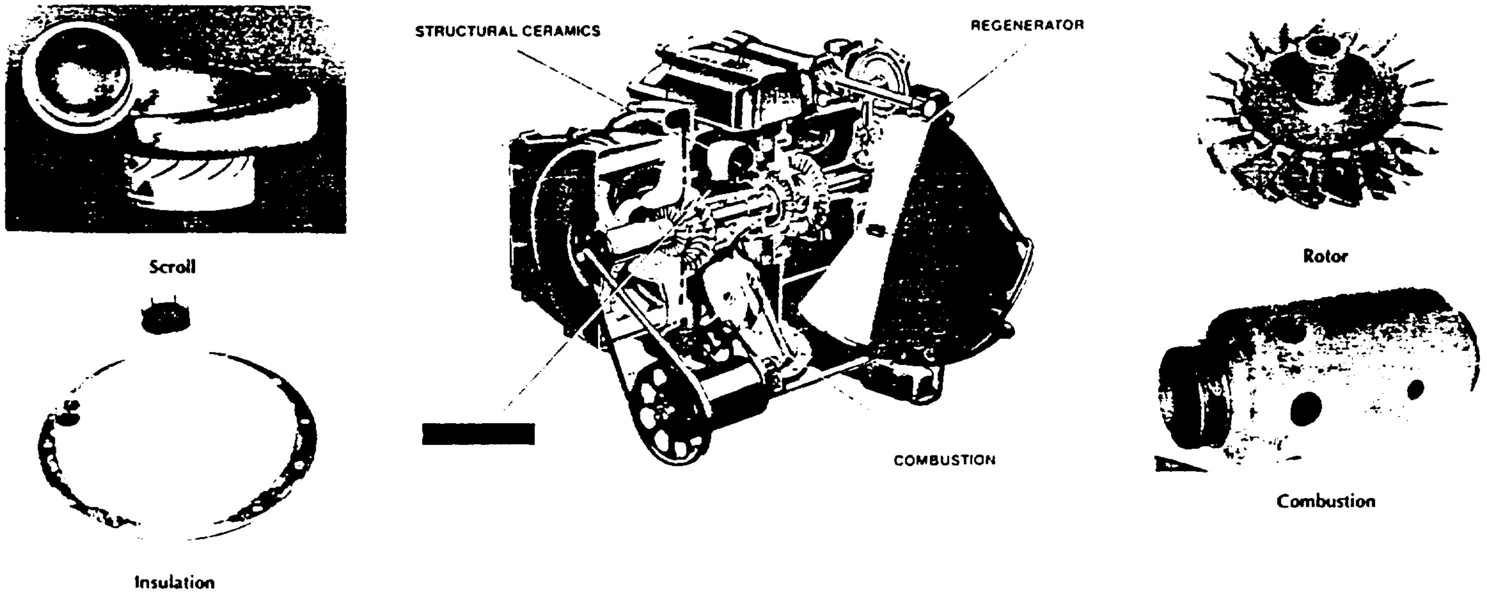

Fig. 8 Gas turbine engine and components. Scroll and rotor are made from structural ceramics. Courtesy of Allison Engine Company

in a phenomenon called subcritical crack growth (SCG). This failure mechanism initiates at a preexisting flaw and continues until a critical length is attained. At that point, the crack grows in an unstable fashion leading to catastrophic failure. The SCG failure mechanism is a time-dependent, load-induced phenomenon. Time-dependent crack growth can also be a function of chemical reaction, environment, debris wedging near the crack tip, and deterioration of bridging ligaments. Fracture mechanism maps, such as the one developed for ceramic materials (Ref 49) depicted in Fig. 9, help illustrate the relative contribution of various failure modes as a function of temperature and stress.

In addition to the determination of the Weibull shape and scale parameters discussed previously, analysis of time-dependent reliability in brittle materials necessitates accurate stress field information, as well as evaluation of distinct parameters reflecting material, microstructural, and/or environmental conditions. Predicted lifetime reliability of brittle material components depends on Weibull and fatigue parameters estimated from rupture data obtained from widely used tests involving flexural or tensile specimens. Fatigue parameter estimates are obtained from naturally flawed specimens ruptured under static (creep), cyclic, or dynamic (constant stress rate) loading. For other specimen geometries, a finite element model of the specimen is also required when estimating these parameters. For a more detailed discussion of time-dependent parameter estimation, the reader is directed to the *CARES/Life (CARES/Life Prediction Program) Users and Programmers Manual* (Ref 50). This information can then be combined with stochastic modeling approaches and incorporated into integrated design algorithms (computer software) in a manner similar to that presented previously for time-independent models. The theoretical concepts upon which these time-dependent algorithms have been constructed and the effects of time-dependent mechanisms, most notably subcritical crack growth and creep, are addressed in the remaining sections of this article.

Although it is not discussed in detail here, one approach to improve the confidence in component reliability predictions is to subject the component to proof testing prior to placing it in service. Ideally, the boundary conditions applied to a component under proof testing simulate those conditions the component would be subjected to in service, and the proof test loads are appropriately greater in magnitude over a fixed time interval. This form of testing eliminates the weakest components and, thus, truncates the tail of the strength distribution curve. After proof testing, surviving components can be placed in service with greater confidence in their integrity and a predictable minimum service life.

Need for Correct Stress State

With increasing use of brittle materials in high-temperature structural applications, the need arises to accurately predict thermomechanical behavior. Most current analytical methods for both subcritical crack growth and creep models use elastic stress fields in predicting the time-dependent reliability response of components subjected to elevated service temperatures. Inelastic response at high temperature has been well documented in the materials science literature for these material systems, but this issue has been ignored by the engineering design community. However, the authors wish to emphasize that accurate predictions of time-dependent reliability demand accurate stress-field information. From a design engineer's perspective, it is imperative that the inaccuracies of making time-dependent reliability predictions based on elastic stress fields are taken into consideration. This section addresses this issue by presenting a recent formulation of a viscoplastic constitutive theory to model the inelastic deformation behavior of brittle materials at high temperatures.

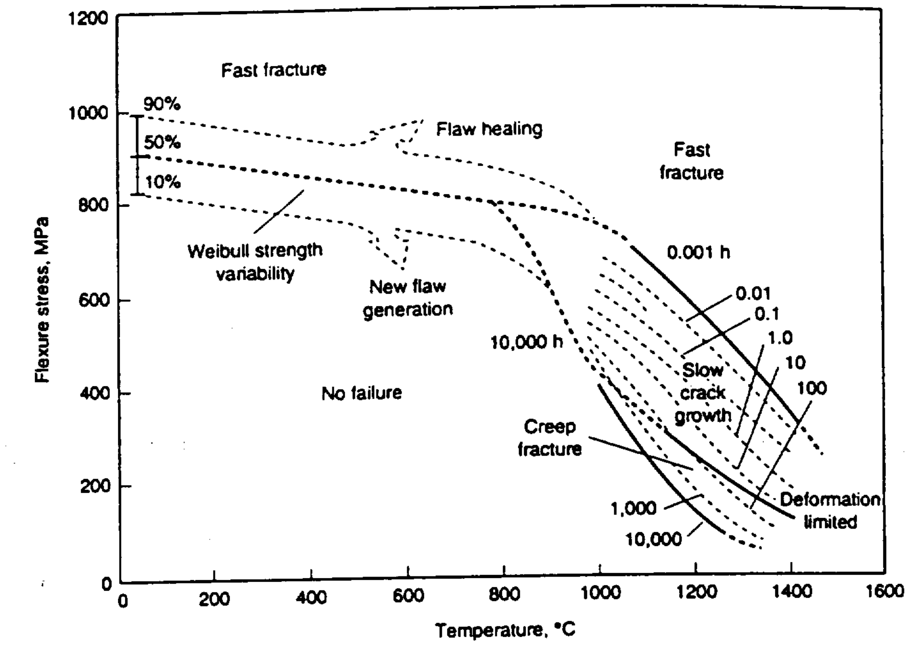

Fig. 9 Fracture mechanism map for hot-pressed silicon nitride flexure bars. Fracture mechanism maps help illustrate the relative contribution of various failure modes as a function of temperature and stress. Source: Ref 49

Early work in the field of metal plasticity indicated that inelastic deformations are essentially unaffected by hydrostatic stress. This is not the case for brittle (e.g., ceramic-based) material systems, unless the material is fully dense. The theory presented here allows for fully dense material behavior as a limiting case. In addition, as pointed out in Ref 51, these materials exhibit different time-dependent behavior in tension and compression. Thus, inelastic deformation models for these materials must be constructed in a manner that admits sensitivity to hydrostatic stress and differing behavior in tension and compression.

A number of constitutive theories for materials that exhibit sensitivity to the hydrostatic component of stress have been proposed that characterize deformation using time-independent classical plasticity as a foundation. Corapcioglu and Uz (Ref 52) reviewed several of these theories b focusing on the proposed form of the individua yield function. The review includes the works o Kuhn and Downey (Ref 53), Shima and Oyan (Ref 54), and Green (Ref 55). Not included is th work by Gurson (Ref 56), who not only developed a yield criteria and flow rule, but also discussed the role of void nucleation. Subsequen work by Mear and Hutchinson (Ref 57) extende Gurson's work to include kinematic hardening o the yield surfaces.

Although the previously mentioned theorie admit a dependence on the hydrostatic component of stress, none of these theories allows different behavior in tension and compression. I addition, the aforementioned theories are somewhat lacking in that they are unable to captur creep, relaxation, and rate-sensitive phenomen exhibited by brittle materials at high temperatur Noted exceptions are the recent work by Ding e al. (Ref 58) and the work by White and Hazim (Ref 59). Another exception is an article by Liu e al. (Ref 60), which is an extension of the wor presented by Ding and coworkers. As thes authors point out, when subjected to elevate service temperatures, brittle materials exhib complex thermomechanical behavior that is i herently time dependent and hereditary in th sense that current behavior depends not only c current conditions, but also on thermomechanic history.

The macroscopic continuum theory formulat in the remainder of this section captures the time-dependent phenomena by developing an e tension of a J_2 plasticity model first proposed b Robinson (Ref 61) and later extended to sinter powder metals by Duffy (Ref 62). Although t viscoplastic model presented by Duffy (Ref 6 admitted a sensitivity to hydrostatic stress, it did not allow for different material behavior in tension and compression.

Willam and Warnke (Ref 63) proposed a yield criterion for concrete that admits a dependence on the hydrostatic component of stress and explicitly allows different material responses in tension and compression. Several formulations of their model exist, that is, a three-parameter formulation and a five-parameter formulation. For simplicity, the overview of the multiaxial derivation of the viscoplastic constitutive model presented here builds on the three-parameter formulation. The attending geometrical implications have been presented elsewhere (Ref 64, 65). A quantitative assessment has yet to be conducted because the material constants have not been suitably characterized for a specific material. The quantitative assessment could easily dovetail with the nascent efforts of White and coworkers (Ref 59).

The complete theory is derivable from a scalar dissipative potential function identified here as Ω. Under isothermal conditions, this function is dependent on the applied stress σ_{ij} and internal state variable α_{ij}:

$$\Omega = \Omega(\sigma_{ij}, \alpha_{ij}) \qquad \text{(Eq 53)}$$

The stress dependence for a J_2 plasticity model or a J_2 viscoplasticity model is usually stipulated in terms of the deviatoric components of the applied stress, $S_{ij} = \sigma_{ij} - (1/3)\,\sigma_{kk}\delta_{ij}$, and a deviatoric state variable, $a_{ij} = \alpha_{ij} - (1/3)\,\alpha_{kk}\delta_{ij}$. For the viscoplasticity model presented here, these deviatoric tensors are incorporated along with the effective stress, $\eta_{ij} = \sigma_{ij} - \alpha_{ij}$, and an effective deviatoric stress, identified as $\Sigma_{ij} = S_{ij} - a_{ij}$. Both tensors, that is, η_{ij} and Σ_{ij}, are utilized for notational convenience.

The potential nature of Ω is exhibited by the manner in which the flow and evolutionary laws are derived. The flow law is derived from Ω by taking the partial derivative with respect to the applied stress:

$$\dot{\varepsilon}_{ij} = \frac{\partial \Omega}{\partial \sigma_{ij}} \qquad \text{(Eq 54)}$$

The adoption of a flow potential and the concept of normality, as expressed in Eq 54, were introduced by Rice (Ref 66). In his work, the above relationship was established using thermodynamic arguments. The authors wish to point out that Eq 54 holds for each individual inelastic state.

The evolutionary law is similarly derived from the flow potential. The rate of change of the internal stress is expressed as:

$$\dot{\alpha}_{ij} = -h\frac{\partial \Omega}{\partial \alpha_{ij}} \qquad \text{(Eq 55)}$$

where h is a scalar function of the inelastic state variable (i.e., the internal stress) only. Using arguments similar to Rice's, Ponter, and Leckie (Ref 67) have demonstrated the appropriateness of this type of evolutionary law.

To give the flow potential a specific form, the following integral format proposed by Robinson (Ref 61) is adopted:

$$\Omega = K^2\left[\left(\frac{1}{2\mu}\right)\int F^n\,dF + \left(\frac{R}{H}\right)\int G^m\,dG\right] \qquad \text{(Eq 56)}$$

where μ, R, H, and K are material constants. In this formulation μ is a viscosity constant, H is a hardening constant, n and m are unitless exponents, and R is associated with recovery. The octahedral threshold shear stress K appearing in Eq 56 is generally considered a scalar state variable that accounts for isotropic hardening (or softening). However, because isotropic hardening is often negligible at high homologous temperatures ($T/T_m \geq 0.5$), to a first approximation K is taken to be a constant for metals. This assumption is adopted in the present work for brittle materials. The reader is directed to Ref 68 for specific details regarding the experimental test matrix needed to characterize these parameters.

The dependence on the effective stress Σ_{ij} and the deviatoric internal stress a_{ij} is introduced through the scalar functions $F = F(\Sigma_{ij}, \eta_{ij})$ and $G = G(a_{ij}, \alpha_{ij})$. Inclusion of η_{ij} and α_{ij} will account for sensitivity to hydrostatic stress. The concept of a threshold function was introduced by Bingham (Ref 69) and later generalized by Hohenemser and Prager (Ref 70). Correspondingly, F is referred to as a Bingham-Prager threshold function. Inelastic deformation occurs only for those stress states where $F(\Sigma_{ij}, \eta_{ij}) > 0$.

For frame indifference, the scalar functions F and G (and hence Ω) must be form invariant under all proper orthogonal transformations. This condition is ensured if the functions depend only on the principal invariants of Σ_{ij}, a_{ij}, η_{ij}, and α_{ij}; that is, $F = F(\tilde{I}_1, \tilde{J}_2, \tilde{J}_3)$, where $\tilde{I}_1 = \eta_{ii}$, $\tilde{J}_2 = (1/2)\,\Sigma_{ij}\Sigma_{ij}$, $\tilde{J}_3 = (1/3)\,\Sigma_{ij}\Sigma_{jk}\Sigma_{ki}$, and $G = G(\hat{I}_1, \hat{J}_2, \hat{J}_3)$, where $I_1 = a_{ii}$, $J_2 = (1/2)a_{ij}a_{ij}$, $J_3 = (1/3)\,a_{ij}a_{jk}a_{ki}$. These scalar quantities are elements of what is known in invariant theory as an integrity basis for the functions F and G.

A three-parameter flow criterion proposed by Willam and Warnke (Ref 63) serves as the Bingham-Prager threshold function, F. The William-Warnke criterion uses the previously mentioned stress invariants to define the functional dependence on the Cauchy stress (σ_{ij}) and internal state variable (α_{ij}). In general, this flow criterion can be constructed from the following general polynomial:

$$F = \lambda\left(\frac{\sqrt{\tilde{J}_2}}{\sigma_c}\right) + B\left(\frac{\tilde{I}_1}{\sigma_c}\right) - 1 \qquad \text{(Eq 57)}$$

where σ_c is the uniaxial threshold flow stress in compression and B is a constant determined by considering homogeneously stressed elements in the virgin inelastic state $\alpha_{ij} = 0$.

Note that a threshold flow stress is similar in nature to a yield stress in classical plasticity. In addition, λ is a function dependent on the invariant J_3 and other threshold stress parameters that are defined momentarily. The specific details in deriving the final form of the function F can be found in Willam and Warnke (Ref 63), and this final formulation is stated here as:

$$F(\tilde{I}_1, \tilde{J}_2, \tilde{J}_3) = \frac{1}{\sigma_c}\left[\frac{1}{r(\tilde{\theta})}\right]\left[\frac{2\tilde{J}_2}{5}\right]^{1/2} + \frac{\tilde{I}_1}{3\rho\sigma_c} - 1 \qquad \text{(Eq 58)}$$

for brevity. The invariant $\tilde{I}_1$ in Eq 58 admits a sensitivity to hydrostatic stress. The function F is implicitly dependent on J_3 through the function $r(\tilde{\theta})$, where the angle of similitude, θ, is defined by the expression:

$$\cos(3\tilde{\theta}) = \frac{(3\sqrt{3})\,\tilde{J}_3}{2(\tilde{J}_2)^{3/2}} \qquad \text{(Eq 59)}$$

The invariant $\tilde{J}_3$ accounts for different behavior in tension and compression, because this invariant changes sign when the direction of a stress component is reversed. The parameter ρ characterizes the tensile hydrostatic threshold flow stress. For the Willam-Warnke three-parameter formulation, the model parameters include σ_t, the tensile uniaxial threshold stress, σ_c, the compressive uniaxial threshold stress, and σ_{bc}, the equal biaxial compressive threshold stress.

A similar functional form is adopted for the scalar state function G. However, this formulation assumes a threshold does not exist for the scalar function G and follows the framework of previously proposed constitutive models based on Robinson's viscoplastic law (Ref 61).

Employing the chain rule for differentiation and evaluating the partial derivative of Ω with respect to σ_{ij}, and then with respect to α_{ij}, as indicated in Eq 54 and 55, yields the flow law and the evolutionary law, respectively. These expressions are dependent on the principal invariants (i.e., $\tilde{I}_1$, $\tilde{J}_2$, $\tilde{J}_3$, $\hat{I}_1$, $\hat{J}_2$, and $\hat{J}_3$) the three Willam-Warnke threshold parameters (i.e., σ_t, σ_c, and σ_{bc}), and the flow potential parameters utilized in Eq 56 (i.e., μ, R, H, K, n, and m). These expressions constitute a multiaxial statement of a constitutive theory for isotropic materials and serve as an inelastic deformation model for ceramic materials.

The overview presented in this section is intended to provide a qualitative assessment of the capabilities of this viscoplastic model in capturing the complex thermomechanical behavior exhibited by brittle materials at elevated service temperatures. Constitutive equations for the flow law (strain rate) and evolutionary law have been formulated based on a threshold function that exhibits a sensitivity to hydrostatic stress and allows different behavior in tension and compression. Furthermore, inelastic deformation is treated as inherently time dependent. A rate of inelastic strain is associated with every state of stress. As a result, creep, stress relaxation, and rate sensitivity are phenomena resulting from applied boundary conditions and are not treated separately in an ad hoc fashion. Incorporating this model into a nonlinear finite element code would provide a tool for the design engineer to simulate numerically the inherently time-dependent and hereditary phenomena exhibited by these materials in service.

Life Prediction Reliability Models

Using a time-dependent reliability model such as those discussed in the following section, and the results obtained from a finite element analysis, the life of a component with complex geometry and loading can be predicted. This life is interpreted as the reliability of a component as a function of time. When the component reliability falls below a predetermined value, the associated point in time at which this occurs is assigned the life of the component. This design methodology presented herein combines the statistical nature of strength-controlling flaws with the mechanics of crack growth to allow for multiaxial stress states, concurrent (simultaneously occurring) flaw populations, and scaling effects. With this type of integrated design tool, a design engineer can make appropriate design changes until an acceptable time to failure has been reached. In the sections that follow, only creep rupture and fatigue failure mechanisms are discussed. Although models that account for subcritical crack growth and creep rupture are presented, the reader is cautioned that currently available creep models for advanced ceramics have limited applicability because of the phenomenological nature of the models. There is a considerable need to develop models incorporating both the ceramic material behavior and microstructural events.

Subcritical Crack Growth. A wide variety of brittle materials, including ceramics and glasses, exhibit the phenomenon of delayed fracture or fatigue. Under the application of a loading function of magnitude smaller than that which induces short-term failure, there is a regime where subcritical crack growth occurs and this can lead to eventual component failure in service. Subcritical crack growth is a complex process involving a combination of simultaneous and synergistic failure mechanisms. These can be grouped into two categories: (1) crack growth due to corrosion and (2) crack growth due to mechanical effects arising from cyclic loading. Stress corrosion reflects a stress-dependent chemical interaction between the material and its environment. Water, for example, has a pronounced deleterious effect on the strength of glass and alumina. In addition, higher temperatures also tend to accelerate this process. Mechanically induced cyclic fatigue is dependent only on the number of load cycles and not on the duration of the cycle. This phenomenon can be caused by a variety of effects, such as debris wedging or the degradation of bridging ligaments, but essentially it is based on the accumulation of some type of irreversible damage that tends to enhance crack growth. Service environment, material composition, and material microstructure determine if a brittle material will display some combination of these fatigue mechanisms.

Lifetime reliability analysis accounting for SCG under cyclic and/or sustained loads is essential for the safe and efficient utilization of brittle materials in structural design. Because of the complex nature of SCG, models that have been developed tend to be semiempirical and approximate the behavior of SCG phenomenologically. Theoretical and experimental work in this area has demonstrated that lifetime failure characteristics can be described by consideration of the crack growth rate versus the stress intensity factor (or the range in the stress intensity factor). This is graphically depicted (see Fig. 10) as the logarithm of crack growth rate versus the logarithm of the mode I stress intensity factor. Curves of experimental data show three distinct regimes or regions of growth. The first region (denoted by I in Fig. 10) indicates threshold behavior of the crack, where below a certain value of stress intensity the crack growth is zero. The second region (denoted by II in Fig. 10) shows an approximately linear relationship of stable crack growth. The third region (denoted by III in Fig. 10) indicates unstable crack growth as the materials critical stress intensity factor is approached. For the stress-corrosion failure mechanism, these curves are material and environment sensitive. This SCG model, using conventional fracture mechanics relationships, satisfactorily describes the failure mechanisms in materials where at high temperatures, plastic deformations and creep behave in a linear viscoelastic manner (Ref 71). In general, at high temperatures and low levels of stress, failure is best described by creep rupture, which generates new cracks (Ref 72). The creep rupture process is discussed further in the next section.

The most-often-cited models in the literature regarding SCG are based on power-law formulations. Other theories, most notably Wiederhorn's (Ref 73), have not achieved such widespread usage, although they may also have a reasonable physical foundation. Power-law formulations are used to model both the stress-corrosion phenomenon and the cyclic fatigue phenomenon. This modeling flexibility, coupled with their widespread acceptance, make these formulations the most attractive candidates to incorporate into a design methodology. A power-law formulation is obtained by assuming the second crack growth region is linear and that it dominates the other regions. Three power-law formulations are u
for modeling brittle materials: the power law
Paris law, and the Walker equation. The p
law (Ref 71, 74) describes the crack velocity
function of the stress intensity factor and im
that the crack growth is due to stress corro
For cyclic fatigue, either the Paris law (Ref 7
Walker's (Ref 76, 77) modified formulatio
the Paris law is used to model the SCG. The
law describes the crack growth per load cyc
a function of the range in the stress inte
factor. The Walker equation relates the c
growth per load cycle to both the range in
crack tip stress intensity factor and the maxi
applied crack tip stress intensity factor. It is u
for predicting the effect of the *R*-ratio (the ra
the minimum cyclic stress to the maximum c
stress) on the material strength degradation.

Expressions for time-dependent reliabilit
usually formulated based on the mode I eq
lent stress distribution transformed to its eq
lent stress distribution at time $t = 0$. Inves
tions of mode I crack extension (Ref 78)
resulted in the following relationship for
equivalent mode I stress intensity factor:

$$K_{Ieq}(\Psi, t) = \sigma_{Ieq}(\Psi, t)\, Y \sqrt{a(\Psi, t)} \qquad \text{(E}$$

where $\sigma_{Ieq}(\Psi, t)$ is the equivalent mode I stre
the crack, Y is a function of crack geometry, a (
is the appropriate crack length, and Ψ represe
spatial location within the body and the orient
of the crack. In some models (such as the ph
menological Weibull NSA and the PIA model
represents a location only. Y is a function of
geometry; however, herein it is assumed co
with subcritical crack growth. Crack growth
function of the equivalent mode I stress inte

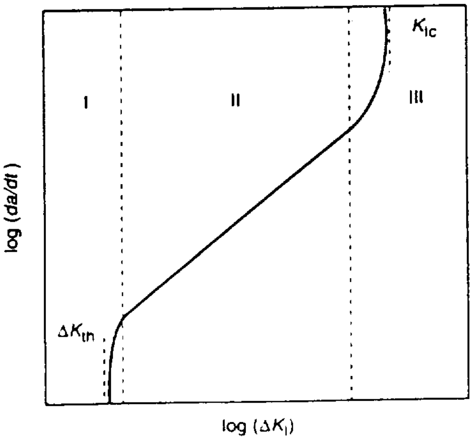

Fig. 10 Schematic illustrating three different regimes of crack growth

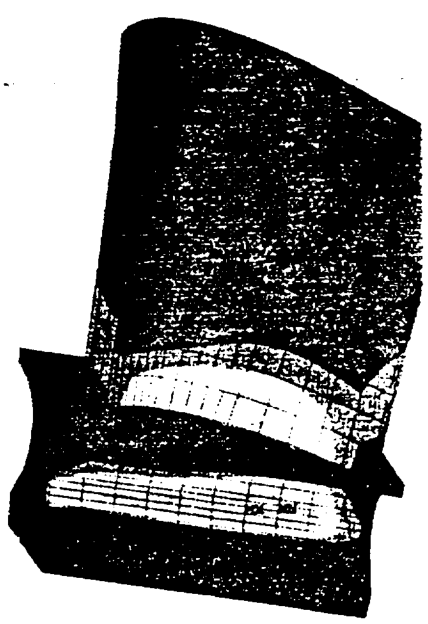

Fig. 11 Stress contour plot of first-stage silicon turbine rotor blade for a natural-gas-fired
trial turbine engine for cogeneration. The blade is rot
14,950 rpm. Courtesy of Solar Turbines Inc.

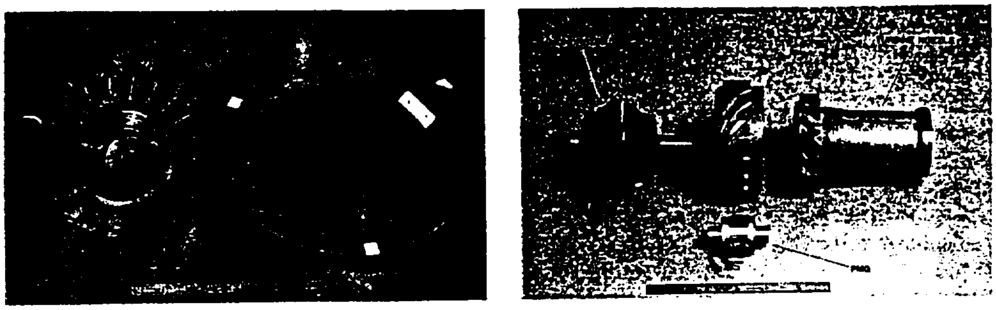

(a)

(b)

Fig. 12 (a) Ceramic turbine wheel and nozzle for advanced auxiliary power unit. (b) Ceramic components for small expendable turbojet. Courtesy of Sundstrand Aerospace Corporation

factor is assumed to follow a power-law relationship:

$$\frac{da\,(\Psi,t)}{dt} = A\,K_{\mathrm{Ieq}}^{N}\,(\Psi,t) \tag{Eq 61}$$

where A and N are material/environmental constants. The transformation of the equivalent stress distribution at the time of failure, $t = t_f$, to its critical effective stress distribution at time $t = 0$ is expressed (Ref 79, 80):

$$\sigma_{\mathrm{Ieq},0}\,(\Psi,t_f) = \left[\frac{\int_0^{t_f} \sigma_{\mathrm{Ieq}}^{N}\,(\Psi,t)\,dt}{B} + \sigma_{\mathrm{Ieq}}^{N-2}\,(\Psi,t_f)\right]^{1/(N-2)} \tag{Eq 62}$$

where

$$B = \frac{2}{A\,Y^2\,K_{\mathrm{Ic}}^{N-2}\,(N-2)} \tag{Eq 63}$$

is a material/environmental fatigue parameter, K_{Ic} is the critical stress intensity factor, and $\sigma_{\mathrm{Ieq}}\,(\Psi, t_f)$ is the equivalent stress distribution in the component at time $t = t_f$. The dimensionless fatigue parameter N is independent of fracture criterion. B is adjusted to satisfy the requirement that for a uniaxial stress state, all models produce the same probability of failure. The parameter B has units of stress^2 × time.

Because SCG assumes flaws exist in a material, the weakest-link statistical theories discussed previously are required to predict the time-dependent lifetime reliability for brittle materials. An SCG model (e.g., the previously discussed power law, Paris law, or Walker equation) is combined with either the two- or three-parameter Weibull cumulative distribution function to characterize the component failure probability as a function of service lifetime. The effects of multiaxial stresses are considered by using the PIA model, the Weibull NSA method, or the Batdorf theory. These multiaxial reliability expressions were outlined in the previous section on time-independent reliability analysis models, and, for brevity, are not repeated here. The reader is directed to see the previous section or, for more complete details, to consult Ref 50.

Creep Rupture. For brittle materials, the term creep can infer two different issues. The first relates to catastrophic failure of a component from a defect that has been nucleated and propagates to critical size. This is known as creep rupture to the design engineer. Here, it is assumed that failure does not occur from a defect in the original flaw population. Unlike SCG, which is assumed to begin at preexisting flaws in a component and continue until the crack reaches a critical length, creep rupture typically entails the nucleation, growth, and coalescence of voids which eventually form macrocracks, which then propagate to failure. The second issue related to creep reflects back on SCG as well as creep rupture, that is, creep deformation. This section focuses on the former, while the latter (i.e., creep deformation) is discussed in a previous section.

Currently, most approaches to predict brittle material component lifetime due to creep rupture employ deterministic methodologies. Stochastic methodologies for predicting creep life in brittle material components have not reached a level of maturity comparable to those developed for predicting fast-fracture and SCG reliability. One such theory is based on the premise that both creep and SCG failure modes act simultaneously (Ref 81). Another alternative method for characterizing creep rupture in ceramics was developed by Duffy and Gyekenyesi, (Ref 82), who developed a time-dependent reliability model that integrates continuum damage mechanics principles and Weibull analysis. This particular approach assumes that the failure processes for SCG and creep are distinct and separable mechanisms.

The remainder of this section outlines this approach, highlighting creep rupture with the intent to provide the design engineer with a method to determine an allowable stress for a given component lifetime and reliability. This is accomplished by coupling Weibull theory with the principles of continuum damage mechanics, which was originally developed by Kachanov (Ref 83) to account for tertiary creep and creep fracture of ductile metal alloys.

Ideally, any theory that predicts the behavior of a material should incorporate parameters that are relevant to its microstructure (grain size, void spacing, etc.). However, this would require a determination of volume-averaged effects of microstructural phenomena reflecting nucleation, growth, and coalescence of microdefects that in many instances interact. This approach is difficult even under strongly simplifying assumptions. In this respect, Leckie (Ref 84) points out that the difference between the materials scientists and the engineer is one of scale. He notes the materials scientist is interested in mechanisms of deformation and failure at the microstructural level and the engineer focuses on these issues at the component level. Thus, the former designs the material and the latter designs the component. Here, the engineer's viewpoint is adopted, and readers should note from the outset that continuum damage mechanics does not focus attention on microstructural events, yet this logical first approach does provide a practical model, which macroscopically captures the changes induced by the evolution of voids and defects.

This method uses a continuum-damage approach where a continuity function, ϕ, is coupled with Weibull theory to render a time-dependent damage model for ceramic materials. The continuity function is given by the expression:

$$\phi = [1 - b\,(\sigma_0)^m\,(m+1)t]^{(1/(m+1))} \tag{Eq 64}$$

where b and m are material constants, σ_0 is the applied uniaxial stress on a unit volume, and t is time. From this, an expression for a time to failure, t_f, can be obtained by noting that when $t = t_f$, $\phi = 0$. This results in the following:

$$t_f = \frac{1}{b\,(\sigma_0)^m\,(m+1)} \tag{Eq 65}$$

which leads to the simplification of ϕ as follows:

$$\phi = [1 - (t/t_f)]^{(1/(m+1))} \tag{Eq 66}$$

The above equations are then coupled with an expression for reliability to develop the time-dependent model. The expression for reliability for a uniaxial specimen is:

$$R = \exp\,[\,-V\,(\sigma/\beta)^{\alpha}] \tag{Eq 67}$$

where V is the volume of the specimen, α is the Weibull shape parameter, and β is the Weibull scale parameter. Incorporating the continuity function into the reliability equation and assuming a unit volume yields:

$$R = \exp\,[\,-(\sigma_0/\phi\beta)^{\alpha}] \tag{Eq 68}$$

Substituting for ϕ in terms of the time to failure results in the time-dependent expression for reliability:

$$R = \exp\left\{-\left(\frac{\sigma_0}{\beta}\right)^{\alpha}\left[1-\frac{t}{t_f}\right]^{-(\alpha/m+1)}\right\} \tag{Eq 69}$$

This model has been presented in a qualitative fashion, intending to provide the design engineer with a reliability theory that incorporates the expected lifetime of a brittle material component undergoing damage in the creep rupture regime. The predictive capability of this approach depends on how well the macroscopic state variable ϕ captures the growth of grain-boundary microdefects. Finally, note that the kinetics of damage also depend significantly on the direction of the applied stress. In the development described previously, it was expedient from a theoretical and computational standpoint to use a scalar state variable for damage because only uniaxial loading conditions were considered. The incorporation of a continuum-damage approach within a multiaxial Weibull analysis necessitates the description of oriented damage by a second-order tensor.

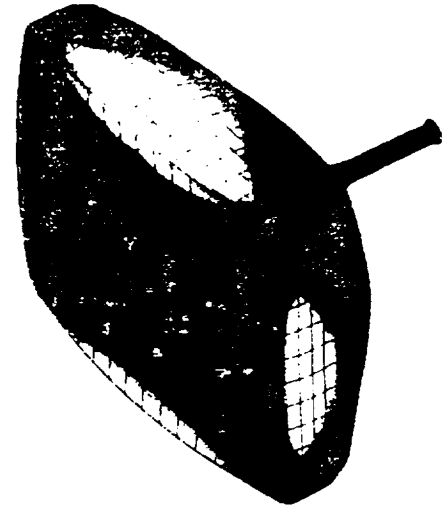

Fig. 13 Stress plot of an evacuated 68 cm (27 in.) diagonal CRT. The probability of failure calculated with CARES/Life was less than 5.0×10^{-3}. Courtesy of Philips Display Components Company

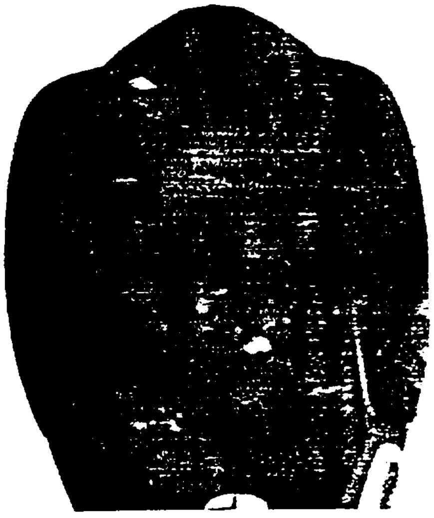

Fig. 14 Stress contour plot of ceramic dental crowi
sulting from a 600 N biting force. Courte
University of Florida College of Dentistry

Life-Prediction Reliability Algorithms

The NASA-developed computer program CARES/*Life* (Ceramics Analysis and Reliability Evaluation of Structures/Life-Prediction program) and the AlliedSignal algorithm ERICA have the capability to evaluate the time-dependent reliability of monolithic ceramic components subjected to thermomechanical and/or proof test loading. The reader is directed to Ref 39 and Ref 40 for a detailed discussion of the life-prediction capabilities of the ERICA algorithm. The CARES/*Life* program is an extension of the previously discussed CARES program, which predicted the fast-fracture (time-independent) reliability of monolithic ceramic components. CARES/*Life* retains all of the fast-fracture capabilities of the CARES program and also includes the ability to perform time-dependent reliability analysis due to SCG. CARES/*Life* accounts for the phenomenon of SCG by utilizing the power law, Paris law, or Walker equation. The Weibull cumulative distribution function is used to characterize the variation in component strength. The probabilistic nature of material strength and the effects of multiaxial stresses are modeled using either the PIA, the Weibull NSA, or the Batdorf theory. Parameter estimation routines are available for obtaining inert strength and fatigue parameters from rupture strength data of naturally flawed specimens loaded in static, dynamic, or cyclic fatigue. Fatigue parameters can be calculated using either the median value technique (Ref 85), a least squares regression technique, or a median deviation regression method that is somewhat similar to trivariant regression (Ref 85). In addition, CARES/*Life* can predict the effect of proof testing on component service probability of failure. Creep and material healing mechanisms are not addressed in the CARES/*Life* code.

Life-Prediction Design Examples

Once again, because of the proprietary nature of the ERICA algorithm, the life-prediction examples presented in this section are all based on design applications where the NASA CARES/*Life* algorithm was utilized. Either algorithm should predict the same results cited here. However, at this point in time comparative studies utilizing both algorithms for the same analysis are not available in the open literature. The primary thrust behind CARES/*Life* is the support and development of advanced heat engines and related ceramics technology infrastructure. This U.S. Department of Energy (DOE), and Oak Ridge National Laboratory (ORNL) have several ongoing programs such as the Advanced Turbine Technology Applications Project (ATTAP) (Ref 48, 86) for automotive gas turbine development, the Heavy Duty Transport Program for low-heat-rejection heavy-duty diesel engine development, and the Ceramic Stationary Gas Turbine (CSGT) program for electric power cogeneration. Both CARES/*Life* and the previously discussed CARES program are used in these projects to design stationary and rotating equipment, including turbine rotors, vanes, scrolls, combustors, insulating rings, and seals. These programs are also integrated with the DOE/ORNL Ceramic Technology Project (CTP) (Ref 87) characterization and life prediction efforts (Ref 88, 89).

The CARES/*Life* program has been used to design hot-section turbine parts for the CSGT development program (Ref 90) sponsored by the DOE Office of Industrial Technology. This project seeks to replace metallic hot-section parts with uncooled ceramic components in an existing design for a natural-gas-fired industrial turbine engine operating at a turbine rotor inlet temperature of 1120 °C (2048 °F). At least one stage of blades (Fig. 11) and vanes, as well as the combustor liner, will be replaced with ceramic parts. Ultimately, demonstration of the technology will be proved with a 4000 h engine field test.

Ceramic pistons for a constant-speed drive are being developed. Constant-speed drives are used to convert variable engine speed to a constant output speed for aircraft electrical generators. The calculated probability of failure of the piston is less than 0.2×10^{-8} under the most severe limit-load condition. This program is sponsored by the U.S. Navy and ARPA (Advanced Rese
Projects Agency, formerly DARPA, Defense
vanced Research Projects Agency). As depi
in Fig. 12, ceramic components have been
signed for a number of other applications,
notably for aircraft auxiliary power units.

Glass components behave in a similar ma
as ceramics and must be designed using reli
ity evaluation techniques. The possibility
kali strontium silicate glass CRTs spontane
imploding has been analyzed (Ref 91). Ca
ray tubes are under a constant static load d
the pressure forces placed on the outside
evacuated tube. A 68 cm (27 in.) diagonal
was analyzed with and without an implosio
tection band. The implosion protection ba
duces the overall stresses in the tube and,
event of an implosion, also contains the
particles within the enclosure. Stress an
(Fig. 13) showed compressive stresses
front face and tensile stresses on the sides
tube. The implosion band reduced the max
principal stress by 20%. Reliability analysi
CARES/*Life* showed that the implosion p
tion band significantly reduced the probabi
failure to about 5×10^{-5}.

The structural integrity of a silicon carbid
vection air heater for use in an advanced
generation system has been assessed by
and the NASA Lewis Research Center. T
sign used a finned tube arrangement 1.8
in.) in length with 2.5 cm (1 in.) diam
Incoming air was to be heated from 390 to
(734 to 1292 °F). The hot gas flow acr
tubes was at 980 °C (1796 °F). Heat trans
stress analyses revealed that maximum str
dients across the tube wall nearest the in
air would be the most likely source of fail

Probabilistic design techniques are be
plied to dental ceramic crowns, as illust
Fig. 14. Frequent failure of some ceramic
(e.g., 35% failure of molar crowns aft
years), which occurs because of resid

functional stresses, necessitates design modifications and improvement of these restorations. Thermal tempering treatment is being investigated as a means of introducing compressive stresses on the surface of dental ceramics to improve the resistance to failure (Ref 92). Evaluation of the risk of material failure must be considered not only for the service environment, but also from the tempering process.

REFERENCES

1. C.A. Johnson and W.T. Tucker, Advanced Statistical Concepts of Fracture in Brittle Materials, Vol 4, *Engineered Materials Handbook*, ASM International, *Ceramics and Glasses*, 1991, p 708–715
2. W.A. Weibull, The Phenomenon of Rupture in Solids, *Ing. Veten. Akad. Handl.*, No. 153, 1939
3. C.A. Johnson, Fracture Statistics of Multiple Flaw Populations, *Fracture Mechanics of Ceramics*, Vol 5, R.C. Bradt, A.G. Evans, D.P.H. Hasselman, and F.F. Lange, Ed., Plenum Press, 1983, p 365–386
4. W.A. Weibull, A Statistical Distribution Function of Wide Applicability, *J. Appl. Mech.*, Vol 18 (No. 3), Sept 1951, p 293–297
5. F.T. Pierce, "The Weakest Link" Theorems of the Strength of Long and of Composite Specimens, *Text. Inst. J.*, Vol 17, 1926, p T355–T368
6. T.A. Kontorova, A Statistical Theory of Mechanical Strength, *J. Tech. Phys. (USSR)*, Vol 10, 1940, p 886–890
7. J.I. Frenkel and T.A. Kontorova, A Statistical Theory of the Brittle Strength of Real Crystals, *J. Phys. USSR*, Vol 7 (No. 3), 1943, p 108–114
8. J. Hu, "Modeling Size Effects and Numerical Techniques in Structural Reliability Analysis," Master's thesis, Cleveland State University, Cleveland, OH, 1994
9. T.T. Shih, An Evaluation of the Probabilistic Approach to Brittle Design, *Eng. Fract. Mech.*, Vol 13 (No. 2), 1980, p 257–271
10. S.F. Duffy and S.M. Arnold, Noninteractive Macroscopic Statistical Failure Theory for Whisker Reinforced Ceramic Composites, *J. Compos. Mater.*, Vol 24 (No. 3), 1990, p 293–308
11. S.F. Duffy and J.M. Manderscheid, Noninteractive Macroscopic Reliability Model for Ceramic Matrix Composites with Orthotropic Material Symmetry, *J. Eng. Gas Turbines Power (Trans. ASME)*, Vol 112 (No. 4), 1990, p 507–511
12. N.N. Nemeth, J.M. Manderscheid, and J.P. Gyekenyesi, "Ceramics Analysis and Reliability Evaluation of Structures (CARES) Users and Programmers Manual," TP-2916, National Aeronautics and Space Administration, 1990
13. B. Gross and J.P. Gyekenyesi, Weibull Crack Density Coefficient for Polydimensional Stress States, *J. Am. Ceram. Soc.*, Vol 72 (No. 3), 1989, p 506–507
14. R.L. Barnett, C.L. Connors, P.C. Hermann, and J.R. Wingfield, "Fracture of Brittle Materials under Transient Mechanical and Thermal Loading," AFFDL-TR-66-220, U.S. Air Force Flight Dynamics Laboratory, March 1967
15. A.M. Freudenthal, Statistical Approach to Brittle Fracture. Fracture, An Advanced Treatise, *Mathematical Fundamentals*, Vol 2, H. Liebowitz, Ed., Academic Press, 1968, p 591–619
16. J. Margetson, "A Statistical Theory of Brittle Failure for an Anisotropic Structure Subjected to a Multiaxial Stress State, Paper 76-632, American Institute of Aeronautics and Astronautics, July 1976
17. A. Paluszny and W. Wu, Probabilistic Aspects of Designing with Ceramics, *J. Eng. Power*, Vol 99 (No. 4), Oct 1977, p 617–630
18. G.J. DeSalvo, "Theory and Structural Design Application of Weibull Statistics," WANL-TME-2688, Westinghouse Astronuclear Laboratory, 1970
19. J.L. Wertz and P.W. Heitman, "Predicting the Reliability of Ceramic Turbine Components. Advanced Gas Turbine Systems for Automobiles," SP-465, Society of Automotive Engineers, 1980, p 69–77
20. W.H. Dukes, *Handbook of Brittle Material Design Technology*, AGARDograph 152, AGARD, Paris, France, 1971
21. S.B. Batdorf, Fundamentals of the Statistical Theory of Fracture, *Fracture Mechanics of Ceramics*, Vol 3, R.C. Bradt, D.P.H. Hasselman, and F.F. Lange, Plenum Press, 1978, p 1–30
22. S.B. Batdorf and J.G. Crose, A Statistical Theory for the Fracture of Brittle Structures Subjected to Nonuniform Polyaxial Stresses, *J. Appl. Mech.*, Vol 41 (No. 2), June 1974, p 459–464
23. M. Giovan and G. Sines, Biaxial and Uniaxial Data for Statistical Comparison of a Ceramic's Strength, *J. Am. Ceram. Soc.*, Vol 62 (No. 9), Sept 1979, p 510–515
24. M.G. Stout and J.J. Petrovic, Multiaxial Loading Fracture of Al_2O_3 Tubes: I, Experiments, *J. Am. Ceram. Soc.*, Vol 67 (No. 1), Jan 1984, p 14–18
25. J.J. Petrovic and M.G. Stout, Multiaxial Loading Fracture of Al_2O_3 Tubes: II, Weibull Theory and Analysis, *J. Am. Ceram. Soc.*, Vol 67 (No. 1), Jan 1984, p 18–23
26. K. Palaniswamy and W.G. Knauss, On the Problem of Crack Extension in Brittle Solids Under General Loading, *Mech. Today*, Vol 4, 1978, p 87–148
27. D.K. Shetty, Mixed-Mode Fracture Criteria for Reliability Analysis and Design with Structural Ceramics, *J. Eng. Gas Turbines Power (Trans. ASME)*, Vol 109 (No. 3), July 1987, p 282–289
28. S.F. Duffy, L.M. Powers, and A. Starlinger, Reliability Analysis of Structural Components Fabricated from Ceramic Materials Using a Three-Parameter Weibull Distribution, *J. Eng. Gas Turbines Power (Trans. ASME)*, Vol 115 (No. 1), Jan 1993, p 109–116
29. G.D. Quinn, "Flexure Strength of Advanced Ceramics—A Round Robin Exercise," Materials Technology Laboratory TR-89-62 (Available from the National Technical Information Service, AD-A212101, 1989)
30. M.R. Foley, V.K. Pujari, L.C. Sales, and D.M. Tracey, Silicon Nitride Tensile Strength Data Base from Ceramic Technology Program for Reliability Project, *Life Prediction Methodologies and Data for Ceramic Materials*, C.R. Brinkman and S.F. Duffy, Ed., ASTM, to be published
31. L.-Y. Chao and D.K. Shetty, Reliability Analysis of Structural Ceramics Subjected to Biaxial Flexure, *J. Am. Ceram. Soc.*, Vol 74 (No. 2), 1991, p 333–344
32. S.F. Duffy, J.L. Palko, and J.P. Gyekenyesi, Structural Reliability of Laminated CMC Components, *J. Eng. Gas Turbines and Power (Trans. ASME)*, Vol 115 (No. 1), 1993, p 103–108
33. D.J. Thomas and R.C. Wetherhold, Reliability of Continuous Fiber Composite Laminates, *Comput. Struct.*, Vol 17, 1991, p 277–293
34. J.L. Palko, "An Interactive Reliability Model for Whisker-Toughened Ceramics," Master's thesis, Cleveland State University, Cleveland, OH, 1992
35. J. Margetson and N.R. Cooper, Brittle Material Design Using Three Parameter Weibull Distributions, *Proceedings of the IUTAM Symposium on Probabilistic Methods in the Mechanics of Solids and Structures*, S. Eggwertz and N.C. Lind, Ed., Springer-Verlag, 1984, p 253–262
36. S.S. Pai and J.P. Gyekenyesi, "Calculation of the Weibull Strength Parameters and Batdorf Flaw Density Constants for Volume and Surface-Flaw-Induced Fracture in Ceramics," TM-100890, National Aeronautics and Space Administration, 1988
37. J.P. Gyekenyesi and N.N. Nemeth, Surface Flaw Reliability Analysis of Ceramic Components with the SCARE Finite Element Postprocessor Program, *J. Eng. Gas Turbines Power (Trans. ASME)*, Vol 109 (No. 3), July 1987, p 274–281
38. J.P. Gyekenyesi, SCARE: A Postprocessor Program to MSC/NASTRAN for the Reliability Analysis of Structural Ceramic Components, *J. Eng. Gas Turbines Power (Trans. ASME)*, Vol 108 (No. 3), July 1986, p 540–546
39. J.C. Cuccio, P. Brehm, H.T. Fang, J. Hartman, W. Meade, M.N. Menon, A. Peralta, J.Z. Song, T. Strangman, J. Wade, J. Wimmer, and D.C. Wu, "Life Prediction Methodology for Ceramic Components of Advanced Heat Engines, Phase I," ORNL/Sub/89-SC674/1/V1, Vol 1, Final Report, Oak Ridge National Laboratory, March 1995
40. J.C. Cuccio, P. Brehm, H.T. Fang, J. Hartman, W. Meade, M.N. Menon, A. Peralta, J.Z. Song, T. Strangman, J. Wade, J. Wimmer, and D.C. Wu, "Life Prediction Methodology for Ceramic Components of Advanced Heat Engines, Phase I," ORNL/Sub/89-SC674/1/V2, Vol 2, Final Report, Oak Ridge National Laboratory, March 1995
41. C. Baker and D. Baker, Design Practices for Structural Ceramics in Automotive Turbocharger Wheels, *Ceramics and Glasses*, Vol 4, *Engineered Materials Handbook*, ASM International, 1991, p 722–727

42. C.J. Poplawsky, L. Lindberg, S. Robb, and J. Roundy, "Development of an Advanced Ceramic Turbine Wheel for an Air Turbine Starter," Paper 921945, presented at Aerotech '92, Anaheim, CA, Society of Automotive Engineers, 5–8 Oct 1992
43. J.H. Selverian, D. O'Neil, and S. Kang, Ceramic-to-Metal Joints: Part I-Joint Design, *Am. Ceram. Soc. Bull.*, Vol 71 (No. 9), 1992, p 1403–1409
44. J.H. Selverian and S. Kang, Ceramic-to-Metal Joints: Part II-Performance and Strength Prediction, *Am. Ceram. Soc. Bull.*, Vol 71 (No. 10), 1992, p 1511–1520
45. C.L. Snydar, "Reliability Analysis of a Monolithic Graphite Valve," presented at the 15th Annual Conference on Composites, Materials, and Structures (Cocoa Beach, FL), American Ceramic Society, 1991
46. J.A. Salem, J.M. Manderscheid, M.R. Freedman, and J.P. Gyekenyesi, "Reliability Analysis of a Structural Ceramic Combustion Chamber," Paper 91-GT-155, presented at the International Gas Turbine and Aeroengine Congress and Exposition, Orlando, FL, 3–6 June 1991
47. R.R. Wills and R.E. Southam, Ceramic Engine Valves, *J. Am. Ceram. Soc.*, Vol 72 (No. 7), 1989, p 1261–1264
48. J.R. Smyth, R.E. Morey, and R.W. Schultz, "Ceramic Gas Turbine Technology Development and Applications," Paper 93-GT-361, presented at the International Gas Turbine and Aeroengine Congress and Exposition (Cincinnati, OH), 24–27 May 1993
49. G.D. Quinn, Fracture Mechanism Maps for Advanced Structural Ceramics: Part 1; Methodology and Hot-Pressed Silicon Nitride Results, *J. Mater. Sci.*, Vol 25, 1990, p 4361–4376
50. N.N. Nemeth, L.M. Powers, L.A. Janosik, and J.P. Gyekenyesi, "CARES/*Life* Prediction Program (CARES/Life) Users and Programmers Manual," TM-106316, to be published
51. T.-J. Chuang, and S.F. Duffy, A Methodology to Predict Creep Life for Advanced Ceramics Using Continuum Damage Mechanics, *Life Prediction Methodologies and Data for Ceramic Materials*, STP 1201, C.R. Brinkman and S.F. Duffy, Ed., ASTM, 1994, p 207-227
52. Y. Corapcioglu and T. Uz, Constitutive Equations for Plastic Deformation of Porous Materials, *Powder Technol.*, Vol 21, 1978, p 269–274
53. H.A. Kuhn and C.L. Downey, Deformation Characteristics and Plasticity Theory of Sintered Powder Metals, *Int. J. Powder Metall.*, Vol 7, 1971, p 15–25
54. S. Shima and M. Oyane, Plasticity Theory for Porous Metals, *Int. J. Mech. Sci.*, Vol 18, 1976, p 285
55. R.J. Green, A Plasticity Theory for Porous Solids, *Int. J. Mech. Sci.*, Vol 14, 1972, p 215
56. A.L. Gurson, Continuum Theory of Ductile Rupture by Void Nucleation and Growth: Part 1¾ Yield Criteria and Flow Rules for Porous Ductile Media, *J. Eng. Mater. Technol.*, Vol 99, 1977, p 2–15
57. M.E. Mear and J.W. Hutchinson, Influence of Yield Surface Curvature on Flow Localization in Dilatant Plasticity, *Mech. Mater.*, Vol 4, 1985, p 395–407
58. J.-L. Ding, K.C. Liu, and C.R. Brinkman, A Comparative Study of Existing and Newly Proposed Models for Creep Deformation and Life Prediction of Si3N4, *Life Prediction Methodologies and Data for Ceramic Materials*, STP 1201, C.R. Brinkman and S.F. Duffy, Ed., ASTM, 1994, p 62–83
59. C.S. White, and R.M. Hazime, Internal Variable Modeling of the Creep of Monolithic Ceramics, *proceedings of the 11th Biennial Conference on Reliability, Stress Analysis, and Failure Prevention*, O. Jadaan, Ed., American Society of Mechanical Engineers, 1995
60. K.C. Liu, C.R. Brinkman, J.-L. Ding, and S. Liu, Predictions of Tensile Behavior and Strengths of Si_3N_4 Ceramic at High Temperatures Based on a Viscoplastic Model, *ASME Trans.*, 95-GT-388, 1995
61. D.N. Robinson, "A Unified Creep-Plasticity Model for Structural Metals at High Temperature," ORNL/TM 5969, Oak Ridge National Laboratory, 1978
62. S.F. Duffy, A Unified Inelastic Constitutive Theory for Sintered Powder Metals, *Mech. Mater.*, Vol 7, 1988, p 245–254
63. K.J. Willam and E.P. Warnke, Constitutive Model for the Triaxial Behaviour of Concrete, *Int. Assoc. Bridge Struct. Eng. Proc.*, Vol 19, 1975, p 1–30
64. L.A. Janosik and S.F. Duffy, A Viscoplastic Constitutive Theory for Monolithic Ceramic Materials—I, paper 15, *Proceedings of the Physics and Process Modeling (PPM) and Other Propulsion R&T Conference*, Vol I, *Materials Processing, Characterization, and Modeling; Lifing Models*, CP-10193, National Aeronautics and Space Administration, 1997
65. L.A. Janosik and S.F. Duffy, A Viscoplastic Constitutive Theory for Monolithic Ceramics—I, paper No. 96-GT-368, International Gas Turbine Congress, Exposition, and Users' Symposium (Birmingham, UK), American Society of Mechanical Engineers, 10–13 June 1996
66. J.R. Rice, On the Structure of Stress-Strain Relations for Time-Dependent Plastic Deformation in Metals, *J. Appl. Mech.*, Vol 37, 1970, p 728
67. A.R.S. Ponter and F.A. Leckie, Constitutive Relationships for Time-Dependent Deformation of Metals, *J. Eng. Mater. Technol. (Trans. ASME)*, Vol 98, 1976
68. L.A. Janosik, "A Unified Viscoplastic Constitutive Theory for Monolithic Ceramics," Master's thesis, Cleveland State University, Cleveland, OH, 1997, to be published
69. E.C. Bingham, *Fluidity and Plasticity*, McGraw-Hill, 1922
70. K. Hohenemser and W. Prager, Ueber die Ansaetze der Mechanik Isotroper Kontinua, *Z. Angewandte Mathemat. Mech.*, Vol 12, 1932 (in German)
71. A.G. Evans and S.M. Wiederhorn, Crack Propagation and Failure Prediction in Silicon Nitride at Elevated Temperatures, *J. Mater. Sci.*, Vol 9, 1974, p 270–278
72. S.M. Wiederhorn and E.R. Fuller, Jr., Structura Reliability of Ceramic Materials, *Mater. Sci Eng.*, Vol 71, 1985, p 169–186
73. S.M. Wiederhorn, E.R. Fuller, and R. Thomson Micromechanisms of Crack Growth in Ceramics and Glasses in Corrosive Environments *Met. Sci.*, Aug–Sept 1980, p 450–458
74. S.M. Wiederhorn, *Fracture Mechanics of Ceramics*, R.C. Bradt, D.P. Hasselman, and F.F Lange, Ed., Plenum, 1974, p 613–646
75. P. Paris and F. Erdogan, A Critical Analysis o Crack Propagation Laws, *J. Basic Eng.*, Vol 85 1963, p 528–534
76. K. Walker, The Effect of Stress Ratio Durin Crack Propagation and Fatigue for 2024-T3 an 7075-T6 Aluminum, *Effects of Environmer and Complex Load History on Fatigue Lif* STP 462, ASTM, 1970, p 1–14
77. R.H. Dauskardt, M.R. James, J.R. Porter, an R.O. Ritchie, Cyclic Fatigue Crack Growth i SiC-Whisker-Reinforced Alumina Cerami Composite: Long and Small Crack Behavior, *Am. Ceram. Soc.*, Vol 75 (No. 4), 1992, p 759 771
78. P.C. Paris and G.C. Sih, Stress Analysis c Cracks, *Fracture Toughness Testing and Its Ap plications*, STP 381, ASTM, 1965, p 30–83
79. T. Thiemeier, "Lebensdauervorhersage fu Keramische Bauteile Unter Mehrachsig Beanspruchung," Ph.D. dissertation, Universit of Karlesruhe, Germany, 1989 (in German)
80. G. Sturmer, A. Schulz, and S. Wittig, "Lifetir Prediction for Ceramic Gas Turbine Comp nents," Preprint 91-GT-96, American Society Mechanical Engineers, 3–6 June 1991
81. F. Lange, Interrelations Between Creep ar Slow Crack Growth for Tensile Loading Cond tions, *Int. J. Fract.*, Vol 12, 1976, p 739–744
82. S.F. Duffy and J.P. Gyekenyesi, "Time Depen ent Reliability Model Incorporating Continuu Damage Mechanics for High-Temperature C ramics," TM-102046, National Aeronautics ar Space Administration, May 1989
83. L.M. Kachanov, Time of the Rupture Proce Under Creep Conditions, *Izv. Akad. Nauk. SS Otd Tekh. Nauk*, Vol 8, 1958, p 26
84. F.A. Leckie, Advances in Creep Mechani *Creep in Structures*, A.R.S. Ponter and D. Hayhurst, Ed., Springer-Verlag, 1981, p 13
85. K. Jakus, D.C. Coyne, and J.E. Ritter, Analy of Fatigue Data for Lifetime Predictions Ceramic Materials, *J. Mater. Sci.*, Vol 13, 19 p 2071–2080
86. S.G. Berenyi, S.J. Hilpisch, and L.E. Gro close, "Advanced Turbine Technology Applic tions Project (ATTAP)," Proceedings of Annual Automotive Technology Developm Contractor's Coordination Meeting (Dearbo MI), 18–21 Oct 1993, SAE International
87. D.R. Johnson and R.B. Schultz, "The Ceran Technology Project: Ten Years of Progres Paper 93-GT-417, presented at the Internatio Gas Turbine and Aeroengine Congress and position (Cincinnati, OH), 24–27 May 19 American Society of Mechanical Engineers
88. J. Cuccio, "Life Prediction Methodology Ceramic Components of Advanced Heat

gines," Proceedings of the Annual Automotive Technology Development Contractor's Coordination Meeting (Dearborn, MI), 18–21 Oct 1993

89. P.K. Khandelwal, N.J. Provenzano, and W.E. Schneider, "Life Prediction Methodology for Ceramic Components of Advanced Vehicular Engines," Proceedings of the Annual Automotive Technology Development Contractor's Coordination Meeting (Dearborn, MI), 18–21 Oct 1993
90. M. van Roode, W.D. Brentnall, P.F. Norton, and G.P. Pytanowski, "Ceramic Stationary Gas Turbine Development," Paper 93-GT-309, presented at the International Gas Turbine and Aeroengine Congress and Exposition (Cincinnati, OH), 24–27 May 1993, American Society of Mechanical Engineers, 24–27 May 1993
91. A. Ghosh, C.Y. Cha, W. Bozek, and S. Vaidyanathan, Structural Reliability Analysis of CRTs, *Society for Information Display International Symposium Digest of Technical Papers*, Vol XXIII, 17–22 May 1992, Society of Information Display, Playa Del Ray, CA, p 508–510
92. B. Hojjatie, Thermal Tempering of Dental Ceramics, *Proceedings of the ANSYS Conference and Exhibition*, Vol 1, Swanson Analysis Systems Inc., Houston, PA, 1992, p I.73–I.91